University of the National Education Commission

Doctoral School

Discipline: Physical Sciences

Kink Dynamics in the sine-Gordon Model: Interaction with Inhomogeneities

Jacek Gatlik

Doctoral dissertation
under the supervision of
Dr hab. Tomasz Dobrowolski, prof. UKEN
and
Professor Panayotis G. Kevrekidis

KRAKÓW 2024

Uniwersytet Pedagogiczny im. Komisji Edukacji Narodowej w Krakowie

Szkoła Doktoska

Dyscyplina: Nauki Fizyczne

Dynamika kinku w modelu sinus-Gordona: oddziaływanie z niejednorościami

Jacek Gatlik

Praca doktorska
napisana pod kierunkiem
Dra hab. Tomasza Dobrowolskiego, prof. UKEN
oraz
Profesora Panayotisa G. Kevrekidisa

KRAKÓW 2024

I would like to express my gratitude to Professor Tomasz Dobrowolski for his invaluable support and mentoring throughout this journey. His belief in my potential and his guidance have contributed to my academic and personal growth. Most importantly, I am deeply grateful for his unique ability to reveal the elegance and wonder of theoretical physics.

I would like to express my gratitude to Professor Panayotis G. Kevrekidis, whose wisdom and guidance illuminated my path through research. His support and insightful criticism have played a significant role in shaping both this work and my academic journey. I am deeply grateful for his mentorship and the confidence he instilled in me.

List of publications included in this thesis

J. Gatlik and T. Dobrowolski,
Modeling kink dynamics in the sine–Gordon model with position dependent dispersive term,
Physica D: Nonlinear Phenomena, **428**, 133061 (2021)

J. Gatlik and T. Dobrowolski,
The impact of thermal noise on kink propagation through a heterogeneous system,
Physica D: Nonlinear Phenomena, **445**, 133649 (2023)

J. Gatlik, T. Dobrowolski, and Panayotis G. Kevrekidis,
Kink-inhomogeneity interaction in the sine-Gordon model,
Physical Review E, **108**, 034203 (2023)

J. Gatlik, T. Dobrowolski, and Panayotis G. Kevrekidis,
An effective description of the impact of inhomogeneities on the movement of the kink front in 2+1 dimensions,
Physical Review E, **109**, 024205 (2024)

List of publications not included in this thesis

K. Bąk, M. Bąk, J. Gatlik, and A. Błachowski,
Oscillating redox conditions in the Middle–Late Jurassic Alpine Tethys: Insights from selected geochemical indices and ^{57}Fe *Mössbauer spectroscopy*,
Palaeogeography, Palaeoclimatology, Palaeoecology, **537**, 109440 (2020)

K. Komędera, J. Gatlik, A. Błachowski, J. Żukrowski, T.J. Sato, D.Legut, and U.D. Wdowik,
Mössbauer studies of spin and charge modulations in $BaFe_2(As_{1-x}P_x)_2$,
Physical Review B, **103**, 024526 (2021)

K. Komędera, J. Gatlik, A. Błachowski, J. Żukrowski, D. Rybicki, A. Delekta, M. Babij, and Z. Bukowski,
^{57}Fe *and* ^{151}Eu *Mössbauer studies of* $3d-4f$ *spin interplay in* $EuFe_{2-x}Ni_xAs_2$,
Scientific Reports, **11**, 11484 (2021)

M. Karpierz, D. Nalecz, J. Suchanicz, and J. Gatlik,
DFT calculations for some perovskites and their solid solutions,
Physica Status Solidi B, **259**, 2100231 (2022)

Abstract

This doctoral dissertation focuses on a detailed study of the kink solutions of the modified sine-Gordon model. This involves a complex study of the effects of breaking translational invariance due to the presence of localized inhomogeneities and thermal noise. Generalizations to more spatial dimensions are also considered.

The research begins with a modification of the sine-Gordon model with a position-dependent dispersion term, which is essential for understanding the dynamics of the invariant phase difference of the macroscopic wave functions that describe superconducting electrodes in Josephson junctions. These modifications of the sine-Gordon equation make it applicable to junctions with different curvatures. This study further compares simplified descriptions of the kink motion in the junction with an exact field model, highlighting the limitations of traditional collective coordinate approaches and proposing another, in some situations preferable, alternative.

In the next part, the effect of thermal noise on kink propagation in heterogeneous systems, especially in curved long Josephson junctions, is also investigated. An analytical formula, based on the Fokker-Planck equation, was developed to estimate the probability of kink transmission through potential barriers as a function of the system temperature. The analytical approximation in this case turns out to be consistent with numerical simulations, especially at temperatures above 1K.

In addition, the interaction of sine-Gordon kink with localized inhomogeneities was carefully analyzed. The study focuses on how the potential energy barrier implied by the inhomogeneity affects the motion and stability of the kink, especially at velocities close to critical. Effective low-dimensional models are used to simulate kink dynamics, providing an insight into the behavior of the system in both dissipative and non-dissipative environments. These models accurately reproduce the results of the original field model.

This research culminates in an investigation of the effect of inhomogeneities on the motions of the kink front in 2+1 dimensions. An effective equation has been developed to represent the motion of the kink in various scenarios, including quasi-one-dimensional and purely two-dimensional inhomogeneities. This represents a significant advance in our understanding of the spectral characteristics of kink and dynamic interactions with inhomogeneities. Analytical predictions and computational results in these scenarios consistently agree, confirming the validity of the proposed models.

Abstrakt

Niniejsza rozprawa doktorska koncentruje się w szczególności na badaniu rozwiązań kinkowych w zmodyfikowanym modelu sinus-Gordona. Obejmuje ona kompleksową analizę efektów łamania niezmienniczości translacyjnej ze względu na obecność zlokalizowanych niejednorodności. W analizie tej uwzględniano także obecność szumu termicznego. Rozważania zostały również uogólnione na większą liczbę wymiarów przestrzennych.

Badania te rozpoczynają się od uzyskania zmodyfikowanego modelu sinus-Gordona z zależnym od położenia członem dyspersyjnym, którego obecność jest niezbędna do zrozumienia dynamiki niezmienniczej różnicy faz makroskopowych funkcji falowych opisujących elektrody nadprzewodzące z złączach Josephsona. Te modyfikacje równania sinus-Gordona sprawiają, że ma ono zastosowanie do złącz o różnych krzywiznach. Praca ta porównuje uproszczone opisy ruchu kinku w złączu z dokładnym modelem polowym, zwracając uwagę na ograniczenia tradycyjnych podejść opartych o współrzędne kolektywne, a zarazem proponując inną, wykazującą lepsze przybliżenia w niektórych sytuacjach, alternatywę.

W następnej części zbadano wpływ szumu termicznego na propagację kinku w układach niejednorodnych, w szczególności w zakrzywionych, długich złączach Josephsona. Opracowano wzór analityczny, oparty na równaniu Fokkera-Plancka, w celu oszacowania prawdopodobieństwa transmisji kinku przez barierę potencjału w funkcji temperatury układu. Przybliżenie analityczne w tym przypadku okazuje się być zgodne z symulacjami numerycznymi, szczególnie dla temperatur powyżej 1K.

Ponadto dokładnie przeanalizowano interakcję kinku ze zlokalizowanymi niejednorodnościami. Badania te koncentrują się na wpływie bariery potencjału, wynikającej z niejednorodności, na ruch i stabilność kinku szczególnie dla prędkości bliskich wartościom krytycznym. Efektywne modele niskowymiarowe są wykorzystywane do symulacji dynamiki kinku, zapewniając wgląd w zachowanie systemu zarówno w środowiskach dyssypatywnych, jak i nierozpraszających. Modele te dokładnie odtwarzają wyniki oryginalnego modelu polowego.

Zwieńczeniem prowadzonych badań było zbadanie wpływu niejednorodności na ruch frontu kinkowego w 2+1 wymiarach. Opracowano efektywne równanie reprezentujące ruch frontu kinkowego w różnych scenariuszach, w tym z quasi-jednowymiarowymi i czysto dwuwymiarowymi niejednorodnościami. Stanowi to znaczący postęp w naszym zrozumieniu charakterystyki widmowej kinku i dynamicznych interakcji z niejednorodnościami. Przewidywania analityczne i wyniki obliczeń numerycznych w tych scenariuszach zgadzają się, potwierdzając słuszność zaproponowanych modeli.

Contents

1 Introduction

This dissertation comprises a series of four articles focusing on the study of kink dynamics in the sine-Gordon model with particular emphasis on the applicability of the obtained results within the Josephson junction description framework. The articles are placed at the end of this dissertation and are preceded by an extended self-reference presenting the conducted research and introducing the most important topics.

The first section discusses the history of solitons and the Korteweg-de Vries equation used to describe them, in order to show their connection with the sine-Gordon equation and subsequently introduce the most important information related to it. The next section presents the history of the discovery of the Jospehson phenomenon and provides a deep dove into the method of description leading to the sine-Gordon equation. This study concludes with a broad overview of the possible applications and current use of the presented junctions, with special emphasis on the possible application of the results obtained in this thesis. The third section presents the main conclusions and methods used in the articles placed at the end. This section also includes a detailed summary of the work performed by the author within the framework of each article. The last section summarizes and draws conclusions from the conducted research, also indicating possible further avenues for developing this study.

1.1 Solitons

Understanding nonlinear phenomena is essential to unraveling the complexity of the natural world. While many physical systems exhibit linearity within narrow limits, their nonlinear behavior outside these constraints often holds the key to a deeper understanding of their internal dynamics. To get a holistic picture of such systems, their nonlinear characteristics must be meticulously considered. This is particularly important in the field of modern physics, where the study of nonlinear dynamics has revealed intriguing structures such as *solitons*.

In 1834, while working on improving barges on the Union Canal at Hermiston near Edinburgh, Scottish engineer John Scott Russell witnessed an unexpected phenomenon. When the rope towing one of the barges suddenly snapped, Russell observed the formation of a stable, solitary wave, which he called *wave of translation*. He described the discovery in these words:

> I believe I shall best introduce the phenomenon by describing the circumstances of my own first acquaintance with it. I was observing the motion of a boat which was rapidly drawn along a narrow channel by a pair of horses, when the boat suddenly stopped – not so the mass of water in the channel which it had put in motion; it accumulated round the prow of the vessel in a state of violent agitation, then suddenly leaving it behind, rolled forward with great velocity, assuming the form of a large solitary elevation, a rounded, smooth and well-defined heap of water, which continued its course along the channel apparently without change of form or diminution of speed. I followed it on horseback, and overtook it still rolling on at a rate of some eight or nine miles an hour, preserving its original figure some thirty feet long and a foot to a foot and a half in height. Its height gradually diminished, and after a chase of one or two miles I lost it in the windings of the channel. Such,

in the month of August 1834, was my first chance interview with that singular and beautiful phenomenon which I have called the Wave of Translation. [1]

In an attempt to better understand the phenomenon he observed, Russel prepared and conducted a series of laboratory experiments that allowed him to reproduce the conditions and effects of the original observation. The experiment he prepared consisted of dropping a weight at one end of a long water channel. The empirical deductions he made allowed him to observe that the volume of water thus displaced was the same as the volume of water forming the wave. He further demonstrated that the speed u of such a solitary wave can be described by the following relation

$$u^2 = g(h + a), \tag{1}$$

where g is the acceleration of gravity, h describes the depth of undisturbed water, while a describes the amplitude of the wave. Which made it possible to conclude that this solitary wave is a gravitational wave.

1.2 Korteweg–de Vries equation

The model proposed by Russell attracted independent interest from Joseph Boussinesq in 1871 and John William Strutt, Lord Rayleigh in 1876. With the assumption that an observed solitary wave has a length scale that is much greater than the depth of the water of the channel in which it moves, they derived Russell's formula for the velocity u from the equations of motion for an inviscid incompressible fluid [2–6].They also developed a formula for describing the wave profile, which takes the following form

$$\zeta(x, t) = a\,\mathrm{sech}^2(\beta(x - ut)), \tag{2}$$

where $\beta^{-2} = \frac{4h^2(h+a)}{3a}$ for any $a > 0$. However, it is worth mentioning here that the eq. (2) presented above is strictly satisfied only under the assumption of $\frac{a}{h} \ll 1$. However, the previously mentioned studies did not include a simple equation for which the wave profile presented in eq. (2) would be a solution. This last step was accomplished by Diederik Korteweg and Gustav de Vries in their 1895 paper [7]. They showed that if we assume that the given values of ε and σ are sufficiently small, then the equation is of the form

$$\frac{\partial \zeta}{\partial t} = \frac{3}{2}\sqrt{\frac{g}{h}}\left(\frac{2}{3}\varepsilon\frac{\partial \zeta}{\partial \chi} + \zeta\frac{\partial \zeta}{\partial \chi} + \frac{1}{3}\sigma\frac{\partial^3 \zeta}{\partial \chi^3}\right), \tag{3}$$

where the variable χ represents a coordinate that moves alongside a solitary wave. This equation can be easily represented in the form of the well-known KdV equation, i.e.

$$\zeta_t = \frac{3}{2}\sqrt{\frac{g}{h}}\left(\zeta\zeta_X + \frac{1}{3}\sigma\zeta_{X,X,X}\right), \tag{4}$$

where this time $\zeta = \zeta(X, t)$ is treated as a function of time and new space variable

$$X = \chi + \varepsilon\sqrt{\frac{g}{h}}t.$$

In the above equations, the σ parameter contains the γ surface tension according to the relation $\sigma = \frac{1}{3}h^3 - \frac{\gamma h}{g\rho}$ with ρ describing the density of the liquid. Parameter ε is chosen arbitrarily.

Due to the complex nonlinear nature of this equation, further study had to wait for the development of computational capabilities offered by computers. However, before we get to that, it is worth returning for a moment to the original observation made by Roussell. He presents two intriguing descriptions, the explanation of which is only possible in retrospect. First, he presents a wave that has some arbitrary initial profile distinct from a solitary wave, which then evolves into two or more waves, each of which gradually approaches the form of a single solitary wave. The second surprising observation is the situation in which the initial state consists of two waves, the second of which is higher than the first. In such a case, we can see that the higher wave catches up with the shorter one, then overtakes it and continues on its path unchanged and intact. This situation occurs even though the waves do not satisfy the principle of linear superposition. This observation provides a solid basis for assuming that we are dealing with a special type of nonlinear process.

One of the first direct pieces of evidence demonstrating the surprising properties of solitons was the results of research conducted on the MANIAC I computer at Los Alamos National Laboratory. This research was carried out by Enrico Fermi, John Pasta, Stanisław Ulam, and Mary Tsingou and published in 1955 [8]. It focused on a numerical simulation of phonons within a nonlinear lattice framework, which was later found to have a strong connection to the discrete form of the Korteweg-de Vries equation. They noted that the energy was not evenly distributed across the different modes. Considering these insights, Norman Zabusky and Martin David Kruskal in 1965 [9] analyzed the initial value problem associated with the equation

$$\phi_t + \phi\phi_x + \delta^2\phi_{x,x,x} = 0. \tag{5}$$

Assuming as an initial condition a function of the form

$$\phi(x, 0) = \cos \pi x, \qquad 0 \leqslant x \leqslant 2,$$

and assuming that the function and the derivatives (ϕ, ϕ_x, $\phi_{x,x}$) are periodic on a given range $[0, 2]$ for all values of t. They chose as the value of the dissipation $\delta = 0.022$. After a short period of time, they observed that a kind of local equilibrium between the nonlinearity and the action of the dispersion member is produced in the system. This reveals that consistent with Roussell's initial findings, larger waves are formed that overtake the smaller waves. This results in the remarkable realization that nonlinear waves can have intense interactions with one another, yet afterwards revert to a condition as though these interactions had never occurred.

The enduring nature of the wave prompted Zabusky and Kruskal to introduce the term *soliton* (akin to *photon*, *proton*, and similar terms) to highlight the particle-like qualities of these waves that appear to preserve their individuality after a collision. The properties of lone waves can be summarized following P. G. Drazin and R. S. Johnson [10] as follows

(i) represents a wave packet that maintains a consistent speed and shape,
(ii) is localized,
(iii) retains its original form after freely interacting with other solitons, except for a potential phase shift.

These discoveries and the amazing properties of solitons gave rise to intensive research on nonlinear equations such as just Korteweg-de Vries, the Nonlinear Schrödinger equation or the sine-Gordon equation, which is the subject of this paper. However, before going into a detailed description, it is worth mentioning in a few more words the use of solitons in modern physics.

In recent years, the concept of soliton has found applications not only in physics and mathematics but also in chemistry, biology, and medicine. The field in which most experiments and theoretical calculations on solitons have been conducted is definitely optical fibers. In this case, solitons are described using the Manakov system, which consists of Maxwell's equations transformed into cylindrical coordinates. In this description, it is necessary to consider the boundary conditions for the optical fiber and the phenomenon of birefringence. The first observation of soliton propagation was made by P. Emplit and his team in 1987 [11]. Today, solitons are used for high-speed data transmission over long distances using optical fibers.

In materials physics, solitons appear in ferroelectric materials as domain walls, which are areas of lattice dislocation that separate areas of opposite polarity [12]. These walls can move and retain their form, facilitating the switching of polarization states in the domain under certain conditions, such as electrical or mechanical stresses [13]. Similarly, different types of solitons occur in magnets as solutions to nonlinear differential equations such as the nonlinear Schrödinger equation, the Ishimori equation or the Landau-Lifshitz equation [14]. In addition, in the field of atomic physics, the concept of soliton is applicable, in particular atomic Bose-Einstain condensate exhibit soliton behavior [15]. Another interesting example of the occurrence of solitons are biological structures such as proteins and DNA [16]. Here, solitons are associated with the collective movement of these molecules at a low frequency. In addition, neuronal communication can occur through density wave-like signals carried by solitons [17]. More detailed examples of the use of solitons, particularly in the context of the sine-Gordon model, will be presented later in this study.

1.3 Sine-Gordon equation

Although, as will be shown later, the sine-Gordon equation first appeared in 1862, it is worth starting its history with its rediscovery in 1939. At that time, Yakov Frenkel together with Tatiana Kontorova presented the results of their study of *slip* propagation in an infinite chain of elastically bonded atoms. This chain lay on top of a stationary chain made of analogous atoms. The effect they observed can be approximated by a partial differential equation of the form

$$\frac{\partial^2 \phi}{\partial x^2} - \frac{\partial^2 \phi}{\partial t^2} = \sin \phi. \tag{6}$$

The initial term refers to the elastic interaction energy between neighboring atoms, the next term corresponds to their kinetic energy, and the last term refers to the potential energy resulting from the fixed lower chain. It is worth mentioning at this point a few words about the name of this equation. Its form resembles in structure the linear relativistic Klein-Gordon equation

$$\frac{\partial^2 \psi}{\partial x^2} - \frac{1}{c^2}\frac{\partial^2 \psi}{\partial t^2} = \mu^2 \phi.$$

It was this similarity that led to the use of the name *nonlinear Klein-Gordon equation*, and eventually the *sine-Gordon equation*, even though neither Osker Klein nor Walter Gordon had anything to do with its discovery.

Of the possible solutions to the sine-Gordon equation, the most interesting are the solitary waves of the form

$$\phi(\xi) = \phi(x - ut). \tag{7}$$

As can be noted, such solutions are only functions of one independent variable, where u is the velocity of wave propagation [18]. Hence, eq. (6) can be reduced to an ordinary differential equation of the form

$$(1 - u^2)\frac{d^2\phi}{d\xi^2} = \sin\phi. \tag{8}$$

Integration of the above equation leads to

$$\frac{1}{2}(1 - u^2)\frac{d\phi}{d\xi} = -\cos\phi + C. \tag{9}$$

where C is an arbitrary constant of integration. Since we are only looking for stable solutions therefore we can assume additional conditions in the form of $u < 1$ and $C = 1$ [19], and rewrite the eq. (9) in the following form

$$\frac{d\phi}{\sin\frac{\phi}{2}} = \pm\frac{2}{\sqrt{1 - u^2}}d\xi. \tag{10}$$

Using the form so obtained, one can perform the integration leading to the solution

$$\phi(\xi) = 4\arctan\left(e^{\pm\frac{\xi - \xi_0}{\sqrt{1-u^2}}}\right), \tag{11}$$

and finally after changing the variables

$$\phi(x, t) = 4\arctan\left(e^{\pm\frac{x - x_0 - ut}{\sqrt{1-u^2}}}\right), \tag{12}$$

The obtained solution represents a solitary wave moving at a given velocity $|u| < 1$. The $\pm$ sign defines the polarity of the kink, the solution with the $+$ sign is called kink while the one with the $-$ sign is called antikink, both of the solutions are shown in fig. 1.

1.3.1 Kink-antikink scattering solution

The other solution of eq. (6), as demonstrated by G. L. Lamb [20], takes the form of

$$\phi = 4\arctan\left(\frac{X(x)}{T(t)}\right). \tag{13}$$

By inserting this solution into the sine-Gordon equation, it can be shown that functions X and T have to fulfill the conditions

$$(X')^2 = kX^4 + mX^2 + n,$$
$$(T')^2 = -kT^4 + (m - 1)T^2 - n,$$

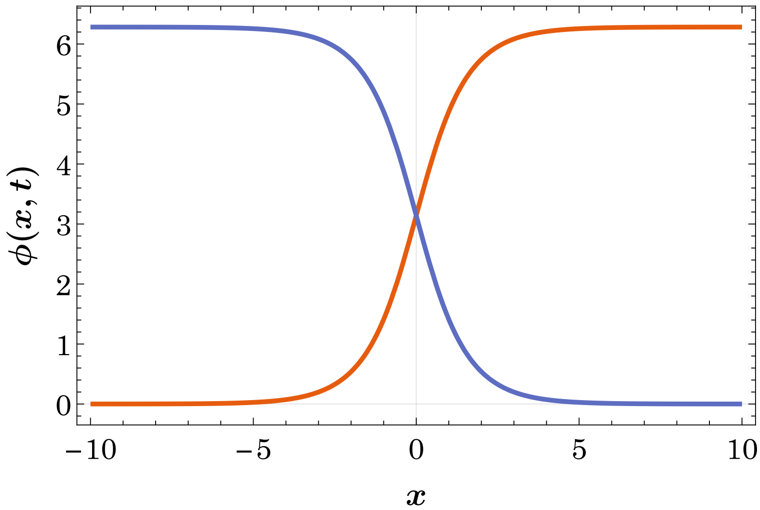

Figure 1: Solution kink (red) and anti-kink (blue), in both cases $x_0 = 0$ and $u = 0$.

where n, m, and k are arbitrary constants.

An interesting example of using a solution defined in this way would be one in which we assume that $k = 0$ and $n = m$. In such a case, the values of X and T can be represented as follows

$$\begin{aligned} X &= \sinh \sqrt{m} x, \\ T &= \frac{m}{m-1} \cosh \sqrt{(m-1)} t. \end{aligned}$$

Thus, the solution in this case will be of the form

$$\phi = 4 \arctan \left(\frac{u \sinh \left(\frac{x}{\sqrt{1-u^2}} \right)}{\cosh \left(\frac{ut}{\sqrt{1-u^2}} \right)} \right) \tag{14}$$

where $u = \sqrt{1 - \frac{1}{m}}$. This solution was originally presented in the work of J. K. Perring and T. H. R. Skyrme, which focused on describing the collision between two kinks [21].

1.3.2 The Bäcklund transformation

A Bäcklund transformation is a transformation that enables a given equation to be transformed into the same or another linear or nonlinear equation. With the existence of such a transformation emerges the possibility of mapping the solutions of one equation to the solutions of another. In particular, the transformation allows for a non-identical transformation of the equation into itself. In this case, it is said to be the auto-Bäcklund transformation. In this regard, one obtain the ability to transform some solutions of a given equation into other solutions of the same equation. First the sine-Gordon equation have to be transformed to the light-cone coordinates

$$\begin{aligned} x \to \zeta &= \frac{1}{2}(x+t), \\ t \to \xi &= \frac{1}{2}(x-t), \\ \phi(x,t) &\to \sigma_0(\zeta, \xi), \end{aligned} \tag{15}$$

which leads to the equation

$$\frac{\partial^2 \sigma_0}{\partial \zeta \partial \xi} = \sin \sigma_0. \tag{16}$$

The equation was initially implemented by Edmond Bour in 1862 while studying surfaces with constant negative curvature [22]. For the sine-Gordon equation, the Bäcklund transformation is of the form [23]

$$\begin{aligned} \frac{\partial}{\partial \zeta}\left(\frac{\sigma_1 - \sigma_0}{2}\right) &= a \sin\left(\frac{\sigma_1 + \sigma_0}{2}\right), \\ \frac{\partial}{\partial \xi}\left(\frac{\sigma_1 + \sigma_0}{2}\right) &= \frac{1}{a} \sin\left(\frac{\sigma_1 - \sigma_0}{2}\right). \end{aligned} \tag{17}$$

After the transformation one get again sine-Gordon equation

$$\frac{\partial^2 \sigma_1}{\partial \zeta \partial \xi} = \sin \sigma_1. \tag{18}$$

By using the basic idea of the Bäcklund transformation, that allows one to transform current solution into a new one. Knowing the solution σ_0, one can obtain a new solution σ_1 satisfying eq. (17). Considering a trivial solution $\sigma_0 = 0$, one obtains

$$\sigma_1 = 4 \arctan\left(e^{a\zeta + \frac{\xi}{a}}\right). \tag{19}$$

In addition, if one introduce a new parameter u

$$u = \frac{1 - a^2}{1 + a^2},$$

and use the transformation eq. (15), we get a kink solution in well known form eq. (12). As can be seen, by application Bäcklund transforamation it becomes possible to obtain an infinite number of new soliton solutions starting from zero-soliton state in the form of $\sigma_0 = 0$.

1.3.3 Inverse scattering transform

Although the method presented above based on the Bäcklund transform allows to obtain an infinite number of solutions using previous ones, there is a more general method that, at least formally, solves the sine-Gordon equation for arbitrary (with certain limitations) initial conditions, which is the *inverse scattering transform*. This technique is a nonlinear version and extension of the Fourier transform, and is used to solve many nonlinear partial differential equations. In very general terms, it involves reconstructing a potential from the scattering data. The method was first presented by C. Gardner, J. Greene, M. Kruskal, and R. Miura in two papers on solving the Korteweg-deVries equation [24, 25].

To introduce this method's operation in the context of the sine-Gordon equation, it is worth first looking at the well-known Schrödinger equation. In this equation, thanks to the known potential, it is possible to determine the so-called scattering data, which are the energy levels along with the number of localized states and the set of all reflection and transmission coefficients. The inverse scattering method uses the same idea but performs it in the opposite direction, thus recovering the potential information of the Schrödinger equation in a situation where the scattering data are known. Of course, the sine-Gordon equation is different from the

Schrödinger equation, but the problem can be solved by relating to it a set of two linear partial differential equations that will have the same potential in the solution.

Using this reasoning in practice, the first step is to associate a system of linear equations with the sine-Gordon equation. This system has an unambiguously given initial condition and the corresponding boundary conditions; therefore, using the direct scattering method, one can easily find the scattering data, which will also be a reflection of the potential at zero time. Then write out the equations that determine the evolution of such a specified system, which results in the knowledge of scattering data for any given time. At this point, therefore, all the information about the evolution of the associated linear problem is given, and it becomes possible to use the inverse scattering method to find the potential corresponding to this data. Because this potential is directly related to the solution of the sine-Gordon equation, therefore the potential at any time greater than zero defines the solution obtained for the given initial conditions.

1.4 Josephson junction

The *Josephson junction* has become a significant component of quantum physics and superconducting technology over the past decades. This breakthrough discovery was made by Brian D. Josephson, a 22-year-old British PhD student at the time, during his work on quantum tunneling. The calculations were published in Physics Letters on July 1, 1962 [26]. Figure 1 shows an illustrative diagram of Josephson's junction. As can be seen, such a junction consists of two superconductors separated by a thin insulator layer. The unusual operation of such a system lies deep in the principles of quantum mechanics and focuses on the ability of the Cooper pairs present in superconductors to tunnel the isolation barrier of the junction. Despite initial doubts about the existence of such a phenomenon [27], it was experimentally confirmed by Philip Anderson and John Rowell of the Bell Labs in Princeton in 1963 [28]. For his groundbreaking work, Brian Josephson was awarded the Nobel Prize in Physics in 1973.

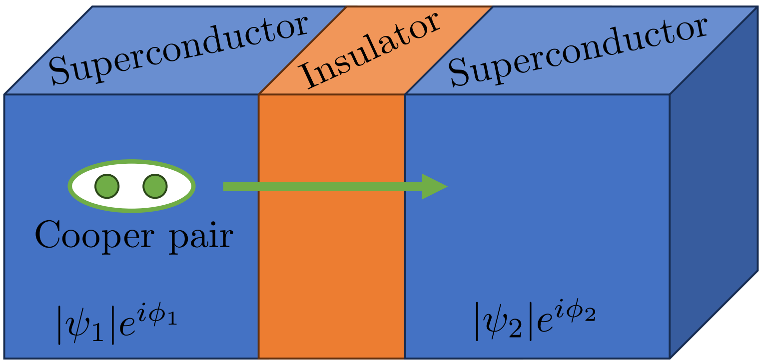

Figure 2: Schematic illustration of a Josephson junction consisting of two superconductors separated by a thin insulator layer.

The sine-Gordon equation presented earlier is directly applicable to the description of the dynamics of quasi-particle excitations in the Josephson junction. The next section present a method for construction of a low-energy effective description of the junction, which results in the appearance of the sine-Gordon equation in this context. The kink solution, in this system represents the *fluxon* - a quasiparticle carrying a quantum of magnetic flux [29].

1.4.1 Derivation of sine-Gordon equation in Josephson junction

As mentioned earlier, in each superconductor, electrons can move as Cooper pairs. If we define R as their density and phi as their quantum phase, one can easily describe the collective macroscopic wave function for all these electron pairs as follows

$$\psi = \sqrt{R}e^{i\phi}. \tag{20}$$

Examining the quantum mechanical properties of two superconductors placed at any distance from each other, it becomes obvious that each superconductor operates in its own unique quantum state, characterized by a distinct wave functions ψ_1 and ψ_2. Moreover, the phases of these wave functions ϕ_1 and ϕ_2 remain uncorrelated. However, the situation changes when the superconductors are sufficiently close to each other. In this case, the phase mentioned earlier becomes correlated because of the occurrence of insulator penetration by Cooper pairs. In this case, the system can be described by two coupled linear Schrödinger equations of the following form

$$\begin{aligned} i\hbar\frac{\partial\psi_1}{\partial t} &= E_1\psi_1 + k\psi_2, \\ i\hbar\frac{\partial\psi_2}{\partial t} &= E_2\psi_2 + k\psi_1. \end{aligned} \tag{21}$$

In the above description, E_1 and E_2 correspond to the value of the energy of the ground state in each of the two discussed superconductors, while the variable k is a coupling constant determined by the characteristics of the junction. This constant tends toward zero as the width of the insulator increases. Assuming a potential difference of V between the insulators, then the energy difference of the ground states can be determined as follows

$$E_1 - E_2 = 2eV.$$

Furthermore, if we choose the value of the average energy appropriately, we can assume that $\frac{E_1+E_2}{2} = 0$ which leads us to a simple relation

$$\begin{aligned} E_1 &= +eV, \\ E_2 &= -eV, \end{aligned}$$

and, as a result, to present eq. (21) in the following form

$$\begin{aligned} i\hbar\frac{\partial\psi_1}{\partial t} &= +eV\psi_1 + k\psi_2, \\ i\hbar\frac{\partial\psi_2}{\partial t} &= -eV\psi_2 + k\psi_1. \end{aligned} \tag{22}$$

This description can now be completed by using eq. (20) written individually for each superconductor in the form of $\psi_1 = \sqrt{R_1}e^{i\phi_1}$ and $\psi_2 = \sqrt{R_2}e^{i\phi_2}$. After inserting the independent forms of the wave functions, the separation of eq. (22) into real and imaginary parts can be made, obtaining the following

$$\begin{aligned}\hbar\frac{\partial R_1}{\partial t} &= -2k\sqrt{R_1R_2}\sin\phi,\\ \hbar\frac{\partial R_2}{\partial t} &= +2k\sqrt{R_1R_2}\sin\phi,\\ \hbar\frac{\partial \phi_1}{\partial t} &= k\sqrt{\frac{R_2}{R_1}}\cos\phi - eV,\\ \hbar\frac{\partial \phi_2}{\partial t} &= k\sqrt{\frac{R_1}{R_2}}\cos\phi + eV,\end{aligned} \tag{23}$$

where $\phi = \phi_2 - \phi_1$ represents the phase difference between the two wave functions. If the superconducting electrodes are made of the same material then the densities of Cooper pairs are equal to each other, i.e. $R_1 = R_2 \equiv R_0$, which allows to simplify the notation

$$\frac{2k}{\hbar}\sqrt{R_1R_2} = \frac{2kR_0}{\hbar} = J_0.$$

Since the change in the density of Cooper pairs in time represents current flow so from the second equation (23) we get

$$J = J_0\sin\phi. \tag{24}$$

Subtracting the last two equations of system eq. (23) leads to the relationship

$$\hbar\frac{d\phi}{dt} = 2eV. \tag{25}$$

Introducing the phase difference expressed in units of magnetic flux into the description

$$\Phi = \frac{\Phi_0}{2\pi}\phi,$$

equation (25) can be written in simple form

$$\frac{d\Phi}{dt} = V. \tag{26}$$

In the above description $\Phi_0 = \frac{h}{2e} \approx 2,1\cdot 10^{-15}Wb$ represents a quantum of magnetic flux. Combining the properties shown in eq. (24) and eq. (26), we can write the relations for Φ as

$$\Phi = \frac{\Phi_0}{2\pi}\arcsin\frac{J}{J_0} \tag{27}$$

With the above equations in place, one can now follow the two significant observations made by Josephson regarding the so-called *the DC Josephson effect* and *the AC Josephson effect*.

If one assumes that in the system under study the potential difference is equall to zero ($V = 0$), then according to eq. (25) the phase is constant $\phi = \text{const}$. Using eq. (24), it can be seen that in this situation, despite the absence of an applied voltage, there will be a finite current density J. The presence of current in the absence of an applied voltage in this system is a consequence of quantum tunneling effect, and the value of the current itself is proportional to the phase difference in the insulator (*Josephson phases*). This phenomenon is called the DC

Josephson effect.

On the other hand, if the potential difference has a constant value different from zero, i.e. $V = \text{const} = V_0$, then by integrating eq. (26) we obtain

$$\Phi = V_0 t + \Phi_C,$$

where Φ_C represents a constant of integration. This information can now be used in eq. eq. (24), leading to a current density in the form of

$$J = J_0 \sin \frac{2\pi}{\Phi_0}(V_0 t + \Phi_C). \tag{28}$$

For the current density thus described, we can also determine an angular frequency as follows

$$\omega_J = \frac{2\pi V_0}{\Phi_0} = \frac{2eV_0}{\hbar}. \tag{29}$$

On the basis of eq. (28), it is easy to see that when a constant voltage is applied to the junction, the phase will change linearly over time, while the current itself will be a sinusoidal AC current. This phenomenon is known as the AC Josephson effect, which shows that the Josephson junction can function as an excellent voltage-to-frequency converter.

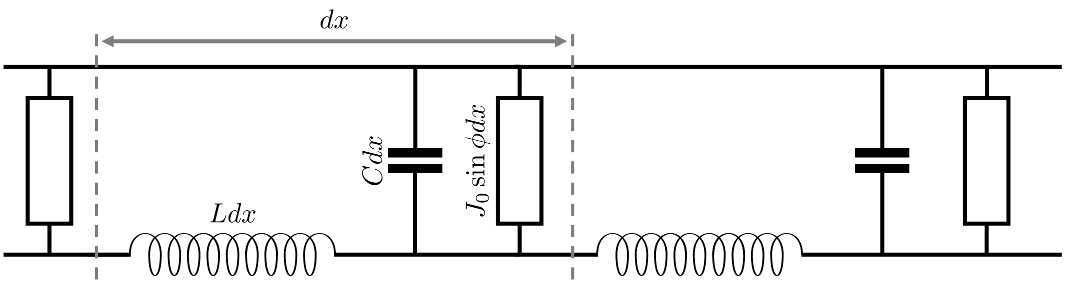

Figure 3: Diagram showing the equivalent circuit of a long Josephson junction with the specified dx element, which is the equivalent circuit per unit length.

The behavior of a point junction can be used to describe a long Josephson junction. As shown in fig. 3, a long Josephson junction can be described as a collection of point junctions. Each point junction in the figure is represented by an equivalent circuit. In particular, by determining a portion of the equivalent circuit dx, we can consider the equivalent circuit per unit length. Assuming that in the junction under study, the insulator layer has a thickness of d and l stands for the width of the superconducting strip, it can be seen that capacitance per unit length is equal to

$$C = \frac{\varepsilon_d \varepsilon_0 l}{d}, \tag{30}$$

and inductance per unit lenght can be written as

$$L = \mu_0 \frac{2\lambda_L + d}{l}. \tag{31}$$

In the above equations, ε_d denotes the dielectric constant of the junction separator, ε_0 is the vacuum permittivity, μ_0 is vacuum magnetic permeability, and λ_L represents the London's penetration depth in the superconductors. Using Kirshohf's voltage law, one can subsequently obtain the following

$$\frac{\partial V}{\partial x} = -L\frac{\partial I}{\partial t}. \tag{32}$$

On the other hand, using Kirshohf's current law one gets

$$\frac{\partial I}{\partial x} = -C\frac{\partial V}{\partial t} - J_0 \sin 2\pi\frac{\Phi}{\Phi_0}. \tag{33}$$

To the above equations one should also add information about the phase change over time

$$\frac{\partial \Phi}{\partial t} = V. \tag{34}$$

The description thus prepared can be combined to obtain a sine-Gordon equation of the following form

$$\frac{\partial^2 \phi}{\partial t^2} - c_J^2\frac{\partial^2 \phi}{\partial x^2} + \omega_p^2 \sin\phi = 0, \tag{35}$$

where

$$c_J = \frac{1}{\sqrt{LC}},$$
$$\omega_p = \sqrt{\frac{2\pi J_0}{\Phi_0 C}}.$$

This equation describes the dynamics of the phase difference in the long Josephson junction. It is worth noting that the above notations allow easy introduction of an additional quantity of the form $\frac{c_J}{\omega_p}$, which has the dimension of length and is called Josephson penetration length. Its value allows to determine whether the junction under study meets the conditions for the description of a long junction or not.

1.4.2 Application of Josephson junction

The Josephson junctions have found numerous technical applications. First, Josephson junctions are used in constructions of SQUIDs (Superconducting Quantum Interference Devices) which are very sensitive magnetometers. Sensitivity of SQUIDs is sufficient to measure magnetic fields of order 10^{-18} T; for comparison, the magnetic fields in animal brains are between 10^{-9} T and 10^{-6} T. This unusual precision makes SQUIDs effective and useful in biology and medicine, especially in cardiology, magneto-gastrography, magneto-encephalography, and others. SQUIDs have also found applications as the sensor in gyroscopes on Gravity Probe B, to observe the dynamical Casimir effect for the first time [30], and were used in D-Wave Systems 2000Q quantum computers. This device is also used in earthquake diagnostics, in explorations of minerals, and in military applications [31].

In the future SQUIDs are expected to have a military application, especially in anti-submarine warfare as a MAD (Magnetic Anomaly Detector). SQUIDs could also find application in SPMR (Superparamagnetic relaxometry). SPMR technology uses superparamagnetic properties of magnetite nanoparticles and SQUID sensitivity. These nanoparticles have no magnetic moment, however become ferromagnetic after being exposed to an external field. When the external magnetic field is removed, they return to the paramagnetic state with some characteristic time. The time depends on the binding of the nanoparticle to the surface, and on its size. SQUIDs are used to detect and localize the nanoparticles by field decaying measurement. It could find possible applications in cancer detection [32].

The second application of the Josephson junction is SET (Single Electron Transistor). This device is a type of a very sensitive switch that uses only single electrons to change the state of the circuit from "on" to "off" position and vice versa by the uses of controlled electron tunnelling to change the value of current. It is made of two junctions that share a low capacitance common electrode named "island" and is capacitive connected to the gate which is the third electrode. Because of the connection, the island's electrical potential may be adjusted. In the "off" state there are no accessible energy levels on the electrode because all energy levels on the island electrode with lower energies are occupied. Therefore, electrons cannot tunnel onto the island electrode. However, when a positive voltage is provided to the gate (the "on" state), the levels of the island are decreased and electrons can tunnel onto it [33].

Because of low power consumption and high operating speed SET could be the key for future nanotechnology devices. SET could also find applications in random access memory and digital data storage technologies. Same of the possible applications are programmable single-electron transistor logic, charge state logic, single-electron spectroscopy, detection of infrared radiation, and super-sensitive electrometers. SET could also be used in standards of temperature and DC current [34].

It seems that in the near future the Josephson junction will find possible applications in digital electronics technology. One of the possible applications is RSFQ electronics (Rapid Single Flux Quantum) relies on quantum effects in Josephson junctions to process digital signals. In this device magnetic flux quanta with digital information are carried by picosecond duration voltage pulses that travel along the superconducting transmission lines. The pulses can be as narrow as 1 picosecond with an amplitude of about 2 mV. It makes this technology useful especially for computer applications. Operating frequency of RSFQ logic could be extremely fast up to hundreds of gigahertz with about 100,000 times lower power consumption than CMOS semiconductor circuits [35]. RSFQ found applications in ultrafast digital signal processing, high performance cryogenic computers and control circuitry for superconducting qubits [36]. Future computers made in this technology could be much faster than the traditional ones and with lower power consumption.

Last but not least example where the Josephson junction could find a possible application is quantum computing [37, 38]. This kind of computers can solve problems by applying different aspects of quantum mechanical states [39]. A quantum computer uses qubits instead of bits in a classical one. A classical bit is represented by one of the logical values 0 or 1. However, in the case of qubits, they are two-dimensional quantum systems. Their Hilbert spaces are spanned by two vectors $|0\rangle$ and $|1\rangle$. This is why, unlike bits, the quantum state of a qubit is a superposition of these states. Increasing the number of qubits also leads to an increase in the number of possible superposition states. Generally, n qubits correspond to 2^n different states of superposition. Comparing it to a classical computer, performing one manipulation on a quantum computer corresponds to doing 2^n operations at the same time in a classical case. This equipment works by manipulating qubits with the predetermined sequence of quantum logic gates. The product of these unitary operators forms the quantum algorithm. On the basis of the Josephson junction, such qubits are proposed in three different types.

1. First is a charge qubit (otherwise known as Cooper-pair box) proposed in 1997 [40]. The charge qubit is made of a small superconducting island connected to a superconducting reservoir through a superconducting tunnel junction (Josephson junction). If Cooper pairs are present in the island it corresponds to the state $|1\rangle$ and the absence corresponds to the state $|0\rangle$. The quantum superposition of those charge states is determined by the gate voltage [37, 41, 42]. In a charge qubit the relaxation time T_2 is on the order of $1 - 2\mu s$ [43].

2. Second is a flux qubit (otherwise known as a persistent current qubits) proposed in 1999 in MIT [44]. It is a short loop superconducting metal, which is interrupted by the Josephson junctions. When the external flux is applied a persistent current flows continually. Here, the basis states are circulating currents that can flow in either a clockwise or counter clockwise orientation. To be able to **uses** it as a qubit a half flux quanta must be applied to the loop to bring the two levels together. For this purpose, the microwave frequency radiation could be used [45].

3. Third is a phase qubit. It is based on SIS Josephson junction and uses energy levels of the "phase particle." At low temperatures (much less than $1K$) quantum energy levels exist in the local minima. The ground state becomes the "0" state and the first excited state the "1" state of the qubit. The difference between the "0" and the "1" state could be changed by the external bias current [46].

For all of the above-mentioned cases, the key to obtaining junctions with the desired properties is to design them appropriately based on achievable parameters. One of the possibilities to obtain the desired parameters is the engineering of the junction geometry. In the literature one can find many examples of junction shaping in order to obtain unique properties, e.g. a junction with an exponentially tapered width [47]; the heart-shaped annular junction [48, 49]; two perpendicular Josephson T-Lines forming a T junction [50]; a similar Y junction [51, 52]; an annular junction delimited by two closely spaced confocal ellipses [53, 54]; and finely change of the curvature of the junction [55–60]. The application of each of these methods allows the junctions with specified and required properties to be obtained.

2 Method and Results

2.1 Modeling kink dynamics in the sine–Gordon model with position dependent dispersive term

The first of the articles included in this dissertation is a paper entitled *Modeling kink dynamics in the sine-Gordon model with position dependent dispersive term*, which was published in 2021 [59]. This study focuses on the modified sine-Gordon equation, which includes a function that explicitly breaks the translational invariance of the original equation. The considered equation has the following form

$$\partial_t^2\phi - \partial_x(\mathcal{F}(x)\partial_x\phi) + \sin\phi = 0, \tag{36}$$

where function $\mathcal{F}$ is given as

$$\mathcal{F} = 1 + \varepsilon g(x), \quad g(x) = \theta(x) - \theta(x-L). \tag{37}$$

The physical motivation for this research is based on the occurrence of the dispersion term presented in the above equation in Josephson junctions. The second section of this article presents the derivation of the discussed equation in the case where the given function $\mathcal{F}$ can be identified with the curvature of the Josephson junction. Starting with a given supercurrent density in the presence of a magnetic field in the junction in the form

$$\vec{j} = \frac{e^*}{m^*}\left[\frac{1}{2}\imath\hbar\left(\psi\nabla\psi^* - \psi^*\nabla\psi\right) - \frac{e^*}{c}\vec{A}\psi\psi^*\right]. \tag{38}$$

Here, e^* and m^* stand for the charge and mass of Cooper pairs, while $\psi = |\psi|e^{i\varphi}$ is the many-particle wave function describing the superconducting electrode. From the above relationship, the phase of the wave function can be determined as a function of the current and the fields present in the system

$$\nabla\varphi = \frac{2e}{\hbar c}\left[\frac{mc}{2|\psi|^2e^2}\vec{j} + \vec{A}\right]. \tag{39}$$

This time e and m denotes the charge and mass of the electron. In curvilinear coordinates based on the junction surface (described in Appendix A of the paper), the useful component of the gradient takes the form of

$$\frac{1}{G}\partial_s\varphi = (\mathbf{grad}\varphi)_s = \frac{2e}{\hbar c}\left[\frac{mc}{2|\psi|^2e^2}j_s{}^{SH} + A_s\right] = \frac{2e}{\hbar c}A_s. \tag{40}$$

The G function is directly related to the curvature of the junction. Then by selecting the integration contour accordingly and using Stokes' theorem, one can relate the phase difference of the wave functions of the superconducting electrodes ϕ to the proper component of the magnetic field H_ρ

$$\frac{1}{G}\partial_s\phi = \frac{1}{G}\left(\frac{\phi(s+ds)-\phi(s)}{ds}\right) = \frac{2e}{\hbar c}d_mH_\rho. \tag{41}$$

The constant d_m describes how deeply the magnetic field penetrates the central region of the junction. On the other hand, the Ampere's circular law with the Maxwell correction leads to

$$\frac{1}{G}\,\partial_s H_\rho = \frac{4\pi}{c}\,j_u + \frac{\varepsilon}{ac}\,\partial_t(\Delta V). \tag{42}$$

In the above formula, ΔV is the potential difference between the lower and upper surfaces of the dielectric layer. Adding the second Josephson's law to these relationships and then averaging the resulting formula with respect to the normal variable and using the notations $\bar{c} = \sqrt{\frac{a}{\varepsilon d_m}}c$ for Swihart velocity and $\lambda_J = \sqrt{\frac{\hbar c^2}{8\pi e d_m j_0}}$ for Josephson penetration depth, we obtain eq. (36). The constant a in the above expressions is the thickness of the dielectric layer, while j_0 is the critical Josephson current density. An important feature of the above derivation is that it does not impose limits on either the curvature values nor on the rate of change of curvature along the junction. The presented derivation of the eq. (36) also shows, the practical area of applicability of the studied modification of the sine-Gordon equation.

The next section describes the possible dynamics of the kink in the studied system. These results are based on the numerical solution of the full field model for different initial conditions and for different values of the parameter ε, which determines the junction curvature. Numerical calculations were performed using *Mathematica* software based on the Adams method. This method is an example of a linear multistep method that, unlike single-step methods, uses information obtained from previous steps. This method uses extrapolative interpolation polynomials built from a certain number of previous derivative values of the analyzed function. In the studied system, there are two possible situations depending on the initial velocity of the kink. In the first case, if the kink velocity is too low, it will reflect from the inhomogeneity and start moving toward the initial position. On the other hand, if the initial speed is sufficiently high, it will pass through the inhomogeneity and continue to move through the system. The limiting velocity is called the critical (threshold) velocity.

The results obtained from the solution of the full field model are compared in the next section with the results obtained from the study of approximate methods. The first one was a comparison of the kink solution energy in homogeneous and inhomogeneous systems. This comparison is based on the assumption that in the initial state, the kink rests at such a large distance from the inhomogeneity that it can be approximately treated with the description of a homogeneous system. In contrast, at the very end of the motion, if its velocity corresponds exactly to the value of the critical velocity, it stops at the limit of the potential barrier possessing only a non-zero value of potential energy. This makes it straightforward to determine the kinetic energy at the beginning in the form of

$$(E_{\mathcal{F}})_{in} = \frac{8}{\sqrt{1-u_c^2}}, \tag{43}$$

and at the end of the motion as

$$(E_{\mathcal{F}})_{fin} = 8 + 4\varepsilon \tanh\frac{L}{2}. \tag{44}$$

By comparing these energies, it is possible to determine the value of the critical velocity, which is equal to

$$u_c = \sqrt{1 - \frac{1}{(1 + \frac{1}{2}\varepsilon \tanh \frac{L}{2})^2}}. \tag{45}$$

To compare the results obtained using this method with those obtained using other methods, a system of ordinary differential equations describing the movement of the kink was also obtained in the following form

$$\begin{aligned} \frac{du}{dt} &= \frac{1}{4}\,\varepsilon\sqrt{1-u^2}\left(\operatorname{sech}^2\frac{L-x_0}{\sqrt{1-u^2}} - \operatorname{sech}^2\frac{x_0}{\sqrt{1-u^2}}\right), \\ \frac{dx_0}{dt} &= u. \end{aligned} \tag{46}$$

The results obtained are presented in Figures 6-9[59]. As can be seen, these results do not satisfactorily reflect the solution of the partial differential equation. As postulated later in the paper, one of the reasons for this inconsistency may be that not all kink participates in the interaction with inhomogeneity. To verify this hypothesis, the concept of active mass was introduced to denote the actual mass of the kink involved in the interaction. This mass was determined from the solutions of the full model, and including it in the framework of the equations of motion (eq. (46)) allowed excellent agreement between the results of the approximate model and the solutions of the full field theory model.

Another approximation model considered was a perturbation scheme based on the method proposed by D. McLaughlin and A. Scott [61]. This approach is built on the separation of the part describing the difference between the sine-Gordon model and the considered field equation, which can be represented as

$$\partial_t^2\phi - \partial_x^2\phi + \sin\phi = \varepsilon\partial_x(g(x)\partial_x\phi) = \varepsilon f(\phi). \tag{47}$$

Using the path presented by the authors of the mentioned article, it is possible to determine the system of effective equations of motion

$$\begin{aligned} \frac{du}{dt} &= \frac{1}{4}\,\varepsilon\sqrt{1-u^2}\left(\operatorname{sech}^2\frac{L-X}{\sqrt{1-u^2}} - \operatorname{sech}^2\frac{X}{\sqrt{1-u^2}}\right), \\ \frac{dX}{dt} &= u + \frac{1}{4}\,\varepsilon u\left(\tanh\frac{X}{\sqrt{1-u^2}} + \tanh\frac{L-X}{\sqrt{1-u^2}} + V(X)\right), \end{aligned} \tag{48}$$

where

$$V(X) = \frac{X}{\sqrt{1-u^2}}\operatorname{sech}^2\frac{X}{\sqrt{1-u^2}} + \frac{L-X}{\sqrt{1-u^2}}\operatorname{sech}^2\frac{L-X}{\sqrt{1-u^2}}. \tag{49}$$

The obtained result allow comparison with both solutions of the full field model and solutions from other approximate models. However, it is worth noting here that the results obtained by this method present the lowest agreement compared with those obtained from the partial differential equation.

The third approach is based on projecting onto the zero mode of the kink solution. This method has been previously used to study the behavior of systems described by the ϕ^4 model in papers [62, 63]. This approach is based on the application of the kink ansatz in the field equation. As presented in detail in the discussed article, such a procedure leads to a system of equations of motion similar to those obtained by energy approximation (eq. (46)).

The last of the presented approaches is based on projection onto energy density. This method has not been used before in the context presented here, and like the active mass concepts introduced earlier, it allows the calculation to take into account a more concentrated distribution near the kink core. The procedure is similar to the projecting onto zero mode method mentioned earlier, except that the mode is replaced by the energy density

$$Eq = 0 \Longrightarrow \langle \operatorname{sech}^2\xi, Eq\rangle \equiv \int_{-\infty}^{\infty} dx \operatorname{sech}^2\xi \, Eq = 0. \tag{50}$$

Which finally leads to the equations of motion in the following form

$$\begin{aligned} &\left(3+u^2\right)\frac{du}{dt} = \frac{4}{\pi}\,\varepsilon\sqrt{1-u^2}\left(\operatorname{sech}^2\frac{L-x_0}{\sqrt{1-u^2}} - \operatorname{sech}^2\frac{x_0}{\sqrt{1-u^2}}\right), \\ &\frac{dx_0}{dt} = u. \end{aligned} \tag{51}$$

The results obtained by this method show, in considered range of parameters, significantly higher agreement than the other methods discussed earlier, and are only slightly poorer than the results that consider the fit parameter in the form of active mass. The last section of this article provides a comprehensive summary of the results discussed, which will also be discussed in section 3 of this thesis.

Authorship contribution: My work as a co-author of this article consisted of partially performing analytical calculations, performing all numerical calculations of the solution of the full model and approximate methods, and partially preparing the final version of the manuscript.

2.2 The impact of thermal noise on kink propagation through a heterogeneous system

The second article was entitled *The impact of thermal noise on kink propagation through a heterogeneous system* and was publisher in 2023 [64]. This research focuses on investigating the effect of thermal noise on the motion of kink in Jospeshon junctions with a given curvature. Within the framework of this article, a sine-Gordon model with disipation due to quasiparticle currents and bias current was considered in the follwoing form

$$\partial_t^2\phi + \alpha\partial_t\phi - \partial_x(\mathcal{F}(x)\partial_x\phi) + \sin\phi = -\Gamma. \tag{52}$$

Using the method presented in the previous article, the potential for the force that represents the barrier associated with the curved part of the Josephson junction was calculated in the form

$$\begin{aligned} V(x_0) = \varepsilon\frac{3}{4\pi}\Bigg[&\arctan\left(\tanh\left(\frac{x_0-x_i}{2}\right)\right) - \arctan\left(\tanh\left(\frac{x_0-x_f}{2}\right)\right) + \\ &\frac{1}{2}\operatorname{sech}(x_0-x_i)\tanh(x_0-x_i) - \frac{1}{2}\operatorname{sech}(x_0-x_f)\tanh(x_0-x_f)\Bigg]. \end{aligned} \tag{53}$$

As before, here too one can apply reasoning in which the kink at the beginning is assumed to be at a very large distance from the inhomogeneity by which it has only non-zero kinetic energy resulting from the given initial velocity

$$E_{in} = \frac{1}{2} m_0 {u_c}^2, \tag{54}$$

and at the end of the motion, if it moves exactly at the critical speed, it will stop at the top of the inhomogeneity occurring in the system with potential energy

$$E_{fin} = V(x_0 = L/2) = \frac{32}{3\pi}\, \varepsilon \left[2 \arctan\left(\tanh \frac{L}{4}\right) + \text{sech}\frac{L}{2} \tanh \frac{L}{2}\right]. \tag{55}$$

Using this information along with the principle of conservation of energy, this leads directly to the determination of the critical velocity value depending on the parameters of the junction as

$$u_c = \sqrt{\frac{8}{3\pi}\, \varepsilon}\, \sqrt{2 \arctan\left(\tanh \frac{L}{4}\right) + \text{sech}\frac{L}{2} \tanh \frac{L}{2}}. \tag{56}$$

In this manner, the controlling physical parameter for the system under study was determined. Having this information, it becomes possible to analyze the effect of temperature on the ability of the kink to pass through the potential barrier present in the system. The analysis of the effect of temperature is based on the assumption that the bias current is a random dependent (fluctuating) variable due to the non-zero temperature at the junction in the form

$$< \Gamma(t) >= \Gamma_0. \tag{57}$$

The described thermal noise can be considered within the white Gaussian noise framework

$$< \Gamma(t)\Gamma(t') >= A\delta(t - t'). \tag{58}$$

To determine the coefficient A appearing in the above equation, the system in thermal equilibrium was considered when the equation describing the position of the kink has the following form

$$\dot{u} + \alpha u = \frac{2}{\pi}\Gamma - r, \tag{59}$$

which, under assumption of constant r, has a following solution

$$u(t) = \frac{2}{\pi}\int_0^t dt'\, \Gamma(t') e^{\alpha(t'-t)} - \frac{r}{\alpha}\,(1 - e^{-\alpha t}). \tag{60}$$

This solution allows to calculate the time correlation function of the velocity and express it in the thermodynamic limit as

$$< u(t)^2 >= \frac{2A}{\pi^2\alpha} + \left(\frac{r}{\alpha}\right)^2 - \frac{4\Gamma_0}{\pi\alpha^2}\, r. \tag{61}$$

After a sufficiently long time, when thermodynamic equilibrium is reached, the fluxon energy can be expressed as

$$E_k = \frac{1}{2}\, m < u(t)^2 >= \frac{1}{2}\, m \left[\frac{2A}{\pi^2\alpha} + \left(\frac{r}{\alpha}\right)^2 - \frac{4\Gamma_0}{\pi\alpha^2}\, r\right]. \tag{62}$$

At the same time, under thermodynamic equilibrium and based on the principle of energy equipartition, it is known that energy will be proportional to temperature as follows

$$E_k = \frac{1}{2}\,kT. \tag{63}$$

These considerations directly lead to the determination of the value of the coefficient A in the following form

$$A = \frac{\pi^2 \alpha k(T - \Delta T)}{2m}, \tag{64}$$

where

$$\Delta T \equiv \frac{m}{k}\left[\left(\frac{r}{\alpha}\right)^2 - \frac{4\Gamma_0}{\pi\alpha^2}\,r\right]. \tag{65}$$

Due to the fact that in the described system there is a bias current, the fluctuations of which are directly related to temperature, it is convenient to transform the above equation in such a way that it contains the threshold value of the current, which directly corresponds to the critical value of the velocity in this system. The above equation takes the form

$$\Delta T = \Omega(\Gamma_c - \Gamma_0) - \omega \tag{66}$$

where

$$\omega \equiv \frac{m}{k}\left[\frac{4\Gamma_c}{\pi\alpha^2}\,r - \left(\frac{r}{\alpha}\right)^2\right], \quad \Omega \equiv \frac{4m}{\pi\alpha^2 k}.$$

Summarizing the above considerations, the bias current dependent on thermal fluctuations is expressed as

$$<\Gamma(t)>= \Gamma_0, \;\; <\Gamma(t)\Gamma(t')>= \frac{\pi^2 \alpha k(T - \Delta T)}{2m}\,\delta(t - t'). \tag{67}$$

This equation becomes the starting point for derivation of the Fokker-Planck equation which is detailed in Appendix B [64] of this article. These calculations lead to an equation describing the stationary solution in the following form

$$P(u) = \sqrt{\frac{m}{2\pi k(T - \Delta T)}}\,\exp\left(-\frac{m}{2k(T - \Delta T)}\,(u - u_s)^2\right). \tag{68}$$

This becomes the basis for determining the total probability of a kink passing through the potential barrier in this system.

$$\Delta P = \int_{u_c}^{\infty} du P(u) = \frac{1}{2}\,\mathrm{erf}\left(\sqrt{\frac{m}{2k(T - \Delta T)}}\;|\; u_c - u_s \;|\right) \tag{69}$$

The results obtained were then compared with those from the solution of the full model. As before, within the framework of solving the partial differential equation, Mathematica software was used with the Adams method as the basis. Temperature fluctuations were generated by randomizing the current bias using a function that allows for high randomness of the variable. Each value of the initial kink velocity was repeated a thousand times to obtain satisfactory statistics. The results derived in this way made it possible to demonstrate the validity of the proposed formula over a wide temperature range. A detailed discussion of the results obtained is given in section 3.

Authorship contribution: My work as a co-author of this article consisted of partially performing analytical calculations, performing all numerical calculations of the solution of the full model for all cases, and reviewing and editing the final version of the manuscript.

2.3 Kink-inhomogeneity interaction in the sine-Gordon model

In the next paper, titled *Kink-inhomogeneity interaction in the sine-Gordon model* and published in 2023 [60], the focus was on a thorough investigation of the behavior of kinks during interactions with inhomogeneities. Unlike the first article, the primary objective here was not to solely determine the controlling physical parameters, but rather to accurately describe the interaction at velocities very close to the critical velocity value. Furthermore, the aim was to investigate stable and quasi-stable solutions for this model. All of these behaviors have been precisely described using models with one and two degrees of freedom. The general equation containing dissipation and current bias was considered in the following form

$$\partial_t^2\phi + \alpha\partial_t\phi - \partial_x(\mathcal{F}(x)\partial_x\phi) + \sin\phi = -\Gamma. \tag{70}$$

First, quasi-static solutions for the kink located on the top of the described inhomogeneity in the case in which both the dissipation and bias current were zero were investigated. A linear stability study of the deformed kink configuration ϕ_0 requires a decomposition of the ϕ field into kink and a small perturbation of the form $\psi = e^{i\omega t}v(x)$

$$-\partial_x\left(\mathcal{F}(x)\,\partial_x v(x)\right) + (\cos\phi_0)\,v(x) = \lambda v(x). \tag{71}$$

As can be seen, the function v satisfies an equation resembling the stationary Schrödinger equation. Using the Newton-Raphson iteration, the identification of quasi-static solution ϕ_0 of the kink was performed. This procedure also calculates the Jacobian, which provides direct information about the kink's eigenfrequencies. The algorithm used in the Newton-Raphson method was prepared using Matlab software. Moreover, the shape of the deformed, due to the existence of inhomogeneity, kink configuration ϕ_0 can be estimated based on the following equation

$$-\partial_x\left(\mathcal{F}(x)\partial_x\chi\right) + (\cos\phi_K)\chi = \varepsilon\partial_x\left(g(x)\partial\phi_K\right), \tag{72}$$

here ϕ_K stands for undeformed kink configuration. It was found that for a kink located on a barrier in the spectrum, there is an unstable mode, which has its origin in the zero mode of the kink solution present in sine-Gordon model without inhomogeneities. The presence of this mode shows, the instability of the ϕ_0 configuration.

Similar considerations have been performed for the case of the existence of current and dissipation in the system. Based on similar reasoning, by application of the Newton-Raphson method, the form of the deformed kink configuration stopped by the potential barrier was established. Moreover, the stability of this configuration was proved on the base of the same reasoning.

In the next part of the article under discussion, the main focus was on the effective description of kink dynamics in inhomogeneities. Initially, attention was concentrated on the change of the Lagrangian density

$$\mathcal{L}_{FSG} = \mathcal{L}_{SG} + \mathcal{L}_{\varepsilon} = \mathcal{L}_{SG} - \frac{1}{2}\varepsilon g(x)(\partial_x \phi)^2. \tag{73}$$

where $\mathcal{L}_{SG}$ describes the Lagrangian density of the sine-Gordon model and $\mathcal{L}_{\varepsilon}$ represents the interaction of the field with inhomogeneity. In order to convert the full field theory model to an ordinary differential equation, ansatz of the form was used

$$\phi_k(t, x) = 4 \arctan e^{x - x_0(t)}. \tag{74}$$

Here x_0 is a collective variable describing the position of the kink. The effective equation of motion describing the dynamics of this variable is of the form

$$\ddot{x}_0 = \varepsilon \left(\frac{1 - x_0 \coth x_0}{\sinh^2 x_0} - \frac{1 - (x_0 - L) \coth (x_0 - L)}{\sinh^2 (x_0 - L)} \right). \tag{75}$$

To obtain a more complete picture of the discussed interactions, projection onto the zero mode, discussed in more detail within the framework of the first article, was also applied. This method allowed to determine the equation of motion in the presence of dissipation and bias current in the system

$$\ddot{x}_0 + \alpha \dot{x}_0 + \varepsilon \left(\frac{x_0 \coth x_0 - 1}{\sinh^2 x_0} - \frac{(x_0 - L) \coth(x_0 - L) - 1}{\sinh^2(x_0 - L)} \right) = \frac{\pi}{4}\Gamma. \tag{76}$$

Both methods can describe the behavior of kink inside inhomogeneities with satisfactory accuracy and correctly predict the value of the first mode in the linear spectrum of kink excitation. In addition, the second method also captured oscillations due to disipation, which occur in the case of a kink whose initial velocity is insufficient to cross the potential barrier. The next section also discusses the other approach based on the non-conservative Lagrangian method, which allows the field equation to be obtained by taking into account the standard conservative Lagrangian and the non-conservative contribution part leads to the equation

$$\partial_\mu \left(\frac{\partial \mathcal{L}}{\partial(\partial_\mu \phi)} \right) - \frac{\partial \mathcal{L}}{\partial \phi} = \lim_{\phi_- \to 0} \left\{ \lim_{\phi_+ \to \phi} \left[\frac{\partial \mathcal{R}}{\partial \phi_-} - \partial_\mu \left(\frac{\partial \mathcal{R}}{\partial(\partial_\mu \phi_-)} \right) \right] \right\}. \tag{77}$$

It is interesting to note that the final equation obtained in this way coincides with equation eq. (76).

The remainder of this paper focuses on a detailed study of the two-degree-of-freedom model, which should allow a better description of the kink dynamics. For this purpose, the ansatz was used in the following form

$$\phi_K(t, x) = 4 \arctan e^{\gamma(t)(x - x_0(t))}. \tag{78}$$

As in the case of methods using a one-degree-of-freedom, also here began with a construction based on a conservative Lagrangian. For an instance in which the inhomogeneity is described by step functions, this leads to a system of the following equations of motion

$$
\begin{aligned}
\ddot{x} + \frac{\dot{\gamma}}{\gamma}\dot{x}_0 + \frac{1}{4}\varepsilon\gamma\left[\operatorname{sech}^2(\gamma x_0) - \operatorname{sech}^2(\gamma(x_0 - L))\right] = 0,\\
\frac{2\pi^2}{3}\frac{\ddot{\gamma}}{\gamma} - \pi^2\frac{\dot{\gamma}^2}{\gamma^2} - 4\gamma^2\dot{x}^2 + 4\left(\gamma^2 - 1\right) + 2\varepsilon\gamma^2\left[\tanh(\gamma x_0) - \tanh(\gamma(x_0 - L))\right]\\
+ 2\varepsilon\gamma^3\left[x_0\operatorname{sech}^2(\gamma x_0) - (x_0 - L)\operatorname{sech}^2(\gamma(x_0 - L))\right] = 0.
\end{aligned}
\tag{79}
$$

A projection onto the zero mode was then performed, resulting in a set of equations for a system with dissipation and bias current present. In particular, this system reduces to eq. (79) if the dissipation and current are zero and has the form

$$
\begin{aligned}
\ddot{x} + \alpha\dot{x}_0 + \frac{\dot{\gamma}}{\gamma}\dot{x}_0 + \frac{1}{4}\varepsilon\gamma\left[\operatorname{sech}^2(\gamma x_0) - \operatorname{sech}^2(\gamma(x_0 - L))\right] = \frac{\pi}{4\gamma}\Gamma,\\
\frac{2\pi^2}{3}\left(\frac{\ddot{\gamma}}{\gamma} + \alpha\frac{\dot{\gamma}}{\gamma}\right) - \pi^2\frac{\dot{\gamma}^2}{\gamma^2} - 4\gamma^2\dot{x}^2 + 4\left(\gamma^2 - 1\right) + 2\varepsilon\gamma^2\left[\tanh(\gamma x_0) - \tanh(\gamma(x_0 - L))\right]\\
+ 2\varepsilon\gamma^3\left[x_0\operatorname{sech}^2(\gamma x_0) - (x_0 - L)\operatorname{sech}^2(\gamma(x_0 - L))\right] = 0.
\end{aligned}
\tag{80}
$$

These results were also compared with the non-conservative Lagrangian method, for which the equations of motion took the following form

$$
\begin{aligned}
\ddot{x}_0 + \frac{\dot{\gamma}}{\gamma}\dot{x}_0 - \frac{1}{8\gamma}\frac{\partial L_\varepsilon}{\partial x_0} = -\alpha\dot{x}_0 + \frac{\pi}{4\gamma}\Gamma,\\
\frac{2\pi^2}{3}\frac{\ddot{\gamma}}{\gamma} - \pi^2\frac{\dot{\gamma}^2}{\gamma^2} - 4\gamma^2\dot{x}_0^2 + 4(\gamma^2 - 1) - \gamma^2\frac{\partial L_\varepsilon}{\partial\gamma} = -\frac{2\pi^2}{3}\alpha\frac{\dot{\gamma}}{\gamma}
\end{aligned}
\tag{81}
$$

The results obtained from the conducted calculations allowed to approximate very well the solutions of the full field-theory model through the proposed methods. In particular, the methods with one degree of freedom satisfactorily describe the motion of the kink inside the inhomogeneities at velocity values close to the critical velocity, and correctly reflect the value of the first oscillating mode in the linear spectrum. The addition of a second degree of freedom allowed to improve the obtained description of the position of the kink, especially in the case of the non-conservative Lagrangian model, which best describes both the behavior and equally correctly reflects the beginning of the continuous spectrum for the linear spectrum of quasi-stable and stable kink solutions. A detailed discussion of the obtained results can be found in section 3.

Authorship contribution: My work as a co-author of this article consisted of partially performing analytical calculations, performing all numerical calculations of the solution of the full model and approximate methods, and partially preparing the final version of the manuscript.

2.4 An effective description of the impact of inhomogeneities on the movement of the kink front in 2+1 dimensions

The culmination of the research conducted in this dissertation is an article entitled *An effective description of the impact of inhomogeneities on the movement of the kink front in 2+1 dimensions*, which was published in 2024 [65]. This study focuses on the analysis of the effects caused by the presence of inhomogeneities on the movement of kink fronts in the 2+1 dimensional case. As before, a sine-Gordon model including a dissipation term and a current bias is also considered alongside with a term describing evolution in the second spatial dimension. The model is described as follows

$$\partial_t^2\phi + \alpha\partial_t\phi - \partial_x(\mathcal{F}(x,y)\partial_x\phi) - \partial_y^2\phi + \sin\phi = -\Gamma. \tag{82}$$

One of the effective methods for describing a system in which dissipation is present is to use the framework introduced in the publications [66, 67]. The presented method is based on a nonconservative Lagrangian density, with the variables of the system duplicated, in which additional term is included to address nonconservative forces

$$\mathcal{L}_N = \mathcal{L}(\phi_1, \partial_t\phi_1, \partial_x\phi_1, \partial_y\phi_1) - \mathcal{L}(\phi_2, \partial_t\phi_2, \partial_x\phi_2, \partial_y\phi_2) + \mathcal{R}. \tag{83}$$

In the above formula, $\mathcal{L}$ stands for standard lagrangian density

$$\mathcal{L}(\phi, \partial_t\phi, \partial_x\phi, \partial_y\phi) = \frac{1}{2}(\partial_t\phi)^2 - \frac{1}{2}\mathcal{F}(x,y)(\partial_x\phi)^2 - \frac{1}{2}(\partial_y\phi)^2 - V(\phi). \tag{84}$$

Assuming the form of the function $\mathcal{R} = -\alpha\phi_-\partial_t\phi_+ - \Gamma\phi_-$ in the above notation, it is possible to determine the model according to eq. (82). On the basis of such a proposed description of the studied system, it becomes possible to perform further calculations to determine an effective 1+1 dimensional model describing the movement of the center of the kink front using the Euler–Lagrange equations. Detailed calculations are thoroughly presented in the article, and as a result, a model of the form is given

$$M\partial_t^2 X - M\partial_y^2 X - \varepsilon\int_{-\infty}^{+\infty} g(x,y)K^{'}(x-X)K^{''}(x-X)dx = -\alpha M\partial_t X + 2\pi\Gamma, \tag{85}$$

where $K(x-X) = \phi_k(t,x)$ from eq. (74). The function $g(x)$ appearing in the above equation defines the inhomogeneity present in this system as a component of the function $\mathcal{F}$ from eq. (82) as follows

$$\mathcal{F}(x,y) = 1 + \varepsilon g(x,y) = 1 + \varepsilon p(x)q(y). \tag{86}$$

In particular, this function can be considered as the product of the part that depends on the x variable and the part that depends on the y variable. Taking this into account, it becomes possible to calculate the integral occurring within eq. (83), which for the case when the inhomogeneity function for the x variable has a stepped form

$$\partial_t^2 X + \alpha\partial_t X - \partial_y^2 X + \frac{1}{8}\varepsilon q(y)\left(\operatorname{sech}\left(\frac{h}{2}+X\right)^2 - \operatorname{sech}\left(\frac{h}{2}-X\right)^2\right) = \frac{1}{4}\pi\Gamma. \tag{87}$$

On the other hand, if one considers the case in which inhomogeneity is characterized by a continuous function

$$p(x) = \frac{1}{2}\left(\tanh\left(x+\frac{h}{2}\right) - \tanh\left(x-\frac{h}{2}\right)\right), \tag{88}$$

then the following equation is obtained

$$\partial_t^2 X + \alpha \partial_t X - \partial_y^2 X + \frac{1}{2}\varepsilon q(y) \left(\frac{(\frac{h}{2} + X)\coth(\frac{h}{2} + X) - 1}{\sinh^2(\frac{h}{2} + X)} - \frac{(\frac{h}{2} - X)\coth(\frac{h}{2} - X) - 1}{\sinh^2(\frac{h}{2} - X)} \right) = \frac{1}{4}\pi\Gamma. \tag{89}$$

Taking the $1 + 1$-dimensional model given in this way, the next part of the article discusses its comparison with the solution of the full field theory model. Initially, these comparisons focus on the case of a homogeneous system in which the parameter describing the height of inhomogeneity is zero. A comparison of the two results for the initial velocity determined from the dissipation constant and the bias current shows very good agreement between the obtained results.

Various scenarios were then analyzed, including deformations of the kink front (sinusoidal and more complex shapes), and comparisons were made at different time intervals.The results indicate that the approximate model accurately reflects the results of the full-field model, especially for slower front deformations. The next section of the paper focuses on the case with uniform inhomogeneity in the y-direction. It analyzes scenarios such as kink reflection from the barrier, interaction with near-critical parameter values and high-speed kink motion. Each scenario was analyzed under different conditions, such as with and without dissipation and external forcing. Comparisons show good agreement between the two models, with minor deviations observed in some cases. The last section of the numerical comparisons presents a situation in which the inhomogeneity is explicitly two-dimensional and takes the form of a peak or well of potential. Various interactions (such as passing through or stopping by the inhomogeneities) are examined, with the approximate model showing good agreement with the full model, especially in long-term simulations.

The numerical results show that the $1 + 1$-dimensional effective model is generally in good agreement with the $2+1$-dimensional full-field model in various scenarios, with some limitations in more complex cases.

Two cases of stable solutions are observed when the full field theory model is solved. The first is a kink trapped in the potential well, whereas the second is a kink that stops before the peak occurring in the system if dissipation is present. To further investigate these phenomena, the last part of the article examines the linear stability in these cases. The linear spectrum of a stable kink solution can be determined based on the following equation

$$-\partial_x \left(\mathcal{F}(x,y)\,\partial_x v(x,y)\right) - \partial_y^2 v(x,y) + (\cos\phi_0)\, v(x,y) = \lambda v(x,y), \tag{90}$$

the function ϕ_0 is determined using the Newtona-Raphsona method. The results obtained were compared with approximate solutions showing satisfactory agreement. A detailed discussion of the results obtained is given in section 3.

Authorship contribution: My work as a co-author of this article consisted of partially performing analytical calculations, performing all numerical calculations of the solution of the full model for all cases, and reviewing and editing the final version of the manuscript.

3 Conclusion

The research presented in this dissertation delves deeply into the dynamics of kink solutions in the modified sine-Gordon model, undertaking a thorough investigation of how localized inhomogeneities which perturb translational invariance and the effect of thermal noise affects kink's motion.

This research is conducted not only in the $1+1$ dimensional case, but also for 2+1 dimensions, including the explicit consideration of two-dimensional inhomogeneities. This involves analyzing how the introduction of additional spatial parameters changes the behavior of kink solutions and affects the stability and evolution in these systems. Exploring multidimensional spaces provides a richer context for understanding the complex interactions and phenomena that occur in the modified sine-Gordon model, particularly in scenarios where conventional analyses may not capture the full spectrum of dynamics present in more complex systems. Through this multifaceted approach, the research aims to provide a more comprehensive understanding of the phenomena behind kink solutions, offering insights that could be crucial to advancing the field and applying these findings to practical usage.

The first article discussed provided insight and understanding of the effect of the presence of inhomogeneities in the system on the controlling physical parameters of the junction. The calculations examined four methods of describing kink dynamics. In the case of the first three methods, which have their previous reflection in the approaches known from the literature, it was possible to propose corrections that, after considering the active mass of the kink in place of its static mass, allow reproducing in a very good way the results of the solution of the field model. However, a new approach for this system is the use of projection on the energy density. The obtained results, which in their idea also allow taking into account the better focused part of the kink, which is actively involved in the interaction with inhomogeneities, show satisfactory agreement with the full model. In addition, it is worth noting here that this method does not require additional fitting of parameters. The results of the critical velocity values depending on the parameters of the junction curvature are directly applicable to experimental systems consisting of Josephson junctions. This is due to the fact that by determining the value of this velocity, it becomes possible to determine the relationship between dissipation and threshold bias current occurring in the system.

Continuing the study of the behavior of the controlling physical parameters in the case of a curved Josephson junction described by the sine-Gordon model, the following study considers the effect of non-zero temperature on the process of potential barrier penetration. Using the Fokker-Planck equation, an analytical model describing the probability of kink transition and reflection was obtained. Comparison of the received results showed that the achieved description reflects the simulations resulting from the solution of the field model very well. The only deviation from the proposed description appears at temperatures less than $1K$. In this case, even the use of the relativistic model did not result in a significant improvement. However, while conducting calculations, it was possible to observe the occurrence of resonance windows, which can explain the obtained discrepancy. The windows correspond to narrow sets of initial parameters for which there is a transition below the critical velocity or its absence above this velocity. This fact makes the estimation of probabilities for values that belong to the ranges of occurrence of resonance windows very difficult, leading at the same time to distortion of the results. The cause and the mechanism causing the occurrence of this phenomenon in the studied system remain unclear. The explanations presented so far are based on the influence of the excited mode present in the linear spectrum of the kink, however, this description is specific to the ϕ^4 model and does not find its direct translation to the issue discussed here. This is due to the fact that in the linear spectrum of kink in the sine-Gordon model such a mode is not present. This issue is an element of further research and an interesting starting point for future studies.

The first article presented in this dissertation primarily focused on determining the controlling physical parameters of the studied system. However, in order to be able to describe the interaction of the kink with inhomogeneities in detail and accurately, it is also crucial to precisely study the very moment of interaction. This issue was addressed in the third article, which very carefully analyzed the interaction between the potential barrier due to the curvature of the junction on the movement of the kink for values very close to critical values, and the existence of stable solutions in this system. In each of the cases discussed, it was possible to prepare approximate models with one and two degrees of freedom that describe the dynamics of the kink very well. The calculations also identified the saddle point and the static solution point, in phase space of the system, for the case of dissipation. Moreover, in both cases, the linear spectrum of the kink solution was determined, which made it possible to identify and describe both the translational mode and the origin of the continuous spectrum.

A generalization of the study discussed above and the culmination of this dissertation is the fourth article, which focuses on the 2+1 dimensional case. The motivation for this research stemmed directly from the results obtained in the earlier study. To be able to effectively describe the evolution of the kink front, a non-conservative Lagrangian method was used here, which allowed to approximate the solutions of the full model very well. This method was evaluated very extensively first by studying the behavior of the kink in a system without inhomogeneities for that with a perturbed initial state. These results confirmed that the proposed 1+1 dimensional model effectively reproduces the solutions of the full-field model. An analogous observation was made when the inhomogeneity present in the system was homogeneous in the direction of the variable transverse to the kink motion. It is worth noting here that in such a case, these results are directly applicable to the 1+1 dimensional case. The resulting confirmation of the usefulness of the proposed model allowed us to move on to the more interesting cases, in which this inhomogeneity is overtly two-dimensional in this system, i.e., it is in the form of a peak or a well of potential. The proposed model also adequately describes the studied dynamics in these cases. However, an unusually important finding here seems to be the fact that in cases where the kink is stopped, either inside the well or in front of the peak, if there is a dissipation in the system, the model captures the final state of the solution very well. The analysis of the line spectrum for the static solutions mentioned earlier is also a very interesting result. Moreover, the behavior of the excited modes present in this spectrum was successfully replicated using the proposed approximate model.

The problems presented in this dissertation form a single whole that explores the interaction between kink and inhomogeneity. These results represent a significant step forward in our understanding of these complex physical processes and provide a basis for further theoretical research as well as practical applications of the obtained results. In the first case, it seems particularly important to continue the current research toward studying inhomogeneities interacting radially with kink. It would also probably be an interesting case to test the proposed model in 3+1 dimensional cases. The explanation and description of the resonance windows observed in the studied system also remains an open problem. The second outcome of the research presented here could be its use in practical applications. For those practical applications of Josephson junctions presented in the introduction, a description of the dynamics of fluxon inside the junction is essential. In addition, the design of junctions with desired properties can be achieved by engineering the geometry of the junction, i.e., changing the curvature. The results obtained can provide a basis for further development of the devices presented earlier and the creation of future electronics based on quantum effects occurring in Josephson junctions.

Acknowledgement

This research has been made possible by the Kosciuszko Foundation The American Centre of Polish Culture This research was supported in part by PLGrid Infrastructure. This research was financed with funds from the project "PROM – International scholarship exchange of PhD candidates and academic staff" within the Operational Programme Knowledge Education Development, co-financed from the European Social Fund; project no. POWR.03.03.00-00-PN13/18.

References

[1] J. S. Russell, “Report on Waves”, in 14th meeting of the British Association for the Advancement of Science (1844), pp. 311–390.

[2] J. Boussinesq, “Théorie de l’intumescence liquide appelée onde solitaire ou de translation se propageant dans un canal rectangulaire”, CR Acad. Sci. Paris **72**, 1871 (1871).

[3] J. Boussinesq, “Théorie générale des mouvements qui sont propagés dans un canal rectangulaire horizontal”, CR Acad. Sci. Paris **73**, 1 (1871).

[4] J. Boussinesq, “Théorie des ondes et des remous qui se propagent le long d’un canal rectangulaire horizontal, en communiquant au liquide contenu dans ce canal des vitesses sensiblement pareilles de la surface au fond”, Journal de mathématiques pures et appliquées **17**, 55–108 (1872).

[5] J. Boussinesq, *Essai sur la théorie des eaux courantes* (Impr. nationale, 1877).

[6] J. W. Strutt and L. Rayleigh, “On waves”, Philos. Mag **5**, 257–79 (1876).

[7] D. J. Korteweg and G. de Vries, “XLI. On the change of form of long waves advancing in a rectangular canal, and on a new type of long stationary waves”, The London, Edinburgh, and Dublin Philosophical Magazine and Journal of Science **39**, 422–443 (1895).

[8] E. Fermi, P. Pasta, S. Ulam, and M. Tsingou, *Studies of the nonlinear problems*, tech. rep. (Los Alamos National Lab.(LANL), Los Alamos, NM (United States), 1955).

[9] N. J. Zabusky and M. D. Kruskal, “Interaction of ”Solitons” in a Collisionless Plasma and the Recurrence of Initial States”, Phys. Rev. Lett. **15**, 240–243 (1965).

[10] P. G. Drazin and R. S. Johnson, “The Korteweg–de Vries equation”, in *Solitons: An Introduction*, 2nd ed., Cambridge Texts in Applied Mathematics (Cambridge University Press, 1989), pp. 1–19.

[11] P. Emplit, J. Hamaide, F. Reynaud, C. Froehly, and A. Barthelemy, “Picosecond steps and dark pulses through nonlinear single mode fibers”, Optics Communications **62**, 374–379 (1987).

[12] A. Weston, E. G. Castanon, V. Enaldiev, F. Ferreira, S. Bhattacharjee, S. Xu, H. Corte-León, Z. Wu, N. Clark, A. Summerfield, T. Hashimoto, Y. Gao, W. Wang, M. Hamer, H. Read, L. Fumagalli, A. V. Kretinin, S. J. Haigh, O. Kazakova, A. K. Geim, V. I. Fal’ko, and R. Gorbachev, “Interfacial ferroelectricity in marginally twisted 2D semiconductors”, Nature Nanotechnology **17**, 390–395 (2022).

[13] J. S. Alden, A. W. Tsen, P. Y. Huang, R. Hovden, L. Brown, J. Park, D. A. Muller, and P. L. McEuen, “Strain solitons and topological defects in bilayer graphene”, Proceedings of the National Academy of Sciences **110**, 11256–11260 (2013).

[14] A. M. Kosevich, V. V. Gann, A. I. Zhukov, and V. P. Voronov, “Magnetic soliton motion in a nonuniform magnetic field”, Journal of Experimental and Theoretical Physics **87**, 401–407 (1998).

[15] P. G. Kevrekidis and D. J. Frantzeskakis, *Emergent nonlinear phenomena in Bose-Einstein condensates Theory and experiment*, CLASSICAL AND QUANTUM MECHANICS, GENERAL PHYSICS (Springer, Germany, 2008).

[16] "Nonlinear Theory of DNA: Statistics of Nonlinear Excitations", in *Nonlinear Physics of DNA* (John Wiley & Sons, Ltd, 2004) Chap. 7, pp. 133–150.

[17] S. S. Andersen, A. D. Jackson, and T. Heimburg, "Towards a thermodynamic theory of nerve pulse propagation", Progress in Neurobiology **88**, 104–113 (2009).

[18] A. Scott, K. Lonngren, and D. Landt, "Active and nonlinear wave propagation in electronics", IEEE Transactions on Plasma Science **1**, 42–42 (1973).

[19] A. Barone, F. Esposito, C. J. Magee, and A. C. Scott, "Theory and applications of the sine-gordon equation", La Rivista del Nuovo Cimento (1971-1977) **1**, 227–267 (1971).

[20] G. L. Lamb, "Analytical Descriptions of Ultrashort Optical Pulse Propagation in a Resonant Medium", Rev. Mod. Phys. **43**, 99–124 (1971).

[21] J. Perring and T. Skyrme, "A model unified field equation", Nuclear Physics **31**, 550–555 (1962).

[22] E. Bour, *Theorie de la deformation des surfaces*, fre (1862).

[23] A. R. Forsyth, *Theory of Differential Equations*, Vol. 6 (New York, 1959).

[24] C. S. Gardner, J. M. Greene, M. D. Kruskal, and R. M. Miura, "Method for Solving the Korteweg-deVries Equation", Phys. Rev. Lett. **19**, 1095–1097 (1967).

[25] C. S. Gardner, J. M. Greene, M. D. Kruskal, and R. M. Miura, "Korteweg-devries equation and generalizations. VI. methods for exact solution", Communications on Pure and Applied Mathematics **27**, 97–133 (1974).

[26] B. Josephson, "Possible new effects in superconductive tunnelling", Physics Letters **1**, 251–253 (1962).

[27] D. G. McDonald, "The Nobel Laureate Versus the Graduate Student", Physics Today **54**, 46–51 (2001).

[28] P. W. Anderson and J. M. Rowell, "Probable Observation of the Josephson Superconducting Tunneling Effect", Phys. Rev. Lett. **10**, 230–232 (1963).

[29] "Fluxon Dynamics", in *Physics and Applications of the Josephson Effect* (John Wiley & Sons, Ltd, 1982) Chap. 10, pp. 264–290.

[30] C. M. Wilson, G. Johansson, A. Pourkabirian, M. Simoen, J. R. Johansson, T. Duty, F. Nori, and P. Delsing, "Observation of the dynamical Casimir effect in a superconducting circuit", Nature **479**, 376–379 (2011).

[31] J. Clarke, *The SQUID handbook Vol 1 Fundamentals and technology of SQUIDs and SQUID systems*, CONDENSED MATTER PHYSICS, SUPERCONDUCTIVITY AND SUPERFLUIDITY (Wiley VCH, Germany, 2004).

[32] E. R. Flynn and H. C. Bryant, "A biomagnetic system for in vivo cancer imaging", Physics in Medicine & Biology **50**, 1273 (2005).

[33] T. A. Fulton, P. L. Gammel, D. J. Bishop, L. N. Dunkleberger, and G. J. Dolan, "Observation of combined Josephson and charging effects in small tunnel junction circuits", Phys. Rev. Lett. **63**, 1307–1310 (1989).

[34] O. Kumar and M. Kaur, “Single electron transistor: Applications & problems”, Int J VLSI Des Commun Syst (VLSICS) **1**, 24–29 (2010).

[35] A. Worsham, J. Przybysz, J. Kang, and D. Miller, “A Single Flux Quantum cross-bar switch and demultiplexer”, IEEE Transactions on Applied Superconductivity **5**, 2996–2999 (1995).

[36] P.-Y. Qu, G.-M. Tang, J.-H. Yang, X.-C. Ye, D.-R. Fan, Z.-M. Zhang, and N.-H. Sun, “Design of an 8-bit Bit-Parallel RSFQ Microprocessor”, IEEE Transactions on Applied Superconductivity **30**, 1–6 (2020).

[37] Y. Nakamura, Y. A. Pashkin, and J. S. Tsai, “Coherent control of macroscopic quantum states in a single-Cooper-pair box”, Nature **398**, 786–788 (1999).

[38] M. H. Devoret and R. J. Schoelkopf, “Superconducting Circuits for Quantum Information: An Outlook”, Science **339**, 1169–1174 (2013).

[39] M. A. Nielsen and I. L. Chuang, *Quantum computation and quantum information* (Cambridge university press, 2010).

[40] A. Shnirman, G. Schön, and Z. Hermon, “Quantum Manipulations of Small Josephson Junctions”, Phys. Rev. Lett. **79**, 2371–2374 (1997).

[41] V. Bouchiat, D. Vion, P. Joyez, D. Esteve, and M. H. Devoret, “Quantum coherence with a single Cooper pair”, Physica Scripta **1998**, 165 (1998).

[42] K. W. Lehnert, B. A. Turek, K. Bladh, L. F. Spietz, D. Gunnarsson, P. Delsing, and R. J. Schoelkopf, “Quantum Charge Fluctuations and the Polarizability of the Single-Electron Box”, Phys. Rev. Lett. **91**, 106801 (2003).

[43] A. A. Houck, J. Koch, M. H. Devoret, S. M. Girvin, and R. J. Schoelkopf, “Life after charge noise: recent results with transmon qubits”, Quantum Information Processing **8**, 105–115 (2009).

[44] T. P. Orlando, J. E. Mooij, L. Tian, C. H. van der Wal, L. S. Levitov, S. Lloyd, and J. J. Mazo, “Superconducting persistent-current qubit”, Phys. Rev. B **60**, 15398–15413 (1999).

[45] V. T. Petrashov, K. G. Chua, K. M. Marshall, R. S. Shaikhaidarov, and J. T. Nicholls, “Andreev Probe of Persistent Current States in Superconducting Quantum Circuits”, Phys. Rev. Lett. **95**, 147001 (2005).

[46] J. M. Martinis, M. H. Devoret, and J. Clarke, “Energy-Level Quantization in the Zero-Voltage State of a Current-Biased Josephson Junction”, Phys. Rev. Lett. **55**, 1543–1546 (1985).

[47] A. Benabdallah, J. G. Caputo, and A. C. Scott, “Exponentially tapered Josephson flux-flow oscillator”, Phys. Rev. B **54**, 16139–16146 (1996).

[48] A. Kemp, A. Wallraff, and A. Ustinov, “Josephson Vortex Qubit: Design, Preparation and Read-Out”, physica status solidi (b) **233**, 472–481 (2002).

[49] A. Kemp, A. Wallraff, and A. Ustinov, “Testing a state preparation and read-out protocol for the vortex qubit”, Physica C: Superconductivity **368**, 324–327 (2002).

[50] D. R. Gulevich and F. V. Kusmartsev, “Flux Cloning in Josephson Transmission Lines”, Phys. Rev. Lett. **97**, 017004 (2006).

[51] D. R. Gulevich, F. V. Kusmartsev, S. Savel'ev, V. A. Yampol'skii, and F. Nori, "Shape Waves in 2D Josephson Junctions: Exact Solutions and Time Dilation", Phys. Rev. Lett. **101**, 127002 (2008).

[52] J.-G. Caputo and D. Dutykh, "Nonlinear waves in networks: Model reduction for the sine-Gordon equation", Phys. Rev. E **90**, 022912 (2014).

[53] R. Monaco, "Engineering double-well potentials with variable-width annular Josephson tunnel junctions", Journal of Physics: Condensed Matter **28**, 445702 (2016).

[54] R. Monaco, J. Mygind, and V. P. Koshelets, "Development of a Josephson vortex two-state system based on a confocal annular Josephson junction", Superconductor Science and Technology **31**, 025003 (2017).

[55] T. Dobrowolski, "Kink motion in a curved Josephson junction", Phys. Rev. E **79**, 046601 (2009).

[56] T. Dobrowolski, "Curved Josephson junction", Annals of Physics **327**, 1336–1354 (2012).

[57] T. Dobrowolski, "Possible curvature effects in the Josephson junction", The European Physical Journal B **86**, 346 (2013).

[58] T. Dobrowolski and A. Jarmoli ński, "Perturbation scheme for a fluxon in a curved Josephson junction", Phys. Rev. E **96**, 012214 (2017).

[59] J. Gatlik and T. Dobrowolski, "Modeling kink dynamics in the sine–Gordon model with position dependent dispersive term", Physica D: Nonlinear Phenomena **428**, 133061 (2021).

[60] J. Gatlik, T. Dobrowolski, and P. G. Kevrekidis, "Kink-inhomogeneity interaction in the sine-Gordon model", Phys. Rev. E **108**, 034203 (2023).

[61] D. W. McLaughlin and A. C. Scott, "Perturbation analysis of fluxon dynamics", Phys. Rev. A **18**, 1652–1680 (1978).

[62] M. B. Fogel, S. E. Trullinger, A. R. Bishop, and J. A. Krumhansl, "Classical Particlelike Behavior of Sine-Gordon Solitons in Scattering Potentials and Applied Fields", Phys. Rev. Lett. **36**, 1411–1414 (1976).

[63] T. Dobrowolski and P. Tatrocki, "A numerical test of the collective coordinate method", Physics Letters A **372**, 2834–2841 (2008).

[64] J. Gatlik and T. Dobrowolski, "The impact of thermal noise on kink propagation through a heterogeneous system", Physica D: Nonlinear Phenomena **445**, 133649 (2023).

[65] J. Gatlik, T. Dobrowolski, and P. G. Kevrekidis, "Effective description of the impact of inhomogeneities on the movement of the kink front in $2+1$ dimensions", Phys. Rev. E **109**, 024205 (2024).

[66] C. R. Galley, "Classical Mechanics of Nonconservative Systems", Phys. Rev. Lett. **110**, 174301 (2013).

[67] C. R. Galley, D. Tsang, and L. C. Stein, *The principle of stationary nonconservative action for classical mechanics and field theories*, 2014.

Physica D 428 (2021) 133061

Contents lists available at ScienceDirect

Physica D

journal homepage: www.elsevier.com/locate/physd

Modeling kink dynamics in the sine–Gordon model with position dependent dispersive term

J. Gatlik, T. Dobrowolski *

Institute of Physics UP, Podchorążych 2, 30-084 Cracow, Poland

ARTICLE INFO

Article history:
Received 28 April 2021
Received in revised form 23 September 2021
Accepted 25 September 2021
Available online 6 October 2021
Communicated by V.M. Perez-Garcia

Keywords:
sine–Gordon model
Soliton
Collective coordinate methods

ABSTRACT

The modification of the sine–Gordon model with explicitly broken translational invariance is studied. Different simplified descriptions of the kink motion are applied and compared. The main problem of the collective coordinate descriptions is identified and a solution is proposed. Some modification of the known collective coordinate approaches is proposed and a new treatment is suggested. The results are compared with the results of the exact field model.

1. Introduction

Solitons, which are solutions of some nonlinear field equations, were introduced to mathematical physics by N. Zabusky and M. Kruskal [1]. The existence of solitons is possible due to the balance between dispersion and nonlinearity of a system. In 1967 a method for solving the initial-value problem for the KdV equation was presented. The method is known as an inverse scattering transform and enables construction of analytical solutions in this model [2]. Originally solitons, discovered in the framework of the Korteweg de Vries equation, explained the behaviour of solitary waves on shallow water channels. It soon turned out that this equation could be successfully used to describe other physical systems such as plasma [3], anharmonic lattices [4], and elastic rods [5]. Moreover, other solitonic equations have been discovered and applied to describe various physical systems. In addition to the KdV equation the most famous integrable systems are defined by the nonlinear Schrödinger [6] and sine–Gordon equation [7–11]. The last of these equations originally appeared in the 19th century, in the context of studying surfaces with a constant negative curvature as the Gauss–Codazzi equation. Currently, this model is used in various ways to describe physical and biological systems. In particular in biology it is applied in the description of living cellular structures, including DNA, microtubules, protein folding and neural impulses [12]. In physics the model has found applications in condensed matter, gravitational and high-energy physics [13–21]. On the other hand, many condensed matter systems can be described by the solitonic equations that are modified by some additional terms which, in an explicit way, break translational invariance. Originally such modifications were included in the kink potential $(1 + \varepsilon g(x))(1 - \cos\phi)$, where ε controls the strength of the modification and $g(x)$ its form [22–24]. In these articles $g(x)$ described microshorts or spatially periodic inhomogeneity. Moreover, spatially inhomogeneous bias current was introduced in article [25]. Modifications of the sine–Gordon model are also discussed in papers [26–46]. In the present article we consider the sine–Gordon equation in the form [46]

$$\partial_t^2\phi - \partial_x\left(\mathcal{F}(x)\,\partial_x\phi\right) + \sin\phi = 0, \tag{1}$$

where $\mathcal{F}(x)$ is some function with explicit position dependence. Analytical studies of the behaviour of the soliton in the presence of inhomogeneity are usually extremely difficult. One of the most popular analytical techniques used in these studies is the collective coordinate method. This technique allows a reduction of the infinite number of the field degrees of freedom to a finite number of particle coordinates. The mechanical degrees of freedom obtained in this way usually describe positions of solitons and their sizes. The particle degrees of freedom were introduced to the effective description of solitons in papers [47–51] where the authors constructed an effective Lagrange and Hamilton description of the scalar field models. In this approach the soliton is reduced to a particle whose translational motion may be coupled to some internal degree of freedom. This internal degree of freedom describes changes of the kink width and therefore the soliton is replaced by a deformable material particle. In this paper we concentrate on the simplest collective coordinate models that describe the position of the kink in the system that, in an explicit way, breaks translational invariance. We consider the process of the interaction of the kink with inhomogeneity present

* Corresponding author.
E-mail address: tomasz.dobrowolski@up.krakow.pl (T. Dobrowolski).

https://doi.org/10.1016/j.physd.2021.133061

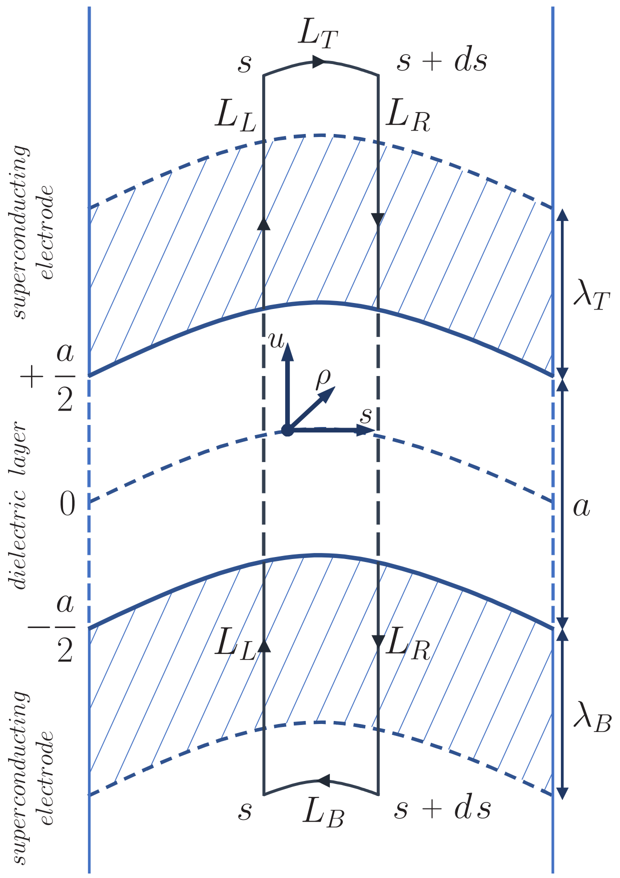

Fig. 1. Cross-section of the Josephson junction along the central line. The position dependent frame is located on the central line. The dielectric layer has thickness a and both superconducting electrodes are penetrated by the magnetic field at a distances λ_T and λ_B equal to London's penetration depths. In reality the thickness of the dielectric layer is much smaller than London penetration depths. The contour consists of two parts, placed deeply in the superconductive electrodes L_T and L_B and two parts L_L and L_R perpendicular to the vector potential $\vec{A}$.

in the system. We chose as a control parameter the critical speed of the kink that separates two regimes. In the first regime the kink is reflected from the inhomogeneity while in the second passes through it. This choice of the control parameter is motivated by the fact that in Eq. (1), supplemented by dissipation and bias current, critical velocity determines directly measurable critical current.

We compare three methods that rely on the collective coordinate that provides the location of the soliton. The first method compares the energy of the kink in homogeneous and inhomogeneous systems [47–52]. The second method is based on the perturbation scheme proposed in the paper [52]. The third method relies on the procedure of projection of the field equation onto the zero mode of the soliton [52–54]. We also propose a method which is based on projection of the field equation onto the energy density of the kink solution. We analyse the results of these methods, and we draw conclusions about the reasons for the discrepancy of the approximate methods with the exact results derived from the field equation. We also, in the example of the energetic approach, propose a method of correction of the collective coordinates approaches.

2. Physical context

In this section we will construct an example that physically justifies the existence of the dispersion term in the form present in Eq. (1). We consider the device made of two superconductive electrodes separated by a very thin dielectric layer. After the discoverer of the principles of operation of this device by Brian D. Josephson, it is called the Josephson junction [55]. A high level of correlation present in the superconductor enables the description of each superconductor (in low energy limit) using the many particle wave function $\psi = |\psi|\, e^{i\varphi}$, where the second power of modulus describes the density of superconductive charge carriers. Moreover, due to small separation of electrodes the macroscopic wave functions of the electrodes overlap which leads to the correlation of the phases of the wave functions of both electrodes. In the low energy limit the leading dynamical variable is the gauge invariant difference of the phases of the above wave functions. In order to find an equation describing the dynamics of this variable in the case when the junction is curved we consider currents and fields present in the junction. In the presence of the electromagnetic fields in the junction the electric current density has the form

$$\vec{j} = \frac{e^*}{m^*}\left[\frac{1}{2}\imath\hbar\left(\psi\nabla\psi^* - \psi^*\nabla\psi\right) - \frac{e^*}{c}\vec{A}\,\psi\psi^*\right], \tag{2}$$

where $\vec{A}$ is a vector potential, c is the speed of light in a vacuum, $m^* = 2m$ is the mass of the Cooper pair and $e^* = 2e$ is its charge (m and e are mass and charge of the electron). After inserting the expression $\psi = |\psi|\, e^{i\varphi}$ into the last equation, we get

$$\vec{j} = |\psi|^2 \frac{e}{m}\left[\hbar\nabla\varphi - \frac{2e}{c}\vec{A}\right]. \tag{3}$$

We aim to obtain the equation for the dynamic of the gauge invariant phase difference of the phases of macroscopic wave functions, and therefore from Eq. (3) we determine the phase gradient

$$\nabla\varphi = \frac{2e}{\hbar c}\left[\frac{mc}{2|\psi|^2 e^2}\vec{j} + \vec{A}\right]. \tag{4}$$

We intend to describe the curved Josephson junction and therefore we use curved coordinates based on the central curve located in the isolator layer of the junction. More specifically, first we choose the surface located in the dielectric layer in this way that it is equally separated from both superconducting electrodes by the distance equal to half of the thickness of the dielectric layer. In the middle of this surface we choose the central line. In particular, if the described surface is a plane (in the case if a junction is not curved) the central curve is a longer symmetry axis of the considered surface. Next we introduce coordinates: the first coordinate, along the curve, we denote by s, the next coordinate ρ parameterizes the direction normal to the curve but located in the surface (geometrically it is a binormal direction to the curve). The last coordinate denoted by u parameterizes the direction normal to the curve, surface and the dielectric layer. Location of the coordinates is presented in Figs. 1, and Fig. 20 in Appendix A. In other words, the curve is fitted to the curvature of the junction. Additionally, we assume that the dynamics is restricted to the direction of the central curve. This is possible if the curve is plane, the magnetic field is parallel to the dielectric layer and has direction of the ρ coordinate. Moreover we presume that the fields are homogeneous in the direction of the ρ variable i.e. they do not depend on this variable. This physical situation can be described by the vector potential having (in appropriate gauge) only A_s component. In these settings we consider the system depicted in Fig. 1. In curved coordinates the last formula simplifies significantly (see Appendix A)

$$\frac{1}{G}\,\partial_s\varphi = (\mathbf{grad}\varphi)_s = \frac{2e}{\hbar c}\left[\frac{mc}{2|\psi|^2 e^2}\, j_s^{SH} + A_s\right] = \frac{2e}{\hbar c}A_s, \tag{5}$$

where j_s^{SH} is shielding current density. We choose the contour (in Fig. 1) in this way that it is closed deeply in superconducting electrodes, out of the region penetrated by the magnetic field and therefore the shielding current vanishes and so reduction of the Cooper pair density has no place. For the contour sections L_T and L_B located in the top and bottom electrodes, this equation can be written using integrals of the vector potential $\vec{A}$

$$\frac{1}{G}\left(\varphi_T(s) - \varphi_T(s+ds)\right) = \frac{2e}{\hbar c}\int_{L_T} dsA_s, \tag{6}$$

$$\frac{1}{G}\left(\varphi_B(s+ds) - \varphi_B(s)\right) = \frac{2e}{\hbar c}\int_{L_B} dsA_s. \tag{7}$$

Adding the last two equations and remembering that the vector potential is perpendicular to the left and right (L_L and L_R) parts of the contour, we get

$$\frac{1}{G}\left(\phi(s+ds) - \phi(s)\right) = \frac{2e}{\hbar c}\oint d\vec{l}\vec{A}, \tag{8}$$

where $\phi(t,s) = \varphi_B(t,s) - \varphi_T(t,s)$. The right side of this equation by the Stokes theorem can be used to find the relationship between the field ϕ and the magnetic field H_ρ i.e.

$$\oint d\vec{l}\vec{A} = \int\int_S d\vec{S}\,\mathbf{curl}\vec{A} = \int\int_S d\vec{S}\vec{H} = d_m ds H_\rho. \tag{9}$$

The last equality is a consequence of the fact that the magnetic field is nonzero only in the layer with thickness $d_m = a + \lambda_T + \lambda_B$, where λ_T and λ_B are London's penetration depths in the top and bottom electrodes. Combining Eqs. (8) and (9) in the limit of small ds we get the relation between ϕ and the magnetic field H_ρ

$$\frac{1}{G}\partial_s\phi = \frac{1}{G}\left(\frac{\phi(s+ds) - \phi(s)}{ds}\right) = \frac{2e}{\hbar c} d_m H_\rho. \tag{10}$$

On the other hand, the Ampere's circular law with the Maxwell correction relates the magnetic field with the current in the central layer of the junction

$$\mathbf{curl}\,\vec{H} = \frac{4\pi}{c}\vec{j} + \frac{1}{c}\partial_t\vec{D}. \tag{11}$$

The u component of Eq. (11) in curved coordinates has the form (see Appendix A)

$$\frac{1}{G}\left[\partial_s H_\rho - \partial_\rho(GH_s)\right] = \frac{4\pi}{c} j_u + \frac{1}{c}\partial_t D_u\,. \tag{12}$$

First we relate the u-th component of the electric displacement field D_u with the appropriate component of the electric field E_u and then with scalar V potential

$$D_u = \varepsilon E_u = \varepsilon(-\partial_u V - \frac{1}{c}\partial_t A_u) = -\varepsilon\partial_u V. \tag{13}$$

We recall that in the situation considered by us the vector potential $\vec{A}$ possess only the A_s component (i.e. $A_u = 0$). The last equation can be used in order to describe the potential jump between the lower and upper surfaces of the dielectric layer

$$aD_u = -\varepsilon(V(a/2) - V(-a/2)) = \varepsilon(V_B - V_T) = \varepsilon\Delta V. \tag{14}$$

Now we put the electric displacement field D_u from Eq. (14) into Eq. (12)

$$\frac{1}{G}\partial_s H_\rho = \frac{4\pi}{c} j_u + \frac{\varepsilon}{ac}\partial_t(\Delta V). \tag{15}$$

We also used the fact that the magnetic field possess only one nonzero component $H_\rho \neq 0$. The potential jump, due to the second Josephson law, is directly related to the time derivative of the phase difference

$$\partial_t\phi = \frac{2e}{\hbar}\Delta V. \tag{16}$$

In order to eliminate the magnetic field H_ρ and the potential jump ΔV from Eq. (15) we use relations (10) and (16)

$$\frac{\hbar c}{2ed_m}\partial_s\left(\frac{1}{G}\partial_s\phi\right) = G\frac{4\pi}{c} j_u + G\frac{\varepsilon}{ac}\frac{\hbar}{2e}\partial_t^2\phi. \tag{17}$$

Next we average the last formula with respect to the normal variable i.e. we divide by the thickness of the dielectric layer a and integrate with respect to the normal variable from the bottom to the top boundaries of the dielectric layer ($\frac{1}{a}\int_{-a/2}^{+a/2} du f$)

$$\frac{\hbar c}{2ed_m}\partial_s\left(\mathcal{F}\,\partial_s\phi\right) = \frac{4\pi}{c} j_u + \frac{\varepsilon}{ac}\frac{\hbar}{2e}\partial_t^2\phi. \tag{18}$$

Here $\frac{1}{a}\int_{-\frac{a}{2}}^{+\frac{a}{2}} du\, G = 1$ and function $\mathcal{F}$ is given by the formula

$$\mathcal{F}(s) = \frac{1}{a}\int_{-\frac{a}{2}}^{+\frac{a}{2}} du\,\frac{1}{G} = \frac{1}{a}\int_{-\frac{a}{2}}^{+\frac{a}{2}} du\,\frac{1}{1 - uK(s)}$$
$$= \frac{1}{aK(s)}\ln\left(\frac{2 + aK(s)}{2 - aK(s)}\right). \tag{19}$$

The current density through the dielectric layer is described by the first Josephson relation $j_u = j_0\sin\phi$ and therefore Eq. (18) becomes an equation for a phase difference ϕ

$$\frac{\hbar c^2}{8\pi\, ed_m}\partial_s\left(\mathcal{F}\,\partial_s\phi\right) = j_0\sin\phi + \frac{\varepsilon}{4\pi a}\frac{\hbar}{2e}\partial_t^2\phi. \tag{20}$$

If we denote $\bar{c} = \sqrt{\frac{a}{\varepsilon d_m}}\,c$ and $\lambda_J = \sqrt{\frac{\hbar c^2}{8\pi ed_m j_0}}$ then the last equation simplifies to the form

$$\frac{1}{\bar{c}^2}\partial_t^2\phi - \partial_s\left(\mathcal{F}\,\partial_s\phi\right) + \frac{1}{\lambda_J^2}\sin\phi = 0, \tag{21}$$

where λ_J is the Josephson penetration depth and $\bar{c}$ is the Swihart velocity. If we use dimensionless units i.e. rescale length by Josephson penetration depth $s \to \frac{1}{\lambda_J}s$ and time by plasma frequency $t \to \omega_P t = \frac{\bar{c}}{\lambda_J}t$ this equation can be simplified as follows

$$\partial_t^2\phi - \partial_s\left(\mathcal{F}(s)\,\partial_s\phi\right) + \sin\phi = 0. \tag{22}$$

On the other hand this equation follows from the lagrangian density

$$\mathcal{L} = \frac{1}{2}(\partial_t\phi)^2 - \frac{1}{2}\mathcal{F}(s)(\partial_s\phi)^2 - V(\phi), \tag{23}$$

where $V(\phi) = 1 - \cos\phi$. The other way of obtaining this equation is presented in article [46].

3. Kink dynamics in the field model

We consider the sine–Gordon model modified by the position dependent function $\mathcal{F}(x)$ which breaks translational invariance of the original model. The modification of this type, is motivated by the studies of the propagation of the fluxons in the curved Josephson junction. The above mentioned model is defined by the following equation of motion

$$\partial_t^2\phi - \partial_x(\mathcal{F}(x)\partial_x\phi) + \sin\phi = 0. \tag{24}$$

The presence of the inhomogeneity represented by the function $\mathcal{F}(x)$ introduces a kind of potential barrier to the system, which could stop the kink during its motion through the system. We presume the form of the function $\mathcal{F}$ which is convenient for analytical studies

$$\mathcal{F}(x) = 1 + \varepsilon g(x), \quad g(x) = \theta(x) - \theta(x - L). \tag{25}$$

We choose the critical velocity as a controlled physical parameter that characterizes the dynamical properties of the original and the effective models. The critical velocity distinguishes two regimes. In the first regime the kink is reflected from inhomogeneity, while in the second it passes through the barrier. This approach is motivated by the results of simulations performed in the model (24). The simulations were carried out, using the Adams method along with the maximum step parameter set to infinity. In each of the counted cases the initial position was taken $x_0 = -50$. The simulations were conducted on the interval $[-300, 350]$. In figures we present only part of this interval. Presumed boundary conditions at the boundaries correspond to a sector with a unit topological charge. In order to avoid the return (to the area of interaction) of the energy radiated during the interaction of the kink with heterogeneity, we additionally applied suppression at the boundaries of the considered area. The obtained results were twofold. For low initial velocities, the kink was reflected from the area of heterogeneity. For higher speeds the passage over the barrier took place. Exemplary results are shown in Fig. 2. In this figure the parameter ε is taken equal to 0.2. Figures show the field configuration at different instants of time for the same initial speeds $u_0 = 0.4100$ in A and $u_0 = 0.5400$ in B. The grey region in the figures represents the area of inhomogeneity (the size of this region is $L = 10$). The same process of interaction of the kink with inhomogeneity for the same values of the initial speeds is presented in Fig. 3. This figure shows the movement of the centre of mass of the kink in the case where there is a reflection and passage of the kink through the potential barrier. The results of all simulations are collected in Fig. 4 that contains the dependence of the critical speed on the ε parameter. Here the critical velocity is determined with an accuracy of 0.0001.

4. Approximate descriptions of the kink dynamics

In the current paper we concentrate on the effective description of the kink motion in this system by comparing several methods.

4.1. Method I - energy approach

The first method is based on the analysis of the energy carried by the kink solution. The reference system is specified by the sine–Gordon (homogeneous) equation

$$\partial_t^2\phi - \partial_x^2\phi + \sin\phi = 0. \tag{26}$$

The total energy of the arbitrary field configuration in this model follows from Noether's theorem

$$E = \int_{-\infty}^{+\infty} dx \left[\frac{1}{2}(\partial_t\phi)^2 + \frac{1}{2}(\partial_x\phi)^2 + (1-\cos\phi)\right]. \tag{27}$$

The model (26) in contradiction to the model (1) is proven to be completely integrable. In particular, an inverse scattering method can be applied in order to construct soliton solutions. The best known solution of the model is the stationary kink given by the function

$$\phi(t,x) = 4\arctan e^{\zeta(t,x)}, \quad \zeta = \gamma(x-ut), \quad \gamma = \frac{1}{\sqrt{1-u^2}}, \tag{28}$$

where u is kink velocity. The energy corresponding to this particular configuration can be obtained by inserting this solution into the formula (27). First we simplify this expression by change of variables

$$E = \frac{1}{2}\int_{-\infty}^{+\infty} dx \left[\left(\frac{\partial\zeta}{\partial t}\right)^2(\partial_\zeta\phi)^2 + \left(\frac{\partial\zeta}{\partial x}\right)^2(\partial_\zeta\phi)^2 + 2(1-\cos\phi)\right]. \tag{29}$$

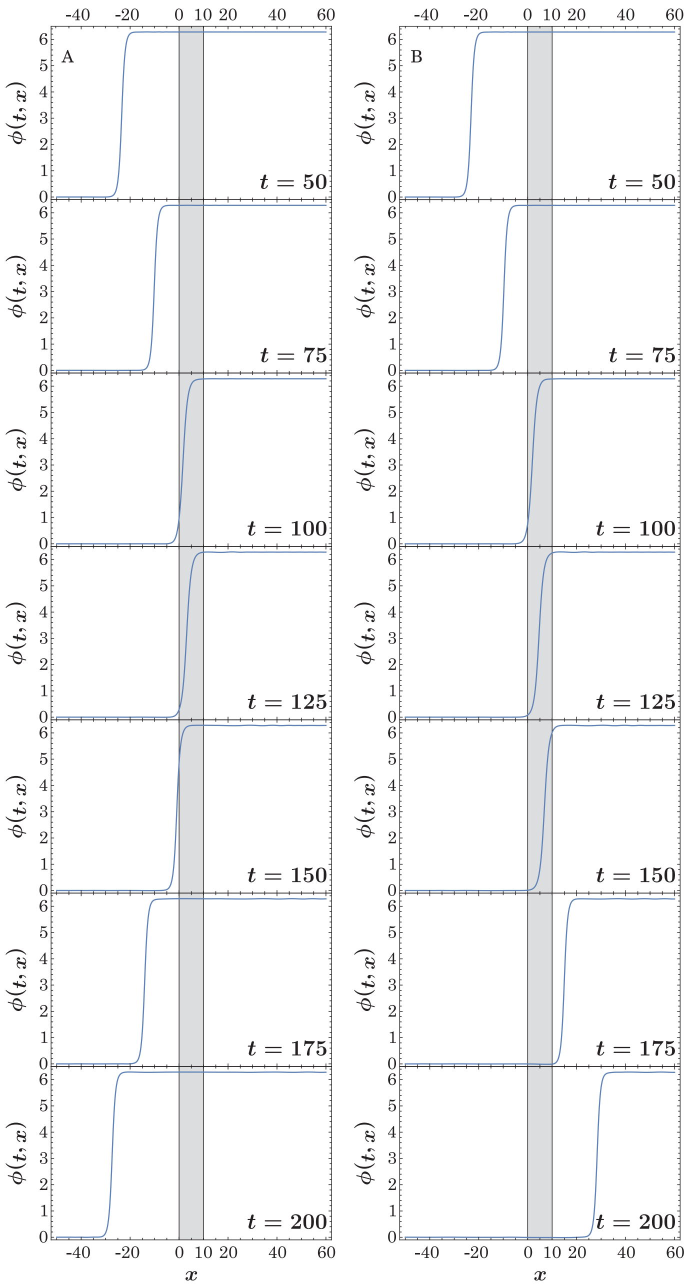

Fig. 2. Field configuration in different instants of time. The grey region of the figure represents inhomogeneity. In figures A the initial velocity of the kink is $u_0 = 0.4100$ and in figures B this parameter is set to $u_0 = 0.5400$. In both cases the initial position of the kink is $x_0 = -50$, $L = 10$ and parameter $\varepsilon = 0.2$.

Next, we use the Bogomolny $(\partial_\zeta\phi)^2 = 2(1-\cos\phi)$ equation in order to transform the potential term

$$E = \frac{1}{2}\int_{-\infty}^{+\infty} dx \left[\left(\frac{\partial\zeta}{\partial t}\right)^2 + \left(\frac{\partial\zeta}{\partial x}\right)^2 + 1\right](\partial_\zeta\phi)^2. \tag{30}$$

Finally we change the integration variables and use the explicit form of the kink solution ($\partial_\zeta\phi = 2\,\mathrm{sech}\zeta$)

$$E = \frac{1}{\sqrt{1-u^2}}\int_{-\infty}^{+\infty} d\zeta\, 4\,\mathrm{sech}^2\zeta = \frac{8}{\sqrt{1-u^2}}. \tag{31}$$

This result suggests that the kink can be seen as an energy knot propagating with constant velocity. The analytical form of the

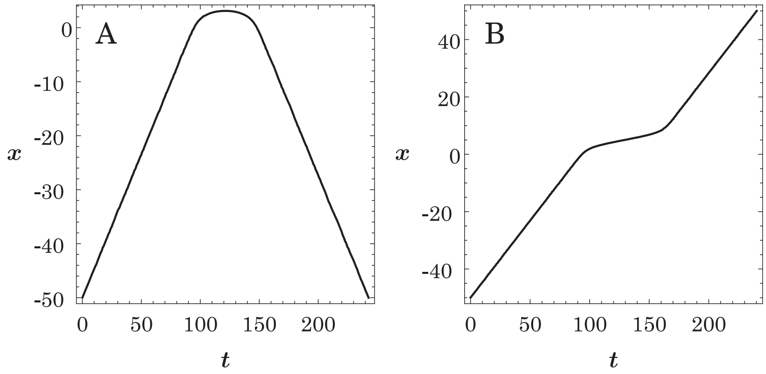

Fig. 3. The trajectory of the centre of mass of the kink. The initial speeds are $u_0 = 0.4100$ in figure A and $u_0 = 0.5400$ in figure B. The inhomogeneity is located in the interval [0, 10]. The initial position of the kink is $x_0 = -50$ and the inhomogeneity parameters are $\varepsilon = 0.2$ and $L = 10$.

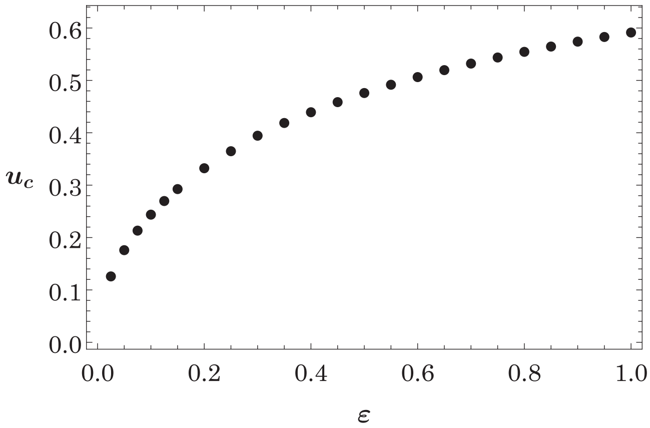

Fig. 4. The critical velocity of the kink as a function of the ε parameter in the field model.

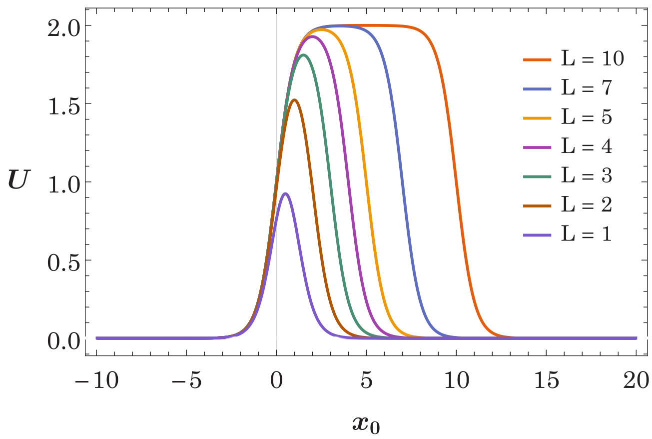

Fig. 5. The effective potential (39), for small velocities (i.e. $\gamma \to 1$). In the figure the function U is compared for $\varepsilon = 0.5$ and different values of L. (For interpretation of the references to colour in this figure legend, the reader is referred to the web version of this article.)

total energy of this field configuration is typical for the relativistic particles. One could show that the relation between momentum, mass, and velocity is also characteristic for the relativistic particles and therefore the kink in the first approximation may be treated as a point particle. The total energy at rest is interpreted as the rest mass of this particle $m_0 = 8$ (in the paper we use units in which $\bar{c} = 1$).

On the other hand, in the modified model (1) the total energy is slightly changed

$$E_{\mathcal{F}} = \int_{-\infty}^{+\infty} dx \left[\frac{1}{2} (\partial_t \phi)^2 + \frac{1}{2} \mathcal{F}(x)(\partial_x \phi)^2 + (1 - \cos\phi) \right]. \tag{32}$$

In the paper we presume the particular form of the function $\mathcal{F}(x)$ which represents inhomogeneity that breaks translational invariance

$$\mathcal{F}(x) = 1 + \varepsilon g(x), \quad g(x) = \theta(x) - \theta(x - L), \tag{33}$$

where $\theta(x)$ is the Heaviside step function. We also presume ansatz in the form

$$\phi(t, x) = 4 \arctan e^{\xi(t,x)}, \tag{34}$$

where this time

$$\xi(t, x) = \gamma(t)(x - x_0(t)), \quad \gamma(t) = \frac{1}{\sqrt{1 - u^2(t)}}, \quad u = \dot{x}_0(t). \tag{35}$$

Compared to the system (27) the energy of the field configuration in the inhomogeneous system has an additional term. The formula (32) for the considered system can be rewritten as follows

$$E_{\mathcal{F}} = E + \frac{1}{2} \int_{-\infty}^{+\infty} dx \,(\mathcal{F}(x) - 1)\,(\partial_x \phi)^2, \tag{36}$$

which simplifies even more for the inhomogeneity described by the formula (33)

$$E_{\mathcal{F}} = E + \frac{1}{2}\,\varepsilon \int_0^L dx(\partial_x \phi)^2. \tag{37}$$

If we insert into this equation the kink ansatz and then perform direct integration we obtain

$$E_{\mathcal{F}} = \frac{8}{\sqrt{1 - u^2}} + U(x_0). \tag{38}$$

One can see that it is enriched by the potential energy $U(x_0)$. The function U is presented in Fig. 5 and its analytical form is the following

$$U(x_0) = 2\gamma\varepsilon(\tanh(\xi(t, x = L)) - \tanh(\xi(t, x = 0))). \tag{39}$$

We assume that at the initial instant of time the kink is located far from the inhomogeneity and therefore in this area U is negligibly small. Moreover, we choose the initial velocity which is barely sufficient to reach the maximum of the potential barrier. Under these conditions the total energy of the kink, at the beginning of its motion, is as follows

$$(E_{\mathcal{F}})_{in} = \frac{8}{\sqrt{1 - u_c^2}}\,.$$

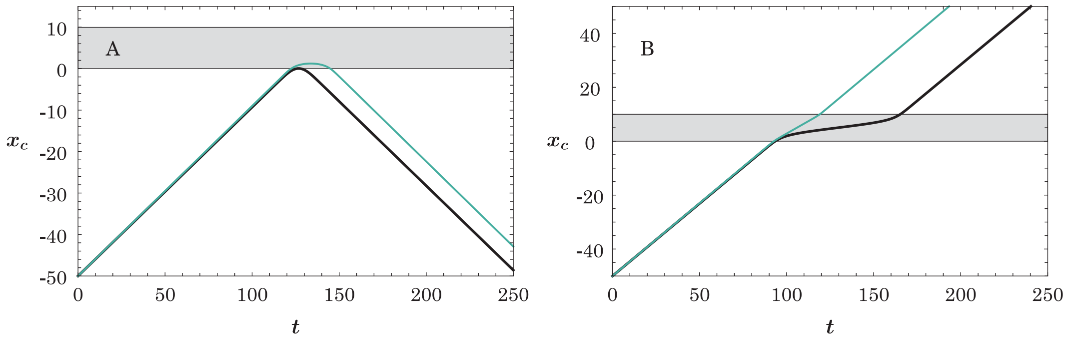

Fig. 6. The interaction of the kink with the inhomogeneity. The black continuous line represents the position of the centre of mass of the kink that follows from the field model and the green line follows from the approximate model (43). The initial position of the kink is $x_0 = -50$ and the initial velocities are respectively $u_0 = 0.4100$ in figure A and $u_0 = 0.5400$ in figure B. The size of the inhomogeneity is $L = 10$ and its amplitude $\varepsilon = 0.2$. (For interpretation of the references to colour in this figure legend, the reader is referred to the web version of this article.)

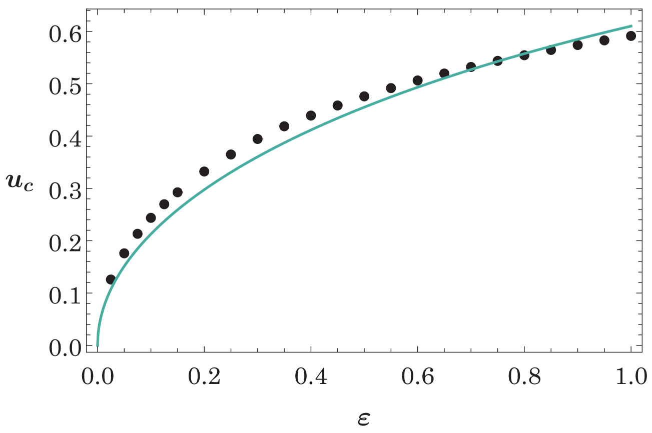

Fig. 7. The dependence of the critical speed u_c on the barrier height ε for $L = 1$. The black points represent numerical results obtained from the field model (24) and the green line represents the results of the simplified Model I (43). The initial position of the kink is $x_0 = -50$. (For interpretation of the references to colour in this figure legend, the reader is referred to the web version of this article.)

At the end of its motion the kink stops at the top of the barrier and therefore has the total energy

$$(E_{\mathcal{F}})_{fin} = 8 + 4\varepsilon \tanh \frac{L}{2},$$

here we replaced U with its maximal value $U_{max} = 4\varepsilon \tanh \frac{L}{2}$. Using conservation of the energy $(E_{\mathcal{F}})_{in} = (E_{\mathcal{F}})_{fin}$ we obtain the relation between the critical velocity and parameters of the barrier

$$u_c = \sqrt{1 - \frac{1}{(1 + \frac{1}{2}\varepsilon \tanh \frac{L}{2})^2}}. \tag{40}$$

In order to have the possibility to compare this approach with other approximate methods we also obtain the ordinary differential equation that describes propagation of the kink. In the present approach the kink is treated as a relativistic point particle in the potential U. Therefore we use the relativistic equation of motion [56]

$$\frac{d}{dt}(m_0 \gamma u) = F, \tag{41}$$

in the above equation the force is calculated as follows

$$F = -\,\partial_{x_0} U(x_0) = -\,2\varepsilon\gamma^2(\mathrm{sech}^2\gamma x_0 - \mathrm{sech}^2\gamma(L - x_0)). \tag{42}$$

The left hand side of Eq. (41) can be simplified after performing its differentiation

$$\frac{d}{dt}\left(\frac{8u}{\sqrt{1-u^2}}\right) = \frac{8\dot{u}}{(1-u^2)^{3/2}}.$$

Eq. (41) can be represented as the system of equations

$$\frac{du}{dt} = \frac{1}{4}\,\varepsilon\sqrt{1-u^2}\left(\mathrm{sech}^2\frac{L-x_0}{\sqrt{1-u^2}} - \mathrm{sech}^2\frac{x_0}{\sqrt{1-u^2}}\right),$$
$$\frac{dx_0}{dt} = u\,. \tag{43}$$

First, the dynamics that follows from this system of equations can be compared with the motion of the centre of mass of the kink that follows from the field model (24). In this model the field dynamics is studied at the interval $[-300, 350]$ and the boundary conditions that correspond to the unit topological charge are adopted. In both approaches the initial position of the kink is $x_0 = -50$, the inhomogeneity parameter is $\varepsilon = 0.2$ and the initial velocities are $u_0 = 0.4100$ in Fig. 6.A and $u_0 = 0.5400$ in Fig. 6.B. The inhomogeneity is represented by the grey region in the figures (it is located in the interval $[0, 10]$). In Fig. 6.A we observe reflection of the kink. In this case some difference appears during the time of interaction with inhomogeneity. The difference is very visible in Fig. 6.B that describes passing the kink through heterogeneity. Finally, we compare the critical velocities that were obtained in the framework of the complete field model (24) with the velocities which result from the approximate method (43). We investigated the dependence of the critical velocity on the magnitude of the potential barrier ε and on its spatial size L. We studied the potentials characterized by the length parameter belonging to the interval $L \in (0, 100]$. We have found that providing the size of the considered barrier is in the interval $L \in (0, 4]$ the system of Eqs. (43) approximates the critical speed relatively well, even for relativistic velocities (see Fig. 7). Let us notice that in this regime the parameter L also affects the height of the barrier and therefore the height of the barrier is smaller than the height indicated by the value of the parameter ε. The approximation becomes much less accurate for $L \in (4, 200]$. In this regime the height of the barrier is uniquely determined by the parameter ε (especially when a clear plateau of the barrier is formed). The discussed model in this regime clearly underestimates the values of the critical speed that follow from the field model (see Figs. 8–9). It is essential that the plots for other $L > 4$ are almost identical as for $L = 10$. In this sense the behaviour shown in Figs. 8–9 is generic for the considered system. For example, Fig. 9 contains data for $L = 200$, as we mentioned earlier, there is no significant change in the dependence of the critical speed on parameter ε in relation to the plot for $L =$

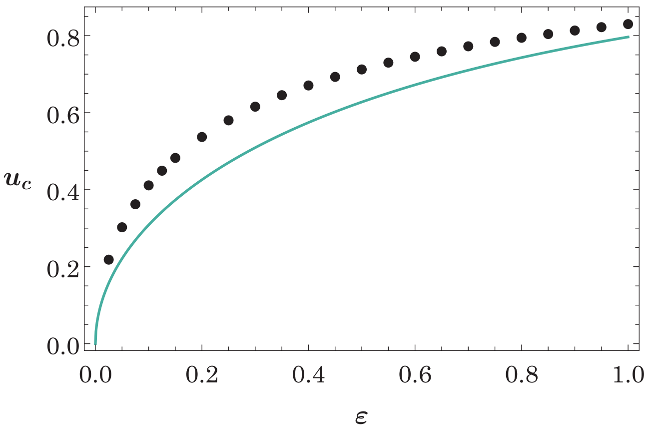

Fig. 8. The dependence of the critical speed u_c of the kink, initially located at $x_0 = -50$, on the barrier height ε for $L = 10$. Similar to the previous figure the black points represent numerical results obtained from the field model (24) and the green line represents the results of the simplified model I (43). (For interpretation of the references to colour in this figure legend, the reader is referred to the web version of this article.)

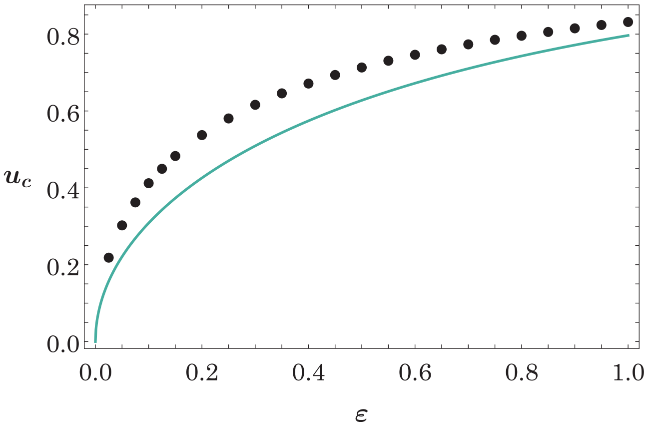

Fig. 9. The dependence of the critical speed u_c on the barrier height ε for $L = 200$. The black points represent numerical results obtained from the field model (24) and the green line represents the results of the simplified model I (43). (For interpretation of the references to colour in this figure legend, the reader is referred to the web version of this article.)

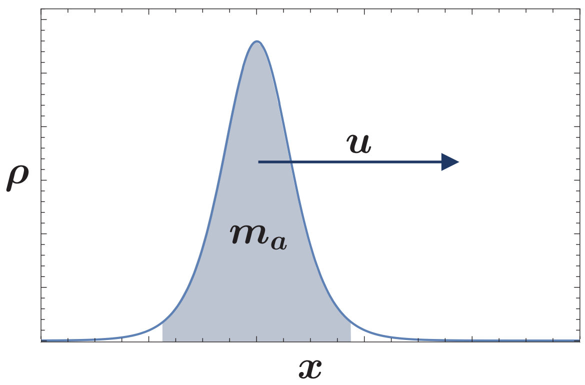

Fig. 10. The part of the kink that is directly involved in interaction.

10. The differences are unnoticeable because they are in fourth decimal place. The other parameters are the same as in Fig. 8.

First we identify the problem. Let us notice that in contradiction to normal effective treatment the kink configuration does not

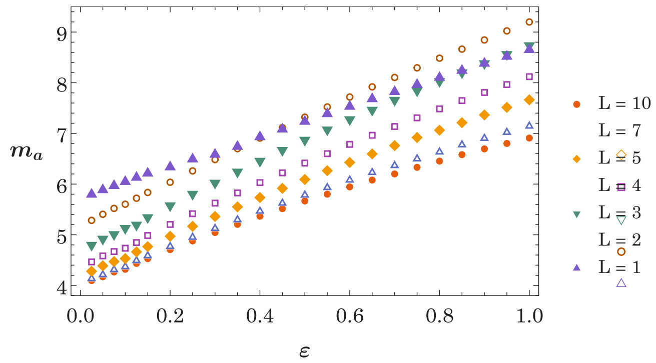

Fig. 11. Active mass for different values of L parameter as function of ε. (For interpretation of the references to colour in this figure legend, the reader is referred to the web version of this article.)

behave like a rigid body of mass $m_0 = 8$. In a real system only part of the kink, where most of the kink energy is concentrated, participates in the interaction (see Fig. 10). One of the reasons is the causality of interactions. We verify this hypothesis making a correction of the kink mass i.e. replacing $m_0 = 8$, present in Eq. (41), by

$$m_a = \mu + \lambda \varepsilon . \tag{44}$$

We claim that only this part of the kink mass in an active way participates in the interaction process. We estimate the mass as a linear function of the parameter ε because it reflects the linear dependence of the potential barrier on its height. Next, we perform a numerical procedure based on Eq. (43) with the kink mass replaced by its active mass i.e.

$$\frac{du}{dt} = \frac{2}{m_a}\, \varepsilon \sqrt{1-u^2} \left(\mathrm{sech}^2 \frac{L - x_0}{\sqrt{1-u^2}} - \mathrm{sech}^2 \frac{x_0}{\sqrt{1-u^2}} \right),$$
$$\frac{dx_0}{dt} = u\,. \tag{45}$$

The resulting masses, that guarantee the best fits, for different potential sizes L, as functions of ε parameter are presented in Fig. 11. Fig. 11 shows that for a small barrier height only half of the total mass of the kink can participate in the interaction. On the other hand for ε close to unity the effective kink mass can slightly exceed its total rest mass $m_0 = 8$, which is related to some deformation of the kink profile during the interaction process. First we compare the dynamics of the centre of mass of the kink following from the field model with the position of the kink predicted by the effective model (45). In Fig. 12 we show comparison of the trajectories for initial velocities $u_0 = 0.4100$ in Fig. 12.A and $u_0 = 0.5400$ in Fig. 12.B. The size of the inhomogeneity is $L = 10$, initial position is $x_0 = -50$ and $\varepsilon = 0.2$. Compatibility for speeds below the critical value is striking. On the other hand above the critical velocity the compatibility is only qualitative. The kink speed in the interaction region is smaller in the effective model than in the original field model. We also performed the systematic studies of the last model (45) in order to obtain the critical velocity. If we take into account the active kink mass then we obtain an excellent agreement of the effective model with the exact field equation (see Fig. 13). In order to check whether a similar problem is present in other effective popular descriptions we study, in the subsequent subsections, the same regime (i.e. for $L > 4$) of the considered system (24).

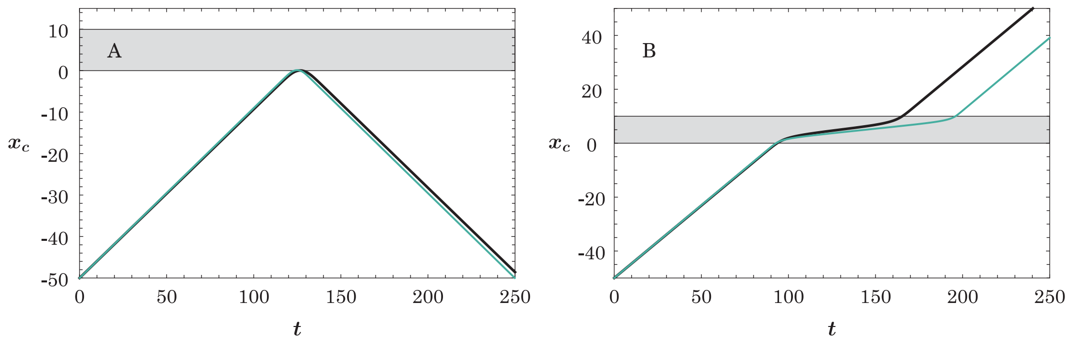

Fig. 12. Comparison of the kink movement obtained on the ground of the field model (black line) and on the ground of the effective model (45) (green line). The parameters of the plot as follows $\varepsilon = 0.2$, $x_0 = -50$, $L = 10$ and $u_0 = 0.4100$ in fig. A or $u_0 = 0.5400$ in fig. B. In both plots $\mu = 4.1076$ and $\lambda = 2.9385$. The grey region represents the interaction area. (For interpretation of the references to colour in this figure legend, the reader is referred to the web version of this article.)

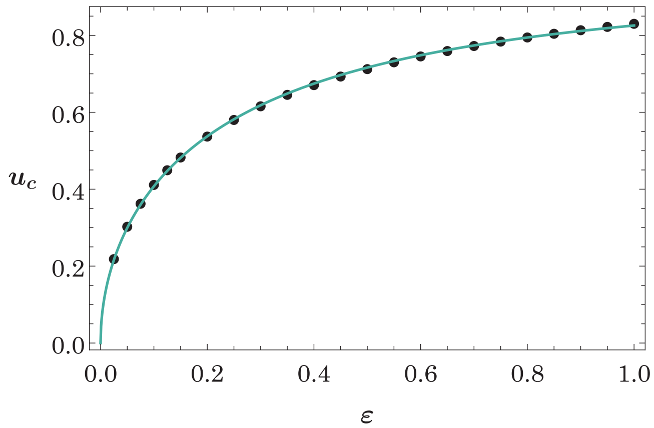

Fig. 13. The dependence of the critical speed u_c on the barrier height ε for $L = 10$ with the active kink mass taken into account. In this plot $\mu = 4.1076$ and $\lambda = 2.9385$. (For interpretation of the references to colour in this figure legend, the reader is referred to the web version of this article.)

4.2. Method II - perturbation scheme

The second method relies on the perturbation scheme that was proposed in the article [52]. According to this approach, one has to separate in the field equation (1) part $\varepsilon f(\phi)$ which is responsible for derogation from the sine–Gordon model

$$\partial_t^2\phi - \partial_x^2\phi + \sin\phi = \varepsilon\partial_x(g(x)\partial_x\phi) = \varepsilon f(\phi). \tag{46}$$

The effective equations of motion of the kink in this case are as follows (see [52])

$$\frac{du}{dt} = -\frac{1}{4}(1-u^2)\int_{-\infty}^{+\infty} dx\, \varepsilon f(\phi(\xi))\,\mathrm{sech}\xi\,, \tag{47}$$

$$\frac{dX}{dt} = u - \frac{1}{4}u\sqrt{1-u^2}\int_{-\infty}^{+\infty} dx\, \varepsilon f(\phi(\xi))\,\xi\,\mathrm{sech}\xi\,, \tag{48}$$

where $\xi = \frac{x-X}{\sqrt{1-v^2}}$, and $X = x_0(t) + \int_0^t dt' u(t')$. We calculate the integrals that define the right sides of the above equations. In the first integral

$$\mathcal{J}_1 = \int_{-\infty}^{+\infty} dx f(\phi(\xi))\,\mathrm{sech}\xi\,, \tag{49}$$

we introduce the explicit form of function f (from Eq. (46)) and make differentiation

$$\mathcal{J}_1 = \int_{-\infty}^{+\infty} dx\,\partial_x g(x)\,\partial_x\phi\,\mathrm{sech}\xi + \int_{-\infty}^{+\infty} dx\, g(x)\,\partial_x^2\phi\,\mathrm{sech}\xi\,. \tag{50}$$

The first term of this integral can be easily integrated because $g(x) = \Theta(x) - \Theta(L-x)$ and $\partial_x g(x) = \delta(x) - \delta(L-x)$. Moreover, in this term $\partial_x\phi = 2\gamma\,\mathrm{sech}\xi$ and so

$$\mathcal{J}_1 = 2\gamma(\mathrm{sech}^2\xi_0 - \mathrm{sech}^2\xi_L) + \int_0^L dx\,\partial_x^2\phi\,\mathrm{sech}\xi\,, \tag{51}$$

where $\xi_L = \gamma(L-X)$ and $\xi_0 = \gamma(-X)$. The function that is under the integral we transform as follows

$$\partial_x^2\phi\,\mathrm{sech}\xi = \frac{1}{2}\partial_x^2\phi\,\partial_\xi\phi = \frac{1}{2}\gamma^2\partial_\xi^2\phi\,\partial_\xi\phi = \frac{1}{4}\gamma^2\partial_\xi\left(\partial_\xi\phi\right)^2,$$

where we used relation $2\,\mathrm{sech}\xi = \partial_\xi\phi$. Now the integral takes the form

$$\mathcal{J}_1 = 2\gamma(\mathrm{sech}^2\xi_0 - \mathrm{sech}^2\xi_L) + \frac{1}{4}\gamma\int_{\xi_0}^{\xi_L} d\xi\,\partial_\xi\left(\partial_\xi\phi\right)^2, \tag{52}$$

and therefore we have

$$\mathcal{J}_1 = 2\gamma(\mathrm{sech}^2\xi_0 - \mathrm{sech}^2\xi_L) + \frac{1}{4}\gamma\left[\left(\partial_\xi\phi(\xi_L)\right)^2 - \left(\partial_\xi\phi(\xi_0)\right)^2\right]. \tag{53}$$

After simplification of two terms the integral reduces to the form

$$\mathcal{J}_1 = \gamma(\mathrm{sech}^2\xi_0 - \mathrm{sech}^2\xi_L). \tag{54}$$

The second integral is quite similar to the first one

$$\mathcal{J}_2 = \int_{-\infty}^{+\infty} dx f(\phi(\xi))\,\xi\,\mathrm{sech}\xi = \int_{-\infty}^{+\infty} dx\,\partial_x(g(x)\partial_x\phi)\,\xi\,\mathrm{sech}\xi\,. \tag{55}$$

We repeat the steps made during the calculation of the first integral and obtain

$$\mathcal{J}_2 = 2\gamma(\xi_0\,\mathrm{sech}^2\xi_0 - \xi_L\,\mathrm{sech}^2\xi_L) + \int_0^L dx\,\partial_x^2\phi\,\xi\,\mathrm{sech}\xi\,. \tag{56}$$

The same steps as we performed between equations (51) and (52) lead to expression

$$\mathcal{J}_2 = 2\gamma(\xi_0\,\mathrm{sech}^2\xi_0 - \xi_L\,\mathrm{sech}^2\xi_L) + \frac{1}{4}\gamma\int_{\xi_0}^{\xi_L} d\xi\,\xi\,\partial_\xi\left(\partial_\xi\phi\right)^2. \tag{57}$$

The function that is integrated we transform as follows

$$\xi\,\partial_\xi\left(\partial_\xi\phi\right)^2 = \partial_\xi\left(\xi\left(\partial_\xi\phi\right)^2\right) - \left(\partial_\xi\phi\right)^2.$$

After performing integration in the first part of the integral we obtain

$$\mathcal{J}_2 = 2\gamma(\xi_0\,\mathrm{sech}^2\xi_0 - \xi_L\,\mathrm{sech}^2\xi_L) + \frac{1}{4}\gamma\left(\xi_L\left(\partial_\xi\phi(\xi_L)\right)^2 - \xi_0\left(\partial_\xi\phi(\xi_0)\right)^2\right) - \frac{1}{4}\gamma\int_{\xi_0}^{\xi_L} d\xi\,\left(\partial_\xi\phi\right)^2. \tag{58}$$

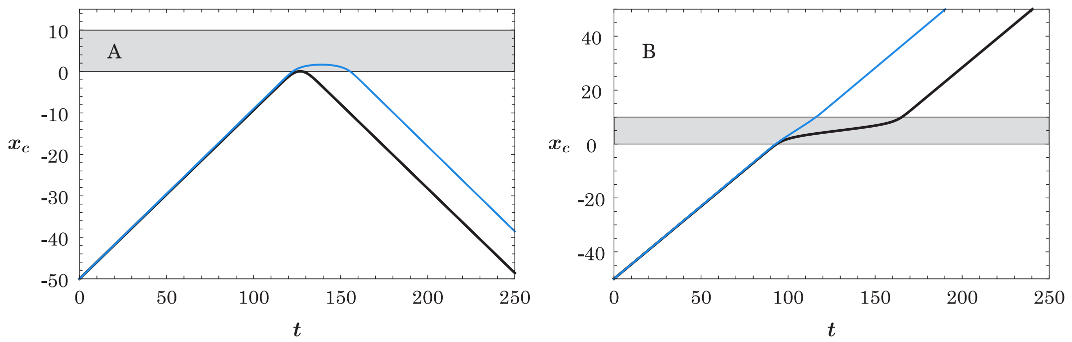

Fig. 14. Comparison of the trajectories that follow from the field model (black line) with the trajectory obtained on the ground of the effective model (61)–(62) (blue line). The parameters of the plot are as follows $L=10$, $\varepsilon=0.2$, $x_0=-50$ and $u_0=0.41$ in fig. A and $u_0=0.54$ in fig. B. (For interpretation of the references to colour in this figure legend, the reader is referred to the web version of this article.)

Subtraction of the first two terms leads to

$$\mathcal{J}_2=\gamma(\xi_0\,\mathrm{sech}^2\xi_0-\xi_L\,\mathrm{sech}^2\xi_L)-\gamma\int_{\xi_0}^{\xi_L}d\xi\,\mathrm{sech}^2\xi. \tag{59}$$

Finally, after integration of the last term we obtain

$$\mathcal{J}_2=\gamma(\xi_0\,\mathrm{sech}^2\xi_0-\xi_L\,\mathrm{sech}^2\xi_L)-\gamma\,\left(\tanh\xi_L-\tanh\xi_0\right). \tag{60}$$

The effective equations of motion of the kink are obtained by implementing integrals (54) and (60) into Eqs. (47)–(48). In the model considered by us the approximate equations of motion for X and u are

$$\frac{du}{dt}=\frac{1}{4}\,\varepsilon\sqrt{1-u^2}\left(\mathrm{sech}^2\frac{L-X}{\sqrt{1-u^2}}-\mathrm{sech}^2\frac{X}{\sqrt{1-u^2}}\right), \tag{61}$$

$$\frac{dX}{dt}=u+\frac{1}{4}\,\varepsilon u\left(\tanh\frac{X}{\sqrt{1-u^2}}+\tanh\frac{L-X}{\sqrt{1-u^2}}+V(X)\right). \tag{62}$$

Here the auxiliary function V has the form

$$V(X)=\frac{X}{\sqrt{1-u^2}}\,\mathrm{sech}^2\frac{X}{\sqrt{1-u^2}}+\frac{L-X}{\sqrt{1-u^2}}\,\mathrm{sech}^2\frac{L-X}{\sqrt{1-u^2}}\,.$$

Having the system of equations (61)–(62) that provide effective description of the field model we may compare the trajectories that follow from both descriptions. In Fig. 14 the motion of the centre of mass of the kink following from the field model is compared with the kink position obtained from an approximate description. In the figure we consider the kink that starts its evolution at $x_0=-50$. The parameters that describe the inhomogeneity are $\varepsilon=0.2$ and $L=10$. Below the critical velocity (for $u_0=0.41$) we observe considerable deviation from the field model. For speeds exceeding the critical velocity (for $u_0=0.54$) the situation is even worse. This time the results that follow from the approximate model defined by (61)–(62) significantly underestimate the values of the field model (24). The results of all simulations are collected in Fig. 15 where the critical velocity of the model (61)–(62) is compared with results of the original field model. In the plot we take $\varepsilon=0.2$, $L=10$ and the initial kink position $x_0=50$.

4.3. Method III - projection onto the zero mode

The third approach is motivated by the method of projection onto the zero mode of the system. This approach was applied to the systems like the ϕ^4 model [53,54]. The method relies on projection of the equation of motion onto the zero mode, present in the linear spectra of excitations of the kink in the homogeneous model (26). In this technique one introduces the kink ansatz (34)–(35) into the field equation

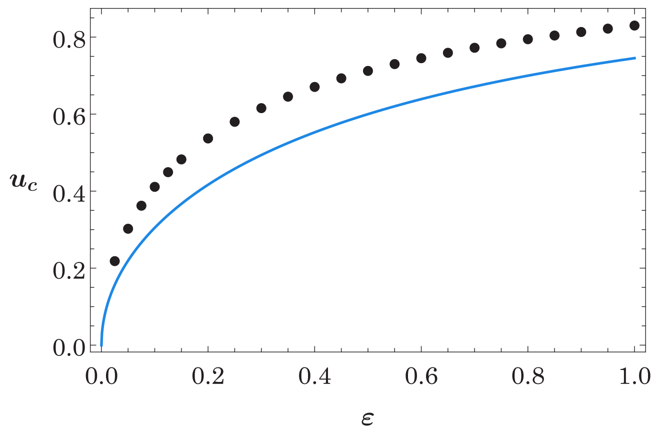

Fig. 15. The critical velocity for $L=10$. The initial position of the kink is taken $x_0=-50$. The black points represent numerical results obtained from the field model (24). The blue line represents the results of the effective dynamical model (61)–(62). (For interpretation of the references to colour in this figure legend, the reader is referred to the web version of this article.)

$$\partial_t^2\phi-\partial_x^2\phi+\sin\phi-\varepsilon\partial_x g(x)\partial_x\phi-\varepsilon g(x)\partial_x^2\phi=0. \tag{63}$$

The resulting equation is a base for obtaining the effective equation satisfied by the collective coordinate

$$\begin{aligned}&\left(\ddot{\xi}-\xi''\right)\partial_\xi\phi+\left(\dot{\xi}^2-\xi'^2\right)\partial_\xi^2\phi+\sin\phi=\\&\varepsilon(\partial_x g)\,\xi'\,\partial_\xi\phi+\varepsilon g\,\left(\xi''\partial_\xi\phi+\xi'^2\partial_\xi^2\phi\right).\end{aligned} \tag{64}$$

Here we denote the derivative with respect to the space variable by prime and the derivative with respect to time is represented by a dot. For the function $\xi(t,x)$ defined by Eq. (35) we have $\xi'=\gamma$, $\xi''=0$ and therefore the above equation is reduced as follows

$$\ddot{\xi}\,\partial_\xi\phi+\left(\dot{\xi}^2-\gamma^2\right)\partial_\xi^2\phi+\sin\phi=\varepsilon(\partial_x g)\,\gamma\,\partial_\xi\phi+\varepsilon g\,\gamma^2\partial_\xi^2\phi. \tag{65}$$

In order to simplify $\sin\phi$ we use equation $(\partial_\xi\phi)^2=2V(\phi)$ which in the model considered by us has the form $4\,\mathrm{sech}^2\xi=2(1-\cos\phi)$. From this formula one can calculate $\sin\phi=-2\,\mathrm{sech}\xi\tanh\xi$ and therefore Eq. (65) is simplified to the form

$$\begin{aligned}&\ddot{\xi}\,\mathrm{sech}\xi+\left(\gamma^2-\dot{\xi}^2-1\right)\mathrm{sech}\xi\tanh\xi\\&\quad=\varepsilon\gamma\,\partial_x g\,\mathrm{sech}\xi-\varepsilon g\,\gamma^2\,\mathrm{sech}\xi\tanh\xi.\end{aligned} \tag{66}$$

Next, we calculate the derivatives of the function $\xi(t,x)$ with respect to time i.e. $\dot{\xi} = \frac{\dot{\gamma}}{\gamma}\xi - \gamma u$, and $\ddot{\xi} = \frac{\ddot{\gamma}}{\gamma}\xi - 2\dot{\gamma}u - \gamma\dot{u}$, where $\dot{x}_0 = u$. In particular the formula for Lorentz factor $\gamma = 1/\sqrt{1-u^2}$ helps to remove the terms $\gamma^2 - 1 - \gamma^2 u^2 = 0$. Now Eq. (66) can be transformed as follows

$$\left(\frac{\ddot{\gamma}}{\gamma}\xi - (2\dot{\gamma}u + \gamma\dot{u})\right)\operatorname{sech}\xi + \left(2\dot{\gamma}u\xi - \left(\frac{\dot{\gamma}}{\gamma}\right)^2\xi^2\right)\operatorname{sech}\xi\tanh\xi$$
$$= \varepsilon\gamma\,\partial_x g\operatorname{sech}\xi - \varepsilon g\,\gamma^2\operatorname{sech}\xi\tanh\xi\,. \tag{67}$$

In order to obtain the equation of motion for the kink position we remove the space variable by projection of Eq. (67) onto the zero mode, which is proportional to the gradient of the kink i.e. $\partial_x\phi \sim \operatorname{sech}\xi$

$$Eq = 0 \Longrightarrow \langle\operatorname{sech}\xi, Eq\rangle \equiv \int_{-\infty}^{\infty} dx\operatorname{sech}\xi\; Eq = 0, \tag{68}$$

where Eq denotes Eq. (67). In this step we calculate the appropriate integrals. In particular we use nonzero integrals

$$\int_{-\infty}^{\infty} dx\operatorname{sech}^2\xi = \frac{2}{\gamma}\quad,\quad \int_{-\infty}^{\infty} dx\,\xi\operatorname{sech}^2\xi\tanh\xi = \frac{1}{\gamma},$$

in order to simplify Eq. (68) to the form

$$\dot{u} + \frac{\dot{\gamma}}{\gamma}u = -\frac{1}{2}\varepsilon\gamma\int_{-\infty}^{+\infty} dx\partial_x g\operatorname{sech}^2\xi$$
$$+ \frac{1}{2}\varepsilon\gamma^2\int_{-\infty}^{+\infty} dxg\operatorname{sech}^2\xi\tanh\xi\,. \tag{69}$$

Next we use the explicit form of the function g and therefore we obtain the following equation

$$\dot{u} + \frac{\dot{\gamma}}{\gamma}u = -\frac{1}{2}\varepsilon\gamma\left(\operatorname{sech}^2\xi_0 - \operatorname{sech}^2\xi_L\right)$$
$$+ \frac{1}{2}\varepsilon\gamma^2\int_0^L dx\operatorname{sech}^2\xi\tanh\xi\,. \tag{70}$$

We calculate the last integral

$$\dot{u} + \frac{\dot{\gamma}}{\gamma}u = -\frac{1}{2}\varepsilon\gamma\left(\operatorname{sech}^2\xi_0 - \operatorname{sech}^2\xi_L\right)$$
$$+ \frac{1}{2}\varepsilon\gamma^2\frac{1}{2\gamma}\left(\operatorname{sech}^2\xi_0 - \operatorname{sech}^2\xi_L\right), \tag{71}$$

and then subtract similar terms obtaining the equation that contains both the speed derivatives and the derivatives of the Lorentz factor

$$\dot{u} + \frac{\dot{\gamma}}{\gamma}u = \frac{1}{2}\varepsilon\gamma\left(\operatorname{sech}^2\xi_L - \operatorname{sech}^2\xi_0\right). \tag{72}$$

Then we simplify the left hand side of this equation by calculating the term that contains the time derivative of the Lorentz factor $\frac{\dot{\gamma}}{\gamma} = \gamma^2 u\dot{u}$.

The final result of this procedure is the system of equations

$$\frac{du}{dt} = \frac{1}{4}\varepsilon\sqrt{1-u^2}\left(\operatorname{sech}^2\frac{L-x_0}{\sqrt{1-u^2}} - \operatorname{sech}^2\frac{x_0}{\sqrt{1-u^2}}\right),$$
$$\frac{dx_0}{dt} = u\,. \tag{73}$$

Let us notice that the system (73) is identical to the previously obtained system of Eqs. (43). The curve $u_c = u_c(\varepsilon)$ that follows from the numerical solution of the last equation was previously presented, for example, in Figs. 7–9. The comments concerning Figs. 7–9 also apply to the model III.

4.4. Method IV - projection onto the energy density

In the last method we propose projection of Eq. (67) onto the energy density of the kink. Due to the fact that the energy density ρ is proportional to the $\rho \sim \operatorname{sech}^2\xi$ it is better localized in the vicinity of the kink position than the zero mode. By analogy to the procedure of fitting the active mass we propose to cut off a larger part of the kink mass because projection onto the zero mode still underestimates the active mass participating in the interaction process. Now we repeat the projection procedure described in the previous section but with zero mode replaced with the energy density

$$Eq = 0 \Longrightarrow \langle\operatorname{sech}^2\xi, Eq\rangle \equiv \int_{-\infty}^{\infty} dx\operatorname{sech}^2\xi\; Eq = 0. \tag{74}$$

This procedure is motivated by the fact that the last projection cuts out an area better focused around the maximum energy density of the kink. The projection of this type removes part of the kink configuration that does not take part in the interaction process. Due to the projection, only the terms for which the relevant integrals do not disappear remain in the equation. In the case considered in this part, only the integrals

$$\int_{-\infty}^{\infty} dx\operatorname{sech}^3\xi = \frac{1}{\gamma}\frac{\pi}{2},\quad \int_{-\infty}^{\infty} dx\,\xi\operatorname{sech}^3\xi\tanh\xi = \frac{1}{\gamma}\frac{\pi}{6}$$

are non-zero and therefore equation (74) reduces to the form

$$\dot{u} + \frac{4}{3}\frac{\dot{\gamma}}{\gamma}u = -\frac{2}{\pi}\varepsilon\gamma\int_{-\infty}^{+\infty} dx\,\partial_x g\operatorname{sech}^3\xi$$
$$+ \frac{2}{\pi}\varepsilon\gamma^2\int_{-\infty}^{+\infty} dxg\operatorname{sech}^3\xi\tanh\xi\,. \tag{75}$$

The use of the function g and its derivative allows us to find the first integral from the right side of the above equation and simplify the second one

$$\dot{u} + \frac{4}{3}\frac{\dot{\gamma}}{\gamma}u = -\frac{2}{\pi}\varepsilon\gamma\left(\operatorname{sech}^3\xi_0 - \operatorname{sech}^3\xi_L\right)$$
$$+ \frac{2}{\pi}\varepsilon\gamma^2\int_0^L dx\operatorname{sech}^3\xi\tanh\xi\,. \tag{76}$$

The last integral can be calculated exactly and therefore we have

$$\dot{u} + \frac{4}{3}\frac{\dot{\gamma}}{\gamma}u = -\frac{2}{\pi}\varepsilon\gamma\left(\operatorname{sech}^3\xi_0 - \operatorname{sech}^3\xi_L\right)$$
$$+ \frac{2}{\pi}\varepsilon\gamma^2\frac{1}{3\gamma}\left(\operatorname{sech}^3\xi_0 - \operatorname{sech}^3\xi_L\right). \tag{77}$$

Subtraction of similar terms leads to the equation

$$\dot{u} + \frac{4}{3}\frac{\dot{\gamma}}{\gamma}u = \frac{4}{3\pi}\varepsilon\gamma\left(\operatorname{sech}^3\xi_L - \operatorname{sech}^3\xi_0\right). \tag{78}$$

Next we remove the time derivative of the Lorentz factor $\dot{\gamma}/\gamma = \gamma^2 u\dot{u}$. The resulting system of equations has the form

$$(3+u^2)\frac{du}{dt} = \frac{4}{\pi}\varepsilon\sqrt{1-u^2}\left(\operatorname{sech}^2\frac{L-x_0}{\sqrt{1-u^2}} - \operatorname{sech}^2\frac{x_0}{\sqrt{1-u^2}}\right),$$
$$\frac{dx_0}{dt} = u. \tag{79}$$

Fig. 16 presents exemplary trajectories of the kink motion that follow from the effective model (79) compared with the trajectory of the centre of kink mass in the field model. In both approaches the parameters of the barrier are fixed at $\varepsilon = 0.2$ and $L = 10$. The initial position of the kink is $x_0 = -50$ its velocity is $u_0 = 0.4100$ in fig. A and $u_0 = 0.5400$ in fig. B. For initial velocities of the kink smaller than the critical value both trajectories are almost identical. If the initial speed exceeds critical velocity then we

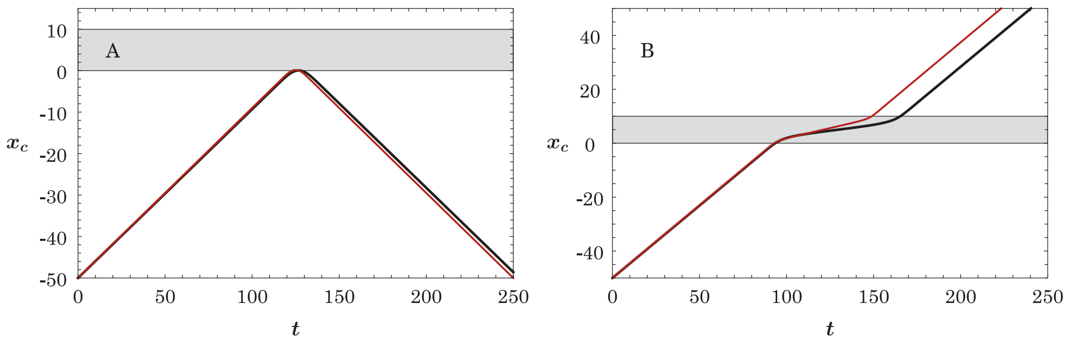

Fig. 16. The trajectory of the centre of kink mass obtained from the field model (24) (black line) compared with the trajectory of the kink obtained from the effective model (79) (red line). The initial position of the kink is $x_0 = -50$ and the parameters that describe barrier are $\varepsilon = 0.2$ and $L = 10$. (For interpretation of the references to colour in this figure legend, the reader is referred to the web version of this article.)

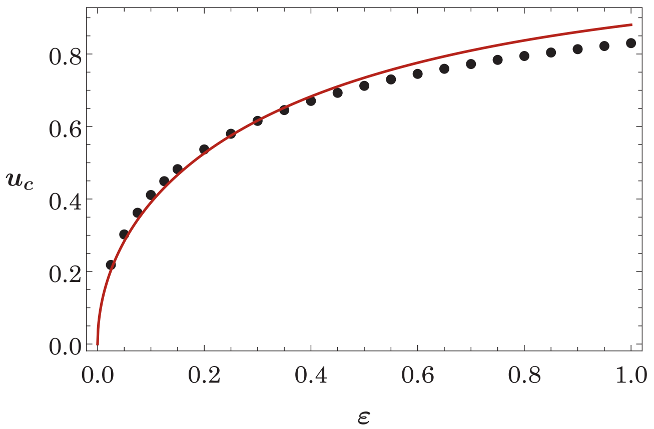

Fig. 17. The critical velocity for $L = 10$. The results of the field model (24) are represented by the black points. The red line represents the result of the effective dynamical model (79). (For interpretation of the references to colour in this figure legend, the reader is referred to the web version of this article.)

observe only qualitative agreement. The results of simulations are collected in Fig. 17. In the plot the spatial size of the inhomogeneity is $L = 10$ and the initial position of the kink $x_0 = -50$. In this figure the outcome of the last equation is compared with the results of the field model (24). We immediately notice the reasonable agreement of the effective model with the field model for small ε. For larger ε we observe an overestimation of the values of u_c.

5. Remarks

In order to better evaluate the validity of the methods we compare the representative results. In Fig. 18 we compare trajectories in the case of inhomogeneity parameters $\varepsilon = 0.2$ and $L = 10$. The initial position of the kink is $x_0 = -50$. The grey region of the figures represents the position of the barrier. The black continuous line represents the trajectory of the centre of mass of the kink. The first and third methods produce the results represented by the green line while the results of second method are represented by the blue one. The red line represents the trajectory obtained in the fourth method. In Fig. 18 A the initial kink speed is below the critical velocity $u_0 = 0.4100$. Comparison of the methods clearly shows excellent agreement between centre of mass position obtained from the field model and the kink position obtained in the framework of the effective Model IV. For speeds exceeding the critical velocity $u_0 = 0.5400$ the fourth model shows only quantitative agreement.

In Fig. 19 we also present the results collected for critical velocity for small values of the barrier height i.e. for small values of parameter ε. In simulations the initial kink position was $x_0 = -50$. The last method (Method IV) produces the results, represented by the red line, which are in good agreement with the exact result (represented by the black dots). In the considered regime three methods (Method I, II and III) have the same level of precision i.e. all these methods significantly underestimate the real values of the critical velocity.

Summing up, we proposed two approaches. In the first approach the Methods I, II and III can be corrected by taking into account the active mass of the kink instead of its total mass. The result of this approach was tested on Method I and it perfectly reproduces the exact result. The second approach (Method IV) is based on projection onto the energy density. The outcome of this approach is in reasonable agreement with the exact result. The advantage of this method lies in the fact that it does not need additional parameter estimation. We also tested models with more degrees of freedom (see Appendix B). Surprisingly, these models do not improve the precision of the description of the system under consideration. We would like to underline that the proper estimation of the critical velocity is crucial for establishing the correct relation between parameters of the inhomogeneity and the critical current in the system (1) enriched with the dissipation term and the bias current. The critical current is a quantity directly measured in experimental systems containing Josephson junctions.

The other issue is an influence of the inhomogeneity represented by the function $\mathcal{F}$ on the linear excitations of the considered model. The sine Gordon equation in the linear approximation

$$\frac{1}{\bar{c}^2}\,\partial_t^2\phi - \partial_x^2\phi + \frac{1}{\lambda_J^2}\,\phi = 0,$$

possess wave solutions that satisfy the following dispersion relation

$$\omega = \bar{c}\sqrt{k^2 + \frac{1}{\lambda_J^2}}\,.$$

In the model considered by us (if we assume $\mathcal{F} = const$) the linearized equation

$$\frac{1}{\bar{c}^2}\,\partial_t^2\phi - \mathcal{F}\partial_x^2\phi + \frac{1}{\lambda_J^2}\,\phi = 0,$$

is satisfied by the plasmons that satisfy a modified relation of dispersion

$$\omega = \bar{c}\sqrt{\mathcal{F}k^2 + \frac{1}{\lambda_J^2}}.$$

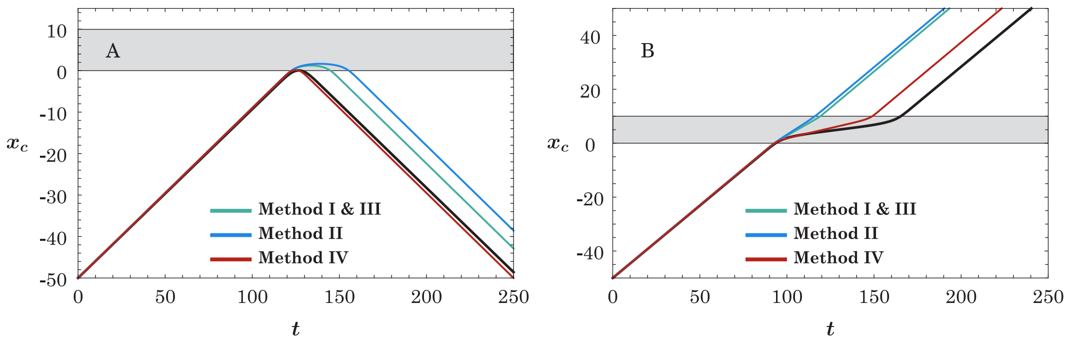

Fig. 18. Comparison of the trajectories obtained for different methods with the trajectory of the centre of mass of the kink obtained on the ground of field model (black line). In the plots $\varepsilon = 0.2$, $L = 10$, $x_0 = -50$. In figure A the initial speed is $u_0 = 0.4100$ and in figure B $u_0 = 0.5400$. (For interpretation of the references to colour in this figure legend, the reader is referred to the web version of this article.)

Knowledge of these relations allows for estimation of the refractive index for the considered system. By definition it is related to the phase velocity u_{ph}

$$n = \frac{\bar{c}}{u_{ph}} = \frac{\bar{c}k}{\omega}.$$

The refractive index of the system with $\mathcal{F} \neq 1$ in relation to the refractive index of the system with $\mathcal{F} = 1$ is as follows

$$n_{\mathcal{F}} = n\sqrt{\frac{k^2 + \frac{1}{\lambda_J^2}}{\mathcal{F}k^2 + \frac{1}{\lambda_J^2}}} = n\sqrt{\frac{1 + \frac{1}{4\pi^2}\frac{\lambda^2}{\lambda_J^2}}{\mathcal{F} + \frac{1}{4\pi^2}\frac{\lambda^2}{\lambda_J^2}}}.$$

In particular for sufficiently short wave excitations i.e. $\lambda \ll \lambda_J$ we can neglect the second terms in the nominator and denominator and we obtain

$$n_{\mathcal{F}} \approx n\frac{1}{\sqrt{\mathcal{F}}} \approx n(1 - \frac{1}{2}\varepsilon g),$$

where we used the formula $\mathcal{F} = 1 + \varepsilon g$. The presence of the potential barrier $\mathcal{F} > 1$ lowers the value of the refraction index in comparison to the system with $\mathcal{F} = 1$. If $n_{\mathcal{F}} < 1$ plane waves can reflect from the barrier. The situation resembles reflection of the radio waves from the ionosphere. We do not consider the opposite regime i.e. $\lambda \gg \lambda_J$, because in the case of the typical Josephson junction it corresponds to the size of the whole junction. We see that the presence of the barrier affects the motion of the kink but it also affects the propagation of plasmons in the system.

The other issue that deserves comment is quantum behaviour of the considered system. Theoretical and experimental research conducted on Josephson junctions suggest that at sufficiently low temperatures (below $100mK$) the fluctuations in the junction change their character from thermal (classical) to quantum [57,58]. The nature of fluctuations is crucial for the mechanism of escape to a finite voltage state. In particular, a position of Switching Current Distribution (SCD) peak in the case of thermal activation is temperature dependent. On the other hand in the case of Macroscopic Quantum Tunnelling (MQT) the position of SCD peaks saturate at low temperatures. It seems that in spite of the relatively big size of the junction at low temperatures it behaves as a quantum system. In particular the kink, in spite of its large size, that is on the level of the Josephson penetration depth, has a relatively small mass. Let us, for a moment, abandon the convention $\bar{c} = 1$. The fluxon rest mass, for conventional superconductors, can be estimated as follows $m_0 \sim 10^{-2}m_e \div 10^{-3}m_e$ (for width of the junction of order 1 µm, m_e is electron mass). It seems that at very low temperatures one can expect tunnelling of the kink through a barrier. Although, this possibility deserves further studies in this article we concentrated on purely classical behaviour.

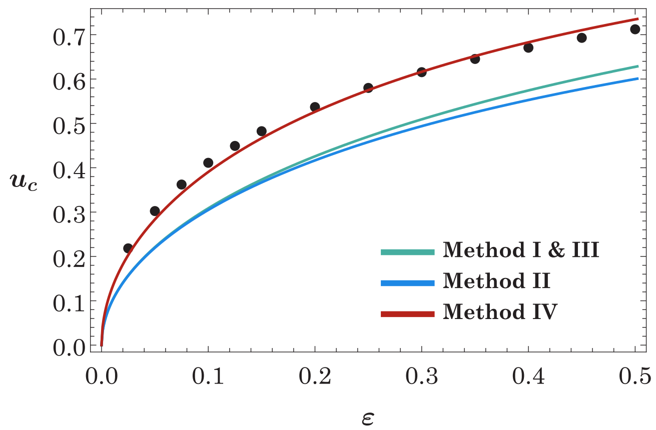

Fig. 19. The effective models compared with the field model for $L = 10$ and small ε. The critical velocity that follows from the first and third model is represented by the green line. The blue line represents the results of the second model. The results of fourth model are represented by the red line. (For interpretation of the references to colour in this figure legend, the reader is referred to the web version of this article.)

CRediT authorship contribution statement

J. Gatlik: Analytical and numerical analysis, Manuscript preparation. **T. Dobrowolski:** Analytical analysis, Manuscript preparation.

Declaration of competing interest

The authors declare that they have no known competing financial interests or personal relationships that could have appeared to influence the work reported in this paper.

Acknowledgement

This research was supported in part by PL–Grid Infrastructure.

Appendix A

Curved coordinates in the vicinity of the central curve play a crucial role for considerations of Section 2. The coordinates are stretched around a curve centrally located in the dielectric layer. First we introduce vector field $\vec{X} = \vec{X}(s)$ parameterized by the space parameter s that describes the position of the curve in the

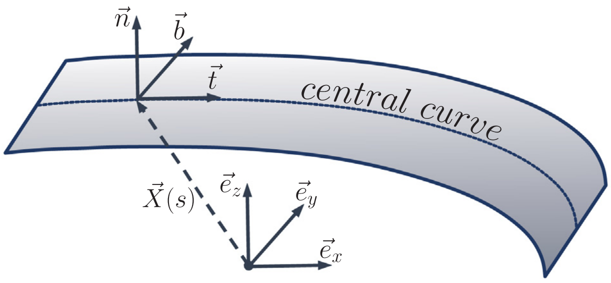

Fig. 20. Frenet frame and the plane curve located on the surface.

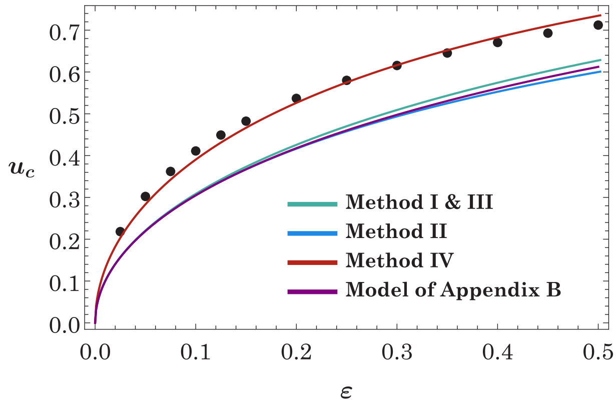

Fig. 21. Comparison of one variable models with two variables model of Appendix B. The figure concerns $\varepsilon = 0.2$ and $L = 10$. (For interpretation of the references to colour in this figure legend, the reader is referred to the web version of this article.)

three dimensional space. The relation between Cartesian and new curved coordinates is given by the formula

$$\vec{x} = \vec{X}(s) + \rho\, \vec{b}(s) + u\, \vec{n}(s), \tag{80}$$

where u and ρ are coordinates that parameterize normal and binormal directions to the curve. Both normal and binormal vectors $\vec{n}$ and $\vec{b}$ are orthogonal to the tangent vector to the curve $\vec{t} = \partial_s \vec{X}$. All those vectors form an orthonormal frame called the Frenet frame

$$\vec{t} \cdot \vec{n} = \vec{t} \cdot \vec{b} = \vec{b} \cdot \vec{n} = 0, \quad \vec{t}^{\,2} = \vec{n}^{\,2} = \vec{b}^{\,2} = 1. \tag{81}$$

The formula (80) is an implicit relationship between Cartesian $(x^i) = (x^1, x^2, x^3) = (x, y, z)$ and curved coordinates $(\sigma^a) = (\sigma^1, \sigma^2, \sigma^3) = (s, \rho, u)$. The change of the vectors belonging to the Frenet frame when one moves along the curve $\vec{X}(s)$ is described by the Frenet–Serret formulas

$$\partial_s \vec{t} = K \vec{n}, \tag{82}$$

$$\partial_s \vec{n} = -K \vec{t} + \omega \vec{b}, \tag{83}$$

$$\partial_s \vec{b} = -\omega \vec{n}, \tag{84}$$

where the coefficients $K(s)$ and $\omega(s)$ represent curvature and the torsion of the curve. In the case of the plane curve (assumed in this article) the torsion disappears $\omega = 0$ and therefore the formulas simplify significantly

$$\partial_s \vec{t} = K \vec{n}, \quad \partial_s \vec{n} = -K \vec{t}, \quad \partial_s \vec{b} = 0. \tag{85}$$

In the calculus we shall need the metric in the curved coordinates

$$g_{ab} = \frac{\partial x^i}{\partial \sigma^a} \frac{\partial x^j}{\partial \sigma^b} \eta_{ij} = \partial_a \vec{x} \cdot \partial_b \vec{x}, \tag{86}$$

where $(\eta_{ij}) = diag(1, 1, 1)$ is a metric in Cartesian coordinates. The derivatives of vector $\vec{x}$ can be calculated based on formula (80) and simplified Frenet–Serret formulas (85)

$$\partial_s \vec{x} = \vec{t} + u\, \partial_s \vec{n} + \rho\, \partial_s \vec{b} = (1 - u\, K) \vec{t} = G \vec{t}, \tag{87}$$

where $G = (1 - u\, K)$ and

$$\partial_u \vec{x} = \vec{n}, \quad \partial_\rho \vec{x} = \vec{b}. \tag{88}$$

By inserting the obtained derivatives (87)–(88) into the expression on the metric (86) and using the orthonormality conditions (81), we get components of the metric tensor in curved coordinates

$$g_{ss} = G^2, \quad g_{uu} = 1, \quad g_{\rho\rho} = 1, \quad g_{su} = 0, \quad g_{s\rho} = 0, \quad g_{u\rho} = 0. \tag{89}$$

In the orthogonal system of coordinates the differential operators are solely determined by diagonal components of the metric tensor. In the case of gradient we have

$$\mathbf{grad}\varphi = \nabla \varphi = \frac{1}{\sqrt{g_{ss}}} (\partial_s \varphi) \vec{t} + \frac{1}{\sqrt{g_{\rho\rho}}} (\partial_\rho \varphi) \vec{b} + \frac{1}{\sqrt{g_{uu}}} (\partial_u \varphi) \vec{n}. \tag{90}$$

In coordinates defined in the vicinity of the central curve gradient operator simplifies to the form

$$\mathbf{grad}\varphi = \nabla \varphi = \frac{1}{G} (\partial_s \varphi) \vec{t} + (\partial_\rho \varphi) \vec{b} + (\partial_u \varphi) \vec{n}. \tag{91}$$

For **curl** operator we have

$$\mathbf{curl}\, \vec{H} = \frac{1}{\sqrt{g_{uu} g_{\rho\rho}}} \left[\partial_\rho (\sqrt{g_{uu}} H_u) - \partial_u (\sqrt{g_{\rho\rho}} H_\rho) \right] \vec{t} + \tag{92}$$

$$\frac{1}{\sqrt{g_{uu} g_{ss}}} \left[\partial_u (\sqrt{g_{ss}} H_s) - \partial_s (\sqrt{g_{uu}} H_u) \right] \vec{b} +$$

$$\frac{1}{\sqrt{g_{ss} g_{\rho\rho}}} \left[\partial_s (\sqrt{g_{\rho\rho}} H_\rho) - \partial_\rho (\sqrt{g_{ss}} H_s) \right] \vec{n}.$$

In the coordinates used by us this operator simplifies to the form

$$\mathbf{curl}\, \vec{H} = \left[\partial_\rho H_u - \partial_u H_\rho \right] \vec{t} + \frac{1}{G} \left[\partial_u (G H_s) - \partial_s H_u \right] \vec{b} + \frac{1}{G} \left[\partial_s H_\rho - \partial_\rho (G H_s) \right] \vec{n}. \tag{93}$$

Appendix B

The model described in this paper can be also studied in the framework of two dimensional "moduli space". In order to obtain this description we start from the field lagrangian

$$L = \int_{-\infty}^{+\infty} dx \left[\frac{1}{2} (\partial_t \phi)^2 - \frac{1}{2} \mathcal{F}(x) (\partial_x \phi)^2 - (1 - \cos \phi) \right]. \tag{94}$$

We introduce to the above formula the kink ansatz (34) where $\xi(t, x) = \gamma(t)(x - x_0(t))$ but this time we treat $x_0(t)$ and $\gamma(t)$ as two independent dynamical variables

$$L = 2 \int_{-\infty}^{+\infty} dx \left[\dot{\xi}^2 - \mathcal{F} \acute{\xi}^2 - 1 \right] \mathrm{sech}^2 \xi. \tag{95}$$

We use $\mathcal{F}$ defined by Eq. (33). Moreover we use the space $\acute{\xi} = \gamma$ and time $\dot{\xi} = \xi \dot{\gamma} / \gamma - \gamma \dot{x}_0$ derivatives of auxiliary function ξ

$$L = 2 \int_{-\infty}^{+\infty} dx \left[\left(\xi \frac{\dot{\gamma}}{\gamma} - \gamma \dot{x}_0 \right)^2 - \gamma^2 - 1 - \varepsilon \gamma g \right] \mathrm{sech}^2 \xi. \tag{96}$$

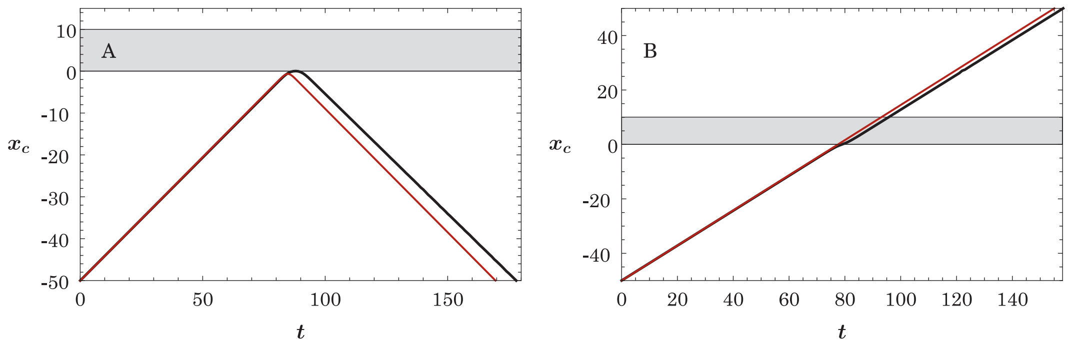

Fig. 22. Kink position of model IV (red line) compared with position of the centre of mass of the kink obtained on the ground of field model (black line). The parameters of the plot are as follows $L = 0.2$ and $\varepsilon = 5$. The initial position of the kink is taken $x_0 = -50$ and the initial velocities $u_0 = 0.59$ in fig. A, $u_0 = 0.65$ in fig. B. (For interpretation of the references to colour in this figure legend, the reader is referred to the web version of this article.)

Next, we do the integration for the variable ξ and rescale an effective lagrangian by a factor of 8

$$L = \frac{1}{2}\gamma\dot{x}_0^2 + \frac{\pi^2}{24}\frac{1}{\gamma^3}\dot{\gamma}^2 - \frac{1}{2}\left(\gamma + \frac{1}{\gamma}\right) - \frac{1}{4}\varepsilon\left(\tanh\gamma(L - x_0) + \tanh\gamma x_0\right). \quad (97)$$

The Euler–Lagrange equations for this lagrangian have a much more extensive form

$$\dot{u} + \frac{\dot{\gamma}}{\gamma}u = \frac{1}{4}\varepsilon\left[\mathrm{sech}^2\gamma(L - x_0) - \mathrm{sech}^2\gamma x_0\right] \quad (98)$$

and

$$\frac{\pi^2}{12}\frac{1}{\gamma^3}\ddot{\gamma} - \frac{\pi^2}{4}\frac{1}{\gamma^4}\dot{\gamma}^2 = \frac{1}{2}\dot{x}_0 + \frac{\pi^2}{8}\frac{1}{\gamma^4}\dot{\gamma}^2 + \frac{1}{2}\frac{1}{\gamma^2} - \frac{1}{2} - \frac{1}{4}\varepsilon\left[(L - x_0)\mathrm{sech}^2\gamma(L - x_0) + x_0\mathrm{sech}^2\gamma x_0\right] \quad (99)$$

but its predictive power (especially for higher speeds) is comparable with previous methods. The comparison of results of the two variable model with other models described in this article for $\varepsilon = 0.2$ and $L = 10$ are presented in Fig. 21. One can see that in spite of the complications of the last model, the results of the model are not better than simple models considered in Section 4. Moreover, we also considered how the addition of localized impurity modes to the kink affects the estimation of critical velocity. We considered an ansatz with four dynamical variables $\gamma(t)$, $x_0(t)$, $A(t)$ and $B(t)$

$$\phi(t, x) = 4\arctan\left(e^{\gamma(t)(x - x_0(t))}\right) + A(t)\varphi_1(x) + B(t)\varphi_2(x), \quad (100)$$

where localized functions $\varphi_1(x) = \mathrm{sech}(x)$ and $\varphi_2(x) = \mathrm{sech}(L - x)$ have been associated with the ends of the barrier. The resulting effective lagrangian $L = L(\gamma(t), x_0(t), A(t), B(t))$ in spite of its complication (even in a small velocity regime) provides a far from satisfactory outcome. The results of this approach are less precise than any of the one and two variable models.

Appendix C

Frequently the Josephson junction is populated by inhomogeneities caused by local change of the critical current density at some specific points of the system. Their presence is described by additional terms in the potential $-\varepsilon\delta(x - x_{imp})(1 - \cos\phi)$, where x_{imp} indicates position of the impurity [52,59,60]. If $\varepsilon < 0$ then such potential describes microshort. On the other hand for $\varepsilon > 0$ it describes microresister. The latter plays a role of a pinning potential for the fluxon.

One might ask whether (by analogy) in formula (25) it is possible to replace the product $\varepsilon g(x)$ by the delta function. Direct implementation of this idea is impossible because of the necessity to differentiate the delta function in the equation of motion (25). On the other hand, the delta function can be represented as the limit of a sequence of Gaussian, bell, or rectangular $F_{\varepsilon,L}(x) = \varepsilon(\theta(x) - \theta(x - L))$ functions [61]. In the last case the delta function is recovered in the limit $\varepsilon \to \infty$, $L \to 0$ and $\varepsilon \cdot L = 1$. In order to reproduce some results in this regime we have to go far beyond the small ε regime. We provide exemplary result for $L = 0.2$ and $\varepsilon = 5$. In Fig. 22 we compare the trajectories of the centre of mass of the kink that follows from the field model and the position of the kink obtained on the ground of the effective model IV. As would be expected, if ε increases, the model gradually loses its predictive power.

References

[1] N.J. Zabusky, M.D. Kruskal, Phys. Rev. Lett. 15 (1965) 240.
[2] C.S. Gardner, J.M. Greene, M.D. Kruskal, R.M. Miura, Phys. Rev. Lett. 19 (1967) 1095.
[3] A. Jeffrey, Q. Jl R. Astr. Soc. 14 (1973) 183.
[4] F. Yoshida, T. Sakuma, J. Phys. Soc. Japan 42 (1977) 1412.
[5] M.P. Soerensen, P.L. Christiansen, P.S. Lomdahi, J. Acoust. Soc. Am. 76 (1984) 871.
[6] Wu-Ming Liu, E. Kengne, Schrödinger Equations in Nonlinear Systems, Springer, Singapore, 2019.
[7] M.J. Ablowitz, P.A. Clarkson, Solitons, Nonlinear Evolutionequations and Inverse Scattering, Cambridge Univ. Press, 1999.
[8] N.F. Pederson, in: S.E. Trullinger, et al. (Eds.), Solitons in Josephson Transmission Lines, in Solitons, Elsevier Science Publishers, Amsterdam, 1986.
[9] L.A. Ferreira, B. Piette, W.J. Zakrzewski, Phys. Rev. E 77 (2008) 036613.
[10] L.A. Ferreira, B. Piette, W.J. Zakrzewski, J. Phys. C 128 (2008) 012027.
[11] C. Adam, M. Haberichter, A. Wereszczynski, Phys. Lett. B 754 (2016) 18.
[12] V.G. Ivancevic, T.T. Ivancevic, J. Geom. Symmetry Phys. 31 (2013) 1.
[13] J. Cuevas-Maraver, P.-G. Kevrekidis, F. Williams (Eds.), The Sine-Gordon Model and Its Applications from Pendula and Josephson Junctions to Gravity and High-Energy Physics, Springer International Publishing, Switzerland, 2014.
[14] A.R. Bishop, T. Schneider, Solitons and Condensed Matter Physics, Springer-Verlag, Berlin, 1981.
[15] A.S. Davydov, Solitons in Molecular Systems, Reidel, Dordrecht, Netherlands, 1985.
[16] A. Barone, G. Paterno, Physics and Applications of the Josephson Effect, Wiley, New York, 1982.
[17] B.D. Josephson, Adv. Phys. 14 (1965) 419.
[18] A. Barone, F. Esposito, C.J. Magee, A.C. Scott, Riv. Nuovo Cimento 1 (1971) 227.
[19] J.D. Gibbon, I.N. James, I.M. Moroz, Phys. Script. 20 (1979) 402.
[20] S.V. Kuplevakhsky, A.M. Glukhov, Phys. Rev. B 73 (2006) 024513.
[21] S.V. Kuplevakhsky, A.M. Glukhov, Phys. Rev. B 76 (2007) 174515.
[22] F. Zhang, Y.S. Kivshar, B.A. Malomed, L. Vzquez, Phys. Lett. A 159 (1991) 318.
[23] L. Morales-Molina, F.G. Mertens, A. Snchez, Phys. Rev. E 72 (2005) 016612.
[24] J.A. Gonzlez, S. Cuenda, A. Snchez, Phys. Rev. E 75 (2007) 036611.
[25] M.B. Fogel, S.E. Trullinger, A.R. Bishop, J.A. Krumhansl, Phys. Rev. B 15 (1977) 1578.

[26] K. Nakajima, Y. Onodera, J. Appl. Phys. 47 (1976) 1620.
[27] A. Benabdallah, J.-G. Caputo, A.C. Scott, Phys. Rev. B 54 (1996) 16139.
[28] A. Kemp, A. Wallraff, A.V. Ustinov, Phys. Stat. Sol. B 233 (2002) 472.
[29] A. Kemp, A. Wallraff, A.V. Ustinov, Physica C 368 (2002) 324.
[30] D.R. Gulevich, F.V. Kusmartsev, Phys. Rev. Lett. 97 (2006) 017004.
[31] D.R. Gulevich, F.V. Kusmartsev, New J. Phys. 9 (2007) 59.
[32] D.R. Gulevich, M. Gaifullin, O.E. Kusmartseva, F.V. Kusmartsev, K. Hirata, Physica C 468 (2008) 1903.
[33] D.R. Gulevich, F.V. Kusmartsev, S. Savel'ev, V.A. Yampol'skii, F. Nori, Phys. Rev. Lett. 101 (2008) 127002.
[34] J.-G. Caputo, D. Dutykh, Phys. Rev. E 90 (2014) 022912.
[35] R. Monaco, J. Phys.: Condens. Matter 28 (2016) 445702.
[36] R. Monaco, J. Mygind, V.P. Koshelets, Supercond. Sci. Technol. 31 (2018) 025003.
[37] C. Gorria, Yu. B. Gaididei, M.P. Soerensen, P.L. Christiansen, J.-G. Caputo, Phys. Rev. B 69 (2004) 134506.
[38] E. Goldobin, A. Sterck, D. Koelle, Phys. Rev. E 63 (2001) 031111.
[39] G. Carapella, G. Costabile, N. Martucciello, M. Cirillo, R. Latempa, A. Polcari, G. Filatrella, Physica C 382 (2002) 337.
[40] G. Carapella, N. Martucciello, G. Costabile, Phys. Rev. B 66 (2002) 134531.
[41] D.R. Gulevich, F.V. Kusmartsev, Supercond. Sci. Technol. 20 (2007) S60.
[42] T. Dobrowolski, Phys. Rev. E 79 (2009) 046601.
[43] T. Dobrowolski, Eur. Phys. J. B 86 (2013) 346.
[44] A. Jarmoliski, T. Dobrowolski, Physica B 514 (2017) 24.
[45] T. Dobrowolski, A. and Jarmoliski, Phys. Rev. E 96 (2017) 012214.
[46] T. Dobrowolski, Ann. Physics 327 (2012) 1336.
[47] M.J. Rice, E.J. Mele, Solid State Commun. 35 (1980) 487.
[48] M.J. Rice, Phys. Rev. B 28 (1983) 3587.
[49] Y.S. Kivshar, B.A. and Malomed, Rev. Modern Phys. 61 (1989) 763.
[50] M. Buttiker, R. Landauer, Phys. Rev. Lett. 43 (1979) 1453.
[51] M. Buttiker, T. Christen, Phys. Rev. Lett. 75 (1995) 1895.
[52] D.W. McLaughlin, A.C. Scott, Phys. Rev. A 18 (1978) 1652.
[53] M.B. Fogel, S.E. Trullinger, A.R. Bishop, J.A. Krumhansl, Phys. Rev. Lett. 46 (1977) 1411.
[54] T. Dobrowolski, P. Tatrocki, Phys. Lett. A 372 (2008) 2834.
[55] B.D. Josephson, Phys. Lett. 1 (1962) 251.
[56] W. Rindler, Introduction to Special Relativity, Claredon Press, Oxford, 1991.
[57] R.F. Voss, R.A. Webb, Phys. Rev. Lett. 47 (1981) 265.
[58] I. Affleck, Phys. Rev. Lett. 46 (1981) 388.
[59] B.A. Malomed, A.V. Ustlnov, J. Appl. Phys. 67 (1990) 3791.
[60] Yu.S. Kivshar, B.A. Malomed, J. Phys. A 21 (1988) 1553.
[61] S. Hassani, Mathematical Physics a Modern Introduction to Its Foundations, Springer-Verlag, New York, 1999.

Physica D 445 (2023) 133649

Contents lists available at ScienceDirect

Physica D

journal homepage: www.elsevier.com/locate/physd

The impact of thermal noise on kink propagation through a heterogeneous system

J. Gatlik, T. Dobrowolski *

Institute of Physics UP, Podchorążych 2, 30-084 Cracow, Poland

A R T I C L E I N F O

Article history:
Received 28 June 2022
Received in revised form 21 December 2022
Accepted 2 January 2023
Available online 7 January 2023
Communicated by R. Kuske

Keywords:
sine–Gordon model
Soliton
Collective coordinates
Thermal noise

A B S T R A C T

The impact of thermal noise on kink motion through the curved region of the long Josephson junction is studied. On the basis of the Fokker–Planck equation the analytical formula that describes the probability of transmission of the kink over the potential barrier is proposed. The analytical results are compared with the simulations based on the field model. It has been numerically shown that above one Kelvin the probabilities of crossing the barrier are correctly described by the formula proposed in the paper.

1. Introduction

In recent years, a significant increase of interest in the construction of a variety of appliances that use superconducting elements is observed. Among the devices manufactured on the basis of superconductors, Josephson junctions occupy a prominent position. The effect of supercurrent flow without any voltage applied was initially predicted by Brian D. Josephson [1,2]. A device known as a Josephson junction consists of two superconductors coupled by some weak link. The weak link can be made of a thin insulating barrier (in S-I-S junctions), normal non-superconducting metal (in S-N-S junctions), or have a form of constriction that weakens the superconductivity at the point of contact (in S-s-S junctions). The effect was experimentally confirmed for the first time by Philip Anderson and John Rowell [3].

Presently there are a variety of devices which contain Josephson junctions in their design [4,5]. They can be classified into three groups. In the first group one can include antennas, amplifiers, filters, bolometers, single photon detectors, magnetometers and many others. The second group consists of digital electronic appliances like digital-to-analogue and analogue-to-digital converters and rapid single flux quantum computing elements. The third group consists of quantum computing devices.

In the context of future practical applications of the Josephson junction it is natural to look for superconducting materials with high critical temperatures. Presently at normal pressure, it is possible to achieve a state of superconductivity at relatively high temperatures in the so-called high-temperature superconductors [6]. An example of such materials is cuprate-perovskite ceramic which has a critical temperature above 90 K. Nowadays one of the highest-temperature superconductors is $HgBa_2Ca_2Cu_3O_{8+\delta}$ with a critical temperature exceeding 133 K [7]. In particular, exceeding the temperature 77 K allows the use of liquid nitrogen, on an industrial scale, in cooling systems of superconducting devices.

The Josephson junction properties required for optimal performance of the appropriate devices can be planned at the design stage of the equipment that uses them. Between multiple approaches directed at obtaining requested properties of Josephson junctions, shape engineering plays a significant role. In this approach, particular modifications of the junction shape are proposed in order to obtain their required properties. For example, in the article [8] the authors proposed a device that consists of a junction with an exponentially tapered width, decreasing toward the load. In this device the junction is preceded by an idle region, where the oxide layer is thicker, preventing the tunnelling of Cooper pairs.

On the other hand, in the heart-shaped annular junction two classical vortex states can be prepared, corresponding to two minima of the potential [9]. The bias current across the junction is used to slant the potential. The strength and direction of the applied external magnetic field plays the role of the control parameters. For example, all these parameters can be used in order to modify the barrier height. The heart-shaped long Josephson junction placed in an in-plane external magnetic field was also considered in article [10]. Based on this geometry the authors

* Corresponding author.
E-mail address: tomasz.dobrowolski@up.krakow.pl (T. Dobrowolski).

https://doi.org/10.1016/j.physd.2023.133649

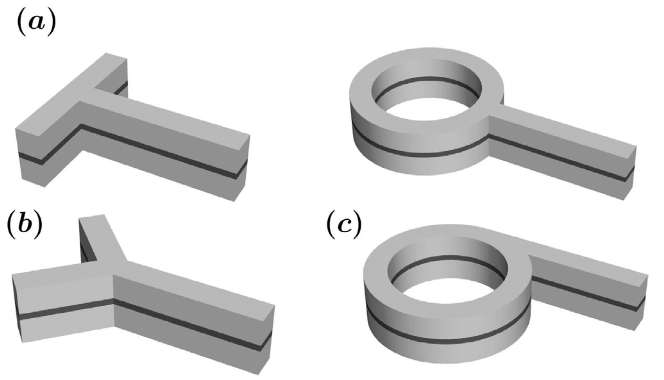

Fig. 1. Examples of different junctions shape (a) T-junctions (top left and right), (b) Y-junction and (c) sigma junction.

designed a classical system with two ground states. At sufficiently low temperatures, this structure is expected to behave as a quantum two-state system.

The other opportunity to modify properties of a junction is formation of the T-shaped geometry [11]. The above mentioned appliance consists of two perpendicular Josephson T-Lines forming a T junction. The particular effect present in the device is the creation of a new vortex when an original vortex, moving along the main Josephson T-line, is passing the T junction. The new vortex created at the T junction begins its motion in the direction perpendicular to the main Josephson T-line. The creation of a new vortex is substantially dependent on the energy of the original vortex. If the kinetic energy of the original vortex is too small then the T junction acts as a barrier and the original vortex is reflected without creation of a new vortex (the ability of introducing new vortices into the system is the reason why systems of this type are called pumps).

A similar, to some degree, proposal is sigma-pump. The main advantage of this system is the lack of the barrier. Instead, the Josephson transmission line is connected with the ring smoothly through the Y junction (Fig. 1). In this pump a nucleation barrier is absent. Moreover, the nucleation energy is gathered by the trapped fluxon during its motion in the potential associated with increasing width. A similar system is considered in articles [12,13].

An interesting possibility is an annular junction delimited by two closely spaced confocal ellipses that is characterized by a periodically modulated width [14,15]. This spatial dependence, in turn, produces a periodic potential that interchangeably attracts and repels the fluxons. In this particular junction, the double-well potential, experienced by an individual fluxon, is produced by an intrinsic non-uniform width.

If the thickness of the dielectric layer in the junction is position dependent then the kink experiences the effective potential originating in heterogeneities present in the system [16]. The threshold value of the bias current in this case is strictly determined by the parameters of the system.

The effects of arbitrary curvature on fluxon motion in curved Josephson junctions were studied in articles [17–21] with curvatures playing the role of potential barriers for kink motion. In particular in [22] the different simplified effective descriptions were compared in order to choose the most suitable for the considered system.

On the other hand, it is also important that physical systems such as the Josephson junction are subject to thermal noise. The impact of the Gaussian white noise on the switching of the system to the voltage state has been studied in the article [23]. The authors, on the base of Kramers theory [24], considered thermally activated switching and showed the differences in the behaviour of the short and long Josephson junctions. Moreover, the switching of the system from the zero-voltage state under the influence of Levy noise has been studied in [25]. The effects of white and coloured noise on the dynamics of the short and long Josephson junctions were considered additionally in the article [26]. The authors noted the existence of resonant activation and noise enhanced stability. The results obtained throw light upon the role played by different noise sources in the dynamics of superconductive devices.

The dynamics of a long Josephson junction in the framework of the sine–Gordon model with a white noise source have been studied in article [27]. The authors demonstrated that for homogeneous bias current distribution the mean escape time tends to a constant, while for inhomogeneous current distribution the mean escape time quickly decreases after approaching a few Josephson lengths. The problem of the temperature dependence of the mean escape time for annular and linear system was addressed in the paper [28]. The authors demonstrated that the fluctuational stability of the linear structure is significantly lower than for the annular one.

However, the heat transport in thermally-biased long Josephson tunnel junctions is discussed in a series of articles. For example, in article [29] it was demonstrated that the phase-dependent component of the heat current through the junction displays a coherent diffraction. Moreover, it was shown that the junction warms up in the position occupied by the solitons. This observation led to the idea of a superconducting thermal router in which the thermal transport can be locally mastered through solitons [30]. The position of the solitons would change due to the applied magnetic field and the bias current. The soliton-induced thermal effects when the soliton speed approaches the Swihart velocity were considered. In addition, the appropriate material selection of superconductors forming the junction to observe fast thermal effects was discussed in [31]. The fast solitonic Josephson heat oscillator, whose frequency is in tune with the oscillation frequency of the magnetic drive, and its application as a tunable thermal source for nanoscale heat engines and coherent thermal machines were discussed in [32]. The same system is studied in [33], where the authors observe that, starting from a homogeneous system, they finally observe some inhomogeneously-distributed temperature profiles.

In the present article we study the curved system with bias current and the quasi-particle dissipation taken into account. Moreover this paper is aimed at studying the effects of nonzero temperature of the system on the process of penetration of the potential barrier through the kink. We present the appropriate analytical results and compare them with the results of simulations performed in the field model. The analytical approximations rely mainly on the projection onto energy density method.

2. Kink in curved system

We consider the kink motion in the sine–Gordon model with position dependent dispersive term

$$\partial_t^2 \phi + \alpha \partial_t \phi - \partial_x (\mathcal{F}(x) \partial_x \phi) + \sin \phi = -\Gamma. \quad (1)$$

In the context of the Josephson junction the distances in the above equation are measured in the units of Josephson penetration depth, the time is measured in units of the inverse plasma frequency, α represents the dissipation caused by the quasi-particle currents and Γ is bias current. The function $\mathcal{F}(x)$ contains information about curvature of the junction. The physical motivation for description of curvature effects in the framework of this model was described in detail in the articles [19,22]. In those papers it was shown that this modification appears in the description of a curved Josephson junction. The kink solution in this physical situation represents the fluxon propagating along the long junction.

Reduction of the field model (Eq. (1)) to a single mechanical degree of freedom is performed in the framework described in article [22], thanks to the procedure called projection onto energy density. In order to realize this scheme we introduce into field equation the kink like ansatz

$$\phi(t,x) = 4\arctan(e^{\xi(t,x)}),$$

where in nonrelativistic limit the function $\xi(t,x)$ is approximated as follows

$$\xi = x - x_0(t).$$

Here $x_0(t)$ denotes a position of the kink. The kink-like ansatz is the solution of the sine–Gordon model only in the case of an unperturbed system. For further convenience we introduce auxiliary function $g(x)$

$$\mathcal{F}(x) = 1 + \varepsilon g(x),$$

where ε is a dimensionless parameter that controls the magnitude of heterogeneity. We consider the deformation of the system localized between $x = x_i$ and $x = x_f$. To be precise we assume the function $g(x)$ in the form

$$g(x) = \theta(x - x_i) - \theta(x - x_f),$$

where $\theta(x)$ is Heaviside step function. The geometry of this junction is described in Appendix A. In the context of the curved junction the form of this function means constant (nonzero) curvature located between x_i and x_f. According to the method presented in the article [22], the field equation (1) can be transformed to the form

$$\dot{u}\ \mathrm{sech}\xi + u^2\ \mathrm{sech}\xi \tanh\xi + \alpha\, u\ \mathrm{sech}\xi = -\varepsilon\, \partial_x g(x)\ \mathrm{sech}\xi + \varepsilon\, g(x)\ \mathrm{sech}\xi \tanh\xi + \frac{1}{2}\Gamma, \tag{2}$$

where u denotes the kink speed i.e. $u \equiv \dot{x}_0$. The projection onto energy density in co-moving, with kink, reference frame relies on integration of Eq. (2) with the energy density profile

$$Eq = 0 \Rightarrow \int_{-\infty}^{+\infty} dx\ \mathrm{sech}^2\xi\ Eq = 0. \tag{3}$$

Here Eq denotes the difference of the expression on the left-hand side and the right-hand side of Eq. (2). This procedure is quite similar to the projection onto zero mode of the kink. The only difference lies in the fact that this profile is better localized in the neighbourhood of the kink position. There is also a more fundamental reason for choosing this profile. In systems with explicitly broken invariance with respect to spatial translations the zero mode does not exist while the energy density is still well defined. As the final outcome of elimination of the space variable we obtain the equation for the kink position

$$\dot{u} + \alpha u = \frac{2}{\pi}\Gamma - \varepsilon\frac{4}{3\pi}\left(\ \mathrm{sech}^3(x_i - x_0(t)) - \ \mathrm{sech}^3(x_f - x_0(t))\right), \tag{4}$$

where during integration we used the formula

$$\partial_x g(x) = \delta(x - x_i) - \delta(x - x_f).$$

The bracket from the right side of Eq. (4) represents the force originated in the curved region of the junction. The potential for this force represents the barrier associated with the curved region (Fig. 2)

$$V(x_0) = \varepsilon\frac{3}{4\pi}\ \Big[\ \arctan(\tanh(\frac{x_0 - x_i}{2})) - \arctan(\tanh(\frac{x_0 - x_f}{2})) + \tag{5}$$

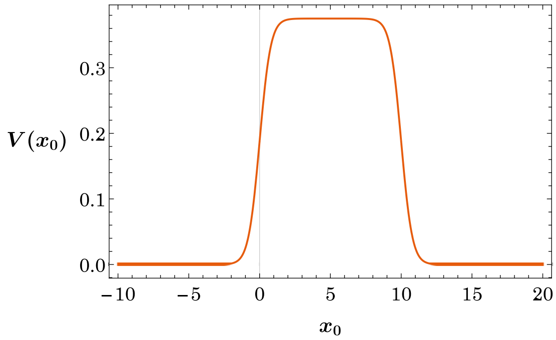

Fig. 2. The potential $V(x_0)$ that represents the presence of the curved region located between $x_i = 0$ and $x_f = L = 10$. The parameter ε is equal to one.

$$\frac{1}{2}\ \mathrm{sech}(x_0 - x_i)\tanh(x_0 - x_i) - \frac{1}{2}\ \mathrm{sech}(x_0 - x_f)\tanh(x_0 - x_f)\ \Big]\ .$$

In this paper, location of the inhomogeneity is assumed to be between $x_i = 0$ and $x_f = L$.

In order to estimate the value of the critical speed that separates the kinks reflected from the barrier from those which pass over the barrier, we separate the problem of movement in the barrier potential from the motion under the influence of constant force represented by constant bias current. The total energy of the kink that moves in the potential $V(x_0)$ is $E = \frac{1}{2}m_0u^2 + V(x_0)$, where kink mass is equal $m_0 = 8$. At the beginning of its motion the kink moves almost freely having only kinetic energy

$$E_{in} = \frac{1}{2}m_0{u_c}^2.$$

We assume that at the end of its motion the kink stops on the top of the barrier having only the potential energy

$$E_{fin} = V(x_0 = L/2) = \frac{32}{3\pi}\ \varepsilon\left[2\arctan\left(\tanh\frac{L}{4}\right) + \mathrm{sech}\frac{L}{2}\ \tanh\frac{L}{2}\right].$$

The conservation of the energy leads to the following estimation of the critical velocity

$$u_c = \sqrt{\frac{8}{3\pi}\ \varepsilon}\ \sqrt{2\arctan\left(\tanh\frac{L}{4}\right) + \mathrm{sech}\frac{L}{2}\ \tanh\frac{L}{2}}. \tag{6}$$

This estimation quite well describes the values of the critical velocity even in the case when the bias current and the dissipation term are taken into account. The reason for this is the fact that we work with velocities for which the bias current and dissipation almost cancel each other.

3. The influence of thermal fluctuations on the kink motion

Far from the barrier the last bracket from the right hand side of Eq. (4) describes the residual interaction of the kink with the barrier (which is a consequence of the interaction of the kink tail with the curved region). We will describe how the fluxon approaching the barrier from the left interacts with this barrier. This residual impact will be treated approximately as a position independent small interaction and therefore we consider the following equation

$$\dot{u} + \alpha u = \frac{2}{\pi}\Gamma - r, \tag{7}$$

instead of Eq. (4). Here r is the above mentioned small residual interaction.

Our intention is to describe the influence of the nonzero temperature, of the system, on the process of overcoming the barrier by the fluxon. We assume that the bias current is a random variable i.e. it fluctuates due to the non-zero temperature of the system. The average value of the bias current is denoted by Γ_0

$$\langle \Gamma(t)\rangle = \Gamma_0, \tag{8}$$

where averaging is with respect to all realizations of the thermal noise. In this situation from Eq. (7) we calculate the average value of the stationary speed (in stationary case $\langle \dot{u}\rangle = 0$)

$$u_s = \frac{2}{\pi\alpha}\Gamma_0 - \frac{r}{\alpha}, \tag{9}$$

where the average value of the stationary velocity is denoted by u_s. Moreover, the thermal noise has the character of a white Gaussian noise and therefore the time correlation function of the bias current is assumed in the form

$$\langle \Gamma(t)\Gamma(t')\rangle = A\delta(t-t'). \tag{10}$$

In order to fix the appropriate value of the prefactor A for the system in thermal equilibrium we came back to Eq. (7). The solution of this equation under assumption of constant r reads

$$u(t) = \frac{2}{\pi}\int_0^t dt'\,\Gamma(t')e^{\alpha(t'-t)} - \frac{r}{\alpha}(1-e^{-\alpha t}). \tag{11}$$

Now we are ready to calculate the time correlation function of the velocity

$$\langle u(t)u(\bar{t})\rangle = \left(\frac{2}{\pi}\right)^2\int_0^t dt'\int_0^{\bar{t}} dt''\langle \Gamma(t')\Gamma(t'')\rangle e^{\alpha(t'+t''-t-\bar{t})} \tag{12}$$
$$-\frac{r}{\alpha}(1-e^{-\alpha\bar{t}})\frac{2}{\pi}\int_0^t dt'\langle\Gamma(t')\rangle e^{\alpha(t'-t)}$$
$$-\frac{r}{\alpha}(1-e^{-\alpha t})\frac{2}{\pi}\int_0^{\bar{t}} dt'\langle\Gamma(t')\rangle e^{\alpha(t'-\bar{t})}$$
$$+\left(\frac{r}{\alpha}\right)^2(1-e^{-\alpha\bar{t}})(1-e^{-\alpha t})$$

If we apply formulas (8) and (10) for average and the time correlation of the bias current, and moreover assume $t=\bar{t}$ then we obtain

$$\langle u(t)^2\rangle = \langle u(t)u(\bar{t})\rangle_{\bar{t}=t} = \frac{2A}{\pi^2\alpha}(1-e^{-2\alpha t})$$
$$+\left[\left(\frac{r}{\alpha}\right)^2 - \frac{4\Gamma_0}{\pi\alpha^2}r\right](1-e^{-\alpha t})^2. \tag{13}$$

The system after the required length of time tends to thermodynamic equilibrium and therefore we extract in the last formula the terms that dominate long time behaviour of $\langle u^2\rangle$

$$\langle u(t)^2\rangle = \frac{2A}{\pi^2\alpha} + \left(\frac{r}{\alpha}\right)^2 - \frac{4\Gamma_0}{\pi\alpha^2}r. \tag{14}$$

The kinetic energy of the fluxon after a sufficiently long time reads

$$E_k = \frac{1}{2}m\langle v(t)^2\rangle = \frac{1}{2}m\bar{c}^2\langle u(t)^2\rangle$$
$$= \frac{1}{2}m\bar{c}^2\left[\frac{2A}{\pi^2\alpha} + \left(\frac{r}{\alpha}\right)^2 - \frac{4\Gamma_0}{\pi\alpha^2}r\right], \tag{15}$$

where m is kink mass and the dimensional speed v is related to dimensionless velocity u as follows $v=\bar{c}u$. Here $\bar{c}$ is Swihart velocity. We expect that after an appropriately long time the system tends to thermal equilibrium. On the other hand, in thermodynamic equilibrium, on the basis of the equipartition principle, it is proportional to the temperature T

$$E_k = \frac{1}{2}kT, \tag{16}$$

here k is Boltzmann constant. Comparison of Eqs. (15) and (16) allows the determination of the coefficient A

$$A = \frac{\pi^2\alpha k(T-\Delta T)}{2\,m\bar{c}^2}, \tag{17}$$

where we denoted

$$\Delta T \equiv \frac{m\bar{c}^2}{k}\left[\left(\frac{r}{\alpha}\right)^2 - \frac{4\Gamma_0}{\pi\alpha^2}r\right]. \tag{18}$$

For further convenience, we transform the formula (18) to the form containing the threshold value of the bias current Γ_t

$$\Delta T = \Omega(\Gamma_t - \Gamma_0) - \omega. \tag{19}$$

This threshold value Γ_t separates the values of the bias current for which the particle passes over the barrier from the values for which the reflection occurs. The parameters in the above formula are defined as follows

$$\omega \equiv \frac{m\bar{c}^2}{k}\left[\frac{4\Gamma_t}{\pi\alpha^2}r - \left(\frac{r}{\alpha}\right)^2\right], \quad \Omega \equiv \frac{4\,m\bar{c}^2 r}{\pi\alpha^2 k}.$$

Finally, the average and the time correlation function of bias currents are defined by the formulas

$$\langle\Gamma(t)\rangle = \Gamma_0, \quad \langle\Gamma(t)\Gamma(t')\rangle = \frac{\pi^2\alpha k(T-\Delta T)}{2\,m\bar{c}^2}\delta(t-t'). \tag{20}$$

Eqs. (20) are the starting point for the derivation of the Fokker–Planck equation described in Appendix B. The stationary solution of this equation is the following

$$P(u) = \sqrt{\frac{m\bar{c}^2}{2\pi k(T-\Delta T)}}\exp\left(-\frac{m\bar{c}^2}{2k(T-\Delta T)}(u-u_s)^2\right). \tag{21}$$

This probability is a base for calculation of the total probability of the transmission of the kink through the potential barrier. We have to deal with the transition event whenever the kink speed exceeds the critical velocity

$$\Delta P = \int_{u_c}^{\infty} du P(u) = \frac{1}{2}\,\mathrm{erf}\left(\sqrt{\frac{m\bar{c}^2}{2k(T-\Delta T)}}\mid u_c - u_s\mid\right), \tag{22}$$

in this formula erf denotes an error function. This probability depends, in addition to temperature and residual effects, on the difference of critical u_c and stationary u_s velocities in the system. The critical velocity separates two regimes. In the first regime the particle passes over the barrier and in the second it reflects from the barrier.

The probabilities obtained on the basis of the field model ((1) with stochastic bias current) and analytical result (22) based on the Fokker–Planck approach are compared in Figs. 3–5 for different ranges of temperatures. The fluxon energy used in the plots is $E_f = m\bar{c}^2 = 1.1\cdot 10^{-22}$ J. The field dynamics is studied at the interval $x\in[-300, 350]$. We adopted the boundary conditions that correspond to the unit topological charge, which means that the scalar field is equal to zero on the left edge of the interval and 2π on the right edge of the interval. The sample size for numerical simulations is one thousand, which means that the point corresponding to a given temperature in these figures (derived from the field model (1)) represents one thousand simulations performed for a given initial configuration. In the simulations, it was assumed that the initial position of the kink was equal to $x_0 = -50$. In all figures the bias current is normalized to Josephson critical current. Due to potential applications, the comparison was made for intervals from zero to $T = 50$ K, $T = 20$ K and $T = 5$ K. In all plots the parameters of the shift ΔT given in the formula (19) are fitted so that they take the values $\Omega = 25220.6$ and $\omega = -0.398529$. We decided

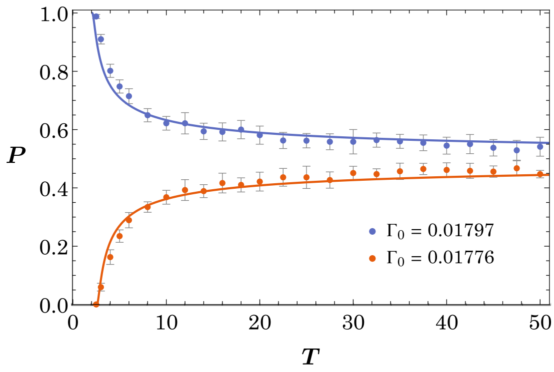

Fig. 3. The probability of transition of the fluxon obtained from the field model compared in the interval $T \in [0K, 50K]$ with the analytical formula. The parameters of the plots are $\alpha = 0.01$, $\varepsilon = 1$, $L = 10$. The blue line and points correspond to the bias current exceeding its threshold value and the red to the bias current below its threshold value.

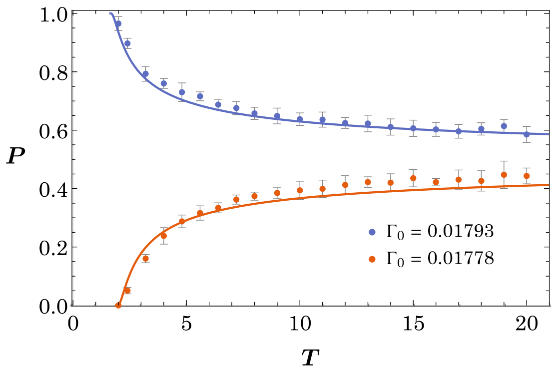

Fig. 4. The probability of transition of the fluxon in the interval $T \in [0K, 20K]$. Comparison of the analytical result with the field model prediction. The parameters of the plots are $\alpha = 0.01$, $\varepsilon = 1$, $L = 10$. The blue line and points represent data for the bias current exceeding its threshold value and the red ones the bias current below its threshold value.

to fit these parameters because the residual interaction is out of our control. Starting from the field model we obtain the fit of ΔT as a function of the absolute value of separation between actual average value of the bias current and its threshold value. This fit is presented in Fig. 6.

In all simulations we assume damping coefficient on the level of $\alpha = 0.01$. Moreover we assumed the size of the inhomogeneity $L = 10$ and we located its position between $x_i = 0$ and $x_f = 10$. The strength of the heterogeneity is fixed at the level of $\varepsilon = 1$. Because a relativistic formula (47) for stationary speed is known therefore we use it in all plots (see Appendix D). On the other hand in Figs. 3–4 the critical velocity is approximated by the non-relativistic formula (6). This choice is motivated by the fairly good compatibility of the approximated formula with the results obtained on the background of the field model. On the other hand in the case of Fig. 5 the accuracy of the formula (6) was insufficient and therefore we used the relativistic model (43) obtained in Appendix C.

Figs. 3–5 show that for the bias currents above the threshold value (blue line for analytical formula and points for the field model), as the temperature increases, the probability of the particle passing over the barrier decreases. The reduction of transition probability is in the direction of the value of one-half, the achievement of which would make such a process completely random. On the other hand, for the bias currents below its threshold value (red line for the formula and points for the field model) as the temperature increases, the probability of the particle passing

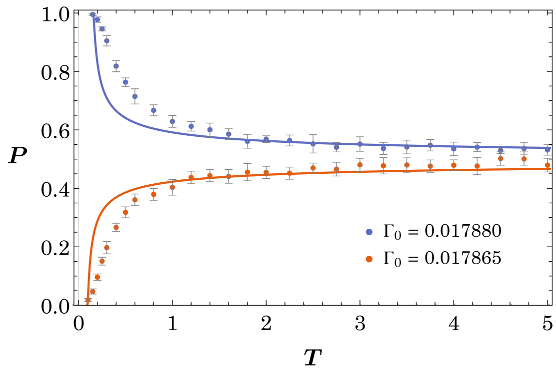

Fig. 5. Transition probability of the fluxon in the interval $T \in [0K, 5K]$. The parameters of the plots are $\alpha = 0.01$, $\varepsilon = 1$, $L = 10$. The blue line and points correspond to the bias current exceeding its threshold value and the red ones to the bias current below its threshold value.

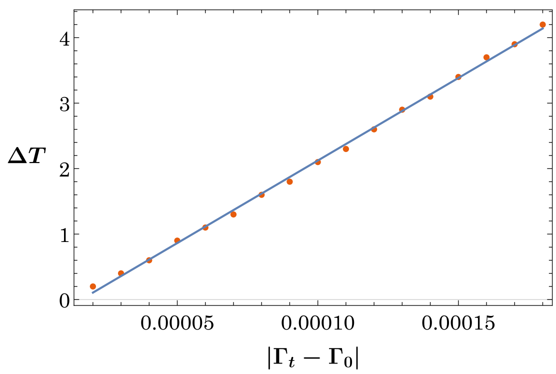

Fig. 6. ΔT as a function of modulus of difference of the threshold value of the bias current and actual average of the bias current. The parameters of the fit are $\Omega = 25220.6$ and $\omega = -0.398529$.

over the barrier also increases. The probability increases gradually towards the half value beyond which the process would be completely random. The comparison of the results of the field model in nonzero temperature with analytical description provided by formula (22) shows a pretty good level of compatibility. The results are consistent in Figs. 3 and 4, while in Fig. 5 there are deviations below one Kelvin. Figs. 3–5 show simulations when the currents slightly differ from the threshold current. On the other hand, if the difference between the average bias current and its threshold value is significant, then thermal fluctuations have a negligible impact on the process of interaction between the kink and the curved region. In this case the interaction is properly described by a deterministic model i.e. if the bias current is below the value of threshold current then the kink is reflected from the curved region. On the other hand if bias current exceeds its threshold value then the kink goes through the curved region. This behaviour is crucial for possible practical applications.

4. Remarks

In the present article we considered the impact of thermal fluctuations on the process of interaction of the kink with the heterogeneous region of the system described by a nearly integrable sine–Gordon model. The physical background of the studies is the influence of the curvature on the fluxon motion in the long Josephson junction. We obtained analytical formulas that describe probabilities of transition through and reflection of the kink from the potential barrier that represents heterogeneity. The main result is based on the Fokker–Planck equation obtained for the considered system (Appendix B). We compared the analytical results with the simulations performed in the framework of the field model for different ranges of temperatures. Due to potential applications the comparison was made for intervals from zero to $T = 50K$, $T = 20$ K and $T = 5$ K. The compatibility of the analytical formula with the numerical simulations is satisfactory in the first (Fig. 3) and the second regime (Fig. 4). In the third regime (Fig. 5) the compliance above one $1K$ is also satisfactory.

The most problematic regime of temperature is presented in Fig. 5. In this interval we resigned from the formula (6) for critical velocity and in order to obtain a better fit we used the relativistic model (43) for estimation of the critical speed (Appendix C). Either way we observed in the small temperature regime presented in Fig. 5 some discrepancy between the result of the field model and our fit located in the interval from $0K$ to $1K$. We identified a probable reason for this problem.

In the low temperature regime we observed occurrence of the resonance windows in the transition process. It means that we observe very narrow regimes of the parameters that correspond to transition below the critical speed and moreover the reflection regimes above the critical velocity. This phenomenon has a place in the effective model (43) and in the original field model (1) as well. This phenomenon is responsible for the ambiguity of the estimation of the critical speed and is responsible for the discrepancy of the approximate description and the results of the field model in Fig. 5. A similar phenomenon was previously observed by many researchers. For example in article [34] in the ϕ^4 model an interaction of the kink with attracting point impurity was studied. The existence of resonance windows in initial speeds below some threshold velocity had found an explanation in the resonant energy exchange between the kink internal mode and its translational mode. This behaviour was first observed numerically by Campbell [35] and his collaborators in the case of kink–antikink scattering in the ϕ^4 model. Presently there is a variety of articles that contain a detailed explanation of the two-bounce resonance observed in kink–antikink collisions [36]. A separatrix map for this problem that explains the complex fractal-like dependence on initial velocity for kink–antikink collisions was also constructed. The chaotic nature of such collisions depends on the transfer of energy to a secondary mode of oscillation [37]. In the frame of the moduli space formalism [38] a spectacular result in reproducing the fractal structure in the formation of the final state was reached in article [39]. The key insight of these articles is that the existence of resonance windows is possible due to the presence of an internal mode in the spectrum of the kink in the ϕ^4 model [40,41]. The situation in the case of the sine–Gordon model is different. The linear spectra of the kink excitations do not contain the discrete internal mode and therefore the structure and the nature of the windows in the model considered in this paper is enigmatic. On the other hand the modification of the sine–Gordon model considered in this article belongs to the so called nearly integrable variations of the original model. The studies on this subject are ongoing and will be presented in the future. To some degree a similar example of the model containing resonance windows in kink–antikink interactions was presented in the article [42]. This article describes the solutions of the ϕ^6 model that does not contain, in its linear spectra of excitations, the discrete internal eigenmodes which, to some degree, resembles our system.

Finally, we would like to underline that the Fokker–Planck equation is derived under the assumption that the resulting noise in the kink velocity is Gaussian distributed. Nonlinearities in the governing equation may result in none Gaussian distribution and hence this potentially may be the origin of a discrepancy between the analytic result and the numerical simulations. On the other hand, deviations from the predictions contained in the derived formula appear at the lowest temperatures, i.e. in the area where non-linear (part originated in noise) effects are the least significant. This is the reason why we started looking for other explanations. At this point, one could be tempted to make a hypothesis that the presence of inhomogeneity causes cooling in a curved region of the system (represented by correction term ΔT). The potential physical mechanism of this cooling may be explained by reduction of the kinetic energy of the phonon-like excitations, present in the system, in the same area where the kink experiences reduction of the kinetic energy as a result of increase of the effective potential. We think that on the deeper level of description the phonons react on the increase of an appropriate effective potential in the curved region of the system.

CRediT authorship contribution statement

J. Gatlik: Conceptualization, Data curation, Formal analysis, Investigation, Methodology, Project administration, Software, Visualization, Writing – review & editing. **T. Dobrowolski:** Conceptualization, Formal analysis, Investigation, Methodology, Resources, Software, Supervision, Validation, Visualization, Writing – original draft.

Declaration of competing interest

The authors declare the following financial interests/personal relationships which may be considered as potential competing interests: Tomasz Dobrowolski reports equipment, drugs, or supplies was provided by PL-Grid Consortium.

Data availability

Data will be made available on request.

Acknowledgements

This research was supported in part by PLGrid Infrastructure, Poland.

Appendix A. Relation between curvature and the shape of the junction

The long Josephson junction considered in the paper is represented by the torsionless and therefore flat curve. The vector field that represents this curve contains two components

$$\vec{X}(x) = x\vec{e}_x + f(x)\vec{e}_x, \tag{23}$$

where the curve is parameterized by the parameter x and the function $f(x)$ represents the shape of the curve. The normal vector to this curve

$$\vec{n} = -\frac{f'(x)}{\sqrt{1+f'(x)^2}}\,\vec{e}_x + \frac{1}{\sqrt{1+f'(x)^2}}\,\vec{e}_y, \tag{24}$$

is fixed by the orthogonality and normalization conditions. Here coma represents the derivative with respect to x. Next we use the definition of curvature and thus it can be easily expressed by the derivatives of the function $f(x)$

$$K(x) = \vec{n}\cdot\vec{X}'' = \frac{f''(x)}{\sqrt{1+f'(x)^2}}. \tag{25}$$

The last formula can be used in order to calculate the shape function $f(x)$, whenever we know the explicit form of the curvature $K = K(x)$ i.e.

$$f''(x) - K(x)\sqrt{1+f'(x)^2} = 0. \tag{26}$$

In particular, for considered in this paper curvature the shape function is presented in Fig. 7. For better visualization we placed two vertical lines (the curved area is located between these two lines).

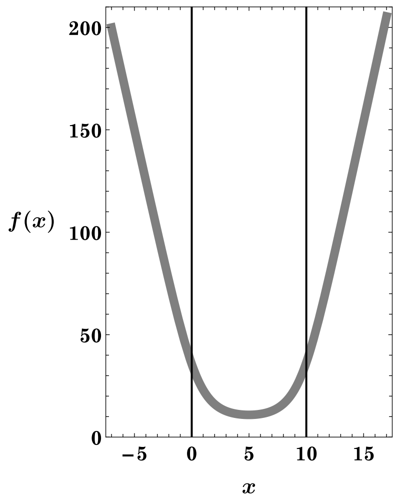

Fig. 7. The shape of the junction that corresponds to the considered in the present article curvature. The curvature is nonzero in the area located between the two black vertical lines.

Appendix B. Fokker–Planck equation

For the sake of completeness of the article we present derivation of the Fokker–Planck equation for the system studied by us. First, let us notice that velocity variation is a random variable with the following mean value

$$\langle \delta u\rangle = \langle \dot{u}\,\delta t\rangle = (-\alpha u - r + \frac{2}{\pi}\,\Gamma_0)\,\delta t, \tag{27}$$

where we used formula (7) and bias current mean value (8). Similarly, formula (20) leads to the expression

$$\langle \delta u \delta u\rangle = \frac{2\alpha k(T-\Delta T)}{m}\,\delta t. \tag{28}$$

Next the conditional probability that the particle which has velocity u at time $t+\delta t$, a moment earlier i.e. at $\bar{t}$, had velocity $\bar{u}$ we denote by $P(u, t+\delta t; \bar{u}, \bar{t})$. Taylor expansion of this probability with respect to final time reads

$$P(u, t+\delta t; \bar{u}, \bar{t}) = P(u, t; \bar{u}, \bar{t}) + \partial_t P(u, t; \bar{u}, \bar{t})\delta t, \tag{29}$$

where we ignored the terms of second and higher orders in δt. On the other hand we can obtain this expansion starting from the Chapman–Kolmogorov equation

$$P(u, t+\delta t; \bar{u}, \bar{t}) = \int_{-\infty}^{+\infty} du' P(u, t+\delta t; u', t') P(u', t'; \bar{u}, \bar{t}), \tag{30}$$

which states that, at some intermediate time $\bar{t} < t' < t+\delta t$ the velocity u' belongs to the interval $u' \in (-\infty, +\infty)$. The probability present in this formula can be expressed with the velocity variation δu as follows

$$P(u, t+\delta t; u', t') = \langle f(u-u'-\delta u)\rangle, \tag{31}$$

which can be expanded with respect to velocity

$$P(u, t+\delta t; u', t') = f(u-u') + \langle \delta u\rangle \partial_{u'} f(u-u') + \frac{1}{2}\,\langle \delta u\,\delta u\rangle \partial_{u'}^2 f(u-u'). \tag{32}$$

Truncation at the second order is motivated by the fact that they contain at most linear terms in δt. The Chapman–Kolmogorov formula now reads

$$P(u, t+\delta t; \bar{u}, \bar{t}) = \int_{-\infty}^{+\infty} du' [f(u-u') + \langle \delta u\rangle \partial_{u'} f(u-u') + \frac{1}{2}\,\langle \delta u\,\delta u\rangle \partial_{u'}^2 f(u-u')] P(u', t'; \bar{u}, \bar{t}), \tag{33}$$

Assuming that f and its first derivative disappear at plus/minus infinity and integrating second and third terms by parts we obtain

$$P(u, t+\delta t; \bar{u}, \bar{t}) = \int_{-\infty}^{+\infty} du' f(u-u')[P - \partial_{u'}(\langle \delta u\rangle P) + \frac{1}{2}\,\langle \delta u\,\delta u\rangle \partial_{u'}^2 P], \tag{34}$$

where we have used the fact that $\langle \delta u\,\delta u\rangle$ does not depend on u. From formulas (27) and (28) it is also transparent that the last two terms are linear in δt. Let us also notice that without random variation δu the probability distribution is unambiguously determined as follows $f(u-u') = \delta(u-u')$ and therefore after integration we obtain

$$P(u, t+\delta t; \bar{u}, \bar{t}) = P(u, t; \bar{u}, \bar{t}) - \partial_u \left(\langle \delta u\rangle P(u, t; \bar{u}, \bar{t})\right) + \frac{1}{2}\,\langle \delta u \delta u\rangle \partial_u^2 P(u, t; \bar{u}, \bar{t}). \tag{35}$$

Next we replace the average and variance of the random variable δu from formulas (27), (28) and we obtain

$$P(u, t+\delta t; \bar{u}, \bar{t}) = P(u, t; \bar{u}, \bar{t}) + \partial_u \left((\alpha u + r - \frac{2}{\pi}\,\Gamma_0) P(u, t; \bar{u}, \bar{t})\right)\delta t + \frac{\alpha k(T-\Delta T)}{m}\,\partial_u^2 P(u, t; \bar{u}, \bar{t})\delta t. \tag{36}$$

Finally, comparison of the above formula with Eq. (29) leads to the following form of the Fokker–Planck equation for the system considered by us

$$\partial_t P = \partial_u \left((\alpha u + r - \frac{2}{\pi}\,\Gamma_0) P + \frac{\alpha k(T-\Delta T)}{m}\,\partial_u P\right). \tag{37}$$

The time independent ($\partial_t P = 0$) normalized solution of this equation reads

$$P(u) = \sqrt{\frac{m}{2\pi k(T-\Delta T)}}\,\exp\left(-\frac{m}{2k(T-\Delta T)}\,(u-u_s)^2\right), \tag{38}$$

where we used (9) in order to identify the presence of the average stationary velocity u_s in the equation.

Appendix C. Effective relativistic description of the kink

In order to obtain a relativistic approximation of the critical speed of the kink we reconsider the projection procedure onto the energy density used in Section 2. We start again with the field equation

$$\partial_t^2 \phi + \alpha \partial_t \phi - \partial_x(\mathcal{F}(x)\partial_x \phi) + \sin\phi = -\Gamma_0. \tag{39}$$

Similarly as before we introduce the kink like ansatz into the field equation

$$\phi(t, x) = 4\arctan(e^{\xi(t,x)}),$$

where this time the function ξ takes its relativistic form

$$\xi = \gamma(t)(x - x_0(t)).$$

Moreover, the function $\mathcal{F}$ is expressed by the auxiliary function $g(x)$

$$\mathcal{F}(x) = 1 + \varepsilon g(x),$$

where dimensionless parameter ε controls the magnitude of curvature. Next we insert the kink ansatz into the field equation (39), obtaining

$$\left[\left(\frac{\ddot{\gamma}}{\gamma}+\alpha\frac{\dot{\gamma}}{\gamma}\right)\xi-(2\dot{\gamma}u+\gamma\dot{u}+\alpha\gamma u)\right]\ \mathrm{sech}\xi+$$
$$\left[(\gamma^2-1-\dot{\gamma}^2u^2)+2\dot{\gamma}u\xi-\left(\frac{\dot{\gamma}}{\gamma}\right)^2\xi^2\right]\mathrm{sech}\xi\tanh\xi-\tag{40}$$
$$\varepsilon\gamma(\partial_x g)\ \mathrm{sech}\xi+\varepsilon\gamma^2 g(x)\ \mathrm{sech}\xi\tanh\xi=-\frac{1}{2}\Gamma_0.$$

We eliminate the spatial variable from the description by projection onto the energy density distribution

$$Eq=0\Rightarrow\int_{-\infty}^{+\infty}dx\ \mathrm{sech}^2\xi\ Eq=0.\tag{41}$$

As a result of this procedure, we obtain a one-dimensional relativistic model describing the location of the kink

$$\dot{u}+\alpha u+\frac{4}{3}u\frac{\dot{\gamma}}{\gamma}=\frac{4}{3\pi}\varepsilon\gamma\left(\mathrm{sech}^3\xi_L-\mathrm{sech}^3\xi_0\right)+\frac{2}{\pi\gamma}\Gamma_0,\tag{42}$$

where we denoted $\xi_L=\gamma(L-x_0(t))$ and $\xi_0=\gamma(-x_0(t))$. On the other hand, introducing to the last equation the Lorentz factor $\gamma=1/\sqrt{1-u^2}$ (we use the units with Swihart velocity equal to one $\bar{c}=1$) we obtain

$$\left(1+\frac{1}{3}u^2\right)\dot{u}+\alpha u(1-u^2)$$
$$=\frac{4}{3\pi}\varepsilon\sqrt{1-u^2}\left(\mathrm{sech}^3\xi_L-\mathrm{sech}^3\xi_0\right)+\frac{2}{\pi}(\sqrt{1-u^2})^3\ \Gamma_0.\tag{43}$$

This equation is a base for estimation of the critical speed in our system in the low temperature regime presented in Fig. 5.

Appendix D. Relativistic approximation of the stationary speed

For the sake of completeness of the presentation, we will also recall the origin and the relativistic value of the kink stationary speed used in this work. The bias current and dissipation present in the system have an opposite effect on fluxon motion leading to mutual equilibration at a certain speed [43]. The dynamics of the soliton in the homogeneous system is described by the equation

$$\partial_t^2\phi+\alpha\,\partial_t\phi-\partial_x^2\phi+\sin\phi=-\Gamma_0.\tag{44}$$

If we multiply both sides of this equation by the time derivative of the field ϕ and next integrate it with respect to the space variable, then we obtain

$$\frac{d}{dt}H^{SG}=-\int_{-\infty}^{+\infty}dx\left[\Gamma_0\,\partial_t\phi+\alpha\,(\partial_t\phi)^2\right],\tag{45}$$

where H^{SG} is the hamiltonian of the sine–Gordon model

$$H^{SG}=\int_{-\infty}^{+\infty}dx\left[\frac{1}{2}(\partial_t\phi)^2+\frac{1}{2}(\partial_x\phi)^2+(1-\cos\phi)\right].$$

Introducing the kink ansatz

$$\phi(t,x)=4\arctan\left(\frac{x-x_0-ut}{\sqrt{1-u^2}}\right)$$

into Eq. (45) leads to the ordinary differential equation for the fluxon velocity

$$\frac{du}{dt}=\frac{1}{4}\pi\Gamma_0(1-u^2)^{\frac{3}{2}}-\alpha\,u(1-u^2).\tag{46}$$

The constant equilibrium ($du/dt=0$) solution of this equation, corresponds to the situation when the power input caused by the bias current is balanced by the loss of power due to dissipation

$$u_s=\frac{1}{\sqrt{1+(\frac{4\alpha}{\pi\Gamma_0})^2}}.\tag{47}$$

This velocity describes the stationary motion of the fluxon in the homogeneous junction.

References

[1] B.D. Josephson, Phys. Lett. 1 (1962) 251.
[2] B.D. Josephson, Rev. Modern Phys. 46 (1974) 251.
[3] P.W. Anderson, J.M. Rowell, Phys. Rev. Lett. 10 (1963) 230.
[4] P. Seidel (Ed.), Applied Superconductivity: Handbook on Devices and Applications, Wiley, 2015, ISBN-13: 978-3527412099.
[5] A.I. Braginski, J. Supercond. Nov. Magn. 32 (2019) 23.
[6] J.G. Bednorz, K.A. Müller, Z. Phys. B 64 (1986) 189.
[7] A. Schilling, M. Cantoni, J.D. Guo, H.R. Ott, Nature 363 (1993) 56.
[8] A. Benabdallah, J-.G. Caputo, A.C. Scott, Phys. Rev. B 54 (1996) 16139.
[9] A. Kemp, A. Wallraff, A.V. Ustinov, Phys. Status Solidi B 233 (2002) 472.
[10] A. Kemp, A. Wallraff, A.V. Ustinov, Physica C 368 (2002) 324.
[11] D.R. Gulevich, F.V. Kusmartsev, Phys. Rev. Lett. 97 (2006) 017004.
[12] D.R. Gulevich, F.V. Kusmartsev, S. Savelev, V.A. Yampol'skii, F. Nori, Phys. Rev. Lett. 101 (2008) 127002.
[13] J-.G. Caputo, D. Dutykh, Phys. Rev. E 90 (2014) 022912.
[14] R. Monaco, J. Phys.: Condens. Matter 28 (2016) 445702.
[15] R. Monaco, J. Mygind, V.P. Koshelets, Supercond. Sci. Technol. 31 (2018) 025003.
[16] T. Dobrowolski, A. Jarmoliński, Phys. Rev. E 101 (2020) 052215.
[17] T. Dobrowolski, Phys. Rev. E 79 (2009) 046601.
[18] T. Dobrowolski, Discrete Contin. Dyn. Syst. Ser. S 4 (2011) 1095.
[19] T. Dobrowolski, Ann. Phys., NY 327 (2012) 1336.
[20] T. Dobrowolski, Eur. Phys. J. B 86 (2013) 346.
[21] T. Dobrowolski, A. Jarmoliński, Phys. Rev. E 96 (2017) 012214.
[22] J. Gatlik, T. Dobrowolski, Physica D 428 (2021) 133061.
[23] M.G. Castellano, G. Torrioli, C. Cosmelli, A. Costantini, F. Chiarello, P. Carelli, G. Rotoli, M. Cirillo, R.L. Kautz, Phys. Rev. B 54 (1996) 15417.
[24] H.A. Kramers, Physica 7 (1940) 284.
[25] C. Guarcello, Chaos Solitons Fractals 153 (2021) 111531.
[26] G. Augello, D. Valenti, A.L. Pankratov, B. Spagnolo, Eur. Phys. J. B 70 (2009) 145–151.
[27] K.G. Fedorov, A.L. Pankratov, Phys. Rev. B 76 (2007) 024504.
[28] K.G. Fedorov, Andrey L. Pankratov, Phys. Rev. Lett. 103 (2009) 260601.
[29] C. Guarcello, F. Giazotto, P. Solinas, Phys. Rev. B 94 (2016) 054522.
[30] C. Guarcello, P. Solinas, A. Braggio, F. Giazotto, Phys. Rev. A 9 (2018) 034014.
[31] C. Guarcello, P. Solinas, A. Braggio, F. Giazotto, Phys. Rev. B 98 (2018) 104501.
[32] C. Guarcello, P. Solinas, A. Braggio, F. Giazotto, Sci. Rep. 8 (2018) 12287.
[33] C. Guarcello, P. Solinas, F. Giazotto, A. Braggio, J. Stat. Mech. (2019) 084006.
[34] Z. Fei, Y.S. Kivshar, L. Vazquez, Phys. Rev. A 46 (1992) 5214.
[35] D.K. Campbell, J.F. Schonfeld, C.A. Wingate, Physica D 9 (1983) 1.
[36] R.H. Goodman, R. Haberman, SIAM J. Appl. Dyn. Syst. 4 (2005) 1195.
[37] R.H. Goodman, Chaos 18 (2008) 023113.
[38] N.S. Manton, K. Oleś, T. Romańczukiewicz, A. Wereszczyński, Phys. Rev. D 103 (2021) 025024.
[39] C. Adam, N.S. Manton, K. Oleś, T. Romańczukiewicz, A. Wereszczyński, Phys. Rev. D 105 (2022) 065012.
[40] I. Takyi, H. Weigel, Phys. Rev. D 94 (2016) 085008.
[41] P.G. Kevrekidis, R.H. Goodman, arXiv:1909.03128 [nlin.PS].
[42] P. Dorey, K. Mersh, T. Romańczukiewicz, Y. Shnir, Phys. Rev. Lett. 107 (2011) 091602.
[43] D.W. McLaughlin, A.C. Scott, Phys. Rev. A 18 (1978) 1652.

PHYSICAL REVIEW E **108**, 034203 (2023)

Kink-inhomogeneity interaction in the sine-Gordon model

Jacek Gatlik [1], Tomasz Dobrowolski [1], and Panayotis G. Kevrekidis [2]
[1] Pedagogical University of Krakow, Podchorążych 2, 30-084 Cracow, Poland
[2] Department of Mathematics and Statistics, University of Massachusetts, Amherst, Massachusetts 01003-4515, USA

(Received 26 May 2023; accepted 21 July 2023; published 8 September 2023)

In the present study the interaction of a sine-Gordon kink with a localized inhomogeneity is considered. In the absence of dissipation, the inhomogeneity considered is found to impose a potential energy barrier. The motion of the kink for near-critical values of velocities separating transmission from barrier reflection is studied. Moreover, the existence and stability properties of the kink at the relevant saddle point are examined and its dynamics is found to be accurately captured by effective low-dimensional models. In the case where there is dissipation in the system, below the threshold value of the current, a stable kink is found to exist in the immediate vicinity of the barrier. The effective particle motion of the kink is investigated obtaining very good agreement with the result of the original field model. Both one and two degree-of-freedom settings are examined with the latter being more efficient than the former in capturing the details of the kink motion.

DOI: 10.1103/PhysRevE.108.034203

I. INTRODUCTION

The sine-Gordon (sG) model originally appeared in the description of surfaces of constant negative curvature embedded in three-dimensional space. This equation constitutes the Gauss-Codazzi integrability condition of the surface [1]. Primarily, the model was introduced to physics in the context of the studies on crystal dislocations [2]. Since then, it has found many applications in describing a variety of physical systems [3,4].

One of the prototypical examples showcasing the relevance of the sG model concerns its application to quasi-one-dimensional ferromagnetic materials with an easy plane anisotropy and their behavior in an external magnetic field [5]. Experimental studies of this system confirm the main theoretical predictions [6–8]. Also, the relevant system has been successfully leveraged to describe ferroelectrics [9–12]. Moreover, the orientation angle of the molecules in liquid crystals has been argued to satisfy an overdamped and externally driven sine-Gordon equation [13]. An additional example where the sG model (especially in its damped-driven variant) has been shown to be experimentally accessible concerns an array of coupled torsion pendula; see for a relatively recent demonstration the experiments in Ref. [14].

Arguably, the most widespread application of the sG model concerns the description of a device called the Josephson junction that emerged as a result of the so-called Josephson effect [15]. Predictions of this work found experimental confirmation a year later [16]. Josephson junctions (JJs) have been thoroughly studied over the years [17,18] and have found numerous practical applications [19]. In order to obtain the most realistic description of the JJs, additional terms were introduced describing the dissipation due to tunneling of normal electrons across the barrier, the dissipation caused by the flow of normal electrons parallel to the barrier and moreover the bias current [18]. Additionally, in the context of condensed matter physics, the presence of inhomogeneities in the form of “impurities” is a fairly common feature. More concretely, in the JJ setting, the typical inhomogeneities are microshorts which are local regions of high Josephson current [3,20,21]. The effect of modulation of the thickness of a dielectric layer separating the two superconducting electrodes has been described in many different ways [22–24]. Another way in which explicitly position-dependent functions enter the sine-Gordon model is presented in the works [25–27]. The latter possibility has been motivated by the widespread relevance of $\mathcal{PT}$-symmetric systems in optical, as well as more generally in dispersive wave systems [28].

A considerable volume of work has also focused on the effect of shape deformation of the junction on its properties [29–34]. In this approach, some modifications of the junction shape are proposed in order to obtain its desired properties. In particular, the influence of the curvature on the dynamics of the gauge invariant phase difference between two superconducting electrodes that comprise the JJ was studied in Refs. [35,36]. The equation that describes this system was obtained on the basis of field dynamics governed by Maxwell’s equations in the insulator and London’s equations in superconducting electrodes with Ginzburg-Landau current of Cooper pairs. The description in this case agrees with the same result obtained on a purely geometrical background as a consequence of the geometrical reduction of the sine-Gordon model to a lower-dimensional curved subspace [37].

In the present work, we focus on describing the interaction of a kinklike effective particle in the sG model with inhomogeneities for initial velocities close to the critical velocity. This choice of initial conditions can render the interaction time significantly longer close to this critical point which highlights all aspects of the interaction. Our interest lies in systematically describing this interaction via a low-dimensional, effective-particle approach, both for the Hamiltonian (conservative) but also for the dissipative partial differential equation (PDE) setting. In addition to exploring the relevant PDE dynamics, emphasis is placed on effective, low-dimensional descriptions of the solitary wave in the corresponding energy landscape. In Sec. II we will describe the field model to be studied. We determine the shape of the kink both in the absence and in the presence of dissipation and external forcing in the system. This section also examines the linear stability of the solutions. Section III is devoted to effective descriptions of different dimensionalities (one- and two-degree of freedom approaches) and the limits of their applicability, as well as the comparison between them, as well as with the original PDE. The last section contains our conclusions and a number of proposed directions for possible future study.

In light of our consideration of heterogeneous variants of the sine-Gordon model, it is relevant to highlight that considerable modeling and computation effort has also been invested in the consideration of periodic heterogeneities in the form of discrete sG models; see, e.g., also the relevant chapter within [4]. Some of the important aspects along these lines that have been considered include the oscillation frequency of the discrete kink in the famous (from dislocation theory) Peierls-Nabarro potential [38], as well as the spontaneous emission of radiation from a propagating discrete sine-Gordon kink [39].

II. SYSTEM DESCRIPTION

In the present article, in line with the above discussion, we study the perturbed sine-Gordon model of the form:

$$\partial_t^2\phi + \alpha\partial_t\phi - \partial_x(\mathcal{F}(x)\partial_x\phi) + \sin\phi = -\Gamma, \tag{1}$$

where the function $\mathcal{F}(x)$ represents the inhomogeneity. More specifically, our motivation for considering this type of modification stems from the need to take into account the curvature in the description of the long Josephson junction. The detailed physical considerations leading to this effective equation are presented in the earlier works in Refs. [35,36]. The same equation can be obtained from the mathematical procedure of projecting the sine-Gordon equation defined in a flat three-dimensional space into a one-dimensional subspace, nontrivially embedded in the initial space [37]. In the above equation α is the dissipation coefficient while Γ represents a constant external forcing. In the context of a Josephson junction, the constant Γ is interpreted as a bias current. In the absence of dissipation and external forcing, the total energy is conserved. For later convenience, we separate the function $\mathcal{F}(x)$ into a part describing the unperturbed system and a term describing its disturbance g,

$$\mathcal{F}(x) = 1 + \varepsilon g(x). \tag{2}$$

The parameter ε controls the magnitude of the perturbation. We will assume that this parameter is small.

A. The nondissipative case with $\alpha = 0$ and $\Gamma = 0$

First, we will focus on describing the simplified case, i.e., one in which the constants α and Γ are equal to zero. Although the energy of a free kink in a homogeneous system (featuring distinct asymptotic equilibria) corresponds to a minimum of energy described by the formula

$$E = \int_{-\infty}^{+\infty} dx\left[\frac{1}{2}(\partial_t\phi)^2 + \frac{1}{2}(\partial_x\phi)^2 + (1-\cos\phi)\right], \tag{3}$$

it can be further lowered in the presence of inhomogeneity. The total energy of the arbitrary field configuration in a heterogeneous system is of the form

$$E_H = \int_{-\infty}^{+\infty} dx\left[\frac{1}{2}(\partial_t\phi)^2 + \frac{1}{2}\mathcal{F}(x)(\partial_x\phi)^2 + (1-\cos\phi)\right]. \tag{4}$$

We describe the process of interaction of the kink with admixture present in the system. In this section, the function g is taken in the form $g(x) = \tanh(x) - \tanh(x-L)$. In this formula, L defines the width of the inhomogeneity.

It is relevant here to briefly discuss the method with which these profiles are obtained. We have utilized a Newton-Raphson iteration which, through its quadratic convergence, has ensured the rapid identification of the relevant kink profiles. The steady-state problem is discretized by means of centered finite differences (of second order) and the accuracy of the findings has been ensured by means of discretizations of different spacing Δx. It should be added that as part of the Newton-Raphson procedure, we also construct the Jacobian evaluated at the kink profile. This, on convergence, provides us with the linearization matrix of the relevant problem that will be used for the numerical identification of the eigenfrequencies ω discussed in more detail in what follows.

The deformation of the kink profile as a function of ε is evident in Fig. 1 showcasing the widening of the kink as ε is increased. From a more quantitative perspective, the deformation of the kink profile for small ε and the stability of this configuration can be examined in the framework of a linearized approximation. To begin with, we assume that the field ϕ is a slightly perturbed kink solution of the model (1) [with $\alpha = 0$ and $\Gamma = 0$]. We insert the decomposition $\phi(t,x) = \phi_0(x) + \psi(t,x)$ into Eq. (1) obtaining, up to linear terms in the ψ correction, the equation

$$\partial_t^2\psi - \partial_x[\mathcal{F}(x)\partial_x\psi] + (\cos\phi_0)\psi = 0. \tag{5}$$

At this point we emphasize that $\phi_0(x)$ can be decomposed into static kink ϕ_K of the sine-Gordon model and a time-independent correction χ depending also on the geometry of the system, i.e., $\phi_0(x) = \phi_K(x) + \chi(x)$. This is intended to capture the steady-state solution of the perturbed (in the presence of the inhomogeneity) problem. In particular, for small values of the parameter ε, the correction $\chi(x)$ can be calculated from the following equation:

$$-\partial_x[\mathcal{F}(x)\partial_x\chi] + (\cos\phi_K)\chi = \varepsilon\partial_x[g(x)\partial\phi_K]. \tag{6}$$

This equation describes the time-independent deformation, which is uniquely determined by the function describing the inhomogeneity and the analytical form of the underlying solution. The solutions of Eq. (6) for different values of ε are presented in Fig. 2. It is clear that the relevant contributions are antisymmetric along the (former) direction of the translational invariance of the homogeneous model kink and, upon addition to the homogeneous static kink, they modify its effective width. Moreover, the profiles of the static (numerically exact up to a prescribed tolerance) solutions $\phi_0(x)$ obtained from the perturbed sine-Gordon model (1) are compared with the function $\phi_K(x) + \chi(x)$, where $\phi_K(x)$ is a static kink solution of the sine-Gordon model in the homogeneous case.

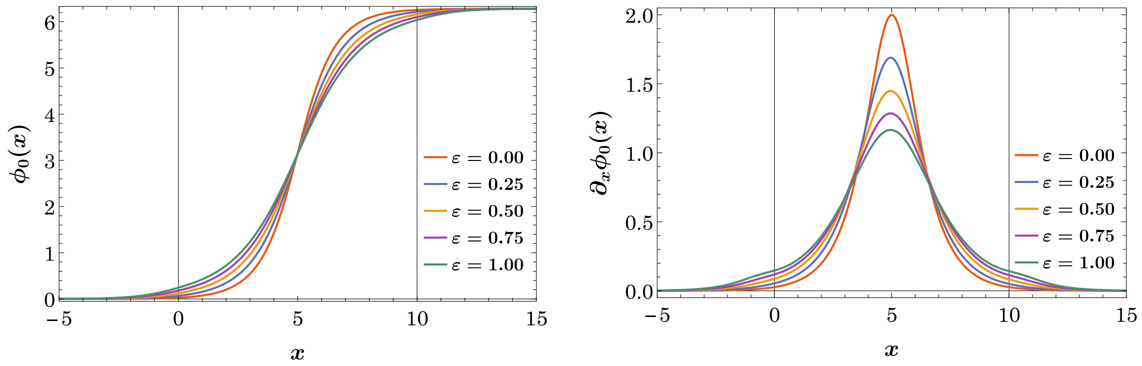

FIG. 1. Profiles of static solutions for different values of ε (left figure) and, for a better visualization, gradients of static configurations (right figure). In all cases, the size of the inhomogeneity is $L = 10$. The inhomogeneity in the figures is located between the vertical lines for $x = 0$ and $x = L$.

The figure shows that, even for $\varepsilon = 1$, there is little difference between the solution derived from Eq. (6) and the numerical solution derived from the field model (1).

On the other hand, Eq. (5) contains information about the time-dependent perturbation of the underlying solution. We then adopt a particular form of the time dependence of the function ψ, i.e., $\psi(t,x) = e^{i\omega t} v(x)$. This standard approach allows us to examine the spectral stability of the underlying configuration ϕ_0,

$$-\partial_x[\mathcal{F}(x)\,\partial_x v(x)] + (\cos\phi_0)\,v(x) = \lambda v(x), \tag{7}$$

where $\lambda = \omega^2$. By abbreviating the left-hand side of the last equation $\hat{\mathcal{L}}\,v(x)$ we obtain the eigenequation for the linearization operator $\hat{\mathcal{L}}$,

$$\hat{\mathcal{L}}\,v(x) = \lambda v(x)\,. \tag{8}$$

The spectrum of the operator $\hat{\mathcal{L}}$ obtained from Eq. (8) consists of a continuous spectrum and a discrete negative value (see Fig. 3). The latter eigenvalue pertains to the previously vanishing eigenfrequency (of the homogeneous limit) associated with the translational invariance of the homogeneous problem. In the present case, the negative associated squared eigenfrequency corresponds to a real eigenvalue illustrating that the relevant static configuration corresponds to an unstable equilibrium, more specifically a saddle point of the (undamped, nondriven) Hamiltonian limit of the system. This, in turn, represents a potential energy maximum of the effective energy landscape, whose energy we expect to separate between the transmission dynamics (for energies higher than that of this configuration) and the reflection features (for energies below those of this maximum).

B. The case with dissipation and external forcing $\alpha \neq 0$ and $\Gamma \neq 0$

For $\Gamma \neq 0$, similarly as in the previous case, during interaction with the inhomogeneity the kink may or may not go over the barrier. The reflection in this case is much more interesting than for $\Gamma = 0$. The physical cause is the presence of a constant force pressing the particle against the potential barrier. For this reason, after the bounce, as we will see in the dynamical simulations below, the kink is again pushed towards the barrier. The presence of dissipation makes subsequent reflections smaller and smaller, until finally the kink stops at a certain distance from the barrier. The form of this resulting static configuration is specified by the equation

$$-\partial_x[\mathcal{F}(x)\partial_x\phi_0] + \sin\phi_0 = -\Gamma. \tag{9}$$

In this equation, the bias current must be less than the threshold value. The current threshold value separates the current values for which kink is stopped before the barrier from the values for which kink overcomes the barrier.

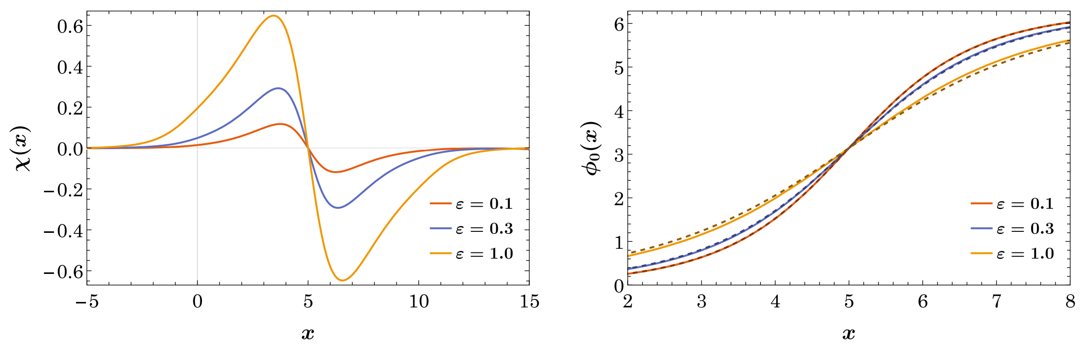

FIG. 2. On the left panel, the $\chi(x)$ value determined from Eq. (6) is shown for different values of ε. On the right panel, the solid line shows the sum of the kink ansatz $\phi_K(x)$ and $\chi(x)$ value for different ε, while the dashed line is the corresponding static solution as determined from Netwon's method.

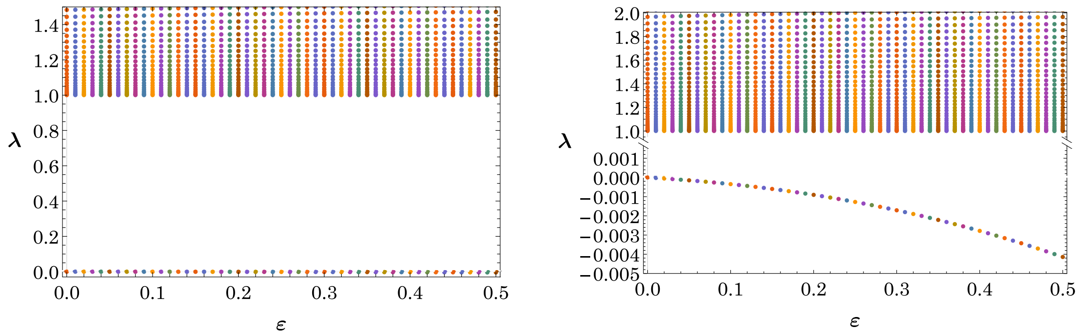

FIG. 3. Squared eigenfrequencies $\lambda = \omega^2$ calculated for the quasistatic configuration depending on the value of ε for $L = 10$. See also the discussion in the text.

The stability of this configuration is tested in the standard way, i.e., we linearize according to: $\phi(t,x) = \phi_0(x) + \psi(t,x)$. The equilibrium configuration itself can be roughly described, as before, by the sum of the free kink and the deformation $\phi_0(x) = \phi_K(x) + \chi(x)$, with the latter now being characterized in addition to the inhomogeneity, also by the bias current. The deformation satisfies the equation

$$-\partial_x[\mathcal{F}(x)\partial_x\chi] + (\cos\phi_K)\chi = \varepsilon\partial_x[g(x)\partial\phi_K] - \Gamma. \quad (10)$$

The left Fig. 4 shows the form of the correction describing the kink deformation coming from inhomogeneities. The right figure once again compares the static configuration obtained from the field model (9) and the configuration obtained as the sum of the kink solution of the homogeneous model (for $\varepsilon = 0$) and the correction derived from the inhomogeneity χ. The very good agreement between the two results for different values of ε shows that the splitting of the configuration ϕ_0 into the correction χ and the kink of the free model ϕ_K provides an accurate description of the static configuration.

On the other hand, to explore the state's spectral stability, we use the linearization decomposition $\psi(t,x) = e^{i\omega t}v(x)$ which, in turn, leads to the eigenvalue problem:

$$\hat{\mathcal{L}}\, v(x) = -\partial_x[\mathcal{F}(x)\,\partial_x v(x)] + (\cos\phi_0)\, v(x) = \lambda v(x). \quad (11)$$

The quantity λ appearing in this equation is related to the eigenfrequency ω as follows $\lambda = \omega(\omega - i\alpha)$ (see Fig. 5), and therefore

$$\psi(t,x) = e^{-\frac{1}{2}\alpha t}e^{\pm i\Omega t}v(x), \quad (12)$$

where $\Omega = \sqrt{\lambda - \frac{\alpha^2}{4}}$. As long as the condition $\lambda > \alpha^2/4$ is satisfied, then one can observe damped oscillations around $\phi_0(x)$, i.e., the relevant fixed point is a stable spiral. On the other hand, when $\alpha^2/4 \geqslant \lambda > 0$ one can observe overdamped behavior of the perturbations

$$\psi(t,x) = e^{-\frac{1}{2}\alpha t}e^{\pm\kappa t}v(x), \quad (13)$$

where $\kappa = \sqrt{\frac{\alpha^2}{4} - \lambda}$. In this case, the relevant fixed point corresponds to a stable node. As we will see below, in this damped-driven case, the system does possess a stable attractor; however, in reconciling with the Hamiltonian picture above, this is not the sole stationary state of the system. Indeed, the former saddle point of the Hamiltonian case typically breaks up (in the presence of damping and driving) through a saddle-node bifurcation into a persistent unstable configuration and an emergent stable one (per the above discussion). We will iterate on this point further through our effective description in what follows.

III. EFFECTIVE DESCRIPTION OF THE KINK-INHOMOGENITY INTERACTION

A. Approximations based on one degree of freedom

Having described the statics of the kink in the presence of the inhomogeneity, we now turn to the corresponding model dynamics in what follows. In this subsection, we will obtain an approximate description of the field system based on

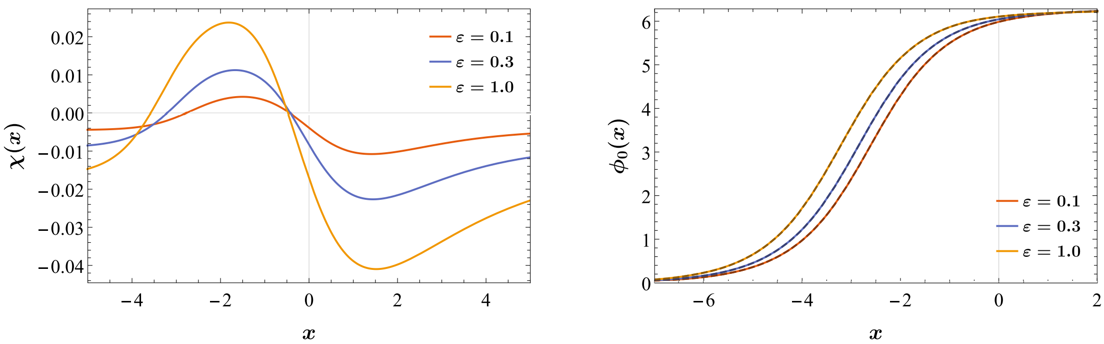

FIG. 4. In the left panel, the $\chi(x)$ value determined from Eq. (10) for different values of ε is shown. In the right panel, the solid line shows the sum of the kink ansatz $\phi_K(x)$ and $\chi(x)$ value for different ε, while the dashed line is the corresponding static solution determined from original field model. In each case $\alpha = 0.01$, while bias current is equal to 0.0045, 0.0093, and 0.017, respectively, for $\varepsilon = 0.1$, 0.3, and 1.0.

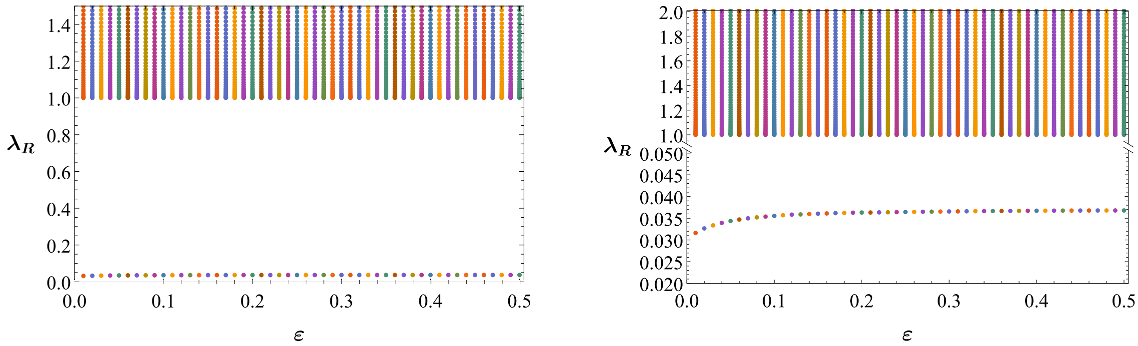

FIG. 5. Dependence of $\lambda_R = \omega^2$ on ε for the static kink solution in the damped-driven sG model, where λ_R is the real part of λ [see under Eq. (11)]. The graph regards the case of $\alpha = 0.01$ and $\Gamma = 0.001$ for each ε.

three approximation methods. The first method is based on a conservative Lagrangian of the system (i.e., an effectively variational method). The second method involves projecting the field equation onto the zero mode of the kink solution (the so-called translational mode, associated with the relevant invariance in the homogeneous limit), while the third one is based on a nonconservative Lagrangian. The last two methods allow the construction of an effective model even if there is a dissipation in the field equation, while the first is solely applicable in the realm of conservative (Lagrangian or Hamiltonian) systems.

1. The construction based on a conservative Lagrangian

We start from the variation of the Lagrangian density

$$\mathcal{L}_{\rm FSG} = \mathcal{L}_{\rm SG} + \mathcal{L}_\varepsilon = \mathcal{L}_{\rm SG} - \tfrac{1}{2}\varepsilon g(x)(\partial_x\phi)^2, \tag{14}$$

where $\mathcal{L}_\varepsilon$ describes the inhomogeneity present in the system and $\mathcal{L}_{\rm SG}$ is the Lagrangian density of the (unperturbed) sine-Gordon model

$$\mathcal{L}_{\rm SG} = \tfrac{1}{2}(\partial_t\phi)^2 - \tfrac{1}{2}(\partial_x\phi)^2 - (1-\cos\phi). \tag{15}$$

A recent discussion of such variational methods for the sG model, including in higher-dimensional settings can be found, e.g., in Ref. [40].

The reduction of the original PDE to a model with one degree of freedom is based on the use of the kink ansatz with the position of the kink used as a collective variable,

$$\phi_k(t,x) = 4\arctan e^{x-x_0(t)}. \tag{16}$$

By inserting the kink ansatz into the Lagrangian density (14) and then integrating with respect to the spatial variable, we obtain the effective Lagrangian for the variable $x_0(t)$,

$$L_{\rm FSG} = \int_{-\infty}^{+\infty} dx\,\mathcal{L}_{\rm FSG} = L_{\rm SG} + L_\varepsilon = L_{\rm SG} - \frac{1}{2}\varepsilon\int_{-\infty}^{+\infty} dx g(x)(\partial_x\phi_K)^2. \tag{17}$$

The form of the interaction is uniquely determined by the function $g(x)$. In the case where $g(x) = 0$ we obtain the Lagrangian of the free particle (after rescaling by the multiplicative constant and eliminating the additive one),

$$L_{\rm FSG} = L_{\rm SG} = \tfrac{1}{2}\dot{x}_0^2. \tag{18}$$

If g is a nontrivial position-dependent function, then the effective Lagrangian is enriched by a potential energy landscape describing the interaction of the kink with the existing inhomogeneity. For example, if the function g consists of unit step functions $g(x) = \theta(x) - \theta(x-L)$, then the Lagrangian assumes the form

$$L_{\rm FSG} = \tfrac{1}{2}\dot{x}_0^2 - \varepsilon[\tanh(x_0) - \tanh(x_0 - L)]. \tag{19}$$

The equation of motion in this case is the following:

$$\ddot{x}_0 = -\varepsilon[\text{sech}^2(x_0) - \text{sech}^2(x_0 - L)]. \tag{20}$$

On the other hand, in the previous section we used the function $g(x) = \tanh(x) - \tanh(x-L)$. In this case the effective Lagrangian reads

$$L_{\rm FSG} = \frac{1}{2}\dot{x}_0^2 - \frac{1}{2}\varepsilon\left\{\coth(x_0) - \frac{x_0}{\sinh^2(x_0)} - \left[\coth(x_0 - L) - \frac{x_0 - L}{\sinh^2(x_0 - L)}\right]\right\}. \tag{21}$$

The potential energy landscape is provided by the term after the $(-)$ sign in Eq. (21) [or similarly in Eq. (19)] and clearly illustrates the existence of a local maximum corresponding to the saddle static kink configuration. The equation of motion for the collective variable is

$$\ddot{x}_0 = \varepsilon\left[\frac{1 - x_0\coth x_0}{\sinh^2 x_0} - \frac{1-(x_0 - L)\coth(x_0 - L)}{\sinh^2(x_0 - L)}\right]. \tag{22}$$

The trajectories obtained from the last equation are compared with center-of-mass trajectories following from the field equation [Eq. (1) with $\alpha = 0$ and $\Gamma = 0$]. Figure 6 shows a good agreement between the effective model and the full field model for small values of ε. The left panel in this figure corresponds to $\varepsilon = 0.01$ while the right panel contains results for $\varepsilon = 0.05$. Each of the panels consists of three figures. The top figure describes the kink reflecting from the inhomogeneity. The initial speed in this case $u = 0.13$ is lower than the critical velocity. The second figure in this panel represents the interaction of the kink whose initial speed $u = 0.145$ is close to the critical velocity. The bottom figure demonstrates the kink passing over the barrier for initial speed $u = 0.16$ exceeding the critical value. Similarly, in the figures of the right panel, the velocities are smaller $u = 0.27$, close to the critical value $u = 0.315$ and above the critical speed for $u = 0.35$. The critical velocities for which the agreement takes

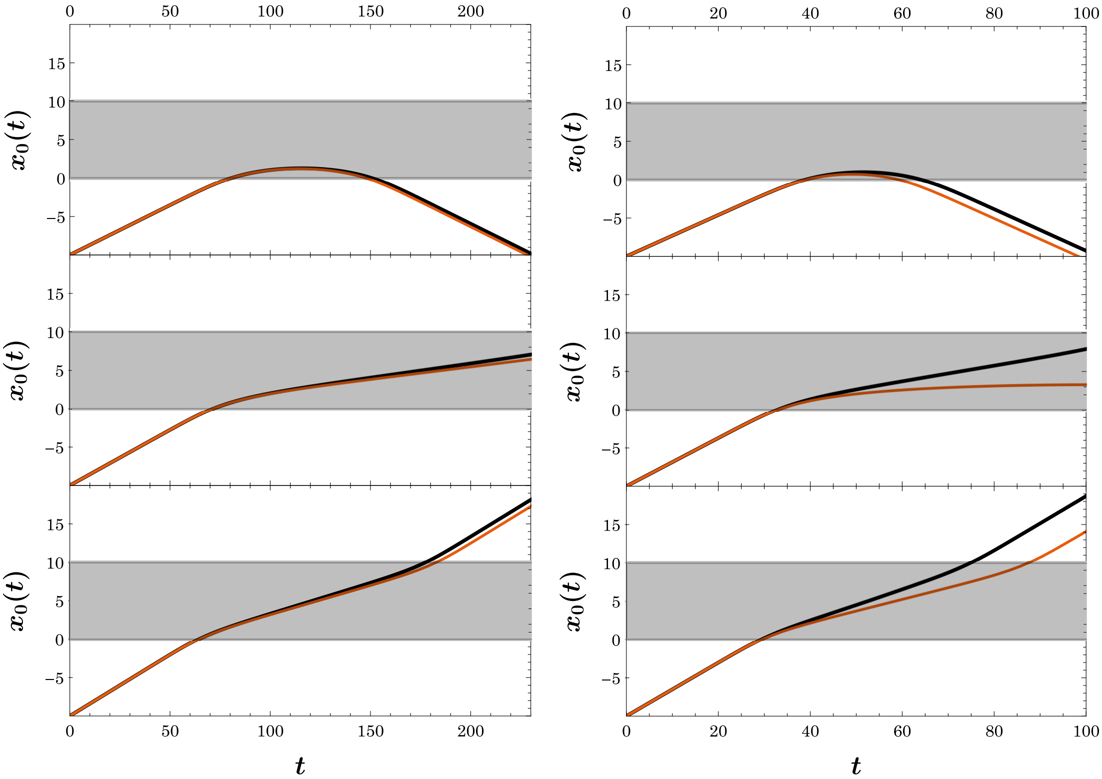

FIG. 6. Comparison of the position of the center of mass of the kink for the solution from the original field model (black line) and the model with one degree of freedom [red (gray) line]. The figures in the left panel are prepared for $\varepsilon = 0.01$ and velocities (starting from the top) 0.13, 0.145, and 0.16. In the right panel $\varepsilon = 0.05$ and velocities (from the top) are 0.27, 0.315, and 0.35.

place are approximately limited to 0.25. For larger values of this parameter, inconsistencies become more significant. The trajectories corresponding to $\varepsilon = 0.02$ are presented in Fig. 7. The initial velocities of the kink are, starting from the top, 0.17, 0.21, and 0.25. The right panel shows the course of these trajectories [represented by the red (gray) line] on the background of the phase space. The phase diagrams show an unstable fixed point at the center of the barrier.

The corresponding potential energy landscape representing the relevant energy maximum can be seen in Fig. 8. In the case we are considering, the location of the fixed point is $x_0 = 5$. Regarding the linear stability in the effective particle model, only one (unstable mode) is naturally present, pertaining to the formerly translational mode of the homogenous sG. A comparison of this mode with the spectrum of linear excitations of the field model ($\alpha = 0$, $\Gamma = 0$) can be found in Fig. 9. The green (light gray) line represents the result obtained from the model with one degree of freedom, while the points represent the spectrum of the $\hat{\mathcal{L}}$ operator. Quantitative agreement occurs only for small values of the ε parameter, yet the qualitative agreement between the two is clearly evident.

2. *The method of projecting onto the zero mode*

In addition to the above method of effective theory construction, other approaches are used in the literature. One of them is the zero mode projection method; see, e.g., a relevant discussion in Ref. [41]. This method, unlike the standard method based on the conservative Lagrangian, is based on the PDE itself and does not hinge on the variational structure of the problem. As such, it allows for an effective description of systems containing dissipative terms. With this in mind, we can construct an effective model for the sine-Gordon model with dissipation described by Eq. (1) with $\alpha \neq 0$ and $\Gamma \neq 0$. Practically, we insert the kink ansatz

$$\phi(t, x) = 4 \arctan e^{\xi(t,x)}, \tag{23}$$

into the field equation (1). This substitution results in the equation

$$(\ddot{\xi} - \xi'' + \alpha\dot{\xi})\partial_\xi\phi + (1 + \dot{\xi}^2 - \xi'^2)\,\partial_\xi^2\phi$$
$$= \varepsilon(\partial_x g)\,\xi'\,\partial_\xi\phi + \varepsilon g\left(\xi''\partial_\xi\phi + \xi'^2\partial_\xi^2\phi\right) - \Gamma\,. \tag{24}$$

The dot denotes the derivative with respect to the time variable while the prime denotes the derivative with respect to the spatial variable. If we want to obtain a model describing the dynamics of one collective variable, i.e., the variable that determines the position of the kink, then we take a particular form of the function $\xi = \xi(t, x)$, i.e.,

$$\xi(t, x) = x - x_0(t).$$

With this substitution, Eq. (24) is reduced to a much simpler form,

$$(-\ddot{x}_0 - \alpha\dot{x}_0)\partial_\xi\phi + \dot{x}_0^2\,\partial_\xi^2\phi - \varepsilon(\partial_x g)\,\partial_\xi\phi - \varepsilon g\,\partial_\xi^2\phi + \Gamma = 0. \tag{25}$$

The final step is the projection of the above equation onto the (former) zero mode, which consists of integration with

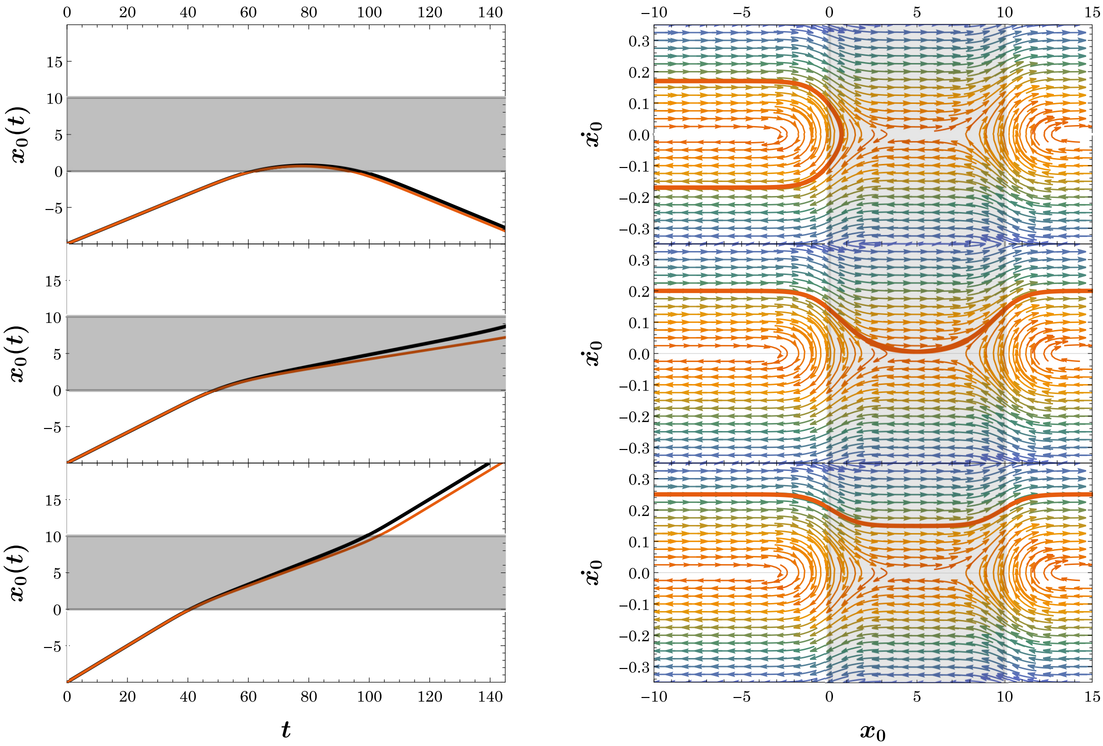

FIG. 7. Comparison of the position of the center of mass of the kink for the solution from the original field model (black line) and the model with one degree of freedom [red (gray) line]. In the figures on the left $\varepsilon = 0.02$ and velocities are (from the top) $u = 0.17$, $u = 0.21$, and $u = 0.25$. On the right are the phase diagrams corresponding to the same parameter values. The gray area represents the position of the inhomogeneity.

the kink ansatz derivative representing the zero mode of the (former) homogeneous model, i.e.,

$$\int_{-\infty}^{+\infty} d\xi \big[(-\ddot{x}_0 - \alpha\dot{x}_0)\partial_\xi\phi + \dot{x}_0^2\,\partial_\xi^2\phi - \varepsilon(\partial_x g)\,\partial_\xi\phi - \varepsilon g\,\partial_\xi^2\phi + \Gamma\big]\partial_\xi\phi = 0. \tag{26}$$

When performing integration, we must adopt a particular form of the function g describing the inhomogeneity. In this part, we assume similarly to the previous one $g(x) = \tanh x - \tanh(x - L)$. As a result of the integration, we obtain an effective equation of the form

$$\ddot{x}_0 + \alpha\dot{x}_0 + \varepsilon\left[\frac{x_0\coth x_0 - 1}{\sinh^2 x_0} - \frac{(x_0 - L)\coth(x_0 - L) - 1}{\sinh^2(x_0 - L)}\right] = \frac{\pi}{4}\Gamma. \tag{27}$$

Note that after removing the terms containing the coefficients α and Γ, the above equation reduces to Eq. (22) and therefore, in this case, the numerical results are included in Figs. 6 and 7.

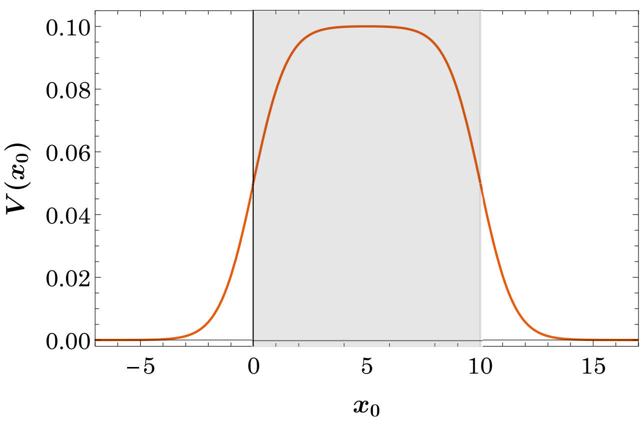

FIG. 8. Graphical representation of the potential represented by the second term (preceded by a minus sign) of Eq. (21). In the figure, we assumed $\varepsilon = 0.1$ and $L = 10$.

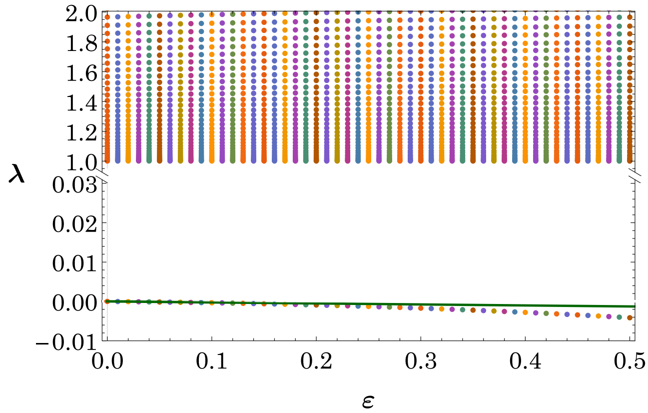

FIG. 9. Comparison of the squared eigenfrequencies $\lambda = \omega^2$ obtained from the field model (in case of $\alpha = 0$, $\Gamma = 0$) with the ones determined from the effective model with one degree of freedom [green (light gray) line].

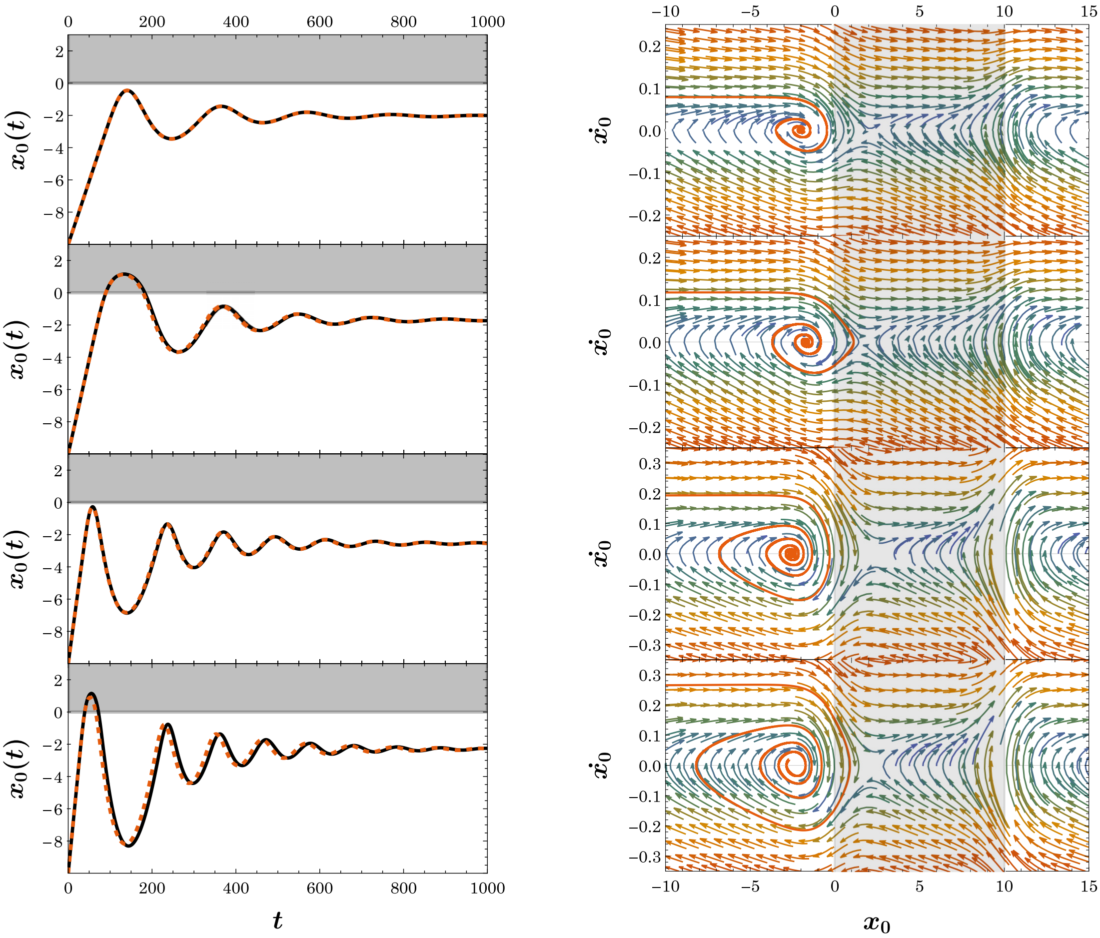

FIG. 10. Comparison of the position of the center of mass of the kink for the solution from the original field model (black line) and the model with one degree of freedom (red dashed line). In the figures on the left $\varepsilon = 0.01$ and bias current from the top 0.001 (top row), 0.0015 (second row), then $\varepsilon = 0.05$ and bias current 0.0025 (third row), 0.0035 (fourth row). In each case, the dissipation is equal to 0.01. On the right are the phase diagrams corresponding to the same parameter values. The gray area represents the position of the inhomogeneity.

On the other hand, if we have dissipation and current present in the system, then below the critical velocity, we observe the effect of multiple reflections from an inhomogeneity. The course of this process is shown in Fig. 10. In these figures, we assume that the dissipation coefficient is $\alpha = 0.01$ and that the bias current Γ is equal to 0.001 in the top left figure and 0.0015 in the second row of the figure, respectively. In both figures, $\varepsilon = 0.01$. The initial velocity of the kink in all cases with dissipation is chosen to be equal to the stationary velocity obtained in the article [20], i.e., according to the formula:

$$u_s = \frac{1}{\sqrt{1 + \left(\frac{4\alpha}{\pi\Gamma}\right)^2}}. \tag{28}$$

Equation (1) at $\varepsilon = 0$ has a solution in the form of a kink moving with constant velocity only when the dissipation occurring in the system is exactly balanced by the forcing in the form of a bias current, i.e., only for stationary velocity u_s. The initial condition describing a kink with velocity $u > u_s$ always, due to the existence of dissipation, slows down to a value of u_s. On the other hand, the initial condition with $u < u_s$, as a result of forcing, accelerates to u_s, i.e., to the velocity at which there is a balancing of forcing with dissipation. For this reason, if the initial velocity takes the value u_s (for $\varepsilon \neq 0$) the velocity changes are related only to the interaction with the inhomogeneity. Note that in both of these cases the kink trajectory resulting from the field model (solid black line) coincides with the trajectory obtained from the effective model (dashed red line). As one can see, in these runs the kink has too-low velocity to penetrate the barrier hence it bounces back; yet the presence of constant forcing causes successive returns toward the barrier. Due to the existence of dissipation in the system, the amplitude of subsequent reflections is reduced. From a dynamical systems perspective, this clearly suggests the existence of a fixed point in the form of a stable spiral, which is unveiled in the phase portrait illustrated in the right panel of the figure. The third and fourth rows of the figure illustrate the relevant features for a larger value of the parameter $\varepsilon = 0.05$ characterizing the inhomogeneity. Respectively, the corresponding bias currents are $\Gamma = 0.0025$, and $\Gamma = 0.0035$. It can be seen that in these cases the deviations of the continuous black and dashed red lines are insignificant and therefore the right panel contains only the phase space of the effective model. In the phase space presented in the figures of the right panel, one can identify two fixed points. The point located on the left side of the barrier, as discussed above, represents

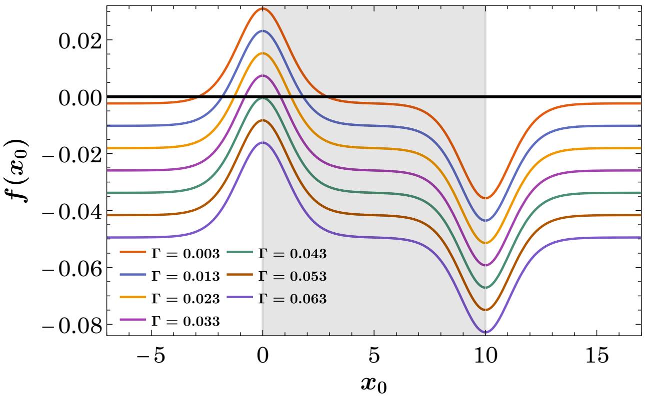

FIG. 11. Graphical representation of the position (and existence) of fixed points for different values of bias current [see Eq. (29)]. These are the places where the function $f(x_0)$ vanishes. In all cases $\varepsilon = 0.1$.

a stable spiral. The trajectories shown in the figures of the left panel are represented on the right panel by using red spirals. The second fixed point is located in the barrier area (representing the analog or remnant of the fixed point present in the conservative case) and has the character of a saddle point. In all panels of Fig. 10, the gray area represents the position of inhomogeneity or more precisely the area located between $x = 0$ and $x = L$. The stable manifold of the saddle represents on each side the separatrix between the trajectories that are transmitted and those that are reflected. The location of the fixed points can be determined by referring to Eq. (27). By transferring the bias current to the left side and zeroing out all derivatives with respect to time to identify the fixed points, we obtain a function $f(x_0)$,

$$f(x_0) \equiv \varepsilon\left[\frac{x_0 \coth x_0 - 1}{\sinh^2 x_0} - \frac{(x_0 - L)\coth(x_0 - L) - 1}{\sinh^2(x_0 - L)}\right] - \frac{\pi}{4}\Gamma = 0, \tag{29}$$

whose zeros indicate the desired equilibria. Figure 11 shows the positions of these points depending on the value of the current. It can be seen that for currents below the threshold value, i.e., for 0.003, 0.013, 0.023, and 0.033 there are two fixed points, a stable one on the left and an unstable one on the right. Physically, the presence of a stable fixed point is related to the fact that the kink, not having enough energy to cross the barrier bounces off it before getting trapped on the stable spiral fixed point. On the other hand, the constant forcing presses the kink to move towards the barrier. At the same time, the kink loses energy due to dissipation which leads to its eventual stopping. The presence of the second fixed point can be interpreted as the kink sliding off the barrier and is an effective remnant of the conservative case with $\Gamma = 0$. For the threshold value of the bias current, i.e., $\Gamma = 0.043$ only an unstable point remains. When the value of the current exceeds the threshold value (e.g., for $\Gamma = 0.053$ and $\Gamma = 0.063$) the fixed points do not occur. In these cases, the barrier is unable to stop the kink because the energy provided by the drive is too high. For negative values of the current, the situation is symmetrical with respect to the barrier, as long as the kink moves from the right side toward the left, i.e., the stable point is on the right side of the barrier while the unstable one is located on the barrier.

Similarly to Fig. 6, Fig. 12 shows the kink interaction with the inhomogeneity for two values of ε. The left panel corresponds to $\varepsilon = 0.01$ while the right one corresponds to $\varepsilon = 0.05$. Initial speeds are determined by the formula (28). In all plots, the dissipation coefficient is equal to $\alpha = 0.01$. In the left panel the bias current Γ is equal, respectively, in the three rows (0.0015, 0.00155, and 0.0016), while in the right panel it is 0036, 0.00384, and 0.0041. In these two panels the upper figures show a reflection of the kink from the barrier (leading to its eventual trapping). The middle figures represent the interaction of the kink with velocity close to the critical speed, ultimately in these cases leading to transmission. The bottom figures show the passage of a kink over a barrier for speeds above the critical velocity. It can be seen that for $\varepsilon = 0.01$ the agreement of the prediction of the approximate equation and the original one is very good while for $\varepsilon = 0.05$ we observe nontrivial discrepancies, which suggest the potential of the latter scenario for further improvement, as concerns its theoretical description. Finally, it is worth noting that the equations of motion in the case of zero mode projection and the method based on the conservative Lagrangian are identical for $\alpha = 0$ and $\Gamma = 0$. This behavior for effective models with one degree of freedom is not a coincidence. In the Appendix, we show that in the case without dissipation the two effective descriptions are equivalent.

3. The method based on nonconservative Lagrangian

Another proposal for obtaining both the original field equation (containing the dissipation) and the effective equation of motion for the collective coordinate reduced description is a method based on the nonconservative Lagrangian density [26,42]. The field equation in this case can be obtained based on the standard conservative Lagrangian density $\mathcal{L}$ and the nonconservative contribution $\mathcal{R}$,

$$\partial_\mu\left[\frac{\partial\mathcal{L}}{\partial(\partial_\mu\phi)}\right] - \frac{\partial\mathcal{L}}{\partial\phi} = \lim_{\phi_-\to 0}\left(\lim_{\phi_+\to\phi}\left\{\frac{\partial\mathcal{R}}{\partial\phi_-} - \partial_\mu\left[\frac{\partial\mathcal{R}}{\partial(\partial_\mu\phi_-)}\right]\right\}\right). \tag{30}$$

In the system we are currently considering, $\mathcal{L} = \mathcal{L}_{\mathrm{FSG}}$ and $\mathcal{R} = -\alpha\phi_-\partial_t\phi_+ - \Gamma\phi_-$. Here ϕ_- and ϕ_+ are auxiliary fields with the property that in the so-called physical limit $\phi_- \to 0$ and $\phi_+ \to \phi$. Equation (30) written above reproduces the field equation (1) with dissipation. The effective Lagrangian and the nonconservative potential at the effective level are obtained by inserting the kink ansatz into the densities and integrating over the spatial variable

$$L = \int_{-\infty}^{+\infty}\mathcal{L}(\phi_K, \partial_\mu\phi_K)dx, \quad R = \int_{-\infty}^{+\infty}\mathcal{R}(\phi_{K\pm}, \partial_\mu\phi_{K\pm})dx. \tag{31}$$

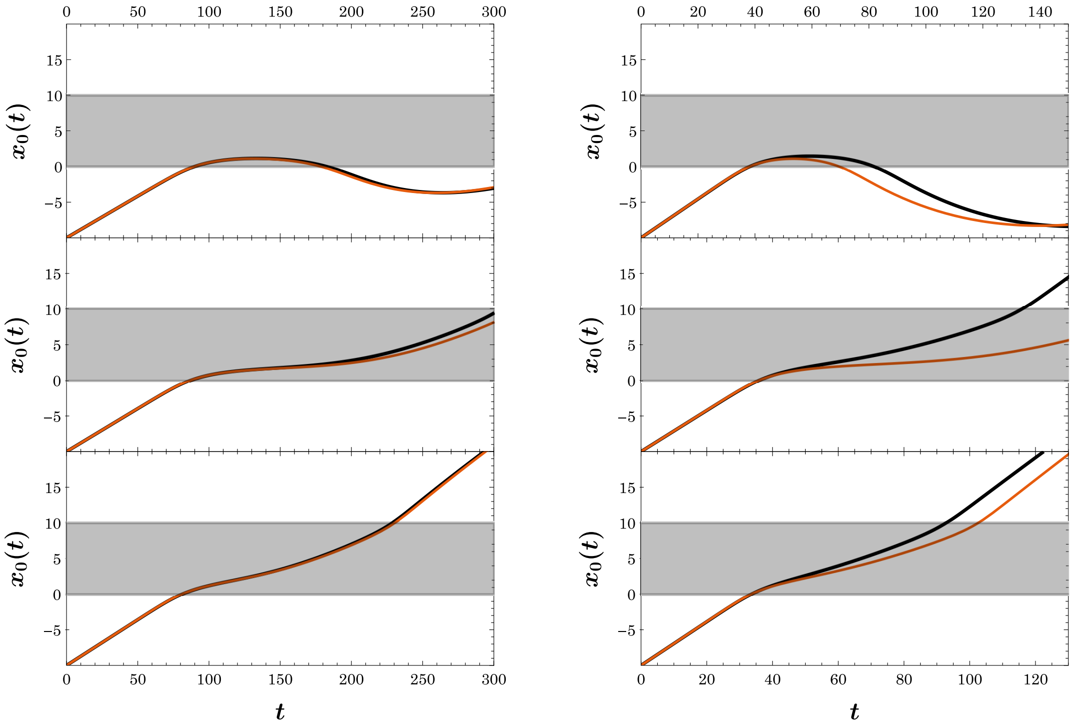

FIG. 12. Comparison of the position of the center of mass of the kink for the solution from the original field model (black line) and the model with one degree of freedom [red (gray) line]. The left panel contains figures for inhomogeneity $\varepsilon = 0.01$ and bias current with values (starting from the top) 0.0015, 0.00155, and 0.00165. On the right panel results for $\varepsilon = 0.05$ are presented. Starting from the top the bias current is 0.0036, 0.00384, and 0.0041. In each case, the disipation was equal to 0.01.

The effective equation has a similar structure to the original one,

$$\partial_t\left(\frac{\partial L}{\partial \dot{x}_0}\right) - \frac{\partial L}{\partial x_0} = \lim_{x_- \to 0}\left\{\lim_{x_+ \to x_0}\left[\frac{\partial R}{\partial x_-} - \partial_t\left(\frac{\partial R}{\partial \dot{x}_-}\right)\right]\right\}. \tag{32}$$

After substituting the effective quantities into Eq. (32), we get

$$\ddot{x}_0 + \varepsilon\left[\frac{x_0 \coth x_0 - 1}{\sinh^2 x_0} - \frac{(x_0 - L)\coth(x_0 - L) - 1}{\sinh^2(x_0 - L)}\right] = -\alpha\dot{x}_0 + \frac{\pi}{4}\Gamma. \tag{33}$$

Note that this equation is identical to Eq. (27) and for $\alpha = 0$ and $\Gamma = 0$ reduces to Eq. (22). Per our previous discussion, the trajectories in this simplified case have been compared with the trajectories obtained in the original field model in Fig. 6, while the case with dissipation ($\alpha \neq 0$ and $\Gamma \neq 0$) has been shown in Figs. 10 and 12.

B. Approximations based on two degrees of freedom

We now turn to representations of the effective solitary wave dynamics using two degrees of freedom. More specifically, we consider the position of the kink $x_0(t)$ and a parameter describing its effective inverse width parametrized by $\gamma(t)$ through the ansatz

$$\phi_K(t, x) = 4 \arctan e^{\gamma(t)[x - x_0(t)]}. \tag{34}$$

Such a functional form is expected to allow us both to better describe the motional effects of the kink and also to capture the (potential) excitation of the kink's vibrational (internal breathing) mode. We now proceed to provide the associated details, providing all three of the effective descriptions used before (one for the Hamiltonian and two for the damped-driven problem).

1. *The construction based on a conservative Lagrangian (for $\alpha = 0$ and $\Gamma = 0$)*

Similarly to the previous section, after integrating the model Lagrangian (14) over the spatial variable x, we obtain in this case a sine-Gordon part of the effective Lagrangian of the form

$$L_{\text{SG}} = 4\gamma\dot{x}_0^2 + \frac{\pi^2}{3\gamma^3}\dot{\gamma}^2 - 4\left(\gamma + \frac{1}{\gamma}\right). \tag{35}$$

The form of the second part of the effective Lagrangian is strongly dependent on the shape of the inhomogeneity, i.e., on the analytical form of the function $g(x)$. For example, for a function consisting of a unit step $g(x) = \theta(x) - \theta(x - L)$ this part of the Lagrangian is as follows:

$$L_\varepsilon = -2\varepsilon\gamma\{\tanh(\gamma x_0) - \tanh[\gamma(x_0 - L)]\}. \tag{36}$$

Then the equations of motion in this case (stemming from the effective Lagrangian $L = L_{\text{SG}} + L_\varepsilon$) have a relatively compact form,

$$\ddot{x} + \frac{\dot{\gamma}}{\gamma}\dot{x}_0 + \frac{1}{4}\varepsilon\gamma\{\text{sech}^2(\gamma x_0) - \text{sech}^2[\gamma(x_0 - L)]\} = 0,$$

$$\frac{2\pi^2}{3}\frac{\ddot{\gamma}}{\gamma} - \pi^2\frac{\dot{\gamma}^2}{\gamma^2} - 4\gamma^2\dot{x}^2 + 4(\gamma^2 - 1) + 2\varepsilon\gamma^2\{\tanh(\gamma x_0) - \tanh[\gamma(x_0 - L)]\} + 2\varepsilon\gamma^3\{x_0\text{sech}^2(\gamma x_0) - (x_0 - L)\text{sech}^2[\gamma(x_0 - L)]\} = 0. \tag{37}$$

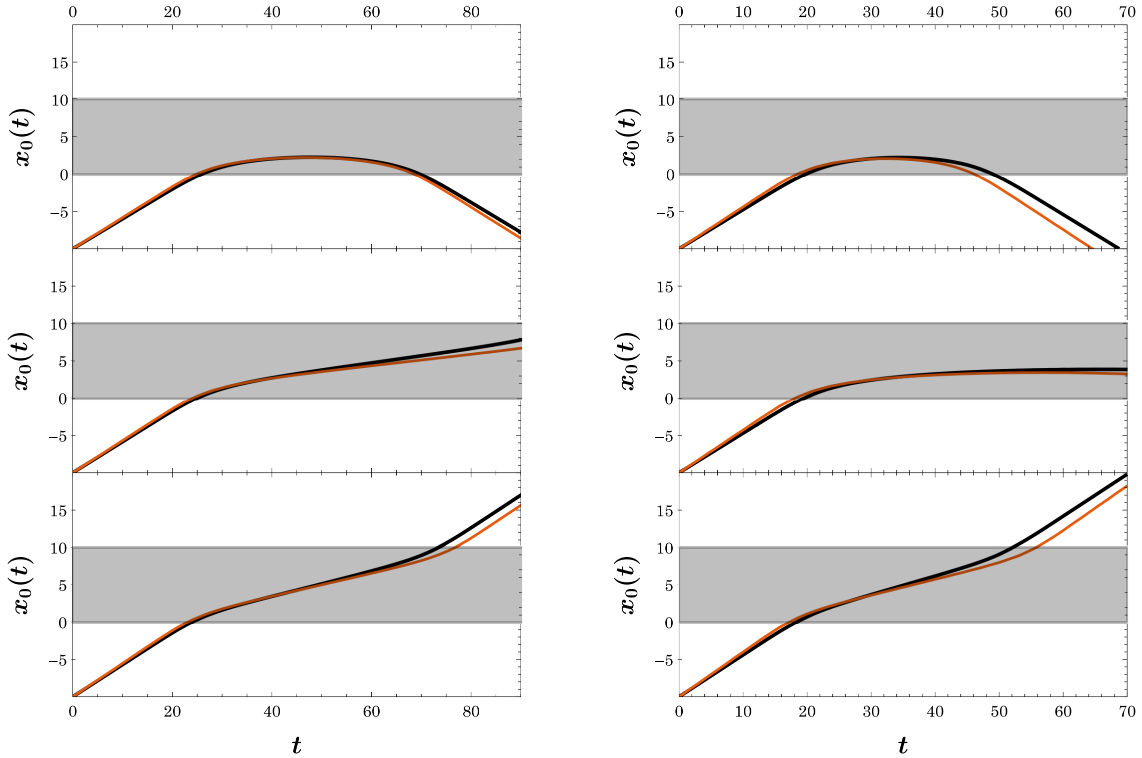

FIG. 13. Comparison of the position of the center of mass of the kink for the solution of the original field model (black line) and the model with two degrees of freedom [red (gray) line] for on the left $\varepsilon = 0.1$ and velocities are (from the top) 0.4, 0.415, and 0.43 and on the right $\varepsilon = 0.2$ and velocities are (from the top) 0.523, 0.53, and 0.56.

Due to the high complexity and length of the formulas, we do not give the form of the equations obtained for $g(x) = \tanh(x) - \tanh(x - L)$; however, these equations are used when comparing the effective model with the field model (1). For completeness of description, the part L_ε of the Lagrangian responsible for the interaction with the inhomogeneity for this case is given as:

$$L_\varepsilon = \frac{8\gamma\epsilon e^{2\gamma x_0}}{(e^{2\gamma x_0} - 1)^2(e^{2\gamma L} - e^{2\gamma x_0})^2}\big(e^{2\gamma L}(e^{2\gamma x_0} - 1)^2 \log(e^{2\gamma L}) + 4\sinh(\gamma L)e^{2\gamma(L+x_0)}\{-\cosh(\gamma L) + \cosh[\gamma(L - 2x_0)] + \log(e^{2\gamma x_0})\sinh[\gamma(L - 2x_0)]\}\big). \tag{38}$$

As before, the effective Lagrangian L_{FSG} consists of two parts, i.e., the effective Lagrangian of the free sine-Gordon model (35) and the Lagrangian describing the interaction with inhomogeneity (38). This effective Lagrangian is used to obtain the equations of motion.

The trajectory describing the movement of the center of mass resulting from Eq. (1) (black line) is compared with the time dependence of the collective variable $x_0(t)$ [red (gray) line] in Fig. 13. In the figure, very good agreement between the effective model and the field model is achieved up to ε values equal to 0.2. In the figures, the parameter L describing the width of the inhomogeneity is equal to 10. It is interesting to note that the introduction of a second variable $\gamma(t)$ significantly improves the predictions of the effective model relative to the $x_0(t)$ variable. On the other hand, predictions about the $\gamma(t)$ variable itself are of more limited value. As a kink approaches the heterogeneity its width becomes suitably modulated. The changes in thickness gradually disappear with time at the field-theoretic level, after which the thickness stabilizes at a level characteristic of the stationary kink solution. Figure 14 compares the thickness of the static kink solution that follows from the effective model and the corresponding value derived from the field model. It can be seen that as ε increases, the model increasingly underestimates the value of the γ variable, although the relevant deviation is quite

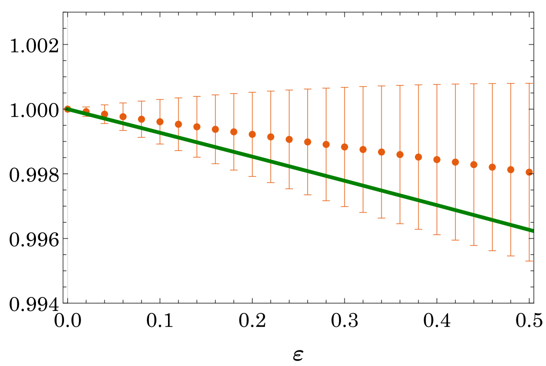

FIG. 14. Fit of γ values depending on the ε determined from the solution of the original PDE (orange dots) with standard error calculated by maximum likelihood estimation compared with the γ determined from a model with two degrees of freedom [green (light gray) line]. The figure describes the evolution when the inhomogeneity is in the form of a combination of hyperbolic tangents. In addition, $\alpha = 0$ and $\Gamma = 0$.

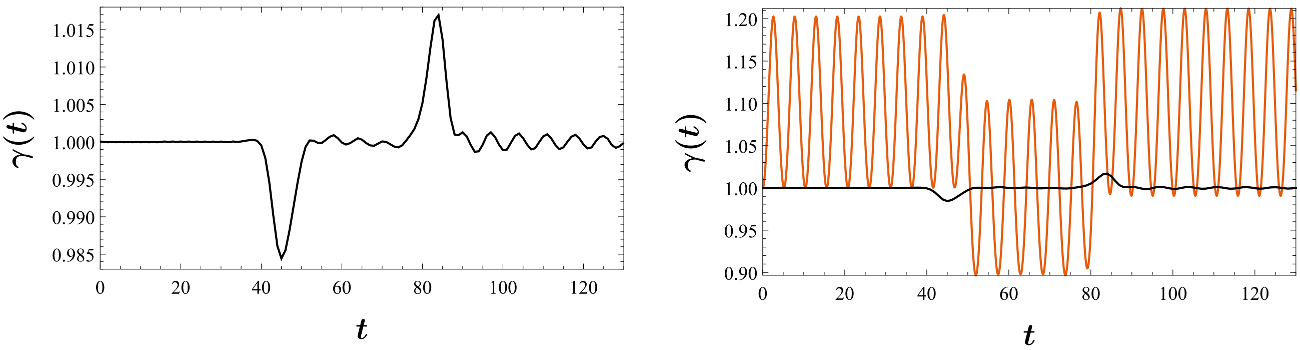

FIG. 15. In the left panel of the figure, the evolution of the $\gamma(t)$ variable in the original field model. The right panel of the figure compares the results of the field model with an effective model with two degrees of freedom. In both cases $\varepsilon = 0.1$.

small and also it is clear that the model captures the nature of the qualitative trend of the effect of the perturbation of ε on the parameter γ. Figure 15 compares the oscillations of the γ variable in the effective model and the oscillations of the kink thickness as the kink passes through the inhomogeneity. The differences here are nontrivial although in both descriptions (i.e., exact and effective) the nature of the vibration changes similarly in the area of inhomogeneity. At the level of Eqs. (37), one can trace this effect in the presence of terms such as the one $\propto \gamma^2\dot{x}^2$ in the dynamical equation for the evolution of $\gamma(t)$. Indeed, while we observe that the field dynamics retain γ to a nearly constant value far from the inhomogeneity, the above mentioned term is "active" in the reduced model equation leading to oscillatory dynamics of the kink width. Indeed, this is a point of potential future improvement of the reduced model as the latter is not presently capturing the Lorentz invariance of the homogeneous kink which would enable it to move with constant speed without inducing a width vibration. Nevertheless, the qualitative trends of variation of $\gamma(t)$ induced by the inhomogeneity are captured by the two-degree-of-freedom model (superimposed to the above-mentioned vibration).

Finally, the two-degree-of-freedom effective model naturally reproduces the two modes belonging to the spectrum of the $\hat{\mathcal{L}}$ operator (see Fig. 16) in the case of the unstable saddle equilibrium of the Hamiltonian model kink centered at the impurity region. The first unstable mode (corresponding to the instability of the kink's position at the center of the inhomogeneity) is associated with the x_0 variable, i.e., pertains to the former translational mode, and the oscillating mode (corresponding to changes in the thickness of the kink) is associated with the γ variable. This second mode is essentially connected with the band edge of the continuous part of the spectrum of the operator $\hat{\mathcal{L}}$. Both modes of the effective model are represented by green (light gray) lines.

2. The method of projecting onto the zero mode (for arbitrary α and Γ)

In the case of two degrees of freedom, we insert $\xi(t, x)$ into Eq. (24) in the form of

$$\xi(t, x) = \gamma(t)[x - x_0(t)].$$

This substitution results in the equation

$$\left[\left(\frac{\ddot{\gamma}}{\gamma} + \alpha\frac{\dot{\gamma}}{\gamma}\right)\xi - (2\dot{x}_0\dot{\gamma} + \alpha\gamma\dot{x}_0 + \gamma\ddot{x}_0)\right]\partial_\xi\phi_K + \left[\left(\frac{\dot{\gamma}}{\gamma}\right)^2\xi^2 - 2\dot{x}_0\dot{\gamma}\xi + (\gamma^2\dot{x}_0^2 - \gamma^2 + 1)\right]\partial_\xi^2\phi_K = \varepsilon\gamma(\partial_x g)\,\partial_\xi\phi_K + \varepsilon\gamma^2 g\,\partial_\xi^2\phi_K - \Gamma. \tag{39}$$

The first of the equations of the two-degree-of-freedom effective model is obtained similarly to the one-degree-of-freedom model, i.e., by projecting to the (former) zero mode. We multiply the above equation by the derivative of the kink ansatz and then perform an integration over the entire domain to remove the dependence on the spatial variable. In the case of the second equation, before calculating the integrals, we additionally multiply the equation by ξ, which changes the parity of the calculated integrals,

$$\ddot{x}_0 + \alpha\dot{x}_0 + \frac{\dot{\gamma}}{\gamma}\dot{x}_0 - \frac{1}{8}\varepsilon\gamma\mathcal{J} = \frac{\pi}{4\gamma}\Gamma,$$
$$\frac{2\pi^2}{3}\left(\frac{\ddot{\gamma}}{\gamma} + \alpha\frac{\dot{\gamma}}{\gamma}\right) - \pi^2\frac{\dot{\gamma}^2}{\gamma^2} - 4\gamma^2\dot{x}^2 + 4(\gamma^2 - 1) - \varepsilon\gamma\mathcal{I}_1 - \varepsilon\gamma^2\mathcal{I}_2 = 0. \tag{40}$$

The integrals appearing in the equations for different forms of the function g describing the inhomogeneity have the form

$$\mathcal{J} = \int_{-\infty}^{+\infty} g(x)(\partial_\xi\phi_K)\big(\partial_\xi^2\phi_K\big)d\xi,$$
$$\mathcal{I}_1 = \int_{-\infty}^{+\infty} [\partial_x g(x)]\,\xi\,(\partial_\xi\phi_K)^2 d\xi,$$
$$\mathcal{I}_2 = \int_{-\infty}^{+\infty} g(x)\,\xi\,(\partial_\xi\phi_K)\big(\partial_\xi^2\phi_K\big)d\xi. \tag{41}$$

In the simplest case where the function g consists of step functions, i.e., $g(x) = \theta(x) - \theta(x - L)$, the equations of motion

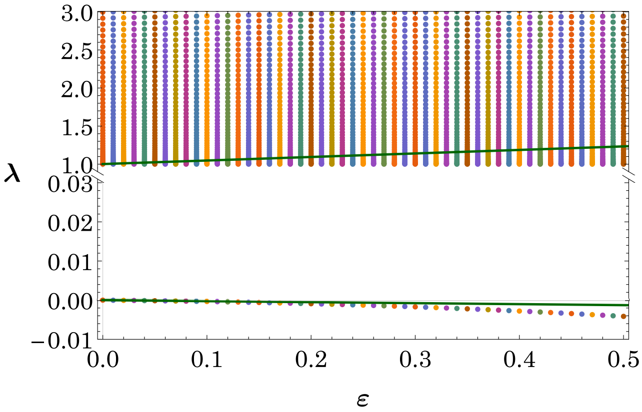

FIG. 16. Comparison of the determined squared eigenfrequencies $\lambda = \omega^2$ from the linearization Jacobian (in case of $\alpha = 0, \Gamma = 0$) with those obtained from the model with two degrees of freedom linearized around the equilibrium state of the latter [green (light gray) line].

can be converted to the form

$$\ddot{x}+\alpha\dot{x}_0+\frac{\dot{\gamma}}{\gamma}\dot{x}_0+\frac{1}{4}\varepsilon\gamma\{\operatorname{sech}^2(\gamma x_0)-\operatorname{sech}^2[\gamma(x_0-L)]\}=\frac{\pi}{4\gamma}\Gamma,$$
$$\frac{2\pi^2}{3}\left(\frac{\ddot{\gamma}}{\gamma}+\alpha\frac{\dot{\gamma}}{\gamma}\right)-\pi^2\frac{\dot{\gamma}^2}{\gamma^2}-4\gamma^2\dot{x}^2+4(\gamma^2-1)$$
$$+2\varepsilon\gamma^2\{\tanh(\gamma x_0)-\tanh[\gamma(x_0-L)]\}+2\varepsilon\gamma^3$$
$$\times\{x_0\operatorname{sech}^2(\gamma x_0)-(x_0-L)\operatorname{sech}^2[\gamma(x_0-L)]\}=0. \tag{42}$$

Note that these equations reduce to the system (37) when we take α and Γ equal to zero.

3. The method based on nonconservative Lagrangian (for arbitrary α and Γ)

As we described in the previous sections, Equation (1) can be obtained using a nonconservative Lagrangian density through Eq. (30), where $\mathcal{R}$ represents the nonconservative contribution. In the case of an effective model with two degrees of freedom, the effective conservative Lagrangian and the effective nonconservative potential are obtained by integrating over the spatial variable (31). The only difference is the assumed ansatz, which in the case of two degrees of freedom has the form described by Eq. (34). In the model defined in this way, we have two effective equations of motion,

$$\partial_t\left(\frac{\partial L}{\partial\dot{x}_0}\right)-\frac{\partial L}{\partial x_0}=\left[\frac{\partial R}{\partial x_-}-\partial_t\left(\frac{\partial R}{\partial\dot{x}_-}\right)\right]_{\rm PL},$$
$$\partial_t\left(\frac{\partial L}{\partial\dot{\gamma}}\right)-\frac{\partial L}{\partial\gamma}=\left[\frac{\partial R}{\partial\gamma_-}-\partial_t\left(\frac{\partial R}{\partial\dot{\gamma}_-}\right)\right]_{\rm PL}. \tag{43}$$

In the physical limit (denoted here by PL) the auxiliary variables x_- and γ_- disappear, while $x_+ \to x_0$ and $\gamma_+ \to \gamma$. On the other hand, the Lagrangian consists of the sine-Gordon part (35) and the interaction term, i.e., $L = L_{\rm SG} + L_\varepsilon$ and therefore the equations of motion can be written as follows:

$$\ddot{x}_0+\frac{\dot{\gamma}}{\gamma}\dot{x}_0-\frac{1}{8\gamma}\frac{\partial L_\varepsilon}{\partial x_0}=\frac{1}{8\gamma}\left[\frac{\partial R}{\partial x_-}-\partial_t\left(\frac{\partial R}{\partial\dot{x}_-}\right)\right]_{\rm PL},$$
$$\frac{2\pi^2}{3}\frac{\ddot{\gamma}}{\gamma}-\pi^2\frac{\dot{\gamma}^2}{\gamma^2}-4\gamma^2\dot{x}_0^2+4(\gamma^2-1)-\gamma^2\frac{\partial L_\varepsilon}{\partial\gamma}$$
$$=\gamma^2\left[\frac{\partial R}{\partial\gamma_-}-\partial_t\left(\frac{\partial R}{\partial\dot{\gamma}_-}\right)\right]_{\rm PL}. \tag{44}$$

The right-hand sides of these equations we obtain by calculating the nonconservative potential and its derivatives in the physical limit,

$$\ddot{x}_0+\frac{\dot{\gamma}}{\gamma}\dot{x}_0-\frac{1}{8\gamma}\frac{\partial L_\varepsilon}{\partial x_0}=-\alpha\dot{x}_0+\frac{\pi}{4\gamma}\Gamma,$$
$$\frac{2\pi^2}{3}\frac{\ddot{\gamma}}{\gamma}-\pi^2\frac{\dot{\gamma}^2}{\gamma^2}-4\gamma^2\dot{x}_0^2+4(\gamma^2-1)-\gamma^2\frac{\partial L_\varepsilon}{\partial\gamma}=-\frac{2\pi^2}{3}\alpha\frac{\dot{\gamma}}{\gamma}. \tag{45}$$

We recall here that the interaction with the inhomogeneity is described by the following integral:

$$L_\varepsilon=-\frac{1}{2}\varepsilon\int_{-\infty}^{+\infty}g(x)(\partial_x\phi_K)^2, \tag{46}$$

where ϕ_K denotes the ansatz (34). For example, in the case of inhomogeneity defined by the unit step functions $g(x) = \theta(x) - \theta(x - L)$ we get equations identical to the formulas (42), obtained previously using the projection approach. A different situation occurs for inhomogeneities defined by hyperbolic tangents $g(x) = \tanh(x) - \tanh(x - L)$. Naturally, if in the system there is dissipation, then we can only use the method based on the nonconservative Lagrangian and the method of projection onto the zero mode. The results of the two methods are found to differ slightly as shown in Fig. 17, favoring the nonconservative Lagrangian method as more accurate. Figure 17 compares trajectories obtained for the inhomogeneity of $g(x) = \tanh(x) - \tanh(x - L)$ using a method based on a nonconservative Lagrangian for two degrees of freedom [red (gray) line] and a zero mode projection [green (light gray) line]. In all figures, the black line represents the result obtained from the full field model PDE. The inhomogeneity in the figures of the left panel corresponds to $\varepsilon = 0.05$, while for the right panel it is $\varepsilon = 0.1$. We used the following currents on the left panel, starting from the top, 0.0032, 0.0037, and 0.0042. On the right panel, the currents are assumed to be (again, starting from the top) 0.005, 0.0054, and 0.0058. In all figures, the dissipation is assumed to be $\alpha = 0.01$. We found that as the parameter ε increases, the method of projecting onto the zero mode to a higher extent than the method based on the nonconservative Lagrangian underestimates the position of the kink.

IV. CONCLUSIONS AND FUTURE WORK

In this paper, we have studied the behavior of the kink in the sine-Gordon model in the presence of a localized inhomogeneity. In the case without dissipation, we focused on the interaction of the kink with the impurity region at speeds

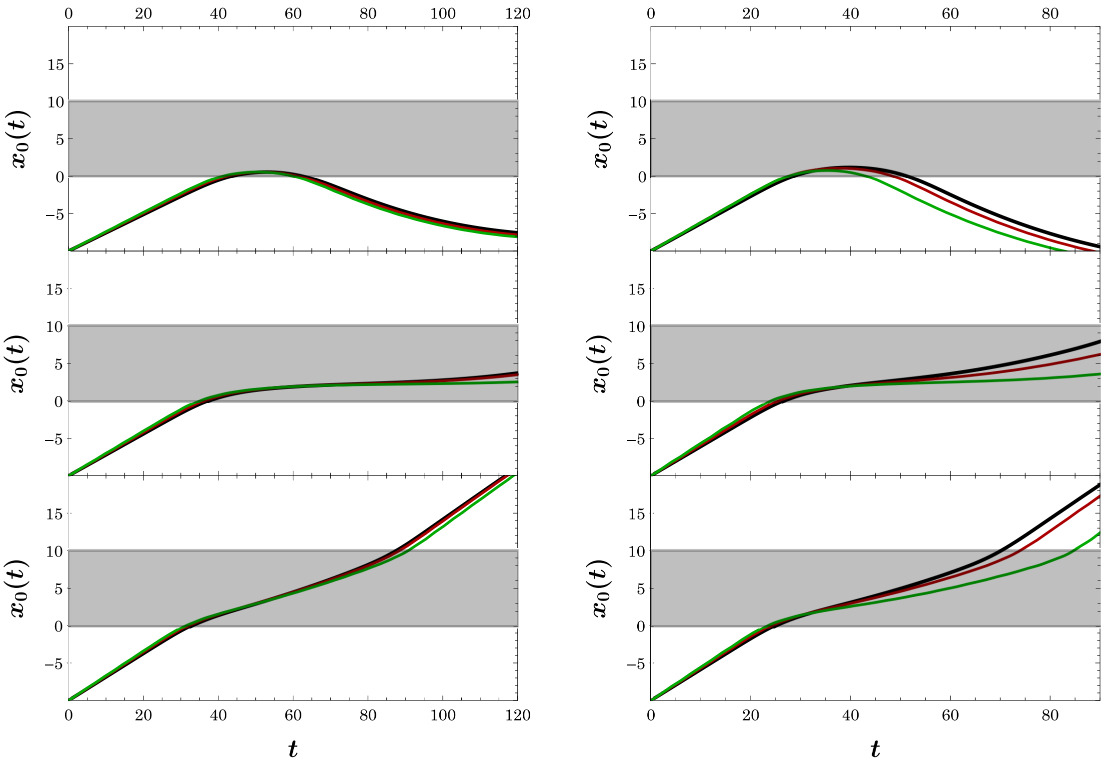

FIG. 17. Comparison of the position of the center of mass of the kink for the solution from the original field model (black line) and models with two degrees of freedom based on projecting onto the zero mode according to (40) [green (light gray) line] and on nonconservative Lagrangian according to (45) [red (gray) line]. The left panel contains figures for inhomogeneity strength $\varepsilon = 0.05$ and bias current with values (starting from the top) 0.0032, 0.0037, and 0.0042. On the right panel, results for $\varepsilon = 0.1$ are presented. Starting from the top, the bias current is 0.005, 0.0054, and 0.0058. In each case, the dissipation was equal to 0.01.

proximal to the critical velocity separating transmission from reflection. In the immediate vicinity of the relevant critical point (which we identified as a saddle), we observed the kink slowing down for an extended time interval at the center of the inhomogeneity. The process of the kink interaction with the inhomogeneity was also described within the framework of effective models with one and two degrees of freedom. As expected, the description with one collective variable works well for small values of the perturbation parameter ε. On the other hand, the inclusion of a second collective variable, effectively characterizing the width of the coherent structure, significantly improves the predictions of the effective model including for somewhat larger values of ε. At the same time, however, the predictions for the second collective variable bear some differences in comparison to the field description albeit in ways that were explained in the associated discussion. In particular, the second collective variable is intended to identify the occurrence of the interaction, while the reduced description also seems to identify a vibrational mode associated with the edge of the continuous spectrum. A more refined representation of the relevant mode that yields a close agreement with the field-theoretic results constitutes a natural question for future study.

The case of interaction of a kink with an inhomogeneity in a system with dissipation and external drive presents further intriguing features in its own right. The passage of the kink through the barrier or reflection depends on the relationship between the external forcing and the dissipation. Particularly interesting here is the process of interaction of the kink with the barrier for bias currents smaller than the threshold current. In this case, we observe successive reflections of the kink from the barrier caused by the bias current pushing it toward the barrier. Oscillations of the kink position are naturally damped due to the presence of dissipation in the system. The shape of the final static configuration can be determined on the basis of a linearized approximation and reveals a stable spiral fixed point of the effective description. The reduced model description of the process of interaction of the kink with the inhomogeneity below the threshold current leads to surprisingly consistent results with those from the original PDE. Moreover, the effective models with two degrees of freedom (for small ε) correctly approximate the excitation spectrum obtained on the ground of the linear approximation (Fig. 16), as well as the associated dynamics. While both related methods are found to be qualitatively adequate, the nonconservative Lagrangian approach developed herein is also found to be highly quantitatively accurate in describing the kink evolution (for one degree of freedom, the different approaches developed are found to yield identical results in suitable limits).

It is also worth noting that in real physical systems we have to deal with various types of random distortions. The most common such disturbance is thermal noise. The natural question then arises regarding the conditions under which the presence of noise does not significantly change the conclusions of this paper. In the case of thermal noise, the parameter that best describes its impact is temperature. In the case of the processes described in our work, in order for its conclusions not to be altered, we would have to assume a temperature low enough so that no thermal creation of kinks or antikinks occurs during evolution. Moreover, the kink would not be subject to Brownian movements in a significant way, and the "phonon dressing" would be negligible. This regime corresponds to the $k_BT << E$ regime reported in Refs. [43,44], where E is the kink energy (k_B is Boltzman's constant); see also Ref. [3].

This study naturally paves the way for a number of future possibilities. On the one hand, our focus here was in the interaction of sine-Gordon kink with an inhomogeneity. Yet, there has been a rich literature exploring the resonant interaction of a ϕ^4 kink with an impurity dating back to Ref. [45] that has recently seen a resurgence of interest in different model variants and associated phenomenologies [46,47]. Another interesting direction concerns the exploration of higher-dimensional variants even of the sine-Gordon variety in order to appreciate the effects of curvature and impurity geometry on the kink dynamics; see for some recent examples [40,48]. Such studies are currently in progress and will be reported in the future.

ACKNOWLEDGMENTS

This research has been made possible by the Kosciuszko Foundation. The American Centre of Polish Culture. This material is based on work supported by the U.S. National Science Foundation under Awards No. PHY-2110030 and No. DMS-2204702 (P.G.K.).

APPENDIX: EQUIVALENCE OF THE FIRST TWO APPROACHES FOR ONE DEGREE OF FREEDOM REDUCED MODELS

In this section, we will consider a class of Lagrangian systems, in the absence of dissipation for which we will demonstrate the equivalence of the first two approaches presented in the main body of the text for one degree of freedom effective descriptions for the wave's center of mass. We assume that stable solutions in the form of solitons are present in this system. The effective description of the position of the soliton in this system is specified by the following equation:

$$\frac{\partial L_{\rm eff}}{\partial x_0} - \frac{d}{dt}\left(\frac{\partial L_{\rm eff}}{\partial \dot{x}_0}\right) = 0. \tag{A1}$$

Here $L_{\rm eff}$ denotes the effective Lagrangian,

$$L_{\rm eff} = \int_{-\infty}^{+\infty} \mathcal{L}(\phi_K, \dot{\phi}_K, \phi_K')dx. \tag{A2}$$

As can be seen, it is obtained by integrating the Lagrangian density of the underlying field theory with respect to the spatial variable. Here $\phi_K = \phi_K[x - x_0(t)]$ denotes the kink solution and $x_0(t)$ is the collective variable that represents the position of the kink. We will consider Lagrangians that contain terms that explicitly break the translational symmetry of the system. An example Lagrangian of this type has the form:

$$\mathcal{L}(\phi_K, \dot{\phi}_K, \phi_K') = \tfrac{1}{2}\mathcal{A}(x)\dot{\phi}_K^2 - \tfrac{1}{2}\mathcal{F}(x)\phi_K'^2 - \mathcal{B}(x)V(\phi_K), \tag{A3}$$

where the dot denotes the time derivative and prime denotes the derivative with respect to space variable x. Here $\mathcal{A}$, $\mathcal{B}$, and $\mathcal{F}$ are arbitrary functions with finite values. In particular, in previous sections of this work, we considered the cases for which $\mathcal{A} = 1$ and $\mathcal{B} = 1$. Applying the definition of the effective Lagrangian (A2) to Eq. (A1) we obtain

$$\int_{-\infty}^{+\infty}\left\{\frac{\partial \mathcal{L}}{\partial x_0} - \frac{d}{dt}\left(\frac{\partial \mathcal{L}}{\partial \dot{x}_0}\right)\right\}dx = 0. \tag{A4}$$

When calculating the derivatives, we must remember that the Lagrangian density depends on the x_0 variable both through the field ϕ_K, its spatial and time derivatives

$$\frac{\partial \mathcal{L}}{\partial x_0} = \frac{\partial \mathcal{L}}{\partial \phi_K}\frac{\partial \phi_K}{\partial x_0} + \frac{\partial \mathcal{L}}{\partial \dot{\phi}_K}\frac{\partial \dot{\phi}_K}{\partial x_0} + \frac{\partial \mathcal{L}}{\partial \phi_K'}\frac{\partial \phi_K'}{\partial x_0}. \tag{A5}$$

Next, we will convert the derivatives with respect to the variable describing the position of the kink x_0 into derivatives with respect to the variable $\xi = x - x_0(t)$,

$$\frac{\partial \mathcal{L}}{\partial x_0} = -\frac{\partial \mathcal{L}}{\partial \phi_K}\frac{\partial \phi_K}{\partial \xi} - \frac{\partial \mathcal{L}}{\partial \dot{\phi}_K}\frac{\partial \dot{\phi}_K}{\partial \xi} - \frac{\partial \mathcal{L}}{\partial \phi_K'}\frac{\partial \phi_K'}{\partial \xi}. \tag{A6}$$

Similarly, we can calculate the derivative with respect to the kink velocity, but this time the dependence on the $\dot{x}_0$ variable occurs in just one term,

$$\frac{\partial \mathcal{L}}{\partial \dot{x}_0} = \frac{\partial \mathcal{L}}{\partial \phi_K}\frac{\partial \phi_K}{\partial \dot{x}_0} + \frac{\partial \mathcal{L}}{\partial \dot{\phi}_K}\frac{\partial \dot{\phi}_K}{\partial \dot{x}_0} + \frac{\partial \mathcal{L}}{\partial \phi_K'}\frac{\partial \phi_K'}{\partial \dot{x}_0} = \frac{\partial \mathcal{L}}{\partial \dot{\phi}_K}\frac{\partial \dot{\phi}_K}{\partial \dot{x}_0}. \tag{A7}$$

The derivative of the field ϕ_K with respect to time explicitly depends in a linear way on the velocity

$$\dot{\phi}_K = \frac{\partial \phi_K}{\partial \xi}\frac{d\xi}{dt} = -\dot{x}_0\frac{\partial \phi_K}{\partial \xi} \tag{A8}$$

and therefore the derivative of $\dot{\phi}_K$ with respect to velocity is equal to

$$\frac{\partial \dot{\phi}_K}{\partial \dot{x}_0} = -\frac{\partial \phi_K}{\partial \xi}. \tag{A9}$$

The relevant contribution of the derivative of the Lagrangian with respect to $\dot{x}_0$ then yields

$$\frac{\partial \mathcal{L}}{\partial \dot{x}_0} = -\frac{\partial \mathcal{L}}{\partial \dot{\phi}_K}\frac{\partial \phi_K}{\partial \xi}. \tag{A10}$$

The obtained derivatives of Lagrangian density with respect to x_0, given by Eq. (A6) and $\dot{x}_0$, set by Eq. (A10), can be used in Eq. (A4), yielding

$$\int_{-\infty}^{+\infty}\left\{-\frac{\partial \mathcal{L}}{\partial \phi_K}\frac{\partial \phi_K}{\partial \xi} - \frac{\partial \mathcal{L}}{\partial \dot{\phi}_K}\frac{\partial \dot{\phi}_K}{\partial \xi} - \frac{\partial \mathcal{L}}{\partial \phi_K'}\frac{\partial \phi_K'}{\partial \xi} + \frac{d}{dt}\left(\frac{\partial \mathcal{L}}{\partial \dot{\phi}_K}\frac{\partial \phi_K}{\partial \xi}\right)\right\}dx = 0. \tag{A11}$$

After performing the differentiation with respect to time, we can separate the part that is multiplied by the zero mode and the other part that we still need to transform

$$\int_{-\infty}^{+\infty}\left\{\frac{d}{dt}\left(\frac{\partial\mathcal{L}}{\partial\dot{\phi}_K}\right)-\frac{\partial\mathcal{L}}{\partial\phi_K}\right\}\frac{\partial\phi_K}{\partial\xi}d\xi-\int_{-\infty}^{+\infty}\left\{\frac{\partial\mathcal{L}}{\partial\phi_K'}\frac{\partial\phi_K'}{\partial\xi}\right\}dx=0. \tag{A12}$$

In the second integral, we transfer the derivative with respect to the spatial variable from the second factor to the first one,

$$\int_{-\infty}^{+\infty}\left\{\frac{\partial\mathcal{L}}{\partial\phi_K'}\frac{\partial\phi_K'}{\partial\xi}\right\}dx=\int_{-\infty}^{+\infty}\frac{\partial}{\partial x}\left\{\frac{\partial\mathcal{L}}{\partial\phi_K'}\left(\frac{\partial\phi_K}{\partial\xi}\right)\right\}dx-\int_{-\infty}^{+\infty}\frac{\partial}{\partial x}\left(\frac{\partial\mathcal{L}}{\partial\phi_K'}\right)\frac{\partial\phi_K}{\partial\xi}dx. \tag{A13}$$

Since the spatial derivative of ϕ_K vanishes at infinity, we can extract the term that contains multiplication by the zero mode,

$$\int_{-\infty}^{+\infty}\left\{\frac{\partial\mathcal{L}}{\partial\phi_K'}\frac{\partial\phi_K'}{\partial\xi}\right\}dx=-\int_{-\infty}^{+\infty}\frac{\partial}{\partial x}\left(\frac{\partial\mathcal{L}}{\partial\phi_K'}\right)\frac{\partial\phi_K}{\partial\xi}d\xi. \tag{A14}$$

The integral that is transformed in this way can be reinserted into Eq. (A12), yielding

$$\int_{-\infty}^{+\infty}\left\{\frac{d}{dt}\left(\frac{\partial\mathcal{L}}{\partial\dot{\phi}_K}\right)+\frac{\partial}{\partial x}\left(\frac{\partial\mathcal{L}}{\partial\phi_K'}\right)-\frac{\partial\mathcal{L}}{\partial\phi_K}\right\}\frac{\partial\phi_K}{\partial\xi}d\xi=0. \tag{A15}$$

In relativistic notation, the last equation can be written as follows:

$$\int_{-\infty}^{+\infty}\left\{\partial_\mu\left(\frac{\partial\mathcal{L}}{\partial(\partial_\mu\phi_K)}\right)-\frac{\partial\mathcal{L}}{\partial\phi_K}\right\}\frac{\partial\phi_K}{\partial\xi}d\xi=0, \tag{A16}$$

where ∂_μ denotes differentiation with respect to space-time variables $x^\mu=(x^0,x^1)=(t,x)$. Note that starting from Eq. (A1) we obtained Eq. (A16), which defines the method of projecting onto the zero mode. On the other hand, going backwards in our calculations from Eq. (A16), we arrive at the effective Eq. (A1), which means that the method based on the conservative Lagrangian is equivalent (in the absence of dissipation) to the method of zero mode projection. Obviously, our considerations apply to the effective model with one degree of freedom, yet the relevant proof applies for arbitrary nonlinearity described by $V(\phi)$ and arbitrary form of the heterogeneity in the model.

Finally, let us also notice that naturally, in the case where $\alpha=0$ and $\Gamma=0$, generally (at the level of field equations as well as effective equations) the approach based on the nonconservative Lagrangian is equivalent to the approach based on the conservative Lagrangian. In this case the nonconservative contribution R is equal to zero, so Eq. (32) reduces to Eq. (A1), showing the equivalence of the two models. Accordingly, in this case, all three approaches are equivalent.

[1] R. McLachlan, A gallery of constant-negative-curvature surfaces, Math. Intell. **16**, 31 (1994).

[2] J. Frenkel and T. Kontorova, On the theory of plastic deformation and twinning, Acad. Sci. U.S.S.R. J. Phys. **1**, 137 (1939).

[3] Y. S. Kivshar and B. A. Malomed, Dynamics of solitons in nearly integrable systems, Rev. Mod. Phys. **61**, 763 (1989).

[4] J. Cuevas-Maraver, P. Kevrekidis, and F. Williams, *The Sine-Gordon Model and Its Applications* (Springer, Cham, 2014).

[5] V. Zharnitsky, I. Mitkov, and M. Levi, Parametrically forced sine-Gordon equation and domain wall dynamics in ferromagnets, Phys. Rev. B **57**, 5033 (1998).

[6] J. K. Kjems and M. Steiner, Evidence for Soliton Modes in the One-Dimensional Ferromagnet $CsNiF_3$, Phys. Rev. Lett. **41**, 1137 (1978).

[7] L. J. de Jongh, C. A. M. Mulder, R. M. Cornelisse, A. J. van Duyneveldt, and J. P. Renard, Energy Absorption from an Oscillating Magnetic Driving Field by Soliton Motions in the Quasi One-Dimensional Ferromagnet $[(CH_3)_4N]NiCl_3$ (TMNC), Phys. Rev. Lett. **47**, 1672 (1981).

[8] M. Steiner, K. Kakurai, and J. K. Kjems, Experimental study of the spindynamics in the 1-D-ferromagnet with planar anisotropy, $CsNiF_3$, in an external magnetic field, Z. Phys. B **53**, 117 (1983).

[9] A. Scott, J. C. Eilbeck, J. D. Gibbon, and H. C. Morris, Solitons and nonlinear wave equations, SIAM Rev. **26**, 293 (1984).

[10] J. Pouget and G. A. Maugin, Solitons and electroacoustic interactions in ferroelectric crystals. I. Single solitons and domain walls, Phys. Rev. B **30**, 5306 (1984).

[11] J. Pouget and G. A. Maugin, Solitons and electroacoustic interactions in ferroelectric crystals. II. Interactions of solitons and radiations, Phys. Rev. B **31**, 4633 (1985).

[12] S. Bugaychuk, L. Kovács, G. Mandula, K. Polgár, and R. A. Rupp, Wave-mixing solitons in ferroelectric crystals, Radiat. Eff. Defects Solids **157**, 995 (2002).

[13] L. Lam, Solitons and field induced solitons in liquid crystals, in *Solitons in Liquid Crystals*, Partially Ordered Systems, edited by L. Lam and J. Prost (Springer, New York, 1992).

[14] J. Cuevas, L. Q. English, P. G. Kevrekidis, and M. Anderson, Discrete Breathers in a Forced-Damped Array of Coupled Pendula: Modeling, Computation, and Experiment, Phys. Rev. Lett. **102**, 224101 (2009).

[15] B. Josephson, Possible new effects in superconductive tunnelling, Phys. Lett. **1**, 251 (1962).

[16] P. W. Anderson and J. M. Rowell, Probable Observation of the Josephson Superconducting Tunneling Effect, Phys. Rev. Lett. **10**, 230 (1963).

[17] A. Barone and G. Paternò, *Physics and Application of the Josephson Effect* (John Wiley & Sons, New York, 1982).

[18] B. A. Malomed, in *The Sine-Gordon Model and Its Applications: From Pendula and Josephson Junctions to Gravity and High-Energy Physics*, edited by J. Cuevas-Maraver,

P. G. Kevrekidis, and F. Williams (Springer International Publishing, Cham, 2014), pp. 1–30.
[19] A. I. Braginski, Superconductor electronics: Status and outlook, J. Supercond. Novel Magn. **32**, 23 (2019).
[20] D. W. McLaughlin and A. C. Scott, Perturbation analysis of fluxon dynamics, Phys. Rev. A **18**, 1652 (1978).
[21] A. Golubov, A. Ustinov, and I. Serpuchenko, Soliton dynamics in inhomogeneous Josephson junction: Theory and experiment, Phys. Lett. A **130**, 107 (1988).
[22] G. Mkrtychyan and V. Shmidt, On the radiation from inhomogeneous Josephson junction, Solid State Commun. **30**, 783 (1979).
[23] B. A. Malomed, Motion of a kink in a spatially modulated sine-Gordon system, Phys. Lett. A **144**, 351 (1990).
[24] T. Dobrowolski and A. Jarmoliński, Josephson junction with variable thickness of the dielectric layer, Phys. Rev. E **101**, 052215 (2020).
[25] A. Demirkaya, D. J. Frantzeskakis, P. G. Kevrekidis, A. Saxena, and A. Stefanov, Effects of parity-time symmetry in nonlinear Klein-Gordon models and their stationary kinks, Phys. Rev. E **88**, 023203 (2013).
[26] P. G. Kevrekidis, Variational method for nonconservative field theories: Formulation and two $\mathcal{PT}$-symmetric case examples, Phys. Rev. A **89**, 010102(R) (2014).
[27] A. Demirkaya, T. Kapitula, P. Kevrekidis, M. Stanislavova, and A. Stefanov, On the spectral stability of kinks in some-symmetric variants of the classical Klein–Gordon field theories, Stud. Appl. Math. **133**, 298 (2014).
[28] V. V. Konotop, J. Yang, and D. A. Zezyulin, Nonlinear waves in $\mathcal{PT}$-symmetric systems, Rev. Mod. Phys. **88**, 035002 (2016).
[29] A. Benabdallah, J. G. Caputo, and A. C. Scott, Exponentially tapered Josephson flux-flow oscillator, Phys. Rev. B **54**, 16139 (1996).
[30] A. Kemp, A. Wallraff, and A. Ustinov, Josephson vortex qubit: Design, preparation and read-out, Phys. Stat. Sol. (b) **233**, 472 (2002).
[31] A. Kemp, A. Wallraff, and A. Ustinov, Testing a state preparation and read-out protocol for the vortex qubit, Physica C **368**, 324 (2002).
[32] D. R. Gulevich and F. V. Kusmartsev, Flux Cloning in Josephson Transmission Lines, Phys. Rev. Lett. **97**, 017004 (2006).
[33] J.-G. Caputo and D. Dutykh, Nonlinear waves in networks: Model reduction for the sine-Gordon equation, Phys. Rev. E **90**, 022912 (2014).
[34] R. Monaco, Engineering double-well potentials with variable-width annular Josephson tunnel junctions, J. Phys.: Condens. Matter **28**, 445702 (2016).
[35] T. Dobrowolski, Curved Josephson junction, Ann. Phys. **327**, 1336 (2012).
[36] J. Gatlik and T. Dobrowolski, Modeling kink dynamics in the sine–Gordon model with position dependent dispersive term, Physica D **428**, 133061 (2021).
[37] T. Dobrowolski, Kink motion in a curved Josephson junction, Phys. Rev. E **79**, 046601 (2009).
[38] R. Boesch and C. R. Willis, Exact determination of the Peierls-Nabarro frequency, Phys. Rev. B **39**, 361 (1989).
[39] R. Boesch, C. R. Willis, and M. El-Batanouny, Spontaneous emission of radiation from a discrete sine-Gordon kink, Phys. Rev. B **40**, 2284 (1989).
[40] R. Carretero-González *et al.*, Kink–antikink stripe interactions in the two–dimensional sine–Gordon equation, Commun. Nonlin. Sci. Numer. Simul. **109**, 106123 (2022).
[41] C. Elphick, E. Meron, and E. A. Spiegel, Patterns of propagating pulses, SIAM J. Appl. Math. **50**, 490 (1990).
[42] C. R. Galley, Classical Mechanics of Nonconservative Systems, Phys. Rev. Lett. **110**, 174301 (2013).
[43] F. Marchesoni, Solitons in a random field of force: A Langevin equation approach, Phys. Lett. A **115**, 29 (1986).
[44] C. Cattuto, G. Costantini, T. Guidi, and F. Marchesoni, Elastic strings in solids: Discrete kink diffusion, Phys. Rev. B **63**, 094308 (2001).
[45] Z. Fei, Y. S. Kivshar, and L. Vázquez, Resonant kink-impurity interactions in the ϕ^4 model, Phys. Rev. A **46**, 5214 (1992).
[46] C. Adam, K. Oles, T. Romanczukiewicz, and A. Wereszczynski, Spectral Walls in Soliton Collisions, Phys. Rev. Lett. **122**, 241601 (2019).
[47] M. Lizunova, J. Kager, S. de Lange, and J. van Wezel, Emergence of oscillons in kink-impurity interactions, J. Phys. A: Math. Theor. **54**, 315701 (2021).
[48] P. G. Kevrekidis, I. Danaila, J.-G. Caputo, and R. Carretero-González, Planar and radial kinks in nonlinear Klein-Gordon models: Existence, stability, and dynamics, Phys. Rev. E **98**, 052217 (2018).

PHYSICAL REVIEW E **109**, 024205 (2024)

Effective description of the impact of inhomogeneities on the movement of the kink front in 2 + 1 dimensions

Jacek Gatlik,[1] Tomasz Dobrowolski,[2] and Panayotis G. Kevrekidis[3]
[1]*Doctoral School, University of the National Education Commission in Krakow, 30-084 Krakow, Poland*
[2]*Department of Computer Physics and Quantum Computing, University of the National Education Commission in Krakow, 30-084 Krakow, Poland*
[3]*Department of Mathematics and Statistics, University of Massachusetts, Amherst, Massachusetts 01003-4515, USA*

(Received 8 November 2023; revised 2 January 2024; accepted 10 January 2024; published 9 February 2024)

In the present work we explore the interaction of a quasi-one-dimensional line kink of the sine-Gordon equation moving in two-dimensional spatial domains. We develop an effective equation describing the kink motion, characterizing its center position dynamics as a function of the transverse variable. The relevant description is valid both in the Hamiltonian realm and in the nonconservative one bearing gain and loss. We subsequently examine a variety of different scenarios, without and with a spatially dependent heterogeneity. The latter is considered both to be one dimensional (y independent) and genuinely two dimensional. The spectral features and the dynamical interaction of the kink with the heterogeneity are considered and comparison with the effective quasi-one-dimensional description (characterizing the kink center as a function of the transverse variable) is also provided. Generally, good agreement is found between the analytical predictions and the computational findings in the different cases considered.

DOI: 10.1103/PhysRevE.109.024205

I. INTRODUCTION

For years, nonlinear field theories have attracted the attention of many researchers. The reasons for this are twofold. First, they appear in the description of physical [1–6], biological [7–9], as well as chemical [10] systems. Second, unlike linear systems, regardless of the practical context, their behavior is far more interesting and challenging to explore. Some of the best-known and well-studied nonlinear field models are the Korteweg–de Vries (KdV) equation [11,12], the nonlinear Schrödinger equation [13,14], and the sine-Gordon model [15]. As shown, these models in $1 + 1$ dimensions are integrable by means of the inverse scattering method [16–18]. The latter allows one, for such integrable models, to obtain, based on appropriately behaving initial data at spatial infinity, the configuration of the fields at any later instant of time. In particular, for appropriately chosen initial data, the explicit analytical form of the soliton solutions can be obtained and the dynamics of such fundamental nonlinear coherent structures can be explored in time. An excellent description of soliton dynamics can be found in classic textbooks on the subject [19–21].

The interest of this paper is focused on the sine-Gordon model. Often, in practical contexts, this model appears in somewhat modified (i.e., perturbed), potentially relevant experimentally versions. These modifications have their origin in the existence of external forcing, dissipation in realistic physical systems or various types of inhomogeneities [22–27]. These modifications, though, significantly affect the integrability property; however, they do not affect the existence of kink solutions. Such models are often referred to as nearly integrable ones. The situation becomes even more complicated when passing from $1 + 1$ to $2 + 1$, as well as to a larger number of dimensions. In the case of the sine-Gordon model, even without any modifications, such higher-dimensional settings are not integrable within the framework of the inverse scattering method [28], nor does the model have the properties that should be satisfied for proving integrability based on the Painlevé test [29–31]. Despite these difficulties, various solutions have been constructed, among others, in the form of a kink front. For instance, a three linked soliton wave-front solution was found which preserves its initial triangle area under evolution [32]. Indeed, it is relevant to recall here that the quasi-one-dimensional (quasi-1D) line kink (i.e., the kink homogeneous in the transverse direction) is trivially still a solution in the higher-dimensional setting.

In higher dimensions, part of the challenge towards describing the dynamics of the solitary waves concerns the fact that the position of the coherent structure is dependent both on the time variable and the "transverse" spatial variable. For a kink, e.g., along the x direction, its center will be y dependent, while for a radial kink, its center can be varying azimuthally. Moreover, kink-antikink interactions have also been studied in the $2 + 1$-dimensional model [33]. The behavior of a kink with radial symmetry has been intriguing to researchers since the early days of soliton theory [34,35]. A fairly interesting phenomenon observed for radial configurations is their alternating expansion and contraction. However, it turns out that in two dimensions such configurations can be destroyed at the origin [36]. Moreover, the evolution of long-lived configurations of breather form has also been studied in the context of the sine-Gordon model in $2 + 1$ dimensions [37]. Another interesting potential byproduct of the radial dynamics can be the formation of breather as a result of collisions with edges as studied in Ref. [38]. Among other things, the influence of various types of inhomogeneities and modifications of the sine-Gordon model on the evolution of the kink front has continued to attract the attention of researchers; see, e.g., the discussions of Refs. [24,39]. New studies devoted to the effect of inhomogeneities on kink dynamics in $2+1$-dimensional systems can also be found in Refs. [40–42].

In the present article, we consider the behavior of the deformed kink front in the presence of the inhomogeneities. The way in which these inhomogeneities enter the equation of motion is motivated by studies conducted in earlier works by some of the present authors [43] for the $1+1$ case and the quasi-$1+1$-dimensional Josephson junction. In this study, we explore how the existence of the mentioned modifications of the sine-Gordon equation have its origin in the curvature of the junction. Our goal, more concretely, is to investigate the stability of static kink fronts in the presence of spatial inhomogeneities in the more computationally demanding and theoretically richer $2+1$-dimensional setting, extending significantly our recent results of the $1+1$-dimensional case. In order to do so, we obtain and test an effective reduced model, leveraging the fundamental nonconservative variational formalism presented in Refs. [44,45]. This formalism enables the formulation of a Lagrangian description of systems with dissipation. An important part of this approach is the introduction of a nonconservative potential in addition to conservative ones giving the possibility of formulating a nonconservative Lagrangian. The Euler-Lagrange equations are then obtained based on this Lagrangian. Here our theoretical emphasis is on utilizing this methodology to provide a reduced ($1+1$-dimensional) description of the center of the kink as a function of the transverse variable.

The work is organized as follows. In the next section, we will define the problem under consideration, namely the evolution sine-Gordon $2+1$-dimensional kinks in the presence of heterogeneities in the medium. We will also construct the effective approximate model obtained based on the nonconservative Lagrangian approach. Section III is divided into four subsections. In the first one, in order to check the obtained effective model and numerical procedures, we analyze the motion of the kink front in a homogeneous system but with dissipation and external forcing. Section III B of this part contains a study of the front propagation in the presence of inhomogeneities homogeneous along the transverse direction. In Sec. III C, we include an analysis of the motion of the kink in a system whose equation has a form analogous to that describing a curved Josephson junction but with an inhomogeneity having a functional dependence on the variable normal to the direction of kink motion. Section IV contains an analysis of the stability of the kink in the presence of the spatial inhomogeneity in the form of potential well and barrier. In Sec. V, we summarize our findings and present our conclusions, as well as some directions for further research efforts. Analytical results on this issue are located in Appendices A, B, and C. The last section contains remarks.

II. MODEL AND THEORETICAL ANALYSIS

A. System description

In the present article we study the perturbed sine-Gordon model in $2+1$ dimensions in the form:

$$\partial_t^2\phi + \alpha\partial_t\phi - \partial_x(\mathcal{F}(x,y)\partial_x\phi) - \partial_y^2\phi + \sin\phi = -\Gamma, \quad (1)$$

where the function $\mathcal{F}(x,y)$ represents the inhomogeneity present in the system, α describes the dissipation caused by the quasiparticle currents, and Γ is the bias current in the Josephson junction setup [39]. For the inhomogeneity, we will typically assume $\mathcal{F}(x,y) = 1 + \varepsilon g(x,y)$, where ε is a small control parameter, while $g(x,y)$ reflects the corresponding spatial variation. To preserve the elliptic character of the spatial portion of the linear operator in the equation we assume that the $|\varepsilon g(x,y)|$ is for any x and y distinctively smaller than 1. When considering the motion of a kink in this two-dimensional system, we assume periodic boundary conditions along the second dimension parametrized by the variable y,

$$\phi(x, y_{\min}, t) = \phi(x, y_{\max}, t),$$
$$\partial_t\phi(x, y_{\min}, t) = \partial_t\phi(x, y_{\max}, t).$$

The initial velocity of the kink when Γ is equal to zero is selected arbitrarily. On the other hand, if both quantities α and Γ are different from zero, then the initial velocity is assumed equal to

$$u_s = \frac{1}{\sqrt{1+\left(\frac{4\alpha}{\pi\Gamma}\right)^2}}. \quad (2)$$

This value corresponds to the movement at the stationary speed obtained in the classic work of Ref. [22]. We use this value because at the initial time the kink is sufficiently far away from the inhomogeneity. With such a large distance at the initial position of the front, the $\mathcal{F}$ function is approximately equal to 1. In this work, we will describe the movement of the kink front, the shape of which will have different forms at the initial instant and which will encounter different types of heterogeneities during propagation. We propose an effective description of this movement within a $1+1$-dimensional model, characterizing the center motion as a function of the transverse variable that we now expand on. In our work, we compare the results of the original model and the effective model to determine the limits of applicability of the proposed simplified description.

B. Nonconservative Lagrangian model

Due to the existence of dissipation in the studied system, we will use the formalism described in the paper [44,45]. The proposed approach introduces a nonconservative Lagrangian in which the variables describing the system are duplicated and an additional term is added to the Lagrangian to account for the nonconservative forces. The variational principle for this Lagrangian only specifies (and matches across acceptable trajectories) the initial data. On the other hand, at the final time, the coordinates and velocities of the two paths are not fixed but for both sets of variables are equal. Doubling the degrees of freedom has this consequence that in addition to the potential function V, one can include an arbitrary function, $\mathcal{R}$ (called nonconservative potential), that couples the two paths. Nonconservative forces present in the system are determined from the potential $\mathcal{R}$. The $\mathcal{R}$ function is responsible for the energy lost by the system. This formalism, in Ref. [26], was applied to describe the $\mathcal{PT}$-symmetric variants of field theories (bearing balanced gain and loss). The referred modification introduced into the field models simultaneously preserves the parity symmetry (P, i.e., $x \to -x$) and the time-reversal symmetry (T, i.e., $t \to -t$). In particular, this approach has been applied to solitonic models such as ϕ^4 and sine-Gordon.

In the current work, we consider the system described by Eq. (1). For $\alpha = 0$ and $\Gamma = 0$, this equation can be obtained from the Lagrangian density

$$\mathcal{L}(\phi, \partial_t\phi, \partial_x\phi, \partial_y\phi) = \tfrac{1}{2}(\partial_t\phi)^2 - \tfrac{1}{2}\mathcal{F}(x, y)(\partial_x\phi)^2 - \tfrac{1}{2}(\partial_y\phi)^2 - V(\phi). \quad (3)$$

The nonconservative Lagrangian density is formed from the Lagrangian density (3) by doubling the number of degrees of freedom,

$$\mathcal{L}_N = \mathcal{L}(\phi_1, \partial_t\phi_1, \partial_x\phi_1, \partial_y\phi_1) - \mathcal{L}(\phi_2, \partial_t\phi_2, \partial_x\phi_2, \partial_y\phi_2) + \mathcal{R}. \quad (4)$$

Much more convenient variables to describe our system with dissipation are the field variables ϕ_+ and ϕ_-. The relationship between the variables ϕ_i, ($i = 1, 2$) and ϕ_+, ϕ_- is of the form $\phi_1 = \phi_+ + \frac{1}{2}\phi_-$ and $\phi_2 = \phi_+ - \frac{1}{2}\phi_-$. The main advantage of using new variables is that in the physical limit (indicated by the characters PL) the ϕ_+ variable reduces to the original variable ϕ while the ϕ_- variable becomes equal to zero and thereby disappears from the description. In the new variables, the nonconservative Lagrangian density is of the form

$$\mathcal{L}_N = (\partial_t\phi_+)(\partial_t\phi_-) - \mathcal{F}(x, y)(\partial_x\phi_+)(\partial_x\phi_-) - (\partial_y\phi_+)(\partial_y\phi_-) - V\left(\phi_+ + \frac{1}{2}\phi_-\right) + V\left(\phi_+ - \frac{1}{2}\phi_-\right) - \alpha\phi_-\partial_t\phi_+ - \Gamma\phi_-. \quad (5)$$

The variational scheme proposed in the paper [44] leads to a Euler-Lagrange equation,

$$\left\{\partial_\mu\left[\frac{\partial\mathcal{L}_N}{\partial(\partial_\mu\phi_-)}\right] - \frac{\partial\mathcal{L}_N}{\partial\phi_-}\right\}_{\text{PL}} = 0, \quad (6)$$

where the subscript μ denotes the partial derivatives with respect to the variables $x^\mu = (t, x, y)$. A particularly convenient form of the field equation is the one that separates the effect of the existence of a nonconservative potential from the rest of the equation,

$$\partial_\mu\left[\frac{\partial\mathcal{L}}{\partial(\partial_\mu\phi)}\right] - \frac{\partial\mathcal{L}}{\partial\phi} = \left\{\frac{\partial\mathcal{R}}{\partial\phi_-} - \partial_\mu\left[\frac{\partial\mathcal{R}}{\partial(\partial_\mu\phi_-)}\right]\right\}_{\text{PL}}. \quad (7)$$

Inserting the Lagrangian density (3) into the above equation and using the form of the function $\mathcal{R} = -\alpha\phi_-\partial_t\phi_+ - \Gamma\phi_-$, we reproduce Eq. (1).

So far, our calculations are exact (i.e., no approximations have been made). Hereafter, we will use a kinklike ansatz in the field $\phi(x, y, t)$, so as to construct an effective (approximate) $1 + 1$-dimensional reduced model describing the dynamics of the kink center. This is a significant step in the vein of dimension reduction; however, it comes at the expense of assuming that the entire field consists of a fluctuating kink (i.e., small radiative wave packets on top of the kink cannot be captured). Nevertheless, this perturbation in the spirit of soliton perturbation theory [24] has a time-honored history of being successful in capturing coherent structure dynamics in such models.

To implement our approach, we introduce a kink ansatz of the form $\phi_i(t, x, y) = K(x - X_i(t, y)) = 4\arctan(e^{x-X_i})$ into the Lagrangian (5) of the field model in $2 + 1$ dimensions and then integrate over the spatial variable x. The resulting effective nonconservative Lagrangian density is as follows:

$$L = L_1 - L_2 + R, \qquad R = R_1 + R_2, \quad (8)$$

where the effective conservative Lagrangian densities are

$$L_1 = \frac{1}{2}M(\partial_t X_1)^2 - \frac{1}{2}\int_{-\infty}^{+\infty}\mathcal{F}(x, y)[K'(x - X_1)^2]dx - \frac{1}{2}M(\partial_y X_1)^2, \quad L_2 = \frac{1}{2}M(\partial_t X_2)^2 - \frac{1}{2}\int_{-\infty}^{+\infty}\mathcal{F}(x, y)[K'(x - X_2)^2]dx - \frac{1}{2}M(\partial_y X_2)^2,$$

and we denote the mass of the kink as $M = \int_{-\infty}^{+\infty}K'(x - X_i)^2 dx = 8$. On the other hand, the two parts of the nonconservative effective potential are, respectively, equal to

$$R_1 = \frac{1}{2}\alpha\int_{-\infty}^{+\infty}[K(x - X_1) - K(x - X_2)] \times [K'(x - X_1)\partial_t X_1 + K'(x - X_2)\partial_t X_2]dx,$$

$$R_2 = -\Gamma\int_{-\infty}^{+\infty}[K(x - X_1) - K(x - X_2)]dx.$$

By analogy with Eq. (7), the (approximate) effective field-theoretic equation for $X(y, t)$ is of the form

$$\partial_t\left[\frac{\partial L}{\partial(\partial_t X)}\right] + \partial_y\left[\frac{\partial L}{\partial(\partial_y X)}\right] - \frac{\partial L}{\partial X} = \left\{\frac{\partial R}{\partial X_-} - \partial_t\left[\frac{\partial R}{\partial(\partial_t X_-)}\right] - \partial_y\left[\frac{\partial R}{\partial(\partial_y X_-)}\right]\right\}_{\text{PL}}, \quad (9)$$

where we use the variables $X_+ = (X_1 + X_2)/2$ and $X_- = X_1 - X_2$ to write the nonconservative potential. Note that the left-hand side of the equation describes a situation in which there are no nonconservative forces, while the right-hand side introduces dissipation and forcing into the system. In Eq. (9), L is a simple conservative Lagrangian density written in terms of the physical variable X,

$$L = \frac{1}{2}M(\partial_t X)^2 - \frac{1}{2}\varepsilon\int_{-\infty}^{+\infty}g(x, y)[K'(x - X)]^2dx - \frac{1}{2}M(\partial_y X)^2. \quad (10)$$

In this formula, we used the decomposition of the $\mathcal{F}$ function into a regular part and a small perturbation, i.e., $\mathcal{F}(x, y) = 1 + \varepsilon g(x, y)$. On the other hand, the function R appearing on the right-hand side of the equation is written in auxiliary variables X_+ and X_-. Note that the left-hand side of Eq. (9) contains the full information about the inhomogeneities present in the system,

$$M\partial_t^2 X - \varepsilon \int_{-\infty}^{+\infty} g(x, y)K'(x - X)K''(x - X)dx - M\partial_y^2 X = \left\{\frac{\partial R}{\partial X_-} - \partial_t\left[\frac{\partial R}{\partial(\partial_t X_-)}\right] - \partial_y\left[\frac{\partial R}{\partial(\partial_t X_-)}\right]\right\}_{\mathrm{PL}}. \tag{11}$$

In order to calculate the right-hand side of the effective field equation, we rewrite the nonconservative potential R to the $X_\pm$ variables,

$$R_1 = \frac{1}{2}\alpha \int_{-\infty}^{+\infty}\left[K\left(x - X_+ - \frac{1}{2}X_-\right) - K\left(x - X_+ + \frac{1}{2}X_-\right)\right]$$
$$\times\left[K'\left(x - X_+ - \frac{1}{2}X_-\right)\left(X_{+t} + \frac{1}{2}X_{-t}\right) + K'\left(x - X_+ + \frac{1}{2}X_-\right)\left(X_{+t} - \frac{1}{2}X_{-t}\right)\right]dx,$$
$$R_2 = -\Gamma \int_{-\infty}^{+\infty}\left[K\left(x - X_+ - \frac{1}{2}X_-\right) - K\left(x - X_+ + \frac{1}{2}X_-\right)\right]dx.$$

We then determine the classical limit of the right-hand side of Eq. (11). In the course of the calculations, we use the asymptotic values of the kink solution. The Euler-Lagrange equation defining the effective 1 + 1-dimensional model is thus identified as

$$M\partial_t^2 X - M\partial_y^2 X - \varepsilon \int_{-\infty}^{+\infty} g(x, y)K'(x - X)K''(x - X)dx = -\alpha M\partial_t X + 2\pi\Gamma. \tag{12}$$

Let us consider the function g being the product of $g(x, y) = p(x)q(y)$, where $p(x)$ corresponds to the inhomogeneity occurring across the direction of the kink motion and $q(y)$ may represent the gaps occurring within this inhomogeneity along the transverse direction. The function $q(y)$ does not depend on x and therefore we can exclude it before the sign of the integral and perform the explicit integration of the expression containing the function $p(x)$. In the first example, the p function is the difference of the step functions $p(x) = \frac{1}{2}[\Theta(x + \frac{h}{2}) - \Theta(x - \frac{h}{2})]$. This form of the p function makes the inhomogeneity exactly localized between the points $x = -h/2$ and $x = h/2$. The Euler-Lagrange equation in this case is

$$\partial_t^2 X + \alpha\partial_t X - \partial_y^2 X + \frac{1}{8}\varepsilon q(y)\left[\mathrm{sech}\left(\frac{h}{2} + X\right)^2 - \mathrm{sech}\left(\frac{h}{2} - X\right)^2\right] = \frac{1}{4}\pi\Gamma. \tag{13}$$

The second example concerns inhomogeneity described by a continuous function

$$p(x) = \frac{1}{2}\left[\tanh\left(x + \frac{h}{2}\right) - \tanh\left(x - \frac{h}{2}\right)\right]. \tag{14}$$

For large values of h, this function can be successfully approximated by a combination of step functions of the form $p(x) = \frac{1}{2}[\Theta(x + \frac{h}{2}) - \Theta(x - \frac{h}{2})]$. However, for smaller values of h, some differences are observed. The effective field equation in this case has a slightly more complex form,

$$\partial_t^2 X + \alpha\partial_t X - \partial_y^2 X + \frac{1}{2}\varepsilon q(y)\left[\frac{\left(\frac{h}{2} + X\right)\coth\left(\frac{h}{2} + X\right) - 1}{\sinh^2\left(\frac{h}{2} + X\right)} - \frac{\left(\frac{h}{2} - X\right)\coth\left(\frac{h}{2} - X\right) - 1}{\sinh^2\left(\frac{h}{2} - X\right)}\right] = \frac{1}{4}\pi\Gamma. \tag{15}$$

This effective 1 + 1-dimensional model is the basis for comparisons with predictions of the initial field Eq. (1) in 2 + 1 dimensions.

III. NUMERICAL RESULTS

This section will be devoted to the comparison of the predictions resulting from the effective 1 + 1-dimensional model and the full 2 + 1-dimensional field model. Our goal is to examine the compatibility of the two descriptions and determine the range of applicability of the approximate model.

A. Kink propagation in the absence of inhomogeneities

Initially, we performed tests to check the compatibility of the two descriptions for a homogeneous system, i.e., for a system for which the parameter representing the strength of inhomogeneity ε is equal to zero. The first check was carried out for an initial condition with a kink of the form of a straight line perpendicular to the x direction, i.e., direction of movement of the kink. The propagation of the kink front is shown in Fig. 1. The left panel shows the results obtained from the field model of Eq. (1). The blue color represents the area for which $\phi < \pi$, and the yellow color corresponds to $\phi > \pi$. The areas are separated by the red line $\phi(t, x, y) = \pi$. We identify this line with the kink front. This panel shows the location of the front sequentially at moments $t = 0, 30, 60, 90, 120$. Each snapshot on the left panel shows a sector of the system located in the interval $y \in [-30, 30]$ with an appropriately selected x interval. It should be noted that the simulations, nevertheless, were conducted on a much wider interval x, i.e., $x \in [-70, 70]$. At the ends of the interval (i.e., for $x = \pm 70$), Dirichlet boundary conditions corresponding to a single-kink topological sector were assumed. The right panel contains a comparison of the evolution of the kink front obtained from the field equation (solid red line) and that obtained from the approximate model (dotted blue line) given by Eq. (15). The comparison was made at instants identical to those on the left panel. Due to the very good agreement, the blue line is barely visible. The simulation was performed for an initial velocity of the kink with $u_0 = u_s = 0.229339$. It can be verified that

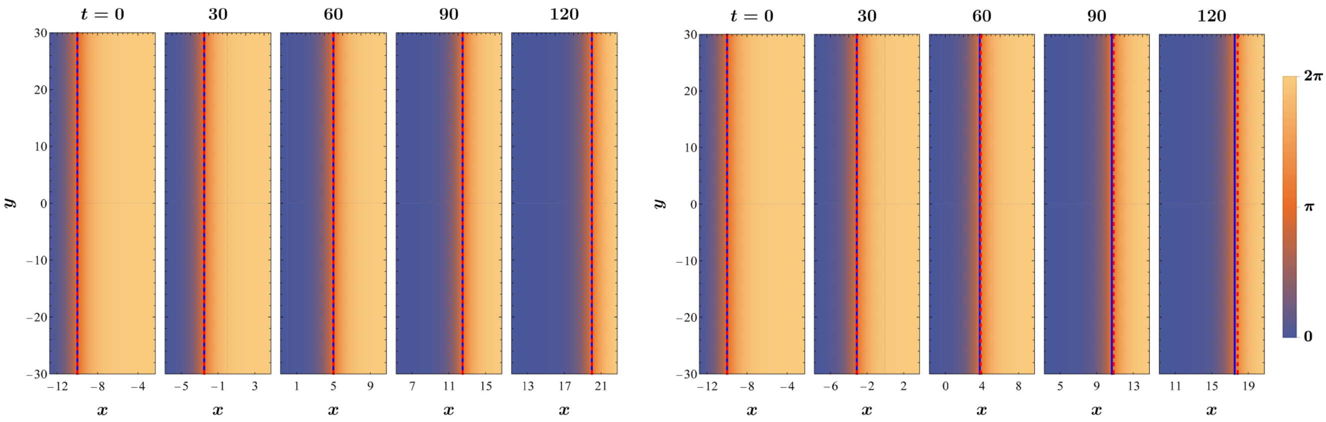

FIG. 1. Comparison of the position of the center of the kink for the results obtained from the full field model and the approximate model. On the left the parameters in the figures shown have values $u = 0.25$, $\Gamma = 0$, and $\alpha = 0$ and on the right $\Gamma = 0.003$, $\alpha = 0.01$ while velocity is equal to u_s according to (2). In both cases $\varepsilon = 0$. The dashed red line is the position of the center of the kink according to the approximate model, while the blue line corresponds to the center of the kink from the solution of the full field model.

this is the steady-state velocity resulting from Eq. (2) for the dissipation constant $\alpha = 0.01$ and bias current $\Gamma = 0.003$. In this work, whenever $\Gamma \neq 0$ and $\alpha \neq 0$ we take the steady-state velocity resulting from Eq. (2) as the initial velocity. It is worth noting that if we were to assume a velocity below the steady-state velocity during motion, then this velocity will increase to the steady-state value due to the existence of an unbalanced driving force in the form of a bias current. On the other hand, if we assume an initial velocity above the stationary velocity, then due to the unbalanced dissipation there will be a slowdown of the front to the stationary velocity. Finally, the initial position of the kink is taken equal to $X_0 = -10$.

A slightly different situation is illustrated in Fig. 2. The first difference is that the bias current is zero $\Gamma = 0$, and so instead of using Eq. (2) we can choose the initial velocity arbitrarily (here we take $u_0 = 0.25$). The second difference is that the shape of the front is deformed at the initial time. Here we assume the sinusoidal form of the deformation described by the formula

$$X(y, t = 0) = X_0 + \lambda \sum_{n=1}^{N} \sin\left(\frac{2\pi n y}{L_y}\right). \tag{16}$$

where $L_y = 60$ is the width of the system along the direction of the y variable. In this figure we show the evolution of the initial configuration with $N = 2$. This is selected with the mindset that any functional form of $X(y, t = 0)$ should, in principle, be decomposable in (such) Fourier modes. The value of X_0 as before is $X_0 = -10$, while the amplitude of the deformation is $\lambda = 0.5$. The value of the dissipation constant in the system is $\alpha = 0.01$. As before, there are no inhomogeneities in the system, i.e., $\varepsilon = 0$. The method of presenting the results is similar to that used in Fig. 1. The left panel illustrates the field configurations obtained from Eq. (1), sequentially at instants $t = 0, 30, 60, 90, 120$. The red solid line represents the kink front at the listed moments of time. On the right panel, the kink positions shown on the left panel (red lines) are compared with those obtained from the effective

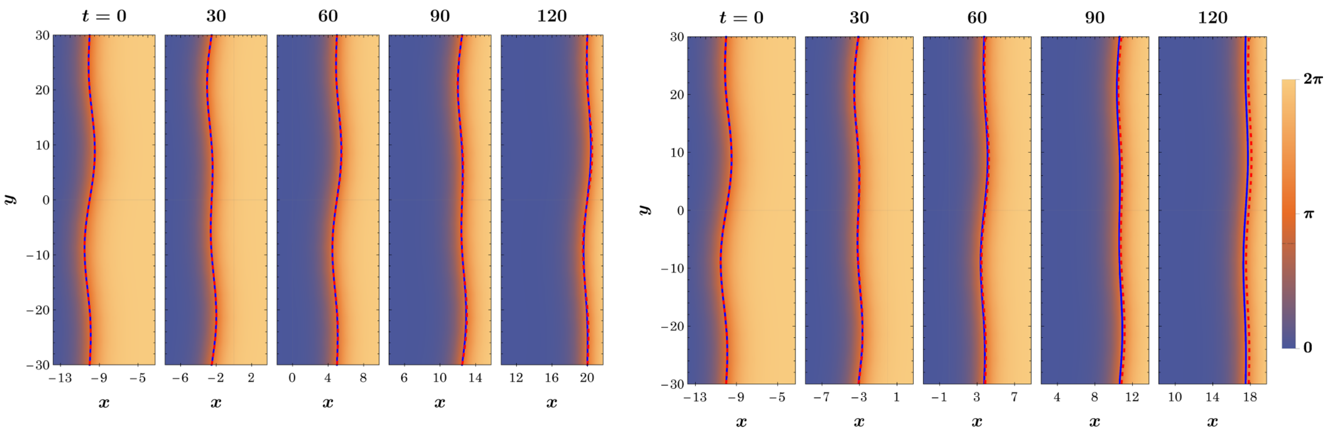

FIG. 2. Comparison of the position of the center of the kink for the results obtained from the full field model and the approximate model with a modification of the initial position of the kink according to Eq. (16) for $N = 2$. On the left the parameters in the figures shown have values $u = 0.25$, $\Gamma = 0$, and $\alpha = 0$ and on the right $\Gamma = 0.003$, $\alpha = 0.01$, and u_s. In both cases $\varepsilon = 0$ and $\lambda = 0.5$.

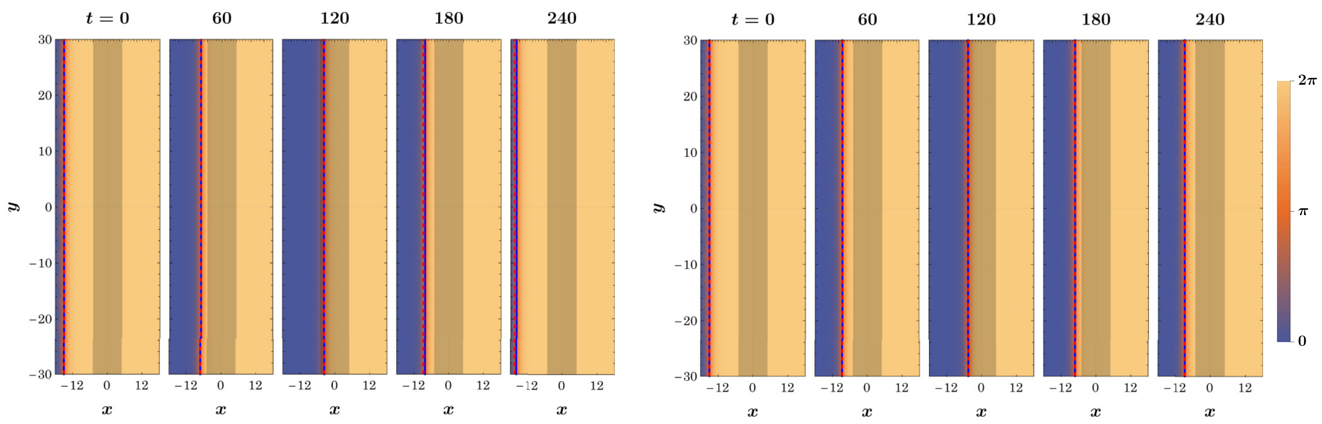

FIG. 3. Comparison of the position of the center of the kink for the results obtained from the full field model and the approximate model. On the left the velocity has value $u = 0.13$, and on the right $\Gamma = 0.00135$, $\alpha = 0.01$, and u_s. In both cases $\varepsilon = 0.01$.

model (15). The results of the effective model are represented by blue dashed lines. As can be seen, until $t = 120$ there are no apparent differences between the results of the field model and the approximate model.

B. Propagation of the front in the presence of an x-axis-directed inhomogeneity

In this subsection, we will assume that the parameter ε in Eqs. (1) and (15) is nonzero. Such an assumption means that there is inhomogeneity in the system. In this work, we will describe the effect of inhomogeneity described by the function $g(x, y) = p(x)q(y)$, where $p(x)$ is given by Eq. (14). In this first introduction of the inhomogeneity, we will assume that $q(y) = 1$, which means that the inhomogeneity is in the form of an elevation of height ε, orthogonal to the x direction (which defines the direction of the kink movement). The spatial size of the inhomogeneity along the x direction is approximated by the parameter h appearing in Eq. (14). In the simulations in this section, we assume $h = 10$ and $\varepsilon = 0.01$. We study three types of kink dynamics.

In the first case, we consider the reflection of the kink from a barrier. The course of this process is shown in Fig. 3. The case of reflection in the absence of external forcing ($\Gamma = 0$) and dissipation ($\alpha = 0$) is shown in the left panel. The initial condition in this case is a straight kink front with a velocity $u = 0.13$. As in the previous section, the kink front is identified with the line $\phi(t, x, y) = \pi$ [obtained from the field Eq. (1)]. The front is represented by the red line. Regions with $\phi(t, x, y) < \pi$ are once again represented as blue areas and $\phi(t, x, y) > 0$ as yellow. On the other hand, the position of the front determined from Eq. (15) is represented by the blue dashed line. The gray area represents the position of the inhomogeneity. The figure shows the position of the front at instants $t = 0, 60, 120, 180$, and 240. The kink at moments $t = 0, 60, 120$ approaches the inhomogeneity while between moments $t = 120$ and $t = 180$ it is reflected and turns around. Finally, at instants between $t = 180$ and $t = 240$ it is already moving towards the initial position. As can be seen, the correspondence of the two descriptions, namely the ones based on Eq. (1) and on Eq. (15), is very good, until $t = 120$, while above this value we observe slight deviations. The right panel shows the same process in the case of occurrence of a dissipation $\alpha = 0.01$ and forcing $\Gamma = 0.00135$ in the system. The course of the front at the same moments as in the left panel also shows very good agreement of the approximate model (15) with the initial model (1), also for $t = 240$. In this figure, the initial velocity of the front is chosen based on the formula (2), i.e., as the stationary velocity. It should be mentioned that the bouncing process in this case is slightly more complex and has an identical (effectively one-dimensional) nature to that described in the one-dimensional case in the paper [43]. It consists of multiple (damped) reflections from the barrier, which eventually ends up stopping before the barrier. As was shown in Ref. [43], this reflects the presence of a stable spiral point at such a location which asymptotically attracts the kink towards the relevant fixed point.

The second case is shown in Fig. 4. The left panel shows the movement of a kink with an initial velocity $u = 0.16$ significantly exceeding the critical speed. In this case, slight deviations are already observed for $t = 120$. On the other hand, the case with dissipation is presented in the right panel. This figure shows a kink front with an initial speed equal to the stationary velocity determined for dissipation $\alpha = 0.01$ and forcing $\Gamma = 0.00185$. In this case, the correspondence of the description obtained from Eq. (1) and Eq. (15) are striking up to $t = 240$. The results obtained in this section are analogous to those described in the paper [43], as the effective motion of the kink is practically one dimensional and the transverse modulation neither plays a critical role to nor destabilizes (as is, e.g., the case in nonlinear Schrödinger type models [46]) the longitudinal motion.

C. Kink propagation for inhomogeneities dependent on both variables

In this section we will consider some examples of heterogeneities bearing a genuinely two-dimensional character, i.e., having a nontrivial dependence not only on the x variable initially aligned with the direction of movement of the kink but also on the y variable, along which the front is initially homogeneous.

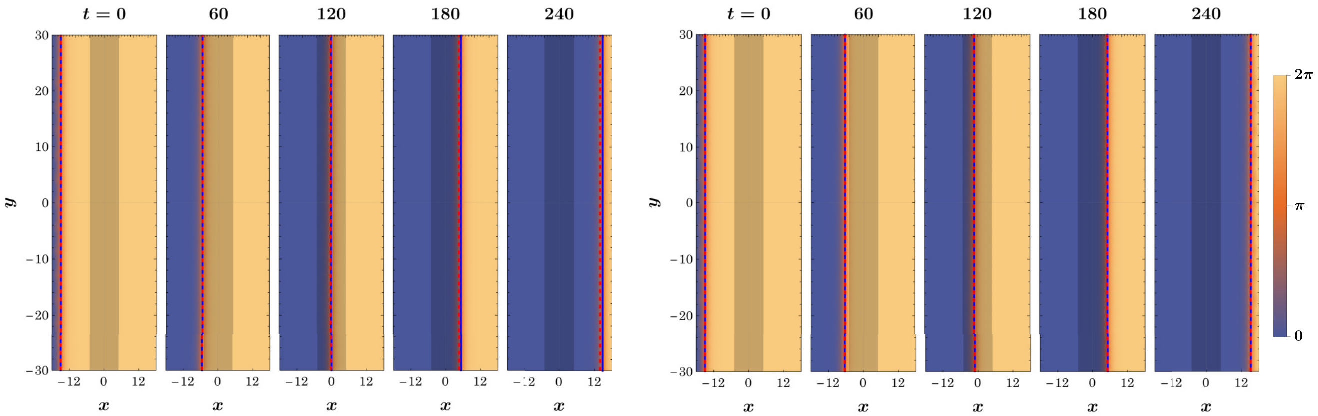

FIG. 4. Comparison of the position of the center of the kink for the results obtained from the full field model and the approximate model. On the left the velocity has value $u = 0.16$, and on the right $\Gamma = 0.00185$, $\alpha = 0.01$, and u_s. In both cases $\varepsilon = 0.01$.

1. Barrier-shaped inhomogeneity

The first example is described by the function $\mathcal{F}(x, y) = 1 + \varepsilon g(x, y) = 1 + \varepsilon p(x)q(y)$. The shape of this function is shown in Fig. 5. In this case, the function $p(x)$ is given by formula (14) while $q(y)$ has the form:

$$q(y) = \frac{1}{2}\left[\tanh\left(y + \frac{d}{2}\right) - \tanh\left(y - \frac{d}{2}\right)\right]. \tag{17}$$

We will consider two cases. In the first case, the kink front passes over the inhomogeneity. In the second case, it is stopped by the inhomogeneity. To be more precise, the kink, in the absence of dissipation and forcing, bounces and returns towards its initial position, while when dissipation and forcing are nonzero the kink stops in front of the inhomogeneity due to the emergence of a stable fixed point there. The results of comparing the initial model (1) with the effective model (12) are very good, as can be seen in Fig. 6. In the simulations, we assumed a parameter describing the strength of the inhomogeneity equal to $\varepsilon = 0.1$. The left panel shows the interaction of the front with the inhomogeneity in the absence of dissipation and forcing. The initial condition in this case is a straight front with a velocity of $u = 0.14$. It can be seen that in the course of the evolution the front deforms (the kink bends around the inhomogeneity, which is represented in the figure as a gray area) and then overcomes it. After crossing the inhomogeneity, the tension of the string (the front of the kink) causes it to vibrate, i.e., it excites a transverse mode of the "kink filament." Obviously, we must remember that local perturbations of the ϕ-field profile can slightly change the distribution of energy density along the kink front. As a consequence of the existence of tension, the string tends to straighten but excess kinetic energy causes it to vibrate in the direction of the motion of the front, in the absence of dissipation and drive. This oscillation persists for a long time because the mechanism of energy reduction associated with its radiation is not very effective. On the other hand, the right panel shows an analogous process in the case where in the system we have a forcing of $\Gamma = 0.0018$ and a dissipation characterized by the coefficient $\alpha = 0.01$. In this case, the initial speed is the stationary velocity determined by the formula (2). The course of the process and the results are analogous to the case without dissipation, i.e., we observe local changes in shape that are similar to the left panel. Nevertheless, after passing over the inhomogeneity, we observe damped vibrations that ultimately lead to straightening of the front, as a result of this damped-driven system's possessing of an attractor (and contrary to the scenario of the conservative Hamiltonian case). The results shown in the figures have also been presented in the form of animations in the associated links. Since in the absence of forcing and dissipation, the mechanism of getting rid of excess energy through radiation is not sufficiently effective, extending the animation time in this case did not lead us to times at which the transverse oscillations of the

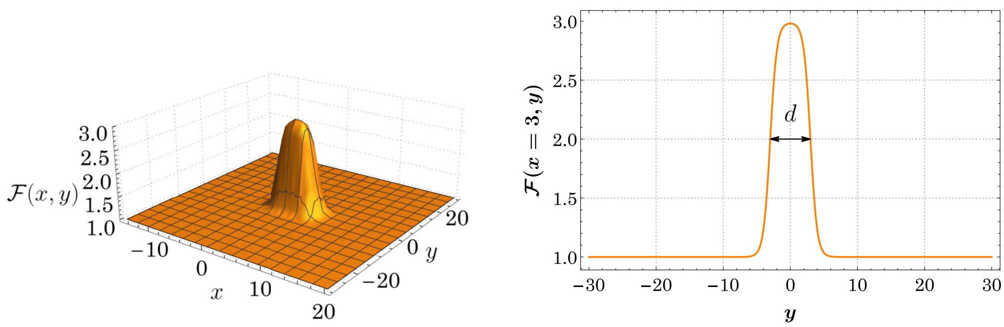

FIG. 5. Left panel presents peak-shaped inhomogeneity $\mathcal{F}(x, y)$, while the right panel shows its section along a line $x = 3$. Both parameters h and d are equal to 6.

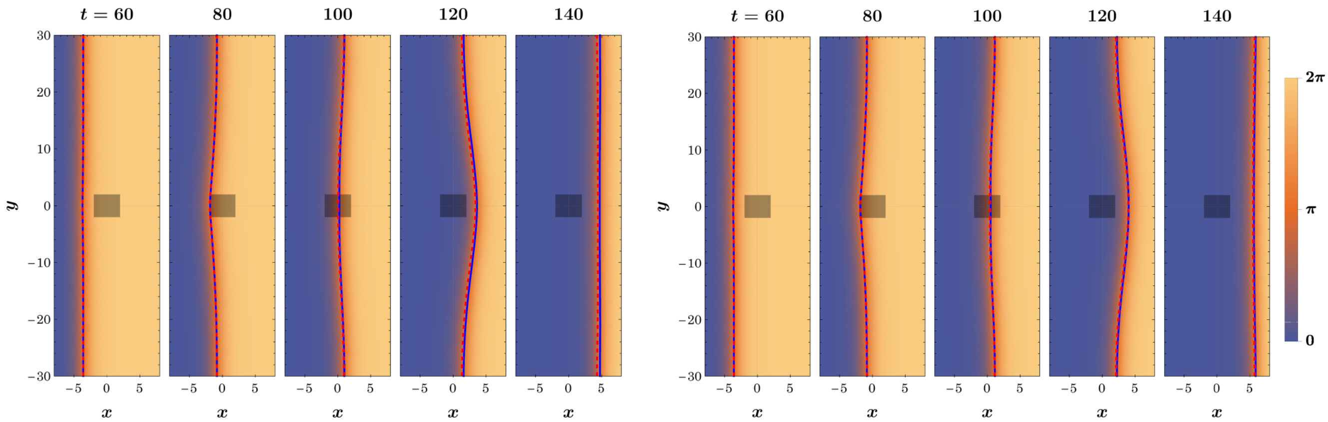

FIG. 6. Passing over heterogeneity. In the left panel, we show the system without forcing and dissipation. The kink front has an initial velocity equal to $u = 0.14$. The right panel shows an analogous process in a system with forcing $\Gamma = 0.0018$ and dissipation $\alpha = 0.01$. In both images the gray area represents the inhomogeneity. Here we have that $\varepsilon = 0.1$. The animations are available at [47].

kink front would disappear. The situation is different when there is dissipation in the system. The animation conducted for long times in the latter setting shows that the kink front straightens.

In the second case, shown in Fig. 7, we take a large value of the inhomogeneity strength $\varepsilon = 0.5$. Accordingly, even a front with a velocity slightly greater than the velocity reported in the previous figure is not sufficient to overcome the inhomogeneity. The left panel shows the process of interaction of a front with initial velocity $u = 0.16$ with the inhomogeneity represented by the gray area of the figure. As can be seen during the interaction the front is attempting to pass over the inhomogeneity; however, it finally bounces back towards its initial position. Despite the large value of ε, and the substantial deformation of the kink filament, the agreement between the original model (1) and the effective model (12) remains very good. The right panel shows an even more interesting interaction of the kink front with the inhomogeneity. In the figure, in addition to the value of the parameter $\varepsilon = 0.5$, a forcing of $\Gamma = 0.0013$ and a dissipation coefficient of $\alpha = 0.01$ are assumed. Initially the front moving towards the inhomogeneity experiences a deformation. Then, a series of damped reflections of the front from the barrier occur. During the reflections and returns, deformations of the entire front occur having the form of vibrations in the direction of motion. The subsequent turning of the front in the direction of the barrier is a consequence of the existence of an external forcing. Vibrations are damped due to the presence of dissipation in the system. What is interesting here is the final shape of the front, which is a consequence of multiple factors. The first factor is, of course, the presence of a barrier that constrains the movement of the front and leads to an energetically induced bending of the kink filament. The second is the presence of forcing, which in the middle is balanced by the presence of the barrier. The situation is different at the ends, where the front does not have "feel" the barrier (and hence is once again straightened). The combination of these factors with the geometric distribution of our inhomogeneity leads to a stable equilibrium analogous to the $1 + 1$-dimensional case in Ref. [43]. Yet the present case also features a spatial bending of the kink profile, given the geometry of the heterogeneity and the tendency to shorten the length of the kink, in a way resembling the notion of string tension at the front.

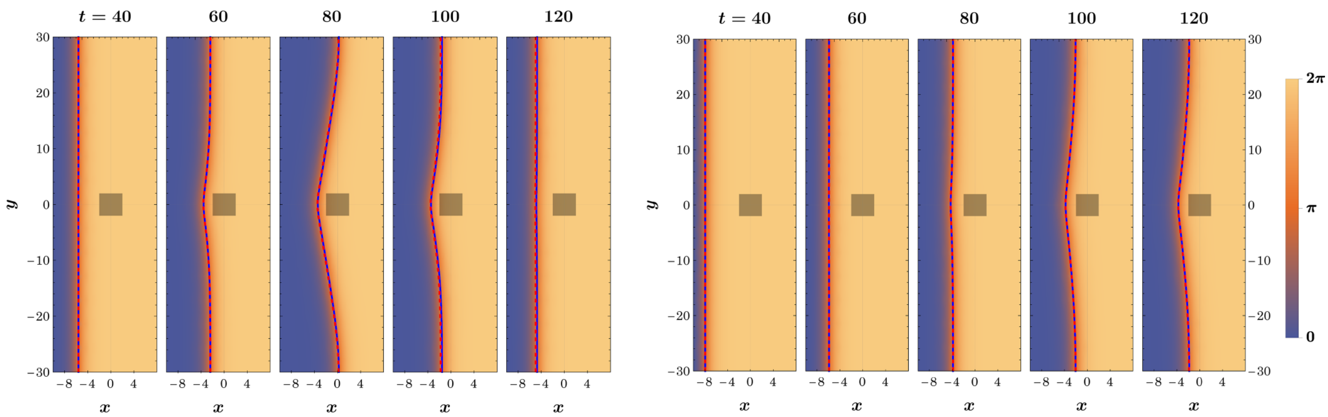

FIG. 7. Reflection (left) and stopping (right) on inhomogeneity. In the left panel, the system without forcing and dissipation is shown. The kink front has an initial velocity equal to $u = 0.16$. The right panel shows an analogous process in a system with forcing $\Gamma = 0.0013$ and dissipation $\alpha = 0.01$. In both pictures, the gray area represents the inhomogeneities with $\varepsilon = 0.5$. The animations are available at [47].

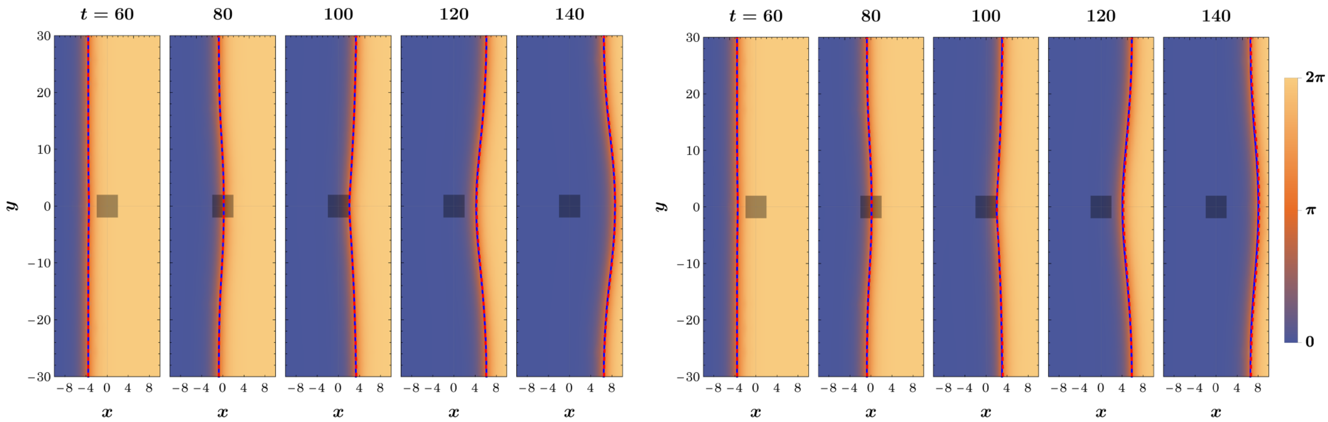

FIG. 8. Passing over the well. In the left panel, the system without forcing and dissipation. The kink front has an initial velocity equal to $u = 0.14$. The right panel shows an analogous process in a system with forcing $\Gamma = 0.0018$ and dissipation $\alpha = 0.01$. In both images the gray area represents the region of inhomogeneity. The parameter describing the depth of the well has a value of $\varepsilon = 0.1$. The animations are available at [47].

2. *Heterogeneity in the form of well*

A slightly different type of inhomogeneity is a potential well. In this section, the well is obtained by replacing $g(x, y)$ in the formula $\mathcal{F}(x, y) = 1 + \varepsilon g(x, y) = 1 + \varepsilon p(x)q(y)$ by $-g(x, y)$ and preserving the form of functions $p(x)$ and $q(y)$. In the relevant dip (rather than bump) of the heterogeneity, the parameters are taken as $h = 6$ and $d = 6$. As in the previous section, we will consider two cases. In the first case, the front passes over the well, and in the second it is stopped by it.

Figure 8 shows the case of a front passing over a well. The left panel describes the case of no forcing and dissipation. The parameter describing the depth of the well is $\varepsilon = 0.1$. The initial velocity of the front is $u = 0.14$ in this case. A straight front during its approach to the inhomogeneity deforms in the middle part which is related to the attraction by the well (cf. with the opposite scenario of the barrier case explored previously). In the course of crossing the well the situation reverses. Due to the attraction by the inhomogeneity, the central part of the kink advances faster (than the outer parts). Then we observe the kink moving outside the well, which, in turn, results in vibrations along the direction of motion. These vibrations persist (in the Hamiltonian case) for a very long time due to the lack of dissipation in the system. The right panel shows the same process, but when in the system there is dissipation $\alpha = 0.01$ and forcing $\Gamma = 0.0018$. The parameter describing the depth of the well is, as before, $\varepsilon = 0.1$. The course of the interaction is similar to that in the left panel. The main difference is that the vibration that the front performs after the impact visibly decays and eventually disappears due to the existence of dissipation in the system. Interestingly, in both cases, the agreement of the approximate model with the original one is very good even for long times. As before, we include animations showing the interaction process both in the case without dissipation and with dissipation.

The situation becomes even more interesting in the case shown in Fig. 9. In this case, we observe the process of interception of the front by the potential well. The left panel of this figure shows the process of interaction in the absence of forcing and dissipation. The depth of the well here is quite large because it is determined by the parameter $\varepsilon = 0.5$. The initial velocity of the kink front is $u = 0.16$. As in the previous figure, initially, due to the attraction of heterogeneity, the front in its central part is pulled into the well. Then there are long-lasting oscillations and deformations of the front, which is the result of interaction with the well. Due to the large value of the parameter ε, the approximation model is less accurate for long times, i.e., ones exceeding $t = 100$.

The right panel illustrates an identical process, i.e., interception of the front by the well but with both dissipation ($\alpha = 0.01$) and external forcing ($\Gamma = 0.0013$) in the system. As in the left panel, the front is initially, in the middle part, pulled into the well and then repeatedly deformed due to interaction with heterogeneity. The important change, once again, is that the deformations of the front, due to dissipation, become gradually smaller. Ultimately, the kink becomes static, adopting a shape different from a straight line, due to the presence of (and attraction to) the heterogeneity. The final shape of the kink is a compromise between the forcing of Γ and the tension of the kink filament. Tension, as already mentioned tends to minimize the length of the front while the forcing pushes the free ends of the front to the right. Due to the large value of the ε parameter, the approximate model has a more limited predictive power for sufficiently long times, e.g., $t > 1000$. The discrepancies between the two descriptions seem to have a time shift nature. However, the presence of dissipation leads to a gradual reduction in the kink's distortion and thus to the differences between the initial model and the approximate one. It turns out that the final configuration is very proximal between the two models. We have put the course of the impact process in the form of an animation in the additional materials.

IV. LINEAR STABILITY OF THE DEFORMED KINK FRONT

In this section we consider the model defined by Eq. (1) with $\alpha = 0$ and $\Gamma = 0$,

$$\partial_t^2\phi - \partial_x(\mathcal{F}(x, y)\partial_x\phi) - \partial_y^2\phi + \sin\phi = 0. \qquad (18)$$

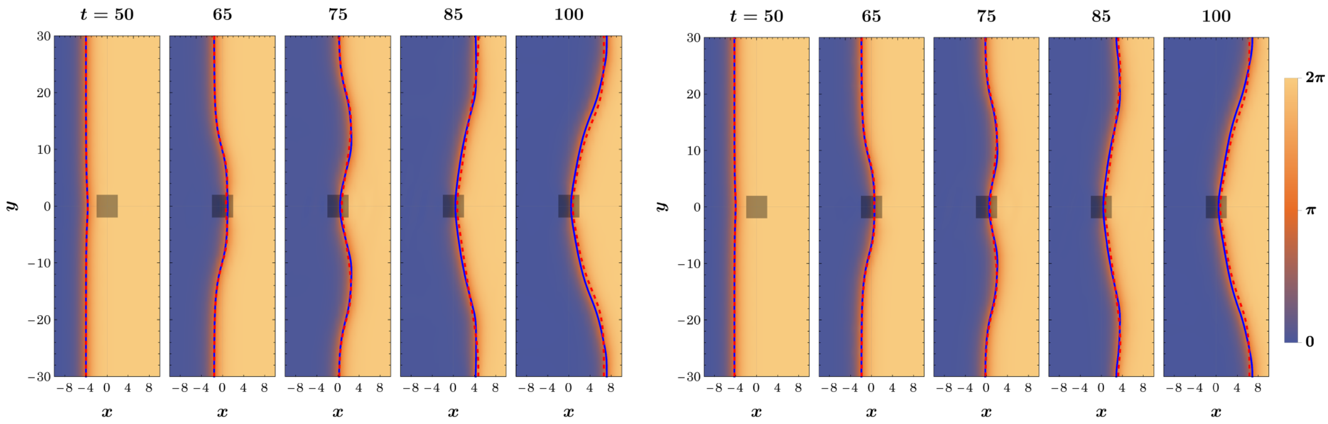

FIG. 9. Intercepting of the kink front through a potential well. On the left, the case without dissipation and forcing is shown. The initial velocity of the front is $u = 0.16$. On the right, the dissipation is $\alpha = 0.01$ while the forcing is $\Gamma = 0.0013$. In both cases, the parameter ε is equal to 0.5. The animations are available at [47].

In the framework of this model we study the stability of the deformed static kink solution $\phi_0(x, y)$ satisfying the equation

$$-\partial_x(\mathcal{F}(x, y)\partial_x\phi_0) - \partial_y^2\phi_0 + \sin\phi_0 = 0. \tag{19}$$

This study of the spectrum of the kink will help us further elucidate the internal vibrational modes of the kink filament observed and discussed in the previous sections. Indeed, whenever kink vibrations are excited, they can be decomposed on the basis of oscillations of the point spectrum of the kink discussed below (while the extended modes of the continuous spectrum represent the small amplitude radiative wave packets within the system). Moreover, this spectral analysis can be leveraged to appreciate which configurations are unstable (e.g., the ones where the kink is sitting on top of a barrier) versus which ones are dynamically stable (e.g., when the kink is trapped by a well).

We introduce into Eq. (19) a configuration ϕ consisting of the solution ϕ_0 and a small correction ψ, i.e., $\phi(t, x, y) = \phi_0(x, y) + \psi(t, x, y)$. Moreover, we assume a separation of variables of the perturbation in terms of its time and space dependence as $\psi(t, x, y) = e^{i\omega t}v(x, y)$. In a linear approximation with respect to the correction, we obtain

$$\begin{aligned} &-\partial_x(\mathcal{F}(x, y)\,\partial_x v(x, y)) - \partial_y^2 v(x, y) + (\cos\phi_0)\,v(x, y) \\ &\quad = \lambda v(x, y), \end{aligned} \tag{20}$$

where $\lambda = \omega^2$. We can briefly write this equation using the $\hat{\mathcal{L}}$ operator, which includes a dependence on the analytical form of inhomogeneity

$$\hat{\mathcal{L}}v + \cos\phi_0\, v = \lambda v. \tag{21}$$

The above equation has the character of a stationary Schrödinger equation with a potential defined by the cosine of the straight kink front configuration ϕ_0 intercepted by the inhomogeneity. An important feature of this configuration, is that, similarly to the $\hat{\mathcal{L}}$ operator, it depends in part on the form of the inhomogeneity. In the region of heterogeneity, it has an analytical form different from that of the free kink (denoted ϕ_K in this work). This modification of the analytical form of the field is a consequence of the interaction of the kink with the inhomogeneity. Based on this equation, an analysis of the excitation spectrum of the static kink captured by the inhomogeneity was carried out. The results can be found in Figs. 10 and 11. Figure 10 shows with dotted lines the dependence of the squares of the frequency on the parameter d describing the transverse size of the inhomogeneity. In the figure, the values of the parameters are assumed to be $h = 4$ and $\varepsilon = 0.1$ (in addition, the size of the system is determined by the values $L_x = 30$ and $L_y = 30$). The lowest energy state in this diagram is the nondegenerate state and it corresponds to the zero mode of the sine-Gordon model without inhomogeneities. In addition, the figure includes the fit obtained for this state using an energy landscape study of the one-degree-of-freedom effective model (see Appendix C for a description of this approach). Note that up to a value of about 0.4 of the d/L_y ratio, this simple model captures the course of the numerical dependence well. Above that lie the excited states. At the scale adopted in the figure,

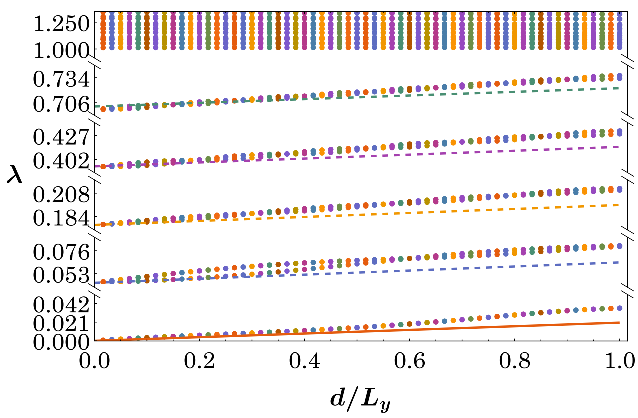

FIG. 10. Squared eigenfrequencies $\lambda = \omega^2$ calculated for the static kink front configuration (trapped by inhomogeneity with the form of a well) depending on the value of d/L_y for $h = 4$, $\varepsilon = 0.1$. The red line represent the eigenvalue of the ground state obtained from the approximate model described in Appendix C.

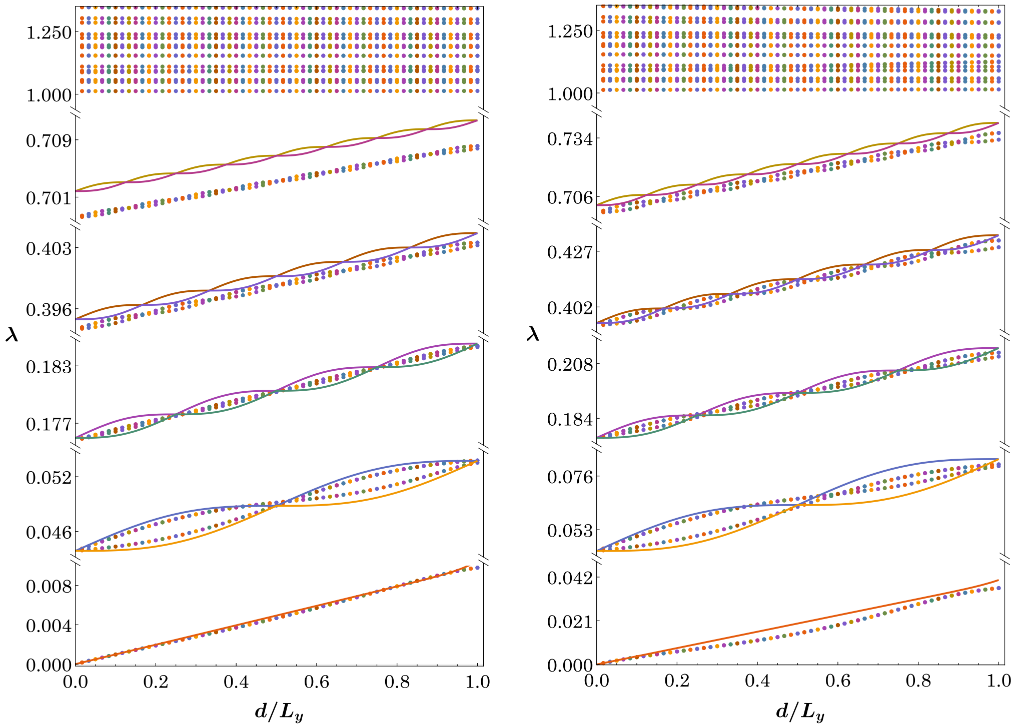

FIG. 11. Detailed graph of squared eigenfrequencies $\lambda = \omega^2$ calculated for the static kink configuration trapped by a well (without dissipation and bias current) depending on the value of d/L_y for $\varepsilon = 0.01$ on the left and $\varepsilon = 0.1$ on the right. In both cases $\varepsilon = 0.1$, $h = 4$. The lines represent the analytical results obtained in Appendix B.

it is almost imperceptible that each line actually consists of two lines running side by side. Note that the increase in the value of λ for the excited states is similar to the increase in the value for the ground state, as indicated by the dashed lines parallel to the red line obtained for the ground state based on the approximate model (Appendix C). Above a value of unity, we encounter the continuous spectrum of the problem. A more detailed plot is shown in Fig. 11. In this figure, it is much clearer that the discrete states (except for the ground state) are described by double lines. The spectrum is shown here for two values of ε. The results for $\varepsilon = 0.01$ are shown in the left panel, while those for $\varepsilon = 0.1$ (as in the previous figure) are shown in the right one. The other parameters are identical. The figure also shows the predictions obtained from the degenerate perturbation theory analysis presented in Appendix B. It can be seen that the analytical result reflects very well the course of the line representing the ground state (especially for small values of ε). The course of the lower excited states is also quite well reproduced. For higher excited states, the similarity of the numerical result to the analytical one is qualitative.

In order to obtain an analytical estimate of the spectrum of linear excitations of the configuration under study, we need, among other things, the form of deformation χ of the kink front with respect to the free kink. The method of obtaining the χ function is presented in Appendix A. To check the analytical formulas obtained by approximating, for example, the function χ in a piecewise form, we performed numerical calculations of the integrals contained in Appendix B based on the approximation (A7). The results are presented in Fig. 12, which was made for the same parameters as in Fig. 11. As can be seen, the improvement in compatibility occurs for the lowest eigenvalues. Specifically, it takes place for the parameter d/L_y close to 1. For higher eigenvalues, the situation does not significantly improve. It turns out that for higher excited states the analytical formula overestimates the separation of states (corresponding to the degenerate states of the zero approximation), while the result obtained with the fit (A7) underestimates this gap. In any event, given the relatively small size of the discrepancy, we do not dwell on this further.

On the other hand, the results for a barrier-like inhomogeneity of the form of Fig. 5 are presented in Fig. 13. The parameters on the left and right panels of this figure are identical and are $h = 4$, $\varepsilon = 0.1$, $L_x = 30$, and $L_y = 30$. The figures differ only in scale. This time, the configuration of the kink lying on top of the destabilizing barrier is found to indeed be unstable, which is manifested by the occurrence of a mode with a negative value of λ (i.e., an imaginary eigenfrequency). This mode corresponds to the translational mode, reflecting in this case the nature of the effective potential (i.e., a barrier creating an effective saddle point). Such a value is a manifestation of the kink drifting away from inhomogeneity. The other modes are quite similar in nature to the excited modes in the case of potential well, which has its origin in the adopted periodic boundary conditions.

V. CONCLUSIONS AND FUTURE CHALLENGES

In the current article we studied the behavior of the kink front in the perturbed 2 + 1-dimensional sine-Gordon model.

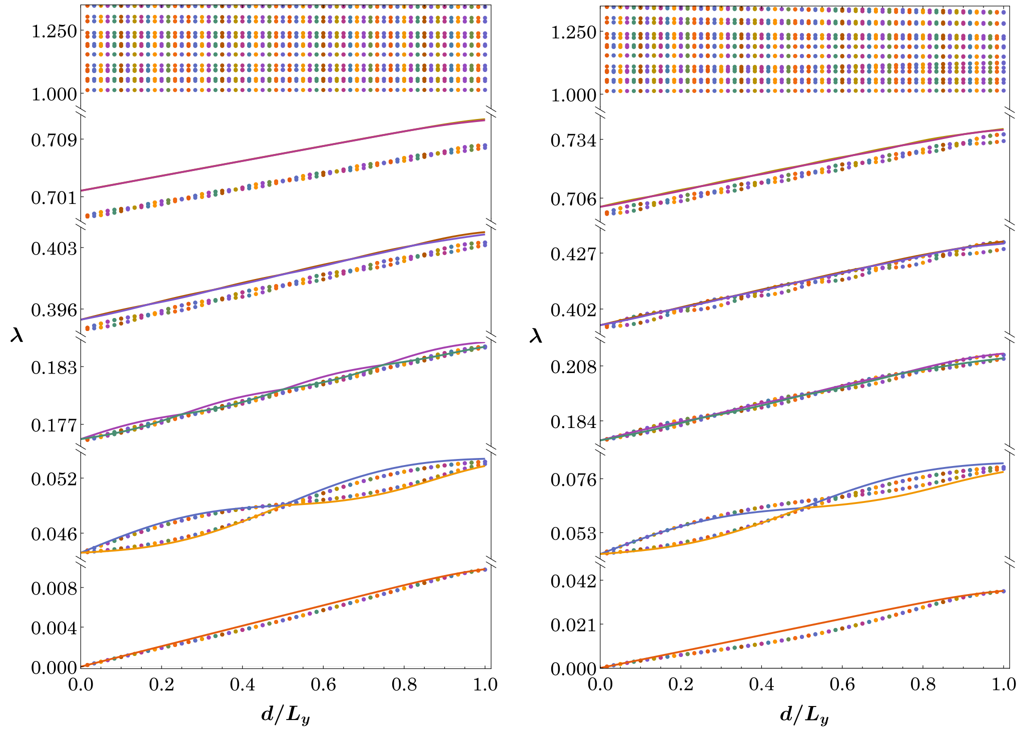

FIG. 12. Detailed graph of squared eigenfrequencies $\lambda = \omega^2$ calculated for the static kink configuration trapped by a well (without dissipation and bias current) depending on the value of d/L_y for $\varepsilon = 0.01$ on the left and $\varepsilon = 0.1$ on the right. In both cases $h = 4$. The lines represent the results of Appendix B with integrals determined numerically for (A7).

The particular type of perturbation is motivated by the study of the dynamics of gauge-invariant phase difference in one- and quasi-one-dimensional curved Josephson junction. We also obtained an effective 1 + 1-dimensional model describing the evolution of the kink front based on the nonconservative Lagrangian method [26,44]. First we tested the usefulness of the approximate model. More concretely, we examined the behavior of the kink starting from the case when there are no inhomogeneities in the system. The agreement between the results of the original and the effective model turned out to be very satisfactory. Subsequently, we explored the movement of the front in a slightly more complex situation. Namely, we examined inhomogeneities of shape independent of the variable transverse to the direction of movement of the front, i.e., the y variable. The results obtained here are in full analogy with the 1 + 1-dimensional model studied earlier [43]. These studies can be directly applied to the description of quasi-one-dimensional Josephson junctions.

The most interesting results were obtained for studies of the behavior of the front in the presence of inhomogeneities with shape genuinely dependent on both spatial variables. This case shows the remarkable richness of the

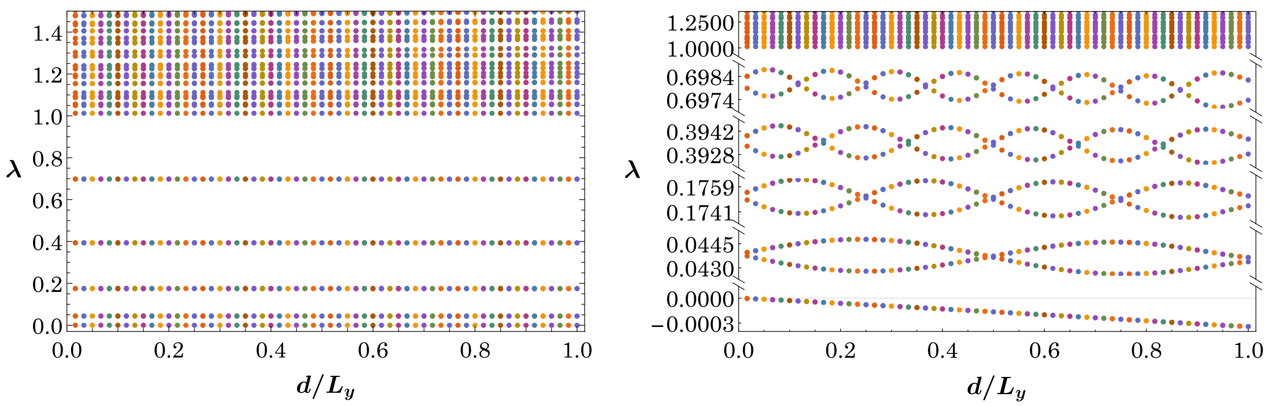

FIG. 13. Squared eigenfrequencies $\lambda = \omega^2$ calculated for the static configuration on top of inhomogeneity (without dissipation and bias current) depending on the value of d/L_y for $h = 4$ and $\varepsilon = 0.1$. The left and right panels differ only in scale.

dynamical behaviors of the kink front interacting with heterogeneity. We studied two types of inhomogeneities. One was in the form of a barrier, while the other was in the form of a well.

Of particular interest is the process of creating a static final state in the case with dissipation and forcing. We deal with the formation of such a state when a front with too low a velocity is stopped (by a sequence of oscillations) before the peak and when a front that is too slow is trapped by a well.

We have analyzed the competing factors that contribute to the formation of the resulting stationary states and have shown that our reduced $1+1$-dimensional description can capture the resulting state very accurately. It is worth noting that the approximate description in each of the studied cases is also accurate for long time evolutions for small values of the parameter describing the strength of heterogeneity. While deviations might occur in some cases for very long times (in Hamiltonian perturbations) or for sufficiently large perturbations in dissipative cases, generally, we found that the reduced kink filament model was very accurate in capturing the relevant dynamics.

Finally, we also studied the stability of a straight kink front captured by a single inhomogeneity of the form of a potential well. In this case, the zero mode of the sine-Gordon model without inhomogeneities turns into an oscillating mode in the model with inhomogeneities. Indeed, the breaking of translational invariance leads to either an effective attractive well or a repulsive barrier (see also the analytical justification in Appendix C) manifested in the presence of an internal oscillation or a saddlelike departure from the inhomogeneous region. In addition, the periodic boundary conditions we have adopted result in a number of additional discrete modes appearing in the system in addition to the ground state and the continuous spectrum. These are effectively the linear modes associated with the quantized wave numbers due to the transverse domain size. In the absence of a genuinely 2D heterogeneity, this picture can be made precise with the respective eigenmodes being $k_y = 2n\pi/L_y$. In the presence of genuinely 2D heterogeneities, the picture is still qualitatively valid, but the modes are locally deformed and then a degenerate perturbation theory analysis is warranted, as shown in Appendix B, where we have provided such an analytical description of the mode structure. This description matches quite well with the numerical results especially for the lower states of the spectrum under study.

Naturally, there are numerous extensions of the present work that are worth exploring in the future. More specifically, in the present setting we have focused on inhomogeneities impacted on by rectilinear kink structures, while numerous earlier works [35,36,38] have considered the interesting additional effects of curvature in the two-dimensional setting. In light of the latter, it would be interesting to examine heterogeneities in such radial cases. Furthermore, in the sine-Gordon case, the absence of an internal mode in the quasi-one-dimensional setting may have a significant bearing of a phenomenology and the possibility of energy transfer type effects that occur, e.g., in the ϕ^4 model [48]. It would, thus, be particularly relevant to explore how the relevant phenomenology generalizes (or is modified) in the latter setting. Finally, while two-dimensional settings have yet to be exhausted (including about the potential of radial long-lived breathinglike states), it would naturally also of interest to explore similar phenomena in the three-dimensional setting. Such studies are presently under consideration and will be reported in future publications.

ACKNOWLEDGMENTS

This research has been made possible by the Kosciuszko Foundation The American Centre of Polish Culture (J.G.). This research was supported in part by PLGrid Infrastructure (T.D. and J.G.). This material is based on work supported by the U.S. National Science Foundation under the Awards No. PHY-2110030 and No. DMS-2204702 (P.G.K.).

APPENDIX A: KINK EXISTENCE AND STABILITY

1. Peak-shaped inhomogeneity

We will consider the case of a kink front stopped by the inhomogeneity (in the form of a barrier; see Fig. 5) in the presence of forcing and dissipation. The static configuration in this case is the solution of the following equation

$$-\partial_x(\mathcal{F}(x,y)\partial_x\phi_0) - \partial_y^2\phi_0 + \sin\phi_0 = -\Gamma. \tag{A1}$$

To begin, we will show that the solution can be represented (for small perturbations) as the sum of a kink profile $\phi_K = 4\arctan e^{x-X_0(y)}$ and a correction that depends only on the shape of the inhomogeneity and the external forcing, i.e., $\phi_0(x,y) = \phi_K(x-X_0) + \chi(x,y)$. The equation satisfied by the correction χ, to leading order, is of the form

$$\begin{aligned} &-\partial_x(\mathcal{F}(x,y)\partial_x\chi) - \partial_y^2\chi + [\cos\phi_K(x-X_0)]\chi \\ &= \varepsilon\partial_x(g(x,y)\partial\phi_K(x-X_0)) - \Gamma. \end{aligned} \tag{A2}$$

The results of simulations performed on the ground of approximation (A2) and the field model (A1) are demonstrated in Fig. 14. This figure shows in the left panel the χ profiles obtained for different values of the ε parameter. Starting from the top, we have $\varepsilon = 0.1$, $\varepsilon = 0.2$, and $\varepsilon = 0.5$. In all cases, $\Gamma = 0.001$. The right panel shows the profile of the static kink front in the same cases. This panel, on the one hand, shows the static kink front obtained from Eq. (A1) (black dashed line) and, on the other hand, the fronts obtained from the solutions of Eq. (A2) for different values of the parameter ε. The red line corresponds to $\varepsilon = 0.1$, the blue line corresponds to $\varepsilon = 0.2$, while the yellow line corresponds to $\varepsilon = 0.5$. These fronts were determined for the $\phi_K + \chi$ configuration. The deformation of the kink center is due to the fact that it is supported by the inhomogeneity in the central part and, on the other hand, at the edges it is stretched by the existing constant forcing. Of course, due to the tension of the kink front, stretching cannot take place unrestrictedly because this would lead to an excessive increase in the total energy stored in the kink configuration. Let us notice that in all cases, qualitatively the shape of the static kink front is correctly reproduced. On the other hand, in the case of $\varepsilon = 0.5$ we observe some quantitative deviations in the central part.

We also test the stability of the above described solution. This is based on the equation which looks identical to Eq. (20); however, the main difference is the relationship of the eigenvalue λ to the frequency. In the case considered in

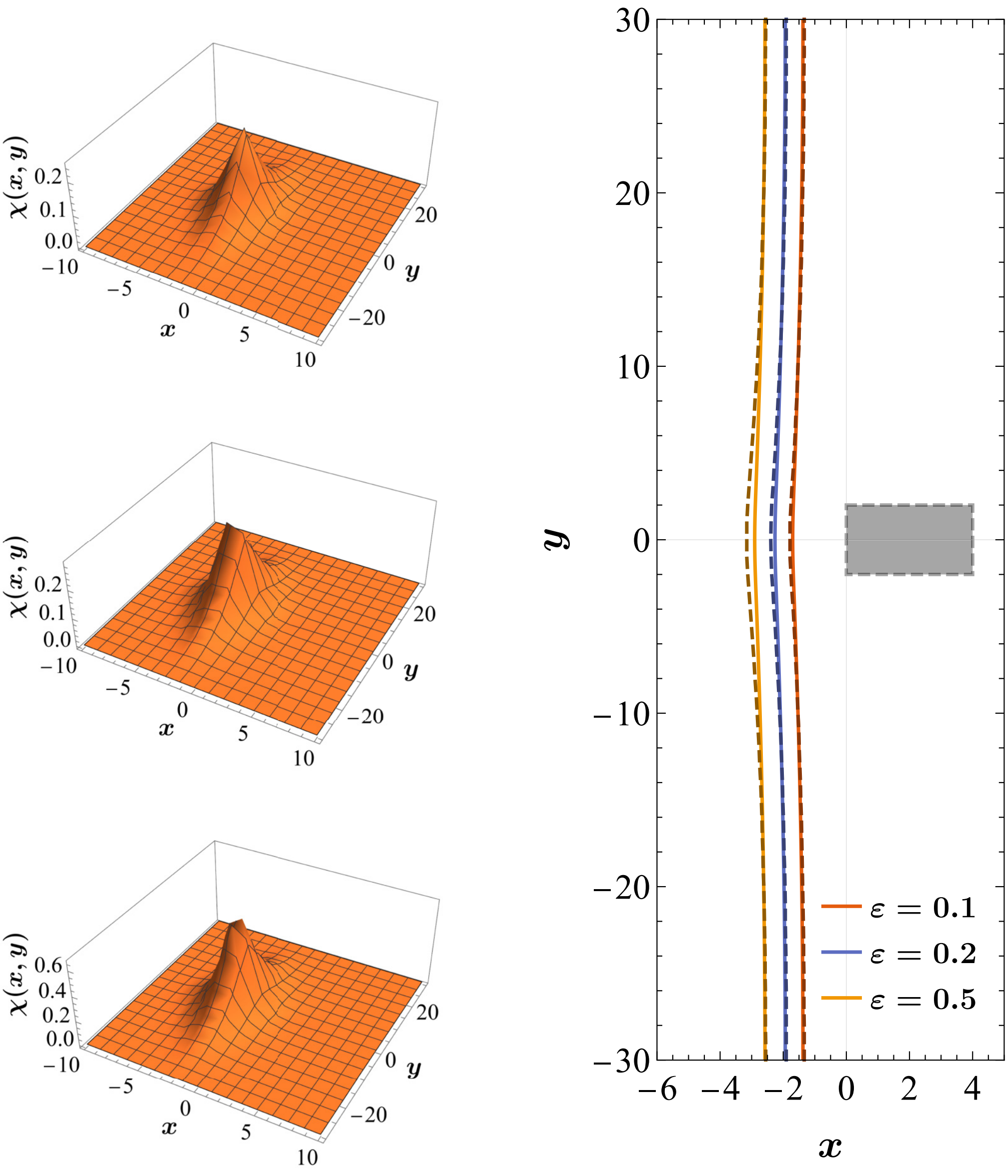

FIG. 14. The left panel shows the function $\chi(x, y)$ for, starting from top, $\varepsilon = 0.1$, 0.2, and 0.5. The right panel compares the shape of the kink front obtained using Eq. (A2) with the exact results represented by the dashed black line, for the same values of ε. The forcing is assumed here to be $\Gamma = 0.001$.

this section $\lambda = \omega(\omega - i\alpha)$. Figure 15 shows the dependence of the square of the frequency ω on the parameter d/L_y. It can be seen that the excitation spectrum determined for the configuration shown in Fig. 14, consists of a ground state, excited states and a continuous spectrum. The form of this spectrum is to a significant degree similar to the excitation spectrum of the kink front trapped by the potential well and shown in Figs. 11 and 12. The main difference from the previous diagrams is that the discrete excited states show less periodicity in comparison with the previous figures.

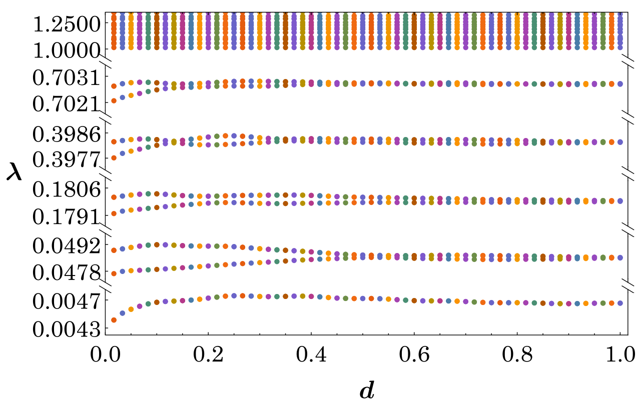

FIG. 15. Graph of squared eigenfrequencies ω^2 calculated for the static kink configuration stopped by a barrier (with dissipation and bias current) depending on the value of d/L_y for $\varepsilon = 0.5$ and $h = 4$.

2. Heterogeneity with a form of well

In this section, we describe the change in the profile of the static kink that results from the existence of an inhomogeneity in the form of a well. We assume that the well is centrally

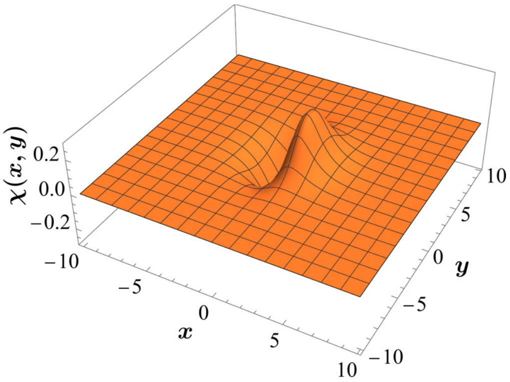

FIG. 16. The shape of the function $\chi(x, y)$, for a static kink front trapped by a well-shaped inhomogeneity. The parameters in the figure are as follows: $d = 4$, $h = 4$, $\varepsilon = 0.1$.

located and has dimensions defined by the parameters h and d, i.e., $\mathcal{F}(x, y) = 1 + \varepsilon g(x, y) = 1 - \varepsilon p(x)q(y)$ and

$$p(x) = \frac{1}{2}\left[\tanh\left(x + \frac{h}{2}\right) - \tanh\left(x - \frac{h}{2}\right)\right]$$

$$\approx \begin{cases} 1, & x \in [-\frac{h}{2}, +\frac{h}{2}] \\ 0, & x \notin [-\frac{h}{2}, +\frac{h}{2}] \end{cases}, \tag{A3}$$

$$q(y) = \frac{1}{2}\left[\tanh\left(y + \frac{d}{2}\right) - \tanh\left(y - \frac{d}{2}\right)\right]$$

$$\approx \begin{cases} 1, & y \in [-\frac{d}{2}, +\frac{d}{2}] \\ 0, & y \notin [-\frac{d}{2}, +\frac{d}{2}] \end{cases}. \tag{A4}$$

The approximate form used to calculate some integrals when determining the analytical form of the eigenvalues (see Appendix B) is also given in the above expression. An example profile obtained from Eq. (A2) in the absence of bias current ($\Gamma = 0$) is shown in Fig. 16. The shape of the χ function, although shown for specific parameter values (i.e., $h = 4$, $d = 4$, and $\varepsilon = 0.1$), is characteristic over a wide range of parameters. The profile shown in Figs. 17 is an even function in the y variable and an odd function in the x variable. The panels of Fig. 17 also include a simple fit in the form of the step function. The parameter χ_0 was chosen so that the areas under the curves $\alpha = \alpha(x)$, $\beta = \beta(y)$ and the fit were identical. In the next section (Appendix B), we use this form of the χ function to approximate the eigenvalues when studying the stability of a static configuration trapped by a well-like inhomogeneity,

$$\chi(x, y) = \chi_0\ \alpha(x)\beta(y), \tag{A5}$$

$$\alpha(x) \approx \begin{cases} -1, & x \in \left[-\frac{h}{2}, 0\right) \\ +1, & x \in \left[0, +\frac{h}{2}\right] \\ 0, & \text{otherwise} \end{cases},$$

$$\beta(y) \approx \begin{cases} +1, & x \in \left[-\frac{d}{2}, +\frac{d}{2}\right] \\ 0, & \text{otherwise} \end{cases}. \tag{A6}$$

In order to validate the analytical expressions (B18) and (B32) for the eigenvalues of the linear excitation operator, we also determined a much better fit for the χ function. We looked for the fit in the form:

$$\chi(x, y) = \chi_0 \tanh(ax)\mathrm{sech}(ax) \times \left(4 \arctan e^{y+\frac{d}{2}} - 4 \arctan e^{y-\frac{d}{2}}\right). \tag{A7}$$

The shape of the fit was compared with the numerical result. Figure 18 shows a very good convergence between the fit (dashed line) and the numerical result (solid line). The figure was made for parameters equal to $\chi_0 = 0.67$, $a = 0.85$, and $h = 4$, respectively. The fit form described by Eq. (A7) was also used to determine the numerical value of the integrals in Appendix B. The results obtained on this basis are presented in Fig. 12. As can be seen for lower eigenvalues, we observe improved agreement with numerical results. Moreover, the improvement is evident for values of d/L_y close to 1.

APPENDIX B: KINK STABILITY IN THE POTENTIAL WELL

In this section, we will present analytical results on the spectrum of linear excitations of a deformed kink bounded by an inhomogeneity in the form of a potential well. We start

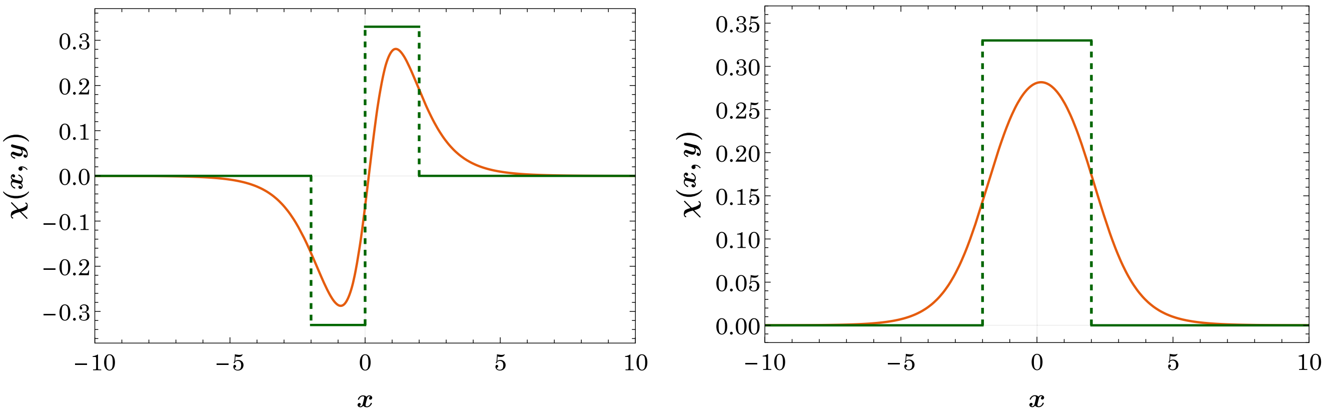

FIG. 17. Cross sections with fitting for $\chi(x, y)$. The value of $\chi_0 = 0.67$ was determined by fit. Here $h = 4$, $d = 4$, and $\varepsilon = 0.1$.

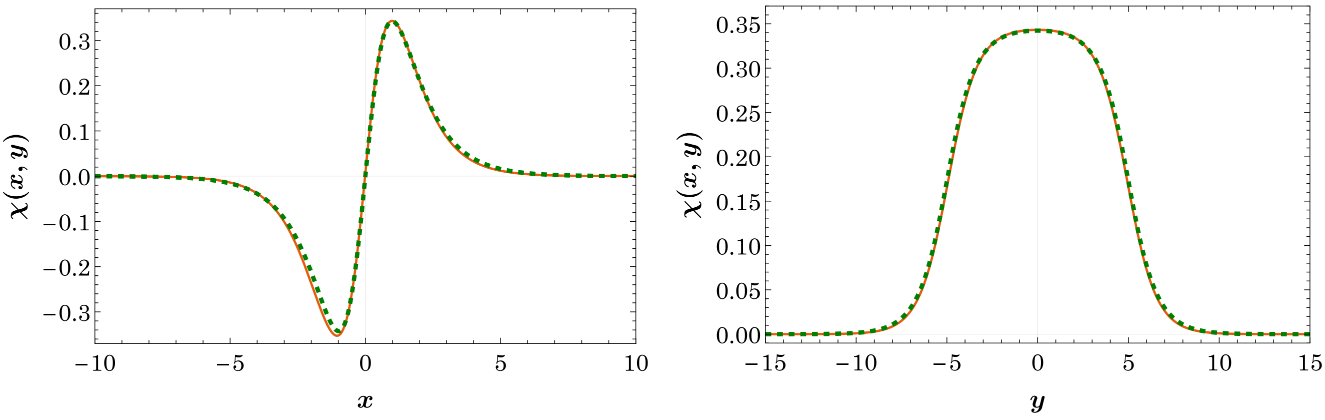

FIG. 18. Cross sections with fitting for $\chi(x, y)$. The dashed green line represents a fit function of the form $\chi(x, y) = \chi_0 \tanh(ax)\text{sech}(ax)(4 \arctan e^{y+\frac{d}{2}} - 4 \arctan e^{y-\frac{d}{2}})$. Here $h = 4$, $d = 10$, and $\varepsilon = 0.1$.

with Eq. (21)

$$\hat{\mathcal{L}}v + \cos\phi_0\, v = \lambda v. \tag{B1}$$

Since we plan to use perturbation calculus in the parameter ε determining the magnitude of the inhomogeneity, we separate the operator $\hat{\mathcal{L}}$ into a part $\hat{\mathcal{L}}_0$ that does not depend on the perturbation parameter and a part $\hat{W}$ preceded by this parameter. The relationships between operators and the other quantities used in this section are summarized as follows:

$$\hat{\mathcal{L}}v = \hat{\mathcal{L}}_0 v + \varepsilon \hat{W} v, \quad \hat{\mathcal{L}}_0 v = -\partial_x^2 v - \partial_y^2 v,$$
$$\hat{W} v = -\partial_x(g(x, y)\,\partial_x v), \quad \mathcal{F}(x, y) = 1 + \varepsilon g(x, y). \tag{B2}$$

According to the results presented in Appendix A, we can separate the static kink configuration in the presence of inhomogeneity into static free kink ϕ_K and deformation associated with the existence of inhomogeneity χ,

$$\phi_0(x, y) = \phi_K(x) + \chi(x, y). \tag{B3}$$

Next, we expand the quantities appearing in formula (B1) with respect to the parameter ε,

$$v = v^{(0)} + \varepsilon v^{(1)} + \varepsilon^2 v^{(2)} + \dots, \tag{B4}$$

$$\lambda = \lambda^{(0)} + \varepsilon\lambda^{(1)} + \varepsilon^2\lambda^{(2)} + \dots,$$
$$\chi = \chi^{(0)} + \varepsilon\chi^{(1)} + \varepsilon^2\chi^{(2)} + \dots. \tag{B5}$$

The function χ is defined in such a way that it does not appear in the zero order, i.e., $\chi^{(0)} = 0$. In addition, since in the system under consideration we assume periodic boundary conditions in the direction of the y variable we also take $v(x, -\frac{1}{2}L_y) = v(x, +\frac{1}{2}L_y)$. Moreover, it is assumed that the inhomogeneity disappears at the edges of the system (in the direction of the variable x), i.e., $g(x, y) \to 0$ for $x \to \pm\frac{1}{2}L_x$. Note also that, like $\partial_x\phi(\pm\frac{1}{2}L_x, y)$, also $\partial_x v(\pm\frac{1}{2}L_x, y)$ disappears at the x boundaries of the area under consideration.

1. The lowest order of expansion

In the lowest order, we get the equation

$$\hat{\mathcal{L}}_0 v^{(0)} + \cos\phi_K\, v^{(0)} = \lambda^{(0)} v^{(0)}, \tag{B6}$$

where $\phi_K(x) = 4\arctan(e^x)$ describes the kink front located at $x = 0$ and stretched along the y axis. For the function $\phi_K(x)$, the equation can be separated into two equations. One depending on the x variable and the other on y. Using periodicity in the y variable, we obtain a series of eigenvalues and eigenfunctions. The ground state in this approximation corresponds to zero eigenvalue

$$\lambda_0^{(0)} = 0, \; v_0^{(0)}(x, y) = A_0\,\text{sech}(x), \; A_0 = \frac{1}{\sqrt{2L_y \tanh\frac{L_x}{2}}}. \tag{B7}$$

The subsequent eigenstates correspond to nonzero eigenvalues

$$\lambda_{n\pm}^{(0)} = \left(\frac{2\pi}{L_y}\right)^2 n^2, \; \begin{cases} v_{n+}^{(0)}(x, y) = A\,\text{sech}(x)\cos\left(2\pi n\frac{y}{L_y}\right) \\ v_{n-}^{(0)}(x, y) = A\,\text{sech}(x)\sin\left(2\pi n\frac{y}{L_y}\right) \end{cases},$$
$$A = \frac{1}{\sqrt{L_y \tanh\frac{L_x}{2}}}. \tag{B8}$$

In the lowest order of the perturbation calculus, all nonzero eigenvalues are degenerate twice. The normalization coefficients A and A_0 were chosen so that the eigenfunctions were normalized to 1 in the sense of the product defined as the integral over the area $[-L_x/2, +L_x/2] \times [-L_y/2, +L_y/2]$, according to the formula

$$\langle u, v\rangle \equiv \int_{-\frac{L_x}{2}}^{+\frac{L_x}{2}} \int_{-\frac{L_y}{2}}^{+\frac{L_y}{2}} u(x, y)v(x, y)dxdy, \tag{B9}$$

where we assume that functions are periodic with respect to the variable y and their x derivatives disappear at the boundaries $x = \pm\frac{L_x}{2}$.

2. The first order of expansion

In the first order of expansion the equation is of the form

$$\hat{\mathcal{L}}_0 v^{(1)} + \cos\phi_K\, v^{(1)} + \hat{G}v^{(0)} = \lambda^{(0)}v^{(1)} + \lambda^{(1)}v^{(0)}. \tag{B10}$$

In order to shorten the formulas that appear in this section, the operator $\hat{G}$ was introduced

$$\hat{G}v^{(0)} \equiv \hat{W}v^{(0)} - (\sin\phi_K)\chi^{(1)}v^{(0)}. \tag{B11}$$

a. Correction to the ground state

We project Eq. (B10) for the ground state onto the state $v_0^{(0)}$ which leads to the equation

$$\langle v_0^{(0)}, (\hat{\mathcal{L}}_0 + \cos\phi_K)\, v_0^{(1)}\rangle + \langle v_0^{(0)}, \hat{G} v_0^{(0)}\rangle = \lambda_0^{(0)}\langle v_0^{(0)}, v_0^{(1)}\rangle + \lambda_0^{(1)}\langle v_0^{(0)}, v_0^{(0)}\rangle. \tag{B12}$$

Due to the normalization of the state $v_0^{(0)}$ and the fact that the operator $\hat{\mathcal{L}}_0 + \cos\phi_K$ is Hermitian, i.e.,

$$\langle v, (\hat{\mathcal{L}}_0 + \cos\phi_K)\, u\rangle = \langle(\hat{\mathcal{L}}_0 + \cos\phi_K)v, u\rangle, \tag{B13}$$

Eq. (B12) can be reduced to the form

$$\lambda_0^{(1)} = \langle v_0^{(0)}, \hat{G} v_0^{(0)}\rangle. \tag{B14}$$

We determine the value of $\lambda_0^{(1)}$ based on Eqs. (B11) and (B2). In this Appendix, we take the following form of $g(x, y) = -p(x)q(y)$. As for the function describing the deformation of the function ϕ_0 resulting from the existence of inhomogeneities, i.e., $\chi^{(1)}$, we write it as follows $\chi^{(1)} = \chi_0\, \alpha(x)\beta(y)$. Under the above conditions, the correction of first order is of the form

$$\lambda_0^{(1)} = \frac{1}{2L_y \tanh\frac{L_x}{2}}(2\chi_0 J_\alpha I_\beta - J_p I_q). \tag{B15}$$

The integrals that appear in the above formula are defined below

$$J_p \equiv \int_{-\frac{L_x}{2}}^{+\frac{L_x}{2}} p(x)\,\mathrm{sech}^2(x)\tanh^2(x)dx, \quad I_q \equiv \int_{-\frac{L_y}{2}}^{+\frac{L_y}{2}} q(y)dy, \tag{B16}$$

$$J_\alpha \equiv \int_{-\frac{L_x}{2}}^{+\frac{L_x}{2}} \alpha(x)\,\mathrm{sech}^3(x)\tanh(x)dx, \quad I_\beta \equiv \int_{-\frac{L_y}{2}}^{+\frac{L_y}{2}} \beta(y)dy. \tag{B17}$$

The $p(x)$ and $q(x)$ functions appearing in the above integrals, in the paper, are taken in the form of (A3) and (A4). On the other hand, the form of the function $\chi(x, y) \approx \chi^{(1)}(x, y)$ is approximated, according to considerations contained in Appendix A in formulas (A6). Two of the above integrals approximately describe the width of the inhomogeneity in the direction of the y variable, i.e., $I_q \approx d$, $I_\beta \approx d$. Consequently, the eigenvalue of the ground state takes the form of

$$\lambda_0 = \lambda_0^{(0)} + \varepsilon\lambda_0^{(1)} + \cdots \approx \frac{\varepsilon}{2\tanh\frac{L_x}{2}}\,\frac{d}{L_y}\,(2\chi_0 J_\alpha - J_p). \tag{B18}$$

To complete the result obtained, we provide the integrals appearing in this formula

$$J_\alpha \approx \frac{2}{3}\left[1 - \mathrm{sech}^3\left(\frac{h}{2}\right)\right], \tag{B19}$$

$$J_p = \coth\left(\frac{h}{2}\right)\left\{\frac{2\tanh\left(\frac{L_x}{2}\right) - \coth\left(\frac{h}{2}\right)\ln\left[\frac{\cosh\left(\frac{L_x+h}{2}\right)}{\cosh\left(\frac{L_x-h}{2}\right)}\right]}{\sinh^2\left(\frac{h}{2}\right)} + \frac{2}{3}\tanh^3\left(\frac{L_x}{2}\right)\right\}. \tag{B20}$$

b. Correction to the degenerate states

In the case of degenerate states, we perform a projection of Eq. (B10) into a state that is a combination of zero-order eigenstates,

$$v_n = \sum_{i=\pm} c_i v_{ni}^{(0)}. \tag{B21}$$

Projection of the equation of the first order written for the degenerate state v_{nj}^0 onto the v state gives

$$\langle v_n, (\hat{\mathcal{L}}_0 + \cos\phi_K)\, v_{nj}^{(1)}\rangle + \langle v_n, \hat{G} v_{nj}^{(0)}\rangle = \lambda_n^{(0)}\langle v_n, v_{nj}^{(1)}\rangle + \lambda_n^{(1)}\langle v_n, v_{nj}^{(0)}\rangle. \tag{B22}$$

Orthonormality of the zero-order states and hermiticity of the operator $\hat{\mathcal{L}}_0 + \cos\phi_K$ leads to a system of equations for the coefficients c_i,

$$\sum_{i=\pm} c_i\langle v_{ni}^{(0)}, \hat{G} v_{nj}^{(0)}\rangle = \lambda_n^{(1)}\sum_{i=\pm} c_i\,\delta_{ij}. \tag{B23}$$

Due to the second degree of degeneracy, we can write the last equation in 2×2 matrix form,

$$\begin{bmatrix} G_{++} - \lambda_n^{(1)} & G_{+-} \\ G_{-+} & G_{++} - \lambda_n^{(1)} \end{bmatrix}\begin{bmatrix} c_+ \\ c_- \end{bmatrix} = \begin{bmatrix} 0 \\ 0 \end{bmatrix}, \tag{B24}$$

where the matrix elements G_{ij} are written in the basis that consists of eigenstates of the zero-order approximation,

$$G_{ij} = \langle v_{ni}^{(0)}, \hat{G} v_{nj}^{(0)}\rangle. \tag{B25}$$

The condition for the existence of nontrivial solutions of the above equation is the zeroing of the determinant (so that nontrivial solutions of the homogeneous system exist)

$$\begin{vmatrix} G_{++} - \lambda_n^{(1)} & G_{+-} \\ G_{-+} & G_{++} - \lambda_n^{(1)} \end{vmatrix} = 0. \tag{B26}$$

According to the above equation, corrections of the first order remove the degeneracy, leading to the eigenvalue corrections:

$$\lambda_{n\pm}^{(1)} = \frac{1}{2}[\,(G_{++} + G_{--}) \pm \sqrt{(G_{++} - G_{--})^2 + 4G_{+-}G_{-+}}\,]. \tag{B27}$$

The expression above is greatly simplified due to the evenness of the $q(-y) = q(y)$ and $\beta(-y) = \beta(y)$ functions in the y variable. This property removes the matrix element $G_{+-} = 0$ which leads to a significant simplification of the last formula,

$$\lambda_{n\pm}^{(1)} = \tfrac{1}{2}[\,(G_{++} + G_{--}) \pm |G_{++} - G_{--}|]. \tag{B28}$$

Matrix elements that appear in the above expression,

$$G_{++} = A^2(2\chi_0 J_\alpha I_\beta^+ - J_p I_q^+), \quad G_{--} = A^2(2\chi_0 J_\alpha I_\beta^- - J_p I_q^-), \tag{B29}$$

are written using integrals

$$I_q^+ = \int_{-\frac{L_y}{2}}^{+\frac{L_y}{2}} q(y)\cos^2\left(2\pi n\frac{y}{L_y}\right)dy,$$

$$I_q^- = \int_{-\frac{L_y}{2}}^{+\frac{L_y}{2}} q(y)\sin^2\left(2\pi n\frac{y}{L_y}\right)dy, \tag{B30}$$

$$I_\beta^+ = \int_{-\frac{L_y}{2}}^{+\frac{L_y}{2}} \beta(y)\cos^2\left(2\pi n\frac{y}{L_y}\right)dy,$$
$$I_\beta^- = \int_{-\frac{L_y}{2}}^{+\frac{L_y}{2}} \beta(y)\sin^2\left(2\pi n\frac{y}{L_y}\right)dy. \quad \text{(B31)}$$

The final result shows the disappearance of the degeneracy of the higher eigenvalues [the integrals J_α and J_p are defined by the formulas (B19) and (B20)]

$$\lambda_{n\pm} = \lambda_n^{(0)} + \varepsilon\lambda_{n\pm}^{(1)} + \cdots \approx \left(\frac{2\pi}{L_y}\right)^2 n^2 + \frac{\varepsilon}{2\tanh\left(\frac{L_x}{2}\right)}(2\chi_0 J_\alpha - J_p)\left[\frac{d}{L_y} \pm \left|\frac{\sin\left(2\pi n\frac{d}{L_y}\right)}{2\pi n}\right|\right]. \quad \text{(B32)}$$

This result was obtained by means of the approximation

$$I_q^\pm \approx \frac{1}{2}L_y\left[\frac{d}{L_y} \pm \frac{\sin\left(2\pi n\frac{d}{L_y}\right)}{2\pi n}\right],$$
$$I_\beta^\pm \approx \frac{1}{2}L_y\left[\frac{d}{L_y} \pm \frac{\sin\left(2\pi n\frac{d}{L_y}\right)}{2\pi n}\right]. \quad \text{(B33)}$$

In addition, the normalization factor A included in formula (B8) was used, while the values of the integrals J_α and J_p are defined by the formulas (B19) and (B20).

APPENDIX C: EIGENVALUE ESTIMATION

In this section, we will estimate the value of $\lambda = \omega^2$ corresponding to the ground state, based on the shape of the energy landscape of the system under study. We consider the Lagrangian density of the sine-Gordon model in the presence of inhomogeneity,

$$\mathcal{L} = \tfrac{1}{2}(\partial_t\phi)^2 - \tfrac{1}{2}\mathcal{F}(x,y)(\partial_x\phi)^2 - \tfrac{1}{2}(\partial_y\phi)^2 - V(\phi). \quad \text{(C1)}$$

The energy density in this model is of the form

$$\rho = \tfrac{1}{2}(\partial_t\phi)^2 + \tfrac{1}{2}\mathcal{F}(x,y)(\partial_x\phi)^2 + \tfrac{1}{2}(\partial_y\phi)^2 + V(\phi). \quad \text{(C2)}$$

As in previous parts $V(\phi) = 1 - \cos\phi$ and $\mathcal{F}(x,y) = 1 + \varepsilon g(x,y)$. Into the expression for the energy density we insert the kink ansatz $\phi_K(t,x) = 4\arctan e^{x - x_0(t)}$, where $x_0 = x_0(t)$ determines the position of the kink. Based on expression (C2), we calculate the energy per unit length of the kink front,

$$E(x_0) = \frac{1}{L_y}\int_{-\frac{L_x}{2}}^{+\frac{L_x}{2}}\int_{-\frac{L_y}{2}}^{+\frac{L_y}{2}} \rho(x,y,x_0)dxdy = \frac{1}{2}m\dot{x}_0^2 + \widetilde{V}(x_0). \quad \text{(C3)}$$

The first term has its origin in the differentiation of the kink ansatz with respect to the time variable $\partial_t\phi_K = -\dot{x}_0\,\partial_x\phi_K$ and $m = 8\tanh\frac{L_x}{2} \approx 8$ is the mass of a free, resting kink (where $L_x = 30$). The next terms define the potential energy. Under the assumption for the form of inhomogeneity $g(x,y) = -p(x)q(y)$, the potential energy can be expressed by two integrals,

$$\widetilde{V}(x_0) = 8 - 2\varepsilon I(d)J(x_0,h), \quad \text{(C4)}$$

where we denoted

$$I(d) = \frac{1}{Ly}\int_{-\frac{L_y}{2}}^{+\frac{L_y}{2}} q(y)dy = \frac{1}{L_y}\ln\left[\frac{\cosh\left(\frac{L_y+d}{2}\right)}{\cosh\left(\frac{L_y-d}{2}\right)}\right] \approx \frac{d}{L_y},$$
$$J(x_0,h) = \int_{-\frac{L_x}{2}}^{+\frac{L_x}{2}} p(x)\mathrm{sech}^2(x-x_0)dx. \quad \text{(C5)}$$

For a more compact result (and because of the rapid disappearance of the p function when approaching the edge), we approximate the second integral as follows:

$$J(x_0,h) \approx \int_{-\infty}^{+\infty} p(x)\mathrm{sech}^2(x-x_0)dx = -\left[\frac{2x_0 + h - \sinh(2x_0+h)}{\cosh(2x_0+h) - 1} - \frac{2x_0 - h - \sinh(2x_0-h)}{\cosh(2x_0-h) - 1}\right]. \quad \text{(C6)}$$

In the vicinity of the center of the well (i.e., for $x_0 = 0$), we can approximate the potential energy (C4) to the accuracy of the harmonic term,

$$\widetilde{V}(x_0) \approx A + Bx_0^2, \quad \text{(C7)}$$

where the expansion coefficients are respectively

$$A = 8 + 4\varepsilon\frac{d}{L_y}\left(\frac{h - \sinh h}{\cosh h - 1}\right), \quad B = 2\varepsilon\frac{d}{L_y}\mathrm{csch}^4\left(\frac{h}{2}\right)[h(2+\cosh h) - 3\sinh h]. \quad \text{(C8)}$$

We can rescale the original potential $\widetilde{V}(x_0)$ by a constant getting a new potential $V(x_0) = \widetilde{V}(x_0) - A$. The effective Lagrangian for this system is thus of the form

$$L = \tfrac{1}{2}m\dot{x}_0^2 - Bx_0^2. \quad \text{(C9)}$$

The effective equation is that of a harmonic oscillator

$$\ddot{x}_0 + \frac{2B}{m}x_0 = 0. \quad \text{(C10)}$$

The eigenfrequency of this oscillator describes, in a manner independent of the perturbation calculus performed in Appendix B (i.e., the latter is at the level of the equation of motion, while here we work at the level of the corresponding Lagrangian and energy functionals), the ground state appearing in the description of the linear stability of a kink trapped by a well-shaped inhomogeneity,

$$\omega^2 = \frac{2B}{m} = \frac{1}{2}\varepsilon\frac{d}{L_y}\mathrm{csch}^4\left(\frac{h}{2}\right)[h(2+\cosh h) - 3\sinh h]. \quad \text{(C11)}$$

The relevant result is showcased in Fig. 10.

[1] J. Frenkel and T. Kontorova, On the theory of plastic deformation and twinning, J. Phys. Acad. Sci. USSR **1**, 137 (1939).

[2] V. Zharnitsky, I. Mitkov, and M. Levi, Parametrically forced sine-gordon equation and domain wall dynamics in ferromagnets, Phys. Rev. B **57**, 5033 (1998).

[3] S. Bugaychuk, L. Kovács, G. Mandula, K. Polgár, and R. A. Rupp, Wave-mixing solitons in ferroelectric crystals, Radiat. Eff. Defects Solids **157**, 995 (2002).

[4] L. Lam, in *Solitons in Liquid Crystals*, edited by L. Lam and J. Prost (Springer, New York, 1992), pp. 9–50.

[5] B. D. Josephson, Possible new effects in superconductive tunnelling, Phys. Lett. **1**, 251 (1962).

[6] J. Perring and T. Skyrme, A model unified field equation, Nucl. Phys. **31**, 550 (1962).

[7] A. Xie, L. vanderMeer, W. Hoff, and R. H. Austin, Long-lived amide I vibrational modes in myoglobin, Phys. Rev. Lett. **84**, 5435 (2000).

[8] D. D. Georgiev, S. Papaioanou, and J. F. Glazebrook, Neuronic system inside neurons: Molecular biology and biophysics of neuronal microtubules, Biomed. Rev. **15**, 67 (2004).

[9] N. R. Walet and W. J. Zakrzewski, A simple model of the charge transfer in dna-like substances, Nonlinearity **18**, 2615 (2005).

[10] J. Bednář, Solitons in radiation chemistry and biology, J. Radioan. Nucl. Chem. **133**, 185 (1989).

[11] N. J. Zabusky and M. D. Kruskal, Interaction of “solitons” in a collisionless plasma and the recurrence of initial states, Phys. Rev. Lett. **15**, 240 (1965).

[12] P. G. Drazin and R. S. Johnson, *Solitons: An Introduction* (Cambridge University Press, Cambridge, UK, 1989).

[13] M. Ablowitz, B. Prinari, and A. Trubatch, *Discrete and Continuous Nonlinear Schrödinger Systems* (Cambridge University Press, Cambridge, UK, 2004).

[14] M. Ablowitz, *Nonlinear Dispersive Waves, Asymptotic Analysis and Solitons* (Cambridge University Press, Cambridge, UK, 2011).

[15] E. Bour, Theorie de la deformation des surfaces, J. l’École impér. polytechn. **22**, 1 (1862).

[16] C. S. Gardner, J. M. Greene, M. D. Kruskal, and R. M. Miura, Method for solving the korteweg-devries equation, Phys. Rev. Lett. **19**, 1095 (1967).

[17] V. E. Zakharov and A. B. Shabat, Exact theory of two-dimensional self-focusing and one-dimensional self-modulation of waves in nonlinear media, J. Exp. Theor. Phys. **34**, 62 (1970).

[18] M. J. Ablowitz, D. J. Kaup, A. C. Newell, and H. Segur, Method for solving the sine-gordon equation, Phys. Rev. Lett. **30**, 1262 (1973).

[19] M. J. Ablowitz and H. Segur, *Solitons and the Inverse Scattering Transform* (Society for Industrial and Applied Mathematics, Philadelphia, PA, 1981).

[20] A. C. Newell, *Solitons in Mathematics and Physics* (Society for Industrial and Applied Mathematics, Philedelphia, PA, 1985).

[21] R. K. Dodd, H. C. Morris, J. C. Eilbeck, and J. D. Gibbon, *Solitons and Nonlinear Wave Equations* (Academic Press, New York, 1982).

[22] D. W. McLaughlin and A. C. Scott, Perturbation analysis of fluxon dynamics, Phys. Rev. A **18**, 1652 (1978).

[23] A. Golubov, A. Ustinov, and I. Serpuchenko, Soliton dynamics in inhomogeneous Josephson junction: Theory and experiment, Phys. Lett. A **130**, 107 (1988).

[24] Y. S. Kivshar and B. A. Malomed, Dynamics of solitons in nearly integrable systems, Rev. Mod. Phys. **61**, 763 (1989).

[25] B. A. Malomed, Motion of a kink in a spatially modulated sine-gordon system, Phys. Lett. A **144**, 351 (1990).

[26] P. G. Kevrekidis, Variational method for nonconservative field theories: Formulation and two $\mathcal{PT}$-symmetric case examples, Phys. Rev. A **89**, 010102(R) (2014).

[27] R. Monaco, Engineering double-well potentials with variable-width annular Josephson tunnel junctions, J. Phys.: Condens. Matter **28**, 445702 (2016).

[28] M. A. Ablowitz and P. A. Clarkson, *Solitons, Nonlinear Evolution Equations and Inverse Scattering*, London Mathematical Society Lecture Note Series (Cambridge University Press, Cambridge, UK, 1991).

[29] M. J. Ablowitz, A. Ramani, and H. Segur, A connection between nonlinear evolution equations and ordinary differential equations of p-type. i, J. Math. Phys. **21**, 715 (1980).

[30] J. Weiss, M. Tabor, and G. Carnevale, The painlevé property for partial differential equations, J. Math. Phys. **24**, 522 (1983).

[31] J. Weiss, The sine-gordon equations: Complete and partial integrability, J. Math. Phys. **25**, 2226 (1984).

[32] J. D. Gibbon and G. Zambotti, The interaction of n-dimensional soliton wave fronts, Nuov. Cim. B **28**, 1 (1975).

[33] R. Carretero-González, L. Cisneros-Ake, R. Decker, G. Koutsokostas, D. Frantzeskakis, P. Kevrekidis, and D. Ratliff, Kink-antikink stripe interactions in the two-dimensional sine-gordon equation, Commun. Nonl. Sci. Numer. Simul. **109**, 106123 (2022).

[34] P. L. Christiansen and O. H. Olsen, Ring-shaped quasi-soliton solutions to the two- and three-dimensional sine-Gordon equation, Phys. Scr. **20**, 531 (1979).

[35] P. L. Christiansen and P. S. Lomdahl, Numerical study of 2+1 dimensional sine-Gordon solitons, Physica D **2**, 482 (1981).

[36] J. Geicke, On the reflection of radially symmetrical sine-Gordon kinks in the origin, Phys. Lett. A **98**, 147 (1983).

[37] B. Piette and W. J. Zakrzewski, Metastable stationary solutions of the radial d-dimensional sine-Gordon model, Nonlinearity **11**, 1103 (1998).

[38] J.-G. Caputo and M. P. Soerensen, Radial sine-Gordon kinks as sources of fast breathers, Phys. Rev. E **88**, 022915 (2013).

[39] B. A. Malomed, The sine-Gordon Model: General background, physical motivations, inverse scattering, and solitons, in *The Sine-Gordon Model and Its Applications: From Pendula and Josephson Junctions to Gravity and High-energy Physics*, edited by J. Cuevas-Maraver, P. G. Kevrekidis, and F. Williams (Springer International Publishing, Cham, 2014), pp. 1–30.

[40] M. A. García-Ñustes, J. F. Marín, and J. A. González, Bubble-like structures generated by activation of internal shape modes in two-dimensional sine-gordon line solitons, Phys. Rev. E **95**, 032222 (2017).

[41] J. F. Marín, Generation of soliton bubbles in a sine-Gordon system with localised inhomogeneities, J. Phys.: Conf. Ser. **1043**, 012001 (2018).

[42] A. G. Castro-Montes, J. F. Marín, D. Teca-Wellmann, J. A. González, and M. A. García-Ñustes, Stability of bubble-like fluxons in disk-shaped Josephson junctions in the presence of a coaxial dipole current, Chaos **30**, 063132 (2020).

[43] J. Gatlik, T. Dobrowolski, and P. G. Kevrekidis, Kink-inhomogeneity interaction in the sine-gordon model, Phys. Rev. E **108**, 034203 (2023).

[44] C. R. Galley, Classical mechanics of nonconservative systems, Phys. Rev. Lett. **110**, 174301 (2013).

[45] C. R. Galley, D. Tsang, and L. C. Stein, The principle of stationary nonconservative action for classical mechanics and field theories, arXiv:1412.3082 (2014).

[46] E. Kuznetsov and S. Turitsyn, Instability and collapse of solitons in media with a defocusing nonlinearity, Zh. Eksp. Teor. Fiz **94**, 129 (1988).

[47] J. Gatlik, T. Dobrowolski, and P. G. Kevrekidis, Animations for Figs. 6–9 (2023), http://tinyurl.com/mu4e3uxc.

[48] R. H. Goodman and R. Haberman, Kink-antikink collisions in the ϕ^4 equation: The n-bounce resonance and the separatrix map, SIAM J. Appl. Dyn. Syst. **4**, 1195 (2005).

Załącznik nr 2 do Zarządzenie nr 0101.4.2022
Dyrektora Szkoły Doktorskiej

JACEK GATLIK
imię, nazwisko/ name

Kraków, dnia/date 10.02.24

OŚWIADCZENIE/ DECLARATION

Świadomy/a odpowiedzialności oświadczam, że przedłożona rozprawa doktorska pt.:
Aware of my responsibility, I declare that the submitted dissertation entitled:

KINK DYNAMICS IN THE SINE-GORDON MODEL: INTERACTION WITH INHOMOGENEITIES

jest mojego autorstwa.
is my own creation.

Jednocześnie oświadczam, że w/w rozprawa nie narusza praw autorskich w rozumieniu Ustawy z dnia 4 lutego 1994 roku o prawie autorskim i prawach pokrewnych (Dz.U. z 2021 r. poz. 1062 z późn. zmianami) oraz dóbr osobistych chronionych prawem cywilnym.

At the same time, I declare that the aforementioned dissertation does not infringe upon copyrights within the meaning of the Act of 4 February 1994 on Copyright and Related Rights (Journal of Laws of 2021, item 1062, as amended) and personal rights protected by civil law.

Przedłożona praca nie zawiera danych empirycznych ani też informacji, które uzyskałem/am w sposób niedozwolony.

The submitted work does not contain empirical data or information that I have obtained by unauthorised means.

Stwierdzam, iż przedstawiona praca w całości ani też w części nie była wcześniej podstawą żadnej innej urzędowej procedury związanej z zakończeniem kształcenia w szkole doktorskiej.

I certify that the submitted work, in whole or in part, has not previously formed the basis of any other official procedure relating to the completion of training in doctoral school.

10.02.24
Data/date

Jacek Gatlik
Podpis doktoranta/ PhD student's signature

Załącznik nr 3 do Zarządzenie nr 0101.4.2022
Dyrektora Szkoły Doktorskiej

Jacek Gatlik
imię, nazwisko/ name

Kraków, dnia/date 10.02.24

OŚWIADCZENIE / DECLARATION
o zgodności wersji elektronicznej z wydrukiem
on the conformity of the electronic version with the hard copy

Ja niżej podpisany/~~podpisana~~* oświadczam, że wersja elektroniczna jest zgodna z wersją papierową rozprawy doktorskiej.
I, the undersigned*, declare that the electronic version is compatible with the paper version of the dissertation.

10.02.24
Data/date

Jacek Gatlik
Podpis doktoranta/ PhD student's signature

*Niewłaściwe skreślić/Delete as appropriate

Załącznik nr 4 do Zarządzenie nr 0101.4.2022
Dyrektora Szkoły Doktorskiej

JACEK GATLIK
imię, nazwisko/ name

Kraków, dnia/date 10.02.24

OŚWIADCZENIE / DECLARATION

Ja niżej podpisany/~~podpisana~~* ~~wyrażam zgodę~~/nie wyrażam zgody* na udostępnianie mojej rozprawy doktorskiej w wersji papierowej i elektronicznej dla celów naukowych i dydaktycznych.
I, the undersigned, ~~consent~~/do not consent* to my dissertation being made available in hard copy and electronic format for research and teaching purposes.

10.02.24
Data/date

Jacek Gatlik
Podpis doktoranta/ PhD student's signature

*Niewłaściwe skreślić/Delete as appropriate